Amine-Decorated Polymer Immobilised Ionic Liquid Stabilised Metal Nanoparticles: Synthesis and Applications in Catalysis

Adhwa Abdulghani Alharbi

A thesis submitted in partial fulfilment of the requirements

for the degree of

Doctor of Philosophy in Chemistry

School of Natural and Environmental Sciences

Newcastle University

September 2024

Abstract

Polymer-immobilised ionic liquid (PIIL) phase catalysis has gained attention due to the increased demand for efficient synthetic protocols and sustainable transformation processes. New methods are needed to improve the sustainability of current chemical processes. The Doherty-Knight group has been focused on developing modified polymer-immobilised ionic liquids to stabilise and modify the reactivity of nanoparticle catalysts. The first chapter explores the unique physical and chemical properties of ionic liquids (ILs) that make them suitable for various applications, including the stabilisation of metal nanoparticles (NPs), as well as the synthesis and application of polymer-immobilized ionic liquids (PIILs).

Chapter 2 describes the synthesis of monomers and heteroatom-functionalised polymer immobilised ionic liquids as supports for the stabilisation of RuNPs. The amino-modified catalyst was found to catalyse the aqueous hydrolysis of $NaBH_4$ efficiently to produce hydrogen under mild conditions. RuNP@NH_2-PIILS exhibited higher activity than RuNP@NH_2-PEGPIILS. Notably, RuNP@NH_2-PIIL achieves one of the highest turnover frequencies (TOF) reported for RuNP-based catalysts (171 $mol_{H2}.mol_{cat}^{-1}.min^{-1}$). In addition, it was recycled up to five times.

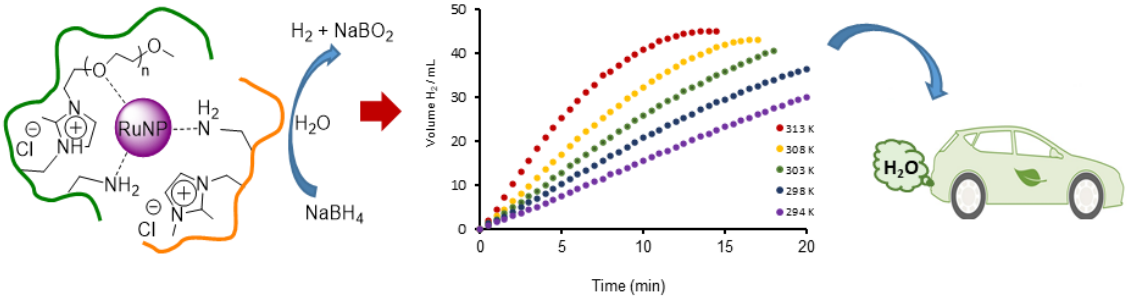

Chapter 3 highlights the efficiency of the RuNP@NH_2-PEGPIILS catalyst for the reduction of quinolines to 1,2,3,4-tetrahydroquinoline (THQ) via 1,2-dihydroquinoline (DHQ). The initial TOF of 610 mol quinoline converted mol Ru^{-1} h^{-1} for the reduction of quinoline is among the highest to be reported for a metal nanoparticle-based catalyst with a conversion of 96% obtained after 4 h at 65°C. A wide range of substituted quinolines were successfully reduced to either the corresponding 1,2-dihydroquinoline or 1,2,3,4-tetrahydroquinoline in short reaction times. Hot filtration experiments showed that the active species was heterogeneous.

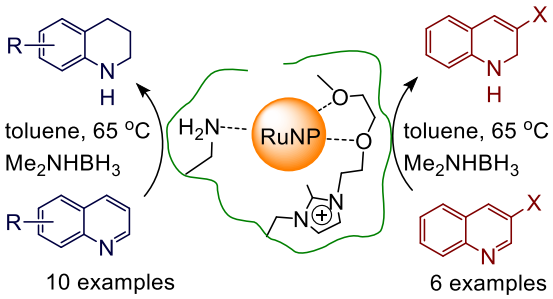

Chapter 4 describes a comparison of RuNP@NH_2-PEGPIILS and PtNP@NH_2-PEGPIILS as catalysts for the dehydrogenation of DMAB and AB. It demonstrated that RuNP@NH_2-PEGPIILS is a more efficient catalyst than PtNP@NH_2-PEGPIILS for the dehydrogenation of DMAB and AB, as RuNP@NH_2-PEGPIILS gave initial TOFs of 8,300 molesH_2.molcat^{-1}.h^{-1} and 21,200 molesH_2.molcat^{-1}.h^{-1}, respectively, compared with 3,050 molesH_2.molcat^{-1}.h^{-1} and 8,500 molesH_2.molcat^{-1}.h^{-1}, respectively, for PtNP@NH_2-PEGPIILS. In addition, RuNP@NH_2-PEGPIILS showed high stability and reusability for the hydrolysis of DMAB over multiple cycles.

Chapter 5 describes the synthesis of a range of RuNPs and PtNPs stabilised by an amine-modified ordered mesoporous silica immobilised ionic liquid (OMSIIL). The examined nanoparticles were shown to be highly efficient catalysts for hydrogen evolution from $NaBH_4$. This work aims to achieve a deeper understanding of this system and identify more effective catalysts for scale-up purposes.

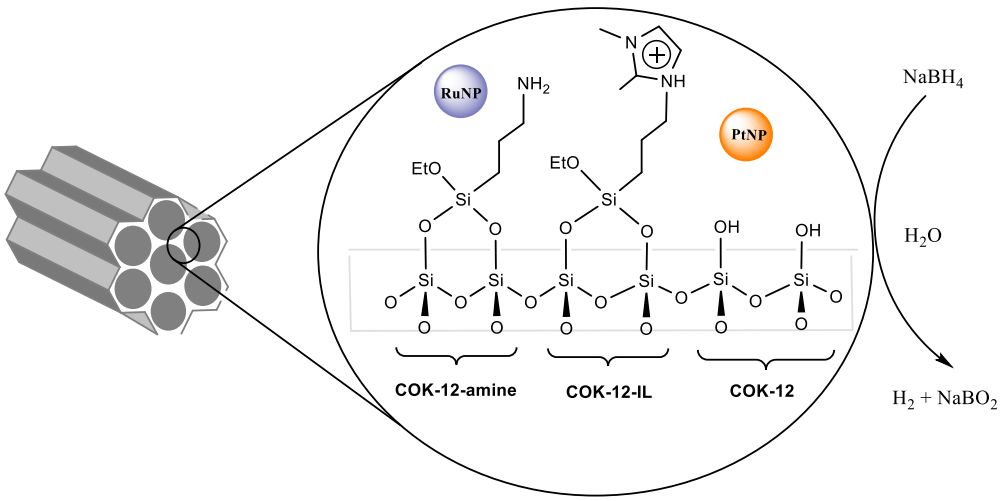

Dedication

This thesis is dedicated to

My beloved parents, Dr. Abdulghani and Naeemah.

My husband Abdulrahman and my children Yasmin and Wesam.

Acknowledgements

I am deeply grateful to my research supervisors, Dr Simon Doherty and Dr Julian Knight, for their exceptional guidance, patience, and unwavering support over the past four years. Their mentorship has been instrumental in shaping this thesis, and I am fortunate to have benefited from their wealth of knowledge and expertise.

I would also like to extend my sincere thanks to the academic collaborators, Dr Tom Chamberlain and his team at Leeds University, whose contributions were crucial to advancing my research. My gratitude further goes to the technical support staff at Newcastle University: Dr Corinne Wills and Dr Casey Dixon (NMR), Dr Henriette Christensen (ICP), Dr Tracey Davey (SEM), and Dr Elisabetta Arca (XPS), for their invaluable assistance.

I am incredibly appreciative of my friends and colleagues from the research group, Dr Hussam Alharbi, Reece Paterson, Sam Power, and Tahmina Begum, for creating such a supportive and vibrant work environment. I also want to acknowledge my dear friends from other groups, Dr Afkar Alshammari and Dr Aeshah Alrubayyi, whose friendship, support, and advice enriched my experience and left me with cherished memories. I want to thank Taibah University for the scholarship and financial support that made this research possible.

With heartfelt appreciation, I thank those who played a pivotal role in my journey of studying abroad and completing this doctoral thesis, particularly my parents, Dr. Abdulghani and Naeemah. Their endless love, sacrifices, and steadfast support have carried me through every phase of my life. I am also deeply thankful to my husband, Abdulrahman, for his encouragement, patience, and unconditional support, which have been my greatest source of strength. To my wonderful children, Yasmin and Wesam, your endless affection and smiles gave me the energy to keep pushing forward. My deepest love and gratitude also go to my brothers, sisters, and friends, whose encouragement has meant the world to me.

Above all, I am profoundly grateful to Allah Almighty (God) for the countless blessings in my life and for giving me the strength and perseverance to complete this journey.

Thank you all.

List of Publications

1. R. Paterson, **A. A. Alharbi**, C. Wills, C. Dixon, L. Šiller, T. W. Chamberlain, A. Griffiths, S. M. Collins, K. Wu, M. D. Simmons, R. A. Bourne, K. R. J. Lovelock, J. Seymour, J. G. Knight and S. Doherty ” Heteroatom modified polymer immobilized ionic liquid stabilized ruthenium nanoparticles: Efficient catalysts for the hydrolytic evolution of hydrogen from sodium borohydride”, Mol. Catal., **2022**, 528, 112476.

2. **A. A. Alharbi**, C. Wills, T. W. Chamberlain, R. A. Bourne, A. Griffiths, S. M. Collins, K. Wu, P. Mueller, J. G. Knight and S. Doherty ” Amino-Modified Polymer Immobilized Ionic Liquid Stabilized Ruthenium Nanoparticles: Efficient and Selective Catalysts for the Partial and Complete Reduction of Quinolines”, ChemCatChem, **2023**, 15, e202300418.

3. Doherty, J. G. Knight, **A. A. Alharbi**, C. Wills, C. Dixon, C. Cheng, F. Russo Abegão, T. W. Chamberlain, H. Yan, A. Griffiths, R. A. Bourne, S. M. Collins, K.-J. Wu and H. Alshaikh.” Selective Partial Reduction of Nitroarenes to the Hydrazoarene Catalyzed by Amine-Modified Ordered Mesoporous Silica Immobilized Ionic Liquid (OMSIIL) Stabilised RuNPs”, ChemCatChem, **2024**, e202400013.

4. **A. A. Alharbi**, C. Wills, C. Dixon, E. Arca, T. W. Chamberlain, A. Griffiths, S. M. Collins, K. Wu, H. Yan, R. A. Bourne, J. G. Knight and S. Doherty “Efcient Hydrogen Evolution from Dimethylamine Borane, Ammonia Borane and Sodium Borohydride Catalyzed by Ruthenium and Platinum Nanoparticles Stabilized by an Amine Modifed Polymer Immobilized Ionic Liquid: a Comparative Study”, Catal. Lett., **2024**, DOI:10.1007/s10562-024-04725-8.S.

List of symbols and abbreviations

AB Ammonia Borane

AIBN Azobisisobutyronitrile

BET Brunauer-Emmett-Teller

CNT Carbon nanotubes

CVD Chemical vapour deposition

DHQ 1,2-dihydroquinoline

DLS Dynamic light scattering

DMA Differential Mobility Analyser

DMAB Dimethylamine Borane

DRS Diffuse Reflectance Spectroscopy

DVB divinylbenzene

Ea Activation energy

EDX Energy Dispersive X-ray

FT-IR Fourier Transform InfraRed

ICP-OES Inductively Coupled Plasma Optical Emission Spectrometry

IL Ionic liquid

MOF Metal Organic Frameworks

NMR Nuclear Magnetic Resonance

NP nanoparticle

OMS Ordered Mesoporous Silica

OMSIIL Ordered Mesoporous Silica Immobilized Ionic Liquid

PEG polyethylene glycol

PIIL Polymer-Immobilised Ionic Liquid

PIILS Polymer-Immobilised Ionic Liquid Phase

ppm parts per million

PS polystyrene

RAFT Reversible addition-fragmentation chain-transfer

ROMP Ring-Opening Metathesis Polymerisation

SCILL Solid Catalyst with Ionic Liquid Layer

SEM Scanning Electron Microscopy

SILP Supported Ionic Liquid Phase

SMPS Scanning Mobility Particle Sizer

TEM Transmission Electron Microscopy

TGA Thermal Gravimetric Analysis

THQ 1,2,3,4-tetrahydroquinoline

TOF turnover frequency

TON turnover number

wt. % Weight percentage of total mass

XPS X-ray Photoelectron Spectroscopy

XRD X-ray Diffraction

δ Chemical shift

Table of Contents

Chapter 1: Introduction

1.1 Nanoparticles

Nanoparticles (NPs) are minute particulate substances with multidimensional shapes that are less than 100 nm in size. They have the potential to alter the physicochemical properties of a substance.[1] According to the International Union of Pure and Applied Chemistry, nanoparticles are particles within the range of 1×10^{-9} and 1×10^{-7} m in dimension,[2] and according to Tiwari *et. al*.,[1] these particles can be zero-dimensional, where all dimensions are at the nanoscale such as nanospheres; one-dimensional (one dimension is much longer than the others), such as nanorods; two-dimensional, having a large surface area in two dimensions such as nanosheets; or three-dimensional, extended in all three dimensions such as, nanostructured networks. They are used in various fields and are composed of a surface layer that can be functionalised with metal ions, surfactants, polymers, and other small molecules; a shell layer, which differs chemically from the core; and a core, which is the central portion of the nanoparticle.[3] Nanoparticles have been widely used in photocatalytic applications to generate and store energy at the nanoscale level.[4] They have also been applied in carbon-carbon and carbon-heteroatom bond formation,[5] redox chemistry, and biomass conversion.

1.1.1 History of Nanoparticles

The American physicist Richard Feynman, a Nobel Prize laureate, is credited as the imaginative pioneer and father of modern nanotechnology. He introduced the concept in 1959 in his lecture titled “There’s Plenty of Room at the Bottom”.[6] However, nanoparticles have been used by humans as far back as the 4th century. One fascinating example of their use is seen in the design of the Lycurgus cup by the Romans. The Lycurgus cup is made of dichroic glass, which changes colour under different lighting conditions. Scientists discovered in 1990 that the phenomenon of dichroism in the Lycurgus cup was made possible by embedded metal nanoparticles that are 50–100 nm in diameter.[7]

In 1857, while studying the preparation of colloidal suspensions of Ruby gold and its properties, Michael Faraday discovered that gold nanoparticles exhibit the phenomenon of dichroism due to their unique optical and electronic properties.[8] This discovery was a notable addition to the progression of nanotechnology. Other significant landmark was the invention

of the Scanning Tunneling Microscope (STM),[9] Atomic Force Microscope (AFM), Scanning Probe Microscopes (SPM), and Transmission Electron Microscopy (TEM),[10] as well as advances in carbon chemistry through the discovery of fullerenes[11] and carbon dots.[12] These discoveries have significantly advanced nanotechnology research due to their broad applicability in various nanotechnological fields.

1.1.2 Classification of nanoparticles

Nanoparticles can be categorised based on their morphology, chemical properties, and physicochemical characteristics into three main groups: carbon-based, organic, and inorganic nanoparticles.

1. **Carbon-based nanoparticles:** This classification comprises nanoparticles entirely made of carbon, including fullerenes, carbon nanotubes (CNTs), graphene, carbon nanofibers, and carbon black.[13]
2. **Organic nanoparticles:** These are biodegradable organic nanoparticles with typical examples including Liposomes, Dendrimers and Micelles.[14] They are generally polymeric or lipid-based and are mainly used in targeted drug delivery in biomedicine.[15]
    i) **Polymeric NPs,** also known as polymer nanoparticles (PNP), are primarily nanospheres or nanocapsules in shape.[16] Nanosphere PNP have a solid mass and adsorbs other molecules at the outer boundary of its spherical surface.[17]
    ii) **Lipid-Based NPs:** These types are typically spherical with a diameter ranging from 10 nm to 100 nm and have a lipid-based solid core and soluble lipophilic molecules as the matrix.[18]
3. **Inorganic Nanoparticles**

These nanoparticles are not derived from a carbon source. They can be subclassified as metal-based, metal oxide-based, semiconductor, and ceramics nanoparticles.

i. **Metal-based Nanoparticles:** These nanoparticles are exclusively made from metal precursors and range in size from 10 nm to 100 nm. They are synthesised using methods that either break down or constructively convert metals into their nanoscale form, not just

through the conversion of metals, as precursors are often used to generate nanoparticles (NPs) by reduction. Metal nanoparticles have unique properties, including their optoelectrical properties, surface characteristics, and surface charge density, which make them essential in various nanotechnology applications. They can be spherical or cylindrical, and have both crystalline and amorphous structures, with high reactivity and sensitivity to environmental factors. Metals such as aluminium, gold, iron, lead, cadmium, cobalt, copper, silver, and zinc are commonly used to produce metal nanoparticles.[19]

ii. **Metal Oxides-Based Nanoparticles:** This category is modified forms of metal-based nanoparticles. They are usually synthesised to improve the properties of their metal nanoparticles. They possess exceptional properties and have an increased reactivity and efficiency compared to their metal counterparts. Common examples include iron oxide, magnetite, aluminum oxide, silicon dioxide, cerium oxide, titania and zinc oxide.[20]

iii. **Semiconductor Nanoparticles:** These are nanoparticles whose properties fall between those of metals and nonmetals.[21] Due to their wide band gaps, they are mainly valuable for photocatalysis, photo optics, and water splitting.[22]

iv. **Ceramics Nanoparticles:** They are made up of non-metallic solids produced via alternative heating and cooling processes. They could be amorphous, porous, dense, or polycrystalline in nature[23] and greatly important in the photodegradation of dyes, imaging applications, and photocatalysis.[24]

1.1.3 Characterisation of Nanoparticles

Nanoparticles can be characterised morphologically, optically, structurally, and through their particle size, surface area, and surface charge. Techniques such as SEM, TEM, X-ray diffraction (XRD), X-ray photoelectron spectroscopy (XPS), particle size analysis, Brunauer–Emmett–Teller (BET), and infrared (IR) have made the characterisation of nanoparticles possible.[25]

I. **Morphological Characterisations:** Due to the influence of morphology on nanoparticles' properties, they are usually characterized using microscopy-based techniques such as TEM, SEM and Polarized Optical Microscopy (POM).[26]

II. **Optical Characterisations:** The techniques used for optical characterisation help study the optical properties of nanoparticles, such as luminescence, reflectivity, absorption, and phosphorescence. These properties play an enormous role in the photocatalytic application of nanoparticles.[27] These techniques, which find their roots in the Beer-Lambert law, include UV spectroscopy, photoluminescence and UV / Diffuse Reflectance Spectroscopy (DRS).[28]

III. **Structural Characterisation:** Nanoparticles' structural characteristics help study the composition and nature of their bonding. Techniques used in structural characterisation include XPS, XRD, Energy Dispersive X-ray (EDX), Raman, BET, and zeta potential analysis.[26]

IV. **Particle Size Characterisation:** Particle size characterisation is arguably the most essential nanoparticle characterisation as it determines if the particle falls under nano or micro scale. It is commonly measured using electron microscopy. Other techniques include the use of Scanning Electron Microscopy (SEM), Transmission Electron Microscopy (TEM), Laser diffraction methods, Photon correlation spectroscopy and centrifugation, Dynamic light dispersing (DLS), and Scanning Mobility Particle Size Analysis (SMPS).[29]

V. **Surface Area Characterisation:** Surface area is another essential factor in nanoparticle characterisation, as a nanoparticle's surface area to volume ratio plays an important role in its performance and properties. Characterisation techniques include BET analysis, titration, nuclear magnetic resonance spectroscopy (NMR), and differential mobility analysis (DMA).[29]

I. **Surface Charge Characterisation:** This characterisation helps to determine a nanoparticle's interaction with a target. Measuring techniques involve the use of a Zeta potentiometer[32] and a Differential Mobility Analyser (DMA).[29]

1.1.4 Synthesis of metal nanoparticles

Nanoparticles can be synthesised by various methods. They can be created using a bottom-up approach, in which the nanoparticles are constructed from simpler substances, or a top-down approach, in which they are derived from bulk materials (Figure 1.1).[30]

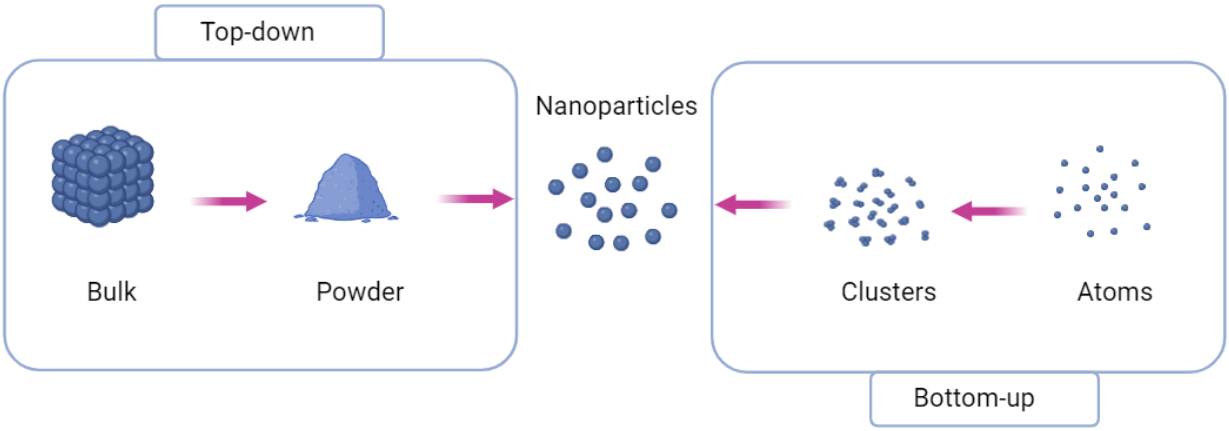

Figure 1.1 Synthesis of nanoparticle.

1. Top-down method

This method, also known as the destructive method, involves synthesising nanomaterial by breaking down bulk material into nanoscale particles. Top-down techniques include mechanical milling, thermal decomposition, nanolithography, sputtering, and laser ablation.[26]

2. Bottom-up method

This method, also known as the constructive method, involves the gradual build-up of nanomaterials from atoms to clusters to nanoparticles. Bottom-up techniques include sol-gel, pyrolysis, chemical vapor deposition (CVD), and biosynthesis.[26]

This approach is a more feasible and widely used technique for the synthesis of metal nanoparticles as it allows for the design of catalysts by providing the ability to regulate the shape, size, and uniformity of the nanoparticles. Moreover, it also permits the control and adjustment of the factors that ultimately determine the catalytic effectiveness and selectivity of the newly created catalyst.[31,32]

1.2 Nanoparticles Stabilisation

Nanoparticles require stabilisation to maintain their size, prevent aggregation, and preserve their functional properties. Without effective stabilisation, several phenomena can occur that compromise the stability and performance of nanoparticles, including Ostwald ripening,[33] aggregation, and surface energy effects.[34]

I. **Surface Energy and Instability:** Due to their small size, nanoparticles possess a high surface energy, which makes them thermodynamically unstable. They tend to lower this energy by either coalescing with other nanoparticles or reacting with their environment, both of which lead to instability. Stabilisation helps reduce the surface energy by coating the nanoparticles with protective agents such as surfactant, polymers or ligands. This barrier prevents undesired reactions and helps maintain the nanoparticles' nanoscale size, preserving their unique properties.[34]

II. **Ostwald Ripening:** One of the main reasons for stabilising nanoparticles is to prevent Ostwald ripening. This process occurs when smaller nanoparticles dissolve, and the material is redeposited onto larger nanoparticles, causing the larger ones to grow at the expense of the smaller ones. This leads to a broader size distribution, reducing the effectiveness of nanoparticles in applications where uniform size is crucial.[33] Stabilisation can mitigate Ostwald ripening by limiting the solubility and mobility of nanoparticles, ensuring they retain their original size and distribution.[35]

III. **Minimising Aggregation:** Nanoparticles have a high surface area-to-volume ratio, making them prone to aggregation. This aggregation is driven by the tendency of nanoparticles to reduce their surface energy by clumping together, leading to larger clusters. When aggregation occurs, it often results in the loss of the desired properties of the nanoparticles, such as reduced reactivity and surface area. Stabilisation methods, such as steric and electrostatic stabilisation, introduce repulsive forces between nanoparticles to prevent them from coming into close contact and aggregating.[36]

IV. **Preserving Functional Properties:** Many of the unique properties of nanoparticles, such as their catalytic activity, optical characteristics, and electrical conductivity, depend on their size and dispersion. When nanoparticles aggregate or grow larger due to Ostwald ripening, these properties can be significantly altered or lost. Stabilisation ensures that nanoparticles remain dispersed and maintain their size, thereby preserving their functional properties for various applications.[37]

To this end, stabilisation is a critical aspect of nanoparticle synthesis and application as it prevents degradation mechanisms such as Ostwald ripening, aggregation, and surface instability. By ensuring that nanoparticles retain their desired size and characteristics,

stabilisation enhances their performance in a wide range of technological and industrial applications.

The stabilisation of metal nanoparticles usually involves three approaches: steric stabilisation, electrostatic stabilisation, and a combination of both (electrosteric stabilisation). Each method provides unique mechanisms to prevent aggregation and preserve nanoparticle stability (Figure 1.2).

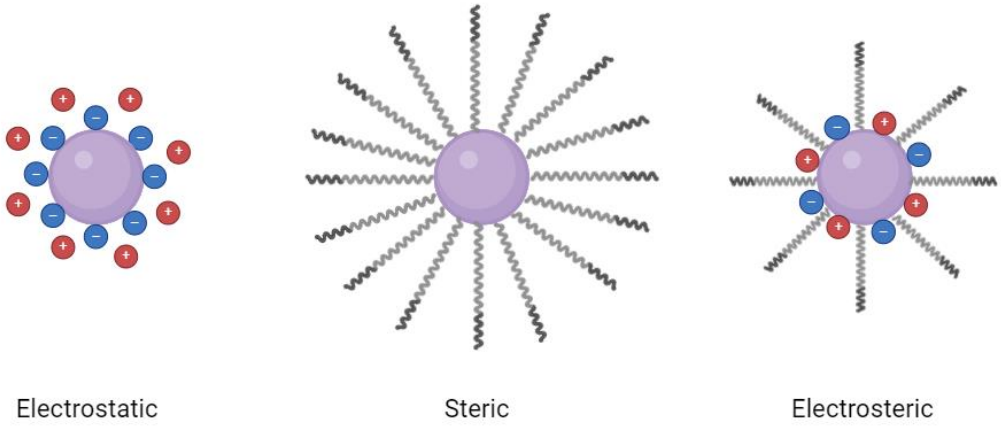

Figure 1.2 : Stabilisation methods of metal nanoparticles.

1. **Electrostatic Stabilisation**

In the stabilisation method known as electrostatic stabilisation, nanoparticles are surrounded by a double layer of electric charge, resulting in repulsive forces when two particles approach each other. According to the Derjaguin, Landau, Verwey and Overbeek (DLVO) theory, colloidal particles with electric charges are initially present, and these charges are evenly distributed over the surface of the nanoparticle. The use of ionic liquids (ILs) provides electrostatic stabilisation to metal nanoparticles by creating a protective shell around them. This protective shell, which is primarily anionic, is responsible for the stability of the metal nanocluster.[38] The documented use of ionic liquids (ILs) has demonstrated their effectiveness in improving stability and providing electrostatic protection against aggregation in metal nanoparticles.[39,40]

2. Steric Stabilisation

The second technique for stabilisation relies on steric repulsion between molecules or ions adsorbed on neighbouring particles, which affects their size and chemical characteristics, thus, establishing the level of stabilisation. The spatial constraints around the surface of nanoparticles generally allow large, bulky molecules to provide stabilisation effectively.[41] When the length of the stabilising agent used is significantly greater than the characteristic size of the nanoparticles, there is a greater chance of forming a sphere that encloses the nanoparticle. A stabilising agent with multiple coordination sites offers advantages as the chelate effect increases the likelihood of the stabilising agent remaining adsorbed. Chemisorption serves as the primary driving force for the strong binding between the stabiliser and the nanoparticle surface.[42] Metals with vacant valence orbitals possess an "electron deficient" surface; thus, atoms or molecules with strongly "donating" π-electrons typically adsorb to the metal nanoparticle surface. Therefore, steric stabilisation plays a crucial role in the process of nanoparticle synthesis.[42,43]

Wang and colleagues have synthesised bimetallic Au-Pd nanoparticles using graphene oxide as a stabilising agent. These nanoparticles function as efficient catalysts for selectively oxidising various alcohols. The metal:graphene oxide ratio was adjusted to control nanoparticle size and minimise cavity space for growth within the graphene oxide sheets. They also introduced titania (TiO_2) as a template to further enhance catalytic activity by forming a two-dimensional graphene oxide layer to prevent particle aggregation under catalytic conditions. This approach eliminated the need for organic surfactants, which could hinder substrate access to the catalyst's active sites.[44]

3. Electrosteric Stabilisation

Large molecules can be functionalised with ionic/polar head groups to achieve a combination of electrostatic and steric stabilisation. Methods for achieving this include the use of amphiphilic polymers,[45] polyacrylate dispersions,[46] designer ionic liquids containing long alkyl chains, and heterogeneous catalyst supports with heteroatom donors (which may include ligands that help stabilise nanoparticles). Electrosteric stabilisation can be provided using bulky and highly charged adsorbents,[47] ionic stabilisers,[48] and heteroatom-donor modified

polymer immobilised ionic liquid (PIIL) supports.[49] These methods can regulate nanoparticle size, distribution, and morphology and improve catalyst activity and selectivity. Furthermore, the application of PIIL-based supports for stabilising metal nanoparticles has been demonstrated to be effective in catalysis, resulting in a longer catalyst lifetimes and increased turnover numbers.[50]

1.3 Nanoparticles for Catalysis

The unique nature and physicochemical characteristics of nanoparticles have made them increasingly important in various areas. They are used in the biomedical field for drug delivery, medication application, and the development of novel nanodevices which can be applied in numerous physical, biological, biomedical, and pharmaceutical applications.[51] Additionally, they are known to aid the manufacturing industry in producing various nanodevices, industrial and household applications,[26] cosmetics and sunscreens,[14] the production of electronic equipment[52] and mechanical industries.[53] The use of nanoparticles as catalysts is essential because they can enhance the reaction rate without being consumed. This is done by reducing the activation energy (Ea) for the reaction (Figure 1.3) and the acceleration in the reaction rate is a measure of the effectiveness of the catalyst. In the case of reactions producing multiple products, a catalyst might promote the formation of specific products, which is known as catalyst selectivity.[54]

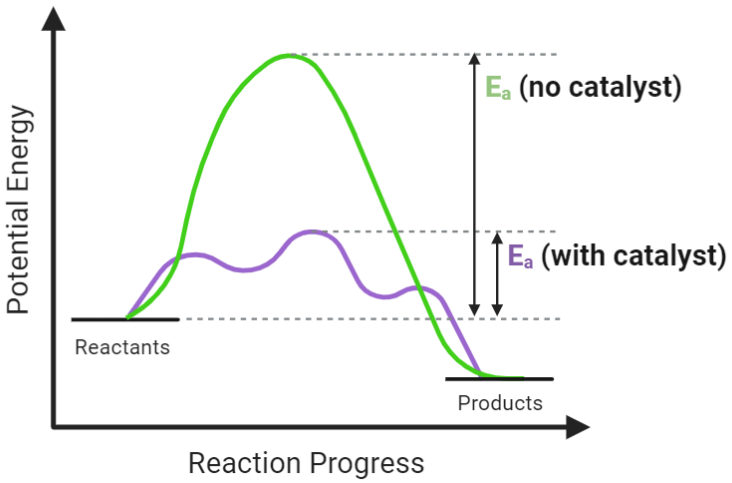

Figure 1.3 The effect of catalyst on activation energy.

There are two types of catalysis:

I. **Homogeneous catalysis** is when the catalyst is dissolved in the same phase as the reaction mixture, usually the liquid phase. This form of catalysis provides the benefit of having distinct and consistent active sites. However, while homogeneous catalysts often show high activity and selectivity, they also come with particular challenges, such as issues with separation from the products and decreased efficiency during recycling due to the loss of catalyst. Additionally, the use of expensive metals and ligands in many homogeneous catalysts can significantly increase the overall cost of the catalytic process.[55]

II. **Heterogeneous catalysis** occurs when the catalyst and reactants are in different phases, such as solid/gas, solid/liquid, or solid/liquid/gas. This type of catalysis is significant because it adheres to the principles of green chemistry and process development in industries.[54] The separation and recovery of the catalyst is often straightforward, with fewer complications due to the distinct difference in solubility and miscibility between the catalyst and the product. Despite the potential advantages, the main challenge in developing new heterogeneous catalysts is achieving high activity and selectivity levels that can rival those of homogeneous catalysts.[56]

Nanoparticle-based catalysts have been applied in hydrogenation, dehydrogenation, automotive off-gas cleaning, oxidation, and C-C and C-heteroatom coupling reactions. They are preferred in several chemical processing industries due to their potential for reducing and enabling more sustainable reaction conditions.[26]

Their high surface area to volume ratio enhances catalytic efficiency, making them valuable tools in advancing green chemistry, renewable energy harvesting and biomass conversion into fuels, as demonstrated in several studies.[57,58] However, a key challenge in their use is nanoparticle aggregation, which reduces active surface area and can negatively affect catalytic performance. To address this, ionic liquids and polymer-immobilised ionic liquids have gained popularity for stabilising nanoparticles and preventing leaching, offering effective solutions while retaining high catalytic activity.[59]

1.4 Ionic Liquids

Ionic liquids (IL) are unique solvents consisting of cations (mostly organic moieties) and anions, which melt below 100 °C.[60] They are also known as liquid electrolytes, ionic melts, fluids, fused salts, or ionic glasses. These compounds are often referred to as salt in their liquid state, but it's important to note that this context is limited to salts with a melting point below 100 °C (212 °F).[60] This sets them apart from molten salts, which have high melting points and are highly viscous and corrosive. The first IL, ethyl ammonium nitrate, was discovered by Paul Walden in 1914. Since then, ILs have garnered significant attention as innovative fluids, leading to interdisciplinary studies from various fields such as chemistry, materials science, chemical engineering, and environmental science.[60,61]

1.4.1 Synthesis of ionic liquids

Ionic liquids are most often composed of large, asymmetric cations such as derivatives of pyridinium, imidazolium, pyrrolidinium, ammonium, phosphonium, and sulfonium, paired with large symmetrical anions like halides, hexafluorophosphate, tetrafluoroborate, and trifluoroacetate. The synthesis typically involves the process of cation and anion metathesis (Figure 1.4). The cation formation can be achieved through protonation with a protic acid, quaternisation of an amine or phosphine, or ternary alkylation of a sulfide with an alkyl halide or dialkyl sulfate. Anion metathesis is then used to replace corrosive halide anions with less reactive, inert anions, this process creates an ionic liquid with desirable chemical properties.[62]

I. **Purification of Ionic Liquids:** The purification of ionic liquids (ILs) is a crucial step to ensure their effectiveness and stability in various applications. After synthesis, ILs often contain residual impurities such as unreacted starting materials, by-products, or trace contaminants. Effective purification techniques, such as washing, filtration, and drying, are employed to remove these impurities. This step is essential to avoid issues such as unwanted reactivity or degradation of the IL's properties. Detailed purification methods have been discussed in the literature.[63] Proper purification ensures that ILs meet the required purity standards for their intended uses, including in catalytic and industrial processes.

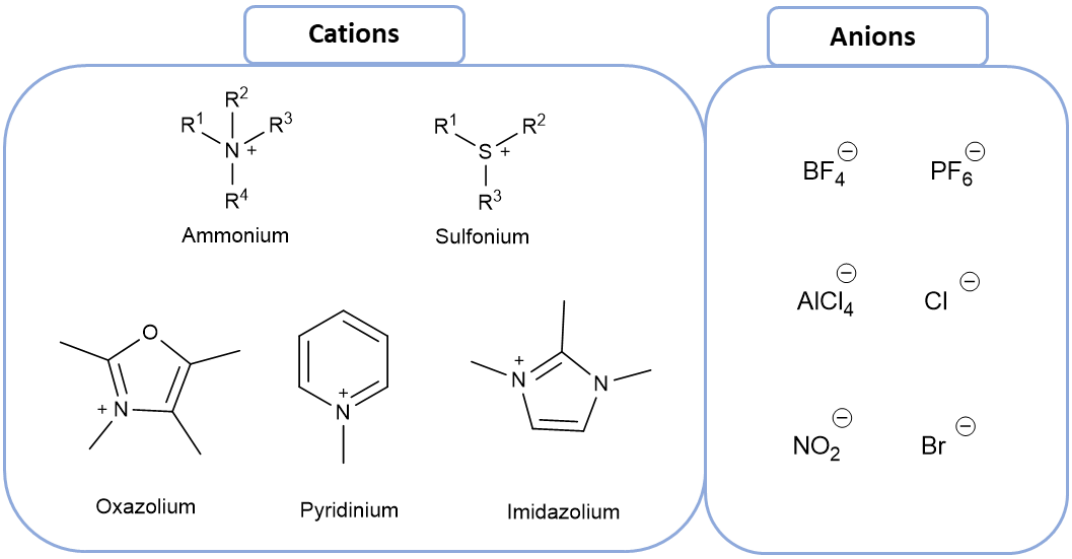

Figure 1.4 Overview of common cations and anions used for designing IL.

1.4.2 Characteristics and types of ionic liquids

Some key characteristics of ionic liquids include low vapour pressure at room temperature, non-flammability, low to poor electrical conductivity, non-ionising properties, high viscosity, high chemical and thermal stability over a broad temperature range, and low melting points. They are excellent solvents for both inorganic and organic compounds, have high ionic conductivity and a wide electrochemical potential window, and can act as catalysts.[64] Ionic liquids are denser than water, with densities ranging from 1 to 1.6 g/mL, and their surface tension and refractive index vary based on the length and branching of the alkyl chain on the cation. Recent research has also indicated that they have low toxicity and are biodegradable.[60,65,66]

Ionic Liquids come in various types and classifications. Some examples include room-temperature ILs, which have a melting point lower than room temperature,[67] and polyionic liquids, which are subclasses of polyelectrolytes featuring an ionic liquid attached to one of the repeat units forming a macromolecular architecture.[68] Task-specific ILs are meant for specific applications,[69] for example, a common task-specific IL is 1-butyl-3-methylimidazolium acesulfame ([C_4mim][Ace]), which is used for the extraction of biomolecules due to its ability

to solubilise a wide range of organic compounds.[70] Additionally, supported IL membranes include composites of ILs supported on metal-organic frameworks.[71]

1.4.3 Applications of ionic liquids

Ionic liquids (ILs) are versatile and have a wide range of applications (Figure 1.5). They are used for storing and handling gases, including the sequestration of CO_2, and serve as a transport medium for reactive gases due to their low vapour pressure and thermal stability. ILs are also used to store solar thermal energy and aid in the recycling of manufactured goods, plastics, and metals. Research has shown that ILs can replace water as an electrolyte in metal-air batteries and function as dispersing agents in paints. ILs play a crucial role in polymer science, particularly in biphasic ethylene polymerisation and cellulose dissolution. Moreover, ILs are important in nanotechnology for extracting and separating novel solvents in analytical chemistry.[72] They also have applications in liquid chromatography, organic synthesis, coupling and hydrogenation reactions, the petroleum industry, biotechnology, membrane separation processes, electrochemical and biosensors, and in the production of insecticides.[73,74]

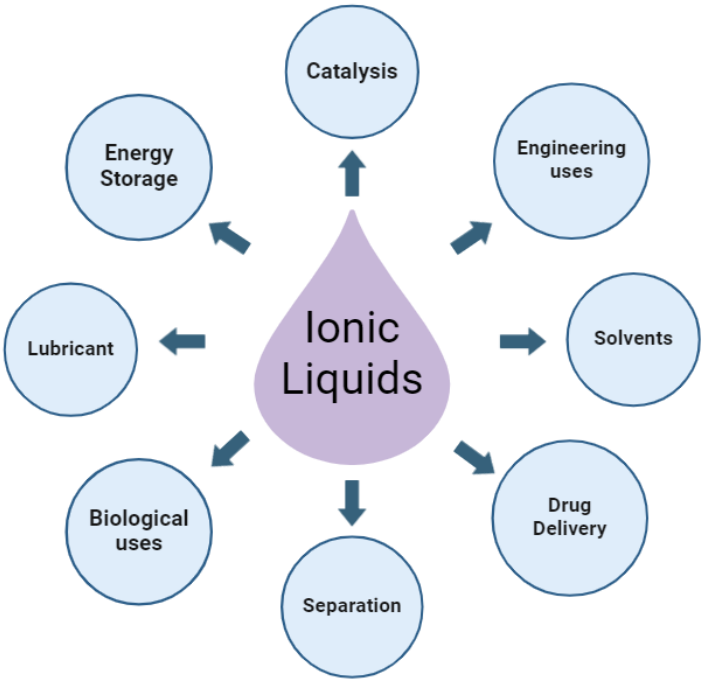

Figure 1.5 Main application areas of Ionic Liquids (IL).

1.4.4 Ionic Liquids in Catalysis

The use of vital natural resources worldwide has risen notably due to population growth and technological advancements. Scientists are attempting to develop more eco-friendly and effective chemical production methods. To address growing demands in an environmentally friendly manner, catalysis has played a crucial role in developing sustainable protocols to enhance the efficiency of chemical processes. In addition to their advantages as eco-friendly solvents, ionic liquids possess numerous favourable characteristics that have led to their application in catalysis.[75]

Industrially, ILs offer several key benefits as they have been shown to enhance reaction selectivity and product yields while operating under mild conditions, which reduces energy consumption and increases overall process efficiency. ILs can also facilitate the recycling of catalysts and the separation of products, which is essential for sustainable manufacturing processes. Furthermore, ILs can be designed to minimise the formation of by-products and improve catalyst stability, making them valuable in large-scale chemical production and refining processes.[63]

As mentioned previously, the diverse range of available cations and anions and their various combinations enable the adjustment and optimisation of properties such as solubility, stability, and reactivity to meet the specific needs of different catalytic processes, such as enhancing reaction rates, improving selectivity, or stabilising catalysts under varying operational conditions. This is particularly crucial in catalysis, as, for example, tailored or 'task-specific' ionic liquids (ILs) have the potential to significantly improve catalyst durability, efficiency, and specificity.[76]

Existing literature predominantly emphasises the utilisation of ILs in catalysis to enhance reaction rates by either activating the catalyst or customising the interaction between the substrate and the solvent to ensure that the reactants are positioned close to the catalyst. Enhancements in selectivity are generally achieved through specific interactions between the IL and the catalyst, thereby altering its activity or attraction to a particular reactive site. Alternatively, ILs can be designed with specific regions that enhance selectivity by facilitating the efficient extraction of the desired product from the active site, thus preventing undesired

side reactions, and ensuring higher product purity. Several comprehensive reviews have thoroughly documented the progress and advancements in this research area, highlighting how ILs can be tailored to optimise selectivity and overall catalytic performance.[67,76,77]

1.5 Supported Ionic Liquid Phase (SILP)

The application of ionic liquids (ILs) in homogeneous catalysis is well established. However, using them often leads to difficulties in isolating the product from the reaction mixture, especially on a large scale[78] as a large volume of IL is required, which is costly and potentially toxic. To minimise the amount of ionic liquid used while retaining its beneficial impact on homogeneous catalysis, the supported IL phase (SILP) was developed (Figure 1.6). A typical SILP system consists of a small amount of a thin IL film spread over a large surface area of a support material such as silica, alumina, or activated carbon.

The SILP system exhibits properties of both homogeneous and heterogeneous catalysts. This means that the substance can be easily separated and reused while also performing as a homogeneous system.[64] An additional benefit of the SILP system is the even distribution of the catalyst within the IL phase, leading to reduced diffusion pathways and minimised adverse effects related to viscosity when using bulk or biphasic IL. SILP systems also demonstrate improved reaction rates as compared to bulk ILs. One of the early uses of SILP involved the saturation of a silica surface with Lewis acid-based ILs, such as aluminium chloride derivatives, catalysts for Friedel-Crafts reactions.[79] Figure 1.7 represents the supported ionic liquid phase (SILP).

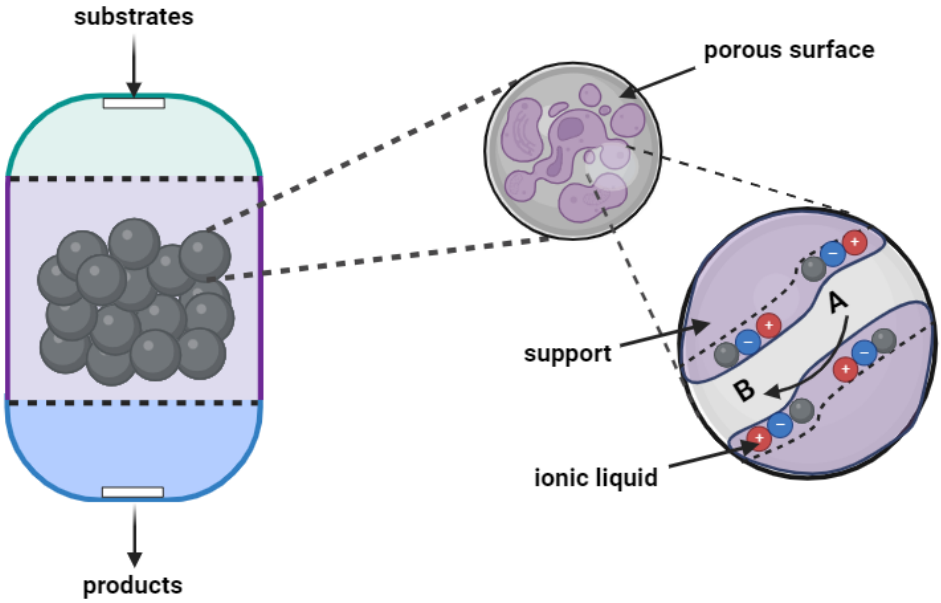

Figure 1.6 Representation of supported ionic liquid phase (SILP).

Four different methodologies have commonly been used for the preparation of SILP materials, as depicted in Figure 1.7. The immersion method (Figure 1.7a) has been the more frequently employed approach for generating SILP-based catalysts. The wet impregnation method is commonly used to immobilise a homogeneous metal complex. This approach involves immersing the supporting material in a solution containing the catalyst or pre-catalyst in an ionic liquid (IL) and an organic solvent to saturate it. Subsequently, the organic solvent is removed by evaporation under vacuum, resulting in the desired dry SILP material. In this method, only the organic solvent evaporates since the IL is non-volatile. Typically, highly porous silica gels with extensive surface areas are employed as the support; however, mesoporous silica and silica-alumina systems such as zeolites have also been used for this purpose.[80,81]

Support materials like alumina have been less frequently used due to their low pore volumes. However, they can be advantageous in specific situations due to their tolerance towards different pH levels. Chiral polymer chitosan,[82] advanced material-based membranes[83] and carbon-based nanotubes (CNTs)[84] are commonly used organic support materials. These SILP systems have catalysed various reactions, such as hydroformylation, hydrogenation, olefin

metathesis, carbonylation, hydroamination, and carbon-carbon coupling.[64,80,85] When confined to the support material, an unexpected scenario has been observed in the SILP system. For example, when Rh-catalysed hydroformylations were performed on SILP materials based on silica, the organometallic complex formed in the thin ionic liquid layer of the impregnated material displayed reduced mobility. This unusual behaviour resulted in a lower diffusion rate of the catalytic species, which restricted the movement of reactants and products through the catalytic system. Consequently, the reaction kinetics were altered, leading to increased selectivity for certain products. This phenomenon is significant as it demonstrated that immobilisation of catalyst in a SILP systems could be used as a tool to control reaction pathways and improve product yields through the manipulation of diffusion processes.[86]

Leaching from SILP materials is a significant problem with immersion-based SILP systems, where the ionic liquid layer is not strongly bonded to the support material. This leaching reduces catalytic efficiency over time, as the active catalyst and/or ionic liquid can be lost into the reaction medium.[87] To address this issue, the covalent anchoring method was introduced in (Figure 1.7b). In this approach, the support surface is modified either by covalent attachment of a specific functionalised IL fragment or by using a sol-gel synthetic protocol that incorporates a hydrolysable ionic liquid silica aprecursor.[87] This covalent anchoring not only prevents leaching but also enhances the stability and reusability of the catalytic system. For example, in the case of Rh-catalysed hydroformylations, covalent immobilisation of the ionic liquid layer has been shown to significantly reduce catalyst degradation and improve turnover numbers.[87] Additionally, this method allows for fine-tuning of the surface properties to optimise catalytic activity and selectivity.

Immobilisation of the catalyst is then achieved through the wet impregnation method, with or without the use of additional IL. For example, the surface of the silica can be altered by covalent bonding followed by immobilisation of either an ionic liquid (IL) acting as a catalyst or a metal catalyst contained within an IL.[88] Modified materials using organocatalysts,[89] where the IL functions as a stabilising medium rather than the catalyst itself, have been extensively applied in aldol catalysis, demonstrating significantly higher catalytic activity and enantioselectivity compared to their homogeneous counterparts. These materials also offer

the benefit of being simple to isolate and recycle, with just a minor reduction in catalytic effectiveness.

Similar results were observed when Mn(III) Salen complexes were immobilised on an imidazolium-functionalised silica support, where the silica was modified with an ionic liquid rather than the Salen ligand itself. This system demonstrated improved enantioselective performance. Notably, often a ligand in the catalyst is modified with an IL-like fragment, such as an imidazolium, to prevent leaching of the catalyst. This approach is also employed when the IL is used as the bulk solvent.[90] IL monolayer functionalisation has also been utilised with other support materials, such as carbon nanotubes (CNTs), which offer enhanced mechanical strength, chemical stability, and a large surface-to-volume ratio. Additionally, surface functionalisation of CNTs with $[C_4mim][PF_6]$ involves the covalent attachment of the IL to the CNTs, allowing for high loadings of IL, up to 55 wt%, without any detectable leaching.[91] The immobilisation of Rh complexes resulted in a highly effective catalyst for the hydrogenation of 1-hexene. These SILP substances displayed outstanding hydrogenation activity in comparison to their oxide-based equivalents and the Rh/IL phase remained intact during recycling.[64,91]

The bonding of SILP support materials through covalent means is not restricted to attaching the IL but has been extended to anchoring the ligand or the catalyst to the IL (Figure 1.7c). For example, Dieter *et al*. functionalised a silica surface with the methylimidazolium cation, which generated N-heterocyclic carbenes (NHCs) upon the addition of $Pd(OAc)_2$. The resulting material formed a palladium-carbene species, which was a highly effective catalyst for the Heck reaction between various haloarenes and olefins.[92]

SILP materials have also been produced by applying a layer of IL over an established heterogeneous catalyst, similar to the immersion method (Figure 1.7d). This process is commonly known as a solid catalyst with an ionic liquid layer (SCILL)[93], and its purpose is to prevent active species from leaching out of the material. For example, adding a hydrophobic IL layer over a covalently immobilised Sc-catalyst on a silica support resulted in a significant improvement in the catalytic activity for the aqueous phase Mukaiyama-aldol reaction.[94]

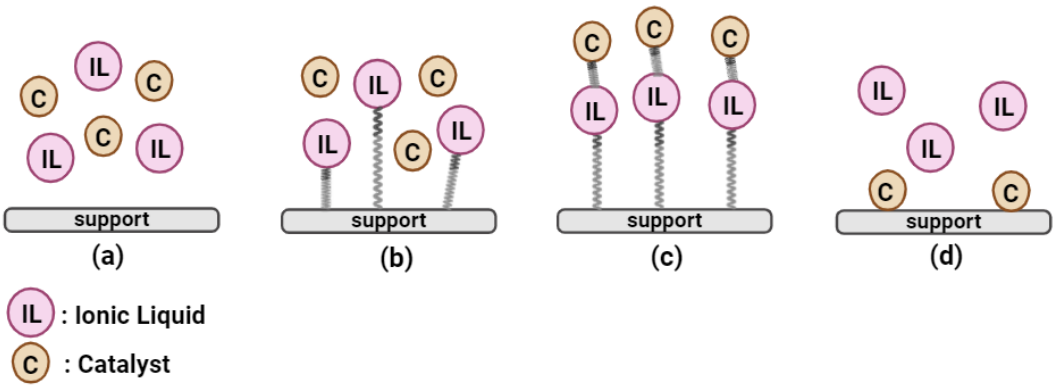

Figure 1.7 Representation of the different methods for the preparation of SILP based materials.

Supported ionic liquids have recently garnered attention for their utilisation with metal complexes. Research has shown that Ru-based supported ionic liquid phase (SILP) systems are efficient catalysts for the low-temperature water-gas shift reaction (WGSR). In the past, it was proposed that Ru-carbonyl species played a significant role in the mechanism, although there is limited detailed knowledge about the active catalytic species. By employing *in situ* diffuse reflectance infrared Fourier transform spectroscopy (DRIFTS) and density functional theory (DFT), researchers identified Ru-carbonyl complexes. It was demonstrated that the chloride bridged ruthenium dimer in $[Ru(CO)_3Cl_2]_2/[C_4C_1C_1Im]Cl/Al_2O_3$ splits to afford an equilibrium mixture of $[Ru(CO)_xCl_y]_n$, with the ionic liquid serving as an effectively infinite chloride reservoir. The research found that the primary species synthesised from $[Ru(CO)_3Cl_2]_2$ is indeed $[Ru(CO)_3Cl_3]^-$.[95] Smaller quantities of chloride-rich species $[Ru(CO)Cl_4]^{2-}$ or $[Ru(CO)_2Cl_4]^{2-}$ and $[Ru(CO)_2Cl_3]^-$ were also present in the SILP. The carbonylation of $RuCl_3/[C_4C_1C_1Im]Cl/Al_2O_3$ using another robust WGSR catalyst led to similar Ru-carbonyl species, confirming the presence of the proposed equilibrium.[95]

The SILP methodology presents several challenges relating to the support materials, impacting the reaction outcome. The complex interactions between the support material, catalyst, and IL can hinder a comprehensive understanding of the mechanism and kinetics of reactions. While confining catalyst particles to a narrow IL layer helps overcome limitations related to mass transport, it can impose undesirable geometric constraints on organometallic complexes, limiting their flexibility and potentially reducing their catalytic activity or selectivity. These constraints can prevent the catalyst from adopting the optimal coordination geometry required for efficient catalysis, thus diminishing its overall effectiveness.

Additionally, there are limitations associated with the chemical stability of the support material when harsh conditions are required for catalysis. For example, silica-based supports exhibit a significant decrease in the catalytic efficiency for the Rh-catalysed hydroformylation of propene due to an irreversible side reaction involving the interaction of the Rh catalyst with the ligand and the acidic silanol groups on the silica surface which results in catalyst deactivation. The silanol groups coordinate to the rhodium center to form a stable, inactive species that cannot participate in further catalysis. As a result, the availability of active catalyst is reduced, leading to a decline in catalytic performance and efficacy.[78]

The application of Supported Ionic Liquid Phase (SILP) materials on a large scale is hindered by various challenges, which in turn restricts the widespread application of SILP catalysis. As a result, it is essential that each catalytic process be thoroughly analysed to gain a comprehensive understanding of the reaction kinetics and mechanism. To address these challenges, current research efforts are concentrated on enhancing the systems, exploring the fundamental properties of the support, and developing new support materials.[96]

1.6 Polymer Immobilised Ionic Liquids (PIIL)

The concept of Polymer Immobilised Ionic Liquid (PIIL) materials involves incorporation of an ionic liquid like monomer into a polymer backbone.[68] These materials offer several advantages over traditional SILP-based systems, including enhanced flexibility, unique swelling characteristics, and the ability to finely control the ionic microenvironment.[97] PIIL materials find applications in various fields such as biotechnology and drug delivery,[98,99] fuel cell technology and energy-based materials.[100] One significant advantage is their ability to prevent leaching into the surrounding solvent which can be achieved through the design of a cross-linked polymer network that effectively encapsulates the active species.; this concept is visually represented in Figure 1.8.

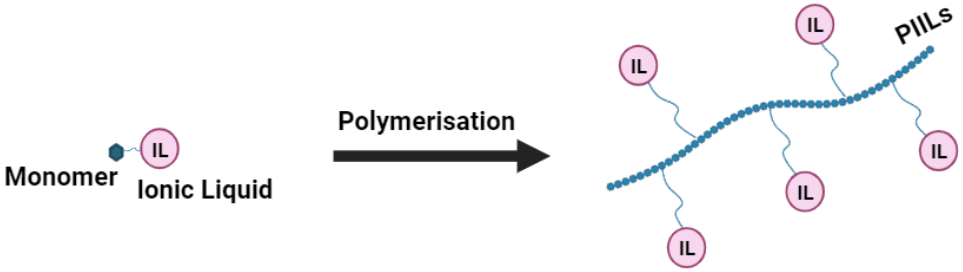

Figure 1.8 Polymer Immobilised Ionic Liquid (PIIL).

The synthesis of PIIL catalyst supports has been achieved using different polymerisation methods, which include step polymerisation, radical polymerisation, living radical polymerisation, ionic polymerisation, and ring-opening metathesis polymerisation.[101,102]

I. **Step polymerisation** is a method for synthesising polymers that involves consecutive organic reactions between reactive functional groups on monomers andproduces polymer backbones with high functionality. In polycondensation reactions, different classes of polymers are formed based on the monomers involved. For instance, polyesters are typically produced by the reaction of diols with diacids, and polyamides are synthesised by reacting diamines with diacids or their derivatives.[103] In contrast, polyethers can be formed from the reaction of alkyl dihalides with nitrogen-containing units, followed by further modification through anion exchange.[104]

II. **Radical polymerisation** is a common and versatile method of chain-growth polymerisation. In this technique, an unsaturated monomer elongates the chain through its active site, which involves initiation, propagation, and termination using free radicals.[105] Living radical polymerisation prevents the propagating polymer from undergoing termination or chain-transfer reactions by ensuring the presence of unreacted monomers. It also ensures that the rate of initiation supersedes that of propagation, providing uniformity between the growing polymer chains and leaving the forming chains with active centres.[105]

III. **In ionic polymerisations,** the active centres are composed of ions or ion pairs. The presence of these anionic charges in the active centre makes them more monomer

specific than radical-initiated systems. They require substituent functionality that can stabilise the active centre.[105]

IV. **Ring-opening polymerisation** is driven by the relief of bond-angle strain and steric repulsion in cyclic monomers. The reaction proceeds through the sequential addition of cyclic monomers (alkanes, alkenes, ethers, phosphates, and siloxanes) to an ionic center.[106] Ring-opening metathesis polymerisation (ROMP) is a notable subclass that uses transition metal-based carbene complexes to produce unsaturated polymers from strained cyclic olefin monomers.[107]

The synthesis of PIIL stabilised nanoparticles (NPs) typically involves combining an ionic liquid-like monomer with a neutral comonomer and if required a neutral or IL cross-linker via polymerisation. Styrene based imidazolium monomers offer a straightforward approach to IL-based polystyrene, which can be impregnated with a metal precursor before reduction to generate metal nanoparticles. Adjustment of the polymer composition has been utilised to manage interactions at the polymer-catalyst interface and achieve improvements in both rate and selectivity.[108]

To this end, Chen *et. al*.[109] demonstrated the application of polymer supports comprising a dual catalyst system of Pd nanoparticles stabilised by sulfonated, water-soluble polymers and heteropolyacids. This support system led to an incredibly active, selective, and high-yielding catalyst for the hydrogenation of phenol, which is important for producing cyclohexanone, a key intermediate in the synthesis of nylon and other chemicals.[110] Additionally, several studies have highlighted the benefits of PIILs in reducing catalyst leaching and enhancing recyclability.[59,64] For instance, the research by Li *et al*.[111] and Han et al. [112] demonstrated that PIILs could effectively address these challenges.

To this end, the development of catalytic systems composed of metal nanoparticles synthesised from organometallic precursors on molecularly modified surfaces (MMSs) has paved the way for multifunctional catalysts with finely-tuned reactivity.[113] These systems, known as NPs@MMSs, provide a bridge between homogeneous and heterogeneous catalysis, offering the ability to precisely control the interaction between nanoparticles and the support material, often leading to enhanced catalytic performance.[113] In particular, ruthenium nanoparticles immobilised on imidazolium-based supported ionic liquid phases (RuNP@SILP)

have shown remarkable activity for CO_2 hydrogenation, achieving turnover numbers (TONs) up to 16,100 and initial turnover frequencies (TOFs) of 1,430 h^{-1}.[114] The introduction of sulfonic acid groups in the ionic liquid modifier was found to enhance catalytic activity by promoting faster desorption of reaction intermediates, demonstrating the potential of ionic liquid-modified systems to optimise catalytic performance.

The work presented in this thesis builds on this foundation and is based on PIILs developed by the Doherty-Knight group and composed of an ionic liquid-like monomer. These IL-functionalised polystyrene-based materials serve as support materials mainly for the stabilisation of metal nanoparticles, due to the ability of the ionic liquid functional groups to interact with and immobilise nanoparticles, preventing aggregation and enhancing their catalytic properties.[115] Among these materials, polymers based on vinyl imidazolium and styrene based monomers are particularly prominent due to their ease of synthesis and their effective stabilisation of metal nanoparticles through ionic interactions and hydrophobic effects, making them highly suitable for catalytic applications. The Doherty/Knight group first reported that polymer-supported linear pyrrolidinium-based PIILPs generated by ring-opening metathesis polymerisation (ROMP) can immobilise a peroxophosphotungstate catalyst.

This catalyst features a polymer matrix that stabilises the ionic liquid and enhances its interaction with peroxometalates, improving both efficiency and reusability. The PIIL-based catalyst demonstrated high effectiveness in epoxidising allylic alcohols and alkenes, showing a significant improvement over the parent $[PW_{12}O_{40}][NEt_4]_3$. Comparative testing revealed that the PIIL-supported system outperformed conventional SILP-supported catalysts, with notable improvements in recycling studies attributed to the enhanced binding affinity within the ionic polymer network.[116]

In a related study, PIIL-based Lewis acid copper catalysts were synthesised through AIBN-initiated radical copolymerisation of styryl-functionalized pyrrolidinium-based ILs with styrene and divinyl benzene crosslinkers. These catalysts exhibited high efficiency and selectivity in the Diels–Alder reaction between N-acryloyloxazolidinone and cyclopentadiene. The performance of these PIIL-based catalysts was compared with catalysts immobilised on conventional inorganic SILP substrates, such as SiO_2 and multi-walled carbon nanotubes (MWCNTs), revealing superior activity and stability in the PIIL-supported systems.[117]

1.7 Heteroatom Donor Modified Supports and NP Catalysis

Recent research has demonstrated that heteroatom donor-modified supports offer distinct advantages over their unmodified counterparts in nanoparticle (NP) catalysis, particularly for key applications like hydrogen production and CO_2 hydrogenation.[118–121] The incorporation of a heteroatom donor such as nitrogen, sulfur, and phosphorus enhances the catalytic performance by fostering stronger metal-support interactions. These interactions are critical for increasing the electron density on metal nanoparticles, which in turn lowers activation energy, improves reaction kinetics, and enhances overall catalytic efficiency. A prime example of such modifications is the use of amine-functionalised supports which facilitate the stabilisation of small, well-dispersed nanoparticles, significantly increasing the active surface area and ensuring better nanoparticle dispersion, which is crucial for efficient catalysis.[122]

Functionalisation with amine groups introduces additional benefits. The electron-rich environment created by nitrogen donors enhances key electron transfer processes in catalytic reactions, directly improving catalytic activity. The basic nature of the amine also plays a pivotal role in increasing hydrogen adsorption and activation, which accelerates reaction rates and leads to more efficient hydrogen-related reactions. For instance, in hydrogen release from a carrier, amine-functionalised mesoporous silica and carbon supports have demonstrated superior catalytic performance, primarily due to their enhanced ability to stabilise catalytic nanoparticles and improve hydrogen uptake at the active sites.[123]

In the context of CO_2 hydrogenation, amine-modified supports exhibit remarkable enhancements in catalytic performance, driven by improved stability and dispersion of metal nanoparticles. Amine groups help maintain the structural integrity of smaller nanoparticles, preventing aggregation and deactivation. Moreover, they significantly improve CO_2 adsorption and activation, facilitating a more efficient conversion of CO_2 into valuable products such as formic acid. These interactions contribute to higher turnover numbers and frequencies and make the process more selective and efficient.[119,123] The combination of enhanced nanoparticle stabilisation, improved substrate binding, and increased local hydrogen and CO_2 concentrations has proven to be highly effective in boosting the overall efficiency and selectivity of catalytic processes.

The use of heteroatom donor-modified supports, especially those functionalised with amine groups, underscores the importance of surface modification to optimise catalyst design for a wide range of applications. By promoting better nanoparticle dispersion, enhancing electron transfer processes, and facilitating substrate activation, these modifications are vital for improving the efficiency of catalytic reactions, particularly in the realm of hydrogen production and CO_2 utilisation.

1.8 Characterisation Methods

There are various techniques that can be used to analyse polymer immobilised nanoparticles including:

I. **X-ray Photoelectron Spectroscopy (XPS)** is a quantitative method used to analyse the surface of materials, specifically to determine the elemental composition and electronic state of the atoms on the material surface. XPS involves the use of a focused beam of X-rays to excite and emit photoelectrons from the top 1-10 nm of the surface being studied. An electron energy analyser is used to measure the energy of the emitted photoelectrons. The identity of the elements present, as well as their chemical states and relative quantities, can be determined from the measured binding energy and photoelectron peak intensity. CasaXPS software is used for spectral analysis, peak fitting, and deconvolution.

II. **Inductively Coupled Plasma Optical Emission Spectrometry (ICP-OES)** is a highly sensitive analytical method employed to quantify the elements in a sample. This technique includes stimulating the atoms and ions in the sample using inductively coupled plasma, which causes the release of electromagnetic radiation at specific wavelengths. By examining the emission intensity, the elemental makeup and concentration in the sample can be precisely determined.

III. **Scanning Electron Microscopy (SEM)** is a powerful imaging technique that enables the detailed visualisation of the surface morphology of a sample. This technique works by scanning the sample with a focused beam of electrons and detecting the secondary electrons that are emitted from the surface. The emitted electrons are then used to create a highly detailed image of the surface topography. SEM is widely used in various

scientific fields to study the microstructure and surface features of materials at a high resolution.

IV. **Transmission Electron Microscopy (TEM)** involves passing an electron beam through a sample or specimen to create an image. The sample can be a suspension or an ultra-thin sample section with a thickness of less than 100 nm. As the electron beam passes through the sample, it interacts with the specimen, resulting in the production of an image. To magnify and focus the specimen image, an imaging device such as a photographic film layer and fluorescent screen or sensors like a charge-coupled device are used.

V. **Thermogravimetric analysis (TGA)** is a thermal analysis technique that entails the continuous measurement of a sample's mass with respect to temperature (or time) in a controlled environment. This approach offers valuable insights into physical processes such as desorption, absorption, and phase changes, as well as chemical processes like solid-gas reactions, oxidation or reduction reactions, thermal decomposition, and chemisorption. TGA is a potent method for examining the stability, composition, and thermal characteristics of a material.

VI. **Energy Dispersive X-Ray Spectroscopy (EDX**) is a technique used for identifying, characterising, and quantifying the elemental compositions of a sample. It relies on the emission of specific X-rays from the sample. A focused beam of high-energy charged particles like electrons or protons is targeted at the sample. This beam interacts with the atom and causes an electron to be ejected from its shell leaving a vacancy. Subsequently, another electron from a higher binding energy level fills this vacancy, which leads to the release of an X-ray with energy equivalent to the difference in the electron level binding energies. The analysis performed by EDX generates a spectrum that displays the peaks associated with the elemental composition of the sample under study.

1.9 Application of polymer immobilised ionic liquid stabilised metal nanoparticles relevant to this thesis.

1.9.1 Catalytic Hydrogen Production.

In recent years, there has been an increasing global demand for energy, leading to the depletion of conventional fossil fuel reserves. As a result, there has been a shift towards exploring alternative energy sources, with hydrogen emerging as a promising option due to its high chemical energy per unit mass. An essential advantage of the use of hydrogen as a fuel is that its combustion only produces water as a by-product, making it environmentally friendly. Hydrogen could significantly reduce air pollution and mitigate the greenhouse effect if used as a fuel in internal combustion engines.[124]

However, hydrogen faces a challenge when it comes to storage and transportation due to its low density in the gaseous state.[124] To address this issue, hydrogen can be stored in the form of a chemical hydride, such as sodium borohydride ($NaBH_4$), which has a high hydrogen gravimetric capacity (10.8 mass%) and is thermally stable and as such offers a solution to the challenge of hydrogen storability and transport.[125]

$$NaBH_4 + 4H_2O \longrightarrow NaB(OH)_4 + 4H_2$$

The hydrolytic dehydrogenation of sodium borohydride is an effective method for releasing hydrogen, and supported metal nanoparticles play a crucial role in catalysing this reaction. Interest in the use of these nanoparticles has recently increased due to their tuneable surface area and size and thereby efficiency. Noble metals such as Ru and Pd are preferred for hydrogen evolution over non-noble metals due to their higher turnover frequencies (TOFs). To this end, there are several reports of metal nanoparticles that have high activities as catalysts for the evolution of hydrogen.[126–130]

1.10 Aims of the project.

The main goal of this project was to build upon the concept of polymer-immobilised ionic liquids (PIIL) developed by the Doherty/Knight research group. The project focused on developing an amine-decorated polymer-immobilised ionic liquid to stabilise metal

nanoparticles and exploring its applications in the hydrogen economy, in particular, as a catalyst for the evolution of hydrogen from storage materials.

The focus of the project was to explore the effect on catalyst performance of modifying the PIIL support with an amine functionality. This modification was designed to impact the interactions between the catalyst and support and enhance activity, selectivity, and reusability. Adjusting the charge density and the loading of an amine heteroatom donor can control morphological growth, nanoparticle activity, and the ionic microenvironment. Therefore, it is highly significant to thoroughly examine the optimal property performance profiles of the polymer-immobilised ionic liquid (PIIL) supported nanoparticles as catalysts. To perform these investigations, this project explored the influence of amine modified PIIL supports on the efficacy of ruthenium and platinum NPs as catalysts for the release of hydrogen from hydrogen-rich boron compounds. Additionally, this project also explored the effectiveness of ruthenium nanoparticles as catalysts for the selective reduction of quinolines.

Finally, the project also developed amine-decorated high-surface-area mesoporous COK-12 silica supports for the stabilisation of Pt and Ru nanoparticles as catalysts for the dehydrogenation of sodium borohydride, ultimately to compare their performance against their PIIL stabilised counterparts.

1.11 References

1. J. N. Tiwari, R. N. Tiwari and K. S. Kim, *Prog. Mater. Sci.*, 2012, **57**, 724–803.

2. M. Vert, Y. Doi, K.-H. Hellwich, M. Hess, P. Hodge, P. Kubisa, M. Rinaudo and F. Schué, *Pure Appl. Chem.*, 2012, **84**, 377–410.

3. Q. Fan, L. Wang, D. Xu, Y. Duo, J. Gao, L. Zhang, X. Wang, X. Chen, J. Li and H. Zhang, *Nanoscale*, 2020, **12**, 11364–11394.

4. X. Yang, Z. Fei, D. Zhao, W. H. Ang, Y. Li and P. J. Dyson, *Inorg. Chem.*, 2008, **47**, 3292–3297.

5. S. Doherty, J. G. Knight, M. A. Carroll, A. R. Clemmet, J. R. Ellison, T. Backhouse, N. Holmes, L. A. Thompson and R. A. Bourne, *RSC Adv.*, 2016, **6**, 73118–73131.

6. R. P. Feynman, *Eng. Sci.*, 1960, **23**, 22–36.

7. D. J. Barber and I. C. Freestone, *Archaeometry*, 1990, **32**, 33–45.

8. M. Faraday, *Philos. Trans. R. Soc. Lond.*, 1997, **147**, 145–181.

9. G. Binnig, H. Rohrer, Ch. Gerber and E. Weibel, *Appl. Phys. Lett.*, 1982, **40**, 178–180.

10. G. Binnig, C. F. Quate and Ch. Gerber, *Phys. Rev. Lett.*, 1986, **56**, 930–933.

11. H. W. Kroto, J. R. Heath, S. C. O'Brien, R. F. Curl and R. E. Smalley, *Nature*, 1985, **318**, 162–163.

12. X. Xu, R. Ray, Y. Gu, H. J. Ploehn, L. Gearheart, K. Raker and W. A. Scrivens, *J. Am. Chem. Soc.*, 2004, **126**, 12736–12737.

13. S. Bhaviripudi, E. Mile, S. A. Steiner, A. T. Zare, M. S. Dresselhaus, A. M. Belcher and J. Kong, *J. Am. Chem. Soc.*, 2007, **129**, 1516–1517.

14. S. A. M. Ealia and M. P. Saravanakumar, *IOP Conf. Ser. Mater. Sci. Eng.*, 2017, **263**, 032019.

15. H. Lu, S. Zhang, J. Wang and Q. Chen, *Front. Nutr.*, 2021, DOI:10.3389/fnut.2021.783831.

16. M. Mansha, I. Khan, N. Ullah and A. Qurashi, *Int. J. Hydrog. Energy*, 2017, **42**, 10952–10961.

17. J. P. Rao and K. E. Geckeler, *Prog. Polym. Sci.*, 2011, **36**, 887–913.

18. M. K. Rawat, A. Jain and S. Singh, *J. Pharm. Sci.*, 2011, **100**, 2366–2378.

19. M. Salavati-Niasari, F. Davar and N. Mir, *Polyhedron*, 2008, **27**, 3514–3518.

20. C. Y. Tai, C.-T. Tai, M.-H. Chang and H.-S. Liu, *Ind. Eng. Chem. Res.*, 2007, **46**, 5536–5541.

21. S. Ali, I. Khan, S. A. Khan, M. Sohail, R. Ahmed, A. ur Rehman, M. S. Ansari and M. A. Morsy, *J. Electroanal. Chem.*, 2017, **795**, 17–25.

22. H. Zeng, J. Li, J. P. Liu, Z. L. Wang and S. Sun, *Nature*, 2002, **420**, 395–398.

23. W. Sigmund, J. Yuh, H. Park, V. Maneeratana, G. Pyrgiotakis, A. Daga, J. Taylor and J. C. Nino, *J. Am. Ceram. Soc.*, 2006, **89**, 395–407.

24. S. C. Thomas, Harshita, P. Kumar Mishra and S. Talegaonkar, *Curr. Pharm. Des.*, 2015, **21**, 6165–6188.

25. L. F. Mabena, S. Sinha Ray, S. D. Mhlanga and N. J. Coville, *Appl. Nanosci.*, 2011, **1**, 67–77.

26. I. Khan, K. Saeed and I. Khan, *Arab. J. Chem.*, 2019, **12**, 908–931.

27. A. K. Singh, V. Dey and R. N. Rai, *Mater. Today Proc.*, 2017, **4**, 1252–1259.

28. A. Pimpin and W. Srituravanich, *Eng. J.*, 2012, **16**, 37–56.

29. S. A. M. Ealia and M. P. Saravanakumar, *IOP Conf. Ser. Mater. Sci. Eng.*, 2017, **263**, 032019.

30. R. S. Rawat, *J. Phys. Conf. Ser.*, 2015, **591**, 012021.

31. M. Zahmakıran and S. Özkar, *Nanoscale*, 2011, **3**, 3462–3481.

32. F. P. da Silva, J. L. Fiorio and L. M. Rossi, *ACS Omega*, 2017, **2**, 6014–6022.

33. S. T. Gentry, S. F. Kendra and M. W. Bezpalko, *J. Phys. Chem. C*, 2011, **115**, 12736–12741.

34. H. T. Phan and A. J. Haes, *J. Phys. Chem. C*, 2019, **123**, 16495–16507.

35. T. W. Hansen, A. T. DeLaRiva, S. R. Challa and A. K. Datye, *Acc. Chem. Res.*, 2013, **46**, 1720–1730.

36. S. Shrestha, B. Wang and P. Dutta, *Adv. Colloid Interface Sci.*, 2020, **279**, 102162.

37. L. Guerrini, R. A. Alvarez-Puebla and N. Pazos-Perez, *Materials*, 2018, **11**, 1154.

38. J. Lyklema, H. P. van Leeuwen and M. Minor, *Adv. Colloid Interface Sci.*, 1999, **83**, 33–69.

39. S. Ding, Y. Guo, M. J. Hülsey, B. Zhang, H. Asakura, L. Liu, Y. Han, M. Gao, J. Hasegawa, B. Qiao, T. Zhang and N. Yan, *Chem*, 2019, **5**, 3207–3219.

40. J. Dupont and J. D. Scholten, *Chem. Soc. Rev.*, 2010, **39**, 1780–1804.

41. D. H. Napper, *J. Colloid Interface Sci.*, 1977, **58**, 390–407.

42. A. Kraynov and T. E., in *Applications of Ionic Liquids in Science and Technology*, ed. S. Handy, InTech, 2011.

43. S. K. M. Henze, O. Bauer, T.-L. Lee, M. Sokolowski and F. S. Tautz, *Surf. Sci.*, 2007, **601**, 1566–1573.

44. J. Wang, S. A. Kondrat, Y. Wang, G. L. Brett, C. Giles, J. K. Bartley, L. Lu, Q. Liu, C. J. Kiely and G. J. Hutchings, *ACS Catal.*, 2015, **5**, 3575–3587.

45. G. Fritz, V. Schädler, N. Willenbacher and N. J. Wagner, *Langmuir*, 2002, **18**, 6381–6390.

46. J. Hang, L. Shi, X. Feng and L. Xiao, *Powder Technol.*, 2009, **192**, 166–170.

47. W. Stawiński, A. Węgrzyn, T. Dańko, O. Freitas, S. Figueiredo and L. Chmielarz, *Chemosphere*, 2017, **173**, 107–115.

48. M. S. Romero-Cano, A. Martín-Rodríguez and F. J. de las Nieves, *Langmuir*, 2001, **17**, 3505–3511.

49. S. Doherty, J. G. Knight, T. Backhouse, E. Abood, H. Al-shaikh, A. R. Clemmet, J. R. Ellison, R. A. Bourne, T. W. Chamberlain, R. Stones, N. J. Warren, I. J. S. Fairlamb and K. R. J. Lovelock, *Adv. Synth. Catal.*, 2018, **360**, 3716–3731.

50. L. M. Martínez-Prieto and B. Chaudret, *Acc. Chem. Res.*, 2018, **51**, 376–384.

51. A. Loureiro, N. G. Azoia, A. C. Gomes and A. Cavaco-Paulo, *Curr. Pharm. Des.*, 2016, **22**, 1371–1390.

52. A. Kosmala, R. Wright, Q. Zhang and P. Kirby, *Mater. Chem. Phys.*, 2011, **129**, 1075–1080.

53. C. S. C. Santos, B. Gabriel, M. Blanchy, O. Menes, D. García, M. Blanco, N. Arconada and V. Neto, *Mater. Today Proc.*, 2015, **2**, 456–465.

54. R. Schlögl, *Angew. Chem. Int. Ed.*, 2015, **54**, 3465–3520.

55. E. V. Anslyn and D. A. Dougherty, *Modern physical organic chemistry*, University science, Sausalito (Calif.), 2006.

56. J. G. de Vries and S. D. Jackson, *Catal. Sci. Technol.*, 2012, **2**, 2009–2009.

57. J. Li, R. Yan, B. Xiao, D. T. Liang and L. Du, *Environ. Sci. Technol.*, 2008, **42**, 6224–6229.

58. M. Akia, F. Yazdani, E. Motaee, D. Han and H. Arandiyan, *Biofuel Res. J.*, 2014, **1**, 16–25.

59. X. Yang, N. Yan, Z. Fei, R. M. Crespo-Quesada, G. Laurenczy, L. Kiwi-Minsker, Y. Kou, Y. Li and P. J. Dyson, *Inorg. Chem.*, 2008, **47**, 7444–7446.

60. J. Flieger, E. Blicharska and A. Czajkowska, *Austin J Anal Pharm Chem*.

61. J. Leier, N. C. Michenfelder and A.-N. Unterreiner, *ChemistryOpen*, 2021, **10**, 72–82.

62. H. Srour, H. Rouault, C. C. Santini and Y. Chauvin, *Green Chem.*, 2013, **15**, 1341–1347.

63. A. I. Siriwardana, in *Electrochemistry in Ionic Liquids: Volume 2: Applications*, ed. A. A. J. Torriero, Springer International Publishing, Cham, 2015, pp. 563–603.

64. Q. Zhang, S. Zhang and Y. Deng, *Green Chem.*, 2011, **13**, 2619–2637.

65. Y. Cao and T. Mu, *Ind. Eng. Chem. Res.*, 2014, **53**, 8651–8664.

66. J. Luo, O. Conrad and I. F. J. Vankelecom, *J. Mater. Chem.*, 2012, **22**, 20574–20579.

67. J. P. Hallett and T. Welton, *Chem. Rev.*, 2011, **111**, 3508–3576.

68. W. Qian, J. Texter and F. Yan, *Chem. Soc. Rev.*, 2017, **46**, 1124–1159.

69. N. L. Mai and Y.-M. Koo, *ACS Sustain. Chem. Eng.*, 2016, **4**, 541–547.

70. L. Benvenutti, A. A. F. Zielinski and S. R. S. Ferreira, *Trends Food Sci. Technol.*, 2019, **90**, 133–146.

71. N. A. Khan, Z. Hasan and S. H. Jhung, *Chem. – Eur. J.*, 2014, **20**, 376–380.

72. J. Liu, G. Jiang, J. Liu and J. Å. Jönsson, *TrAC Trends Anal. Chem.*, 2005, **24**, 20–27.

73. A. Schenzel, A. Hufendiek, C. Barner-Kowollik and M. A. R. Meier, *Green Chem.*, 2014, **16**, 3266–3271.

74. R. E. Teixeira, *Green Chem.*, 2012, **14**, 419–427.

75. P. T. Anastas, M. M. Kirchhoff and T. C. Williamson, *Appl. Catal. Gen.*, 2001, **221**, 3–13.

76. V. I. Pârvulescu and C. Hardacre, *Chem. Rev.*, 2007, **107**, 2615–2665.

77. D. R. MacFarlane, *Chem. Rev.*, 2017, **117**, 6633–6635.

78. A. Riisager, R. Fehrmann, M. Haumann and P. Wasserscheid, in *Regulated Systems for Multiphase Catalysis*, eds. W. Leitner and M. Hölscher, Springer, Berlin, Heidelberg, 2008, pp. 149–161.

79. C. P. Mehnert, *Chem. – Eur. J.*, 2005, **11**, 50–56.

80. C. V. Doorslaer, J. Wahlen, P. Mertens, K. Binnemans and D. D. Vos, *Dalton Trans.*, 2010, **39**, 8377–8390.

81. A. Corma, H. García and A. Leyva, *Tetrahedron*, 2004, **60**, 8553–8560.

82. N. A. H. Rosli, K. S. Loh, W. Y. Wong, R. M. Yunus, T. K. Lee, A. Ahmad and S. T. Chong, *Int. J. Mol. Sci.*, 2020, **21**, 632.

83. L. J. Lozano, C. Godínez, A. P. de los Ríos, F. J. Hernández-Fernández, S. Sánchez-Segado and F. J. Alguacil, *J. Membr. Sci.*, 2011, **376**, 1–14.

84. M. Ruta, I. Yuranov, P. J. Dyson, G. Laurenczy and L. Kiwi-Minsker, *J. Catal.*, 2007, **247**, 269–276.

85. G. M. Ziarani, S. Rohani, A. Ziarati and A. Badiei, *RSC Adv.*, 2018, **8**, 41048–41100.

86. C. Sievers, O. Jimenez, T. E. Müller, S. Steuernagel and J. A. Lercher, *J. Am. Chem. Soc.*, 2006, **128**, 13990–13991.

87. F. Giacalone and M. Gruttadauria, *ChemCatChem*, 2016, **8**, 664–684.

88. M. H. Valkenberg, C. deCastro and W. F. Hölderich, *Green Chem.*, 2002, **4**, 88–93.

89. P. Li, L. Wang, M. Wang and Y. Zhang, *Eur. J. Org. Chem.*, 2008, **2008**, 1157–1160.

90. L.-L. Lou, K. Yu, F. Ding, W. Zhou, X. Peng and S. Liu, *Tetrahedron Lett.*, 2006, **47**, 6513–6516.

91. L. Rodríguez-Pérez, E. Teuma, A. Falqui, M. Gómez and P. Serp, *Chem. Commun.*, 2008, 4201–4203.

92. B. Karimi and D. Enders, *Org. Lett.*, 2006, **8**, 1237–1240.

93. Y. Gu and G. Li, *Adv. Synth. Catal.*, 2009, **351**, 817–847.

94. Y. Gu, C. Ogawa, J. Kobayashi, Y. Mori and S. Kobayashi, *Angew. Chem.*, 2006, **118**, 7375–7378.

95. T. Bauer, R. Stepic, P. Wolf, F. Kollhoff, W. Karawacka, C. R. Wick, M. Haumann, P. Wasserscheid, D. M. Smith, A.-S. Smith and J. Libuda, *Catal. Sci. Technol.*, 2018, **8**, 344–357.

96. M. Haumann, in *Commercial Applications of Ionic Liquids*, ed. M. B. Shiflett, Springer International Publishing, Cham, 2020, pp. 49–67.

97. B. Corain, M. Zecca and K. Jeřábek, *J. Mol. Catal. Chem.*, 2001, **177**, 3–20.

98. J. Venugopal and S. Ramakrishna, *Appl. Biochem. Biotechnol.*, 2005, **125**, 147–157.

99. M. Omedes Pujol, D. J. L. Coleman, C. D. Allen, O. Heidenreich and D. A. Fulton, *J. Controlled Release*, 2013, **172**, 939–945.

100. F. N. Ajjan, M. Ambrogi, G. A. Tiruye, D. Cordella, A. M. Fernandes, K. Grygiel, M. Isik, N. Patil, L. Porcarelli, G. Rocasalbas, G. Vendramientto, E. Zeglio, M. Antonietti, C. Detrembleur, O. Inganäs, C. Jérôme, R. Marcilla, D. Mecerreyes, M. Moreno, D. Taton, N. Solin and J. Yuan, *Polym. Int.*, 2017, **66**, 1119–1128.

101. D. Mecerreyes, *Prog. Polym. Sci.*, 2011, **36**, 1629–1648.

102. J. Yuan, D. Mecerreyes and M. Antonietti, *Prog. Polym. Sci.*, 2013, **38**, 1009–1036.

103. G. Odian, *Principles of Polymerization*, John Wiley & Sons, 2004.

104. F. Li, F. Cheng, J. Shi, F. Cai, M. Liang and J. Chen, *J. Power Sources*, 2007, **165**, 911–915.

105. R. J. Young and P. A. Lovell, *Introduction to Polymers*, CRC Press, Boca Raton, 3rd edn., 2013.

106. O. Nuyken and S. D. Pask, *Polymers*, 2013, **5**, 361–403.

107. J. M. G. Cowie and V. Arrighi, *Polymers: Chemistry and Physics of Modern Materials, Third Edition*, CRC Press, Boca Raton, 3rd edn., 2007.

108. W. Zhu, Y. Yu, H. Yang, L. Hua, Y. Qiao, X. Zhao and Z. Hou, *Chem. – Eur. J.*, 2013, **19**, 2059–2066.

109. Q.-A. Chen, Z.-S. Ye, Y. Duan and Y.-G. Zhou, *Chem Soc Rev*, 2013, **42**, 497–511.

110. X. Kong, Y. Gong, S. Mao and Y. Wang, *ChemNanoMat*, 2018, **4**, 432–450.

111. H. Li, P. S. Bhadury, B. Song and S. Yang, *RSC Adv.*, 2012, **2**, 12525–12551.

112. L. Han, H.-J. Choi, D.-K. Kim, S.-W. Park, B. Liu and D.-W. Park, *J. Mol. Catal. Chem.*, 2011, **338**, 58–64.

113. A. Bordet and W. Leitner, *Acc. Chem. Res.*, 2021, **54**, 2144–2157.

114. S. J. Louis Anandaraj, L. Kang, S. DeBeer, A. Bordet and W. Leitner, *Small*, 2023, **19**, 2206806.

115. M. I. Burguete, E. García-Verdugo, I. Garcia-Villar, F. Gelat, P. Licence, S. V. Luis and V. Sans, *J. Catal.*, 2010, **269**, 150–160.

116. S. Doherty, J. G. Knight, J. R. Ellison, D. Weekes, R. W. Harrington, C. Hardacre and H. Manyar, *Green Chem.*, 2012, **14**, 925–929.

117. S. Doherty, J. G. Knight, J. R. Ellison, P. Goodrich, L. Hall, C. Hardacre, M. J. Muldoon, S. Park, A. Ribeiro, C. A. N. de Castro, M. J. Lourenço and P. Davey, *Green Chem.*, 2014, **16**, 1470–1479.

118. R. Paterson, A. A. Alharbi, C. Wills, C. Dixon, L. Šiller, T. W. Chamberlain, A. Griffiths, S. M. Collins, K. Wu, M. D. Simmons, R. A. Bourne, K. R. J. Lovelock, J. Seymour, J. G. Knight and S. Doherty, *Mol. Catal.*, 2022, **528**, 112476.

119. R. Paterson, L. E. Fahy, E. Arca, C. Dixon, C. Y. Wills, H. Yan, A. Griffiths, S. M. Collins, K. Wu, R. A. Bourne, T. W. Chamberlain, J. G. Knight and S. Doherty, *Chem. Commun.*, 2023, **59**, 13470–13473.

120. A. A. Alharbi, C. Wills, T. W. Chamberlain, R. A. Bourne, A. Griffiths, S. M. Collins, K. Wu, P. Mueller, J. G. Knight and S. Doherty, *ChemCatChem*, 2023, **15**, e202300418.

121. A. A. Alharbi, C. Wills, C. Dixon, E. Arca, T. W. Chamberlain, A. Griffiths, S. M. Collins, K. Wu, H. Yan, R. A. Bourne, J. G. Knight and S. Doherty, *Catal. Lett.*, , DOI:10.1007/s10562-024-04725-8.

122. Q. Liu, X. Yang, L. Li, S. Miao, Y. Li, Y. Li, X. Wang, Y. Huang and T. Zhang, *Nat. Commun.*, 2017, **8**, 1407.

123. K. Mori, S. Masuda, H. Tanaka, K. Yoshizawa, M. Che and H. Yamashita, *Chem. Commun.*, 2017, **53**, 4677–4680.

124. P. Brack, S. E. Dann and K. G. U. Wijayantha, *Energy Sci. Eng.*, 2015, **3**, 174–188.

125. Q. Lai, Y. Sun, T. Wang, P. Modi, C. Cazorla, U. B. Demirci, J. R. Ares Fernandez, F. Leardini and K.-F. Aguey-Zinsou, *Adv. Sustain. Syst.*, 2019, **3**, 1900043.

126. N. Patel, A. Miotello and V. Bello, *Appl. Catal. B Environ.*, 2011, **103**, 31–38.

127. J. Zhu, R. Li, W. Niu, Y. Wu and X. Gou, *Int. J. Hydrog. Energy*, 2013, **38**, 10864–10870.

128. J. W. Jaworski, S. Cho, Y. Kim, J. H. Jung, H. S. Jeon, B. K. Min and K.-Y. Kwon, *J. Colloid Interface Sci.*, 2013, **394**, 401–408.

129. S. Bennici, H. Yu, E. Obeid and A. Auroux, *Int. J. Hydrog. Energy*, 2011, **36**, 7431–7442.

130. Y. Huang, Y. Wang, R. Zhao, P. K. Shen and Z. Wei, *Int. J. Hydrog. Energy*, 2008, **33**, 7110–7115.

Chapter 2: Synthesis of Polymer Immobilised Ionic Liquid Stabilised Ruthenium Nanoparticles and Application in Hydrogen Evolution from Sodium Borohydride.

2.1 Introduction

There is a growing need to find alternative energy sources to replace fossil fuels. This is essential to ensure the supply of sustainable, clean energy and to reduce greenhouse emissions, which are raising global temperatures, leading to extreme and fluctuating weather patterns and negatively impacting the earth's ecosystem.[1] Hydrogen is seen as a promising energy carrier for providing clean and efficient power in stationary, portable, and transport applications[2] as it has a high energy density (142 $MJ \cdot kg^{-1}$ compared to 54 $MJ \cdot kg^{-1}$ for natural gas) and can be produced in high purity from water splitting, with the only by-product being oxygen.[3] However, hydrogen is a flammable gas that can create potentially explosive environments. Therefore, there are significant safety concerns regarding its storage and transportation. Additionally, the compression and liquefaction of hydrogen are energy-intensive processes. Hydrogen storage materials are considered one of the most viable solutions, as they are stable and safe to handle and could allow for on-site hydrogen generation.[3–5] Sodium borohydride is particularly promising as a hydrogen storage material due to its high stability and high hydrogen content (10.8 wt%). It is also non-toxic, inexpensive, and water-soluble[3–6] (Equation 2.1).

$$NaBH_4 + 4H_2O \longrightarrow NaB(OH)_4 + 4H_2$$

Equation 2.1: The reaction of $NaBH_4$ to generate hydrogen.

However, the thermal decomposition of $NaBH_4$ requires temperatures higher than 400 °C and its hydrolysis in water is not fast. Therefore, significant effort has been devoted to developing cost-effective catalysts that can rapidly release hydrogen at normal temperatures for commercial viability. While it has been shown that homogeneous catalysts can assist in the decomposition of hydrogen rich boron compounds,[7,8] there has been a recent increase in interest in the use of noble metal nanoparticles (NPs). The hydrogen generation rate can be controlled by their size, shape, and surrounding environment, and the catalyst can be recovered and reused in much the same manner as a traditional heterogeneous catalyst.[9,10] The high activity of nanoparticles is due to their large surface area, but they tend to aggregate, which limits their practical applications and commercialisation,[11,12] such as in fuel cells and electronic devices.[13,14] One solution to address this problem is to stabilise the nanoparticles

by encapsulating them in a support, such as porous carbon structures,[15] zeolites,[16–18] or mesoporous silica.[19], polymers, MOFs[20] and oxides. This stabilisation strategy can also allow for control of the growth and morphology of the nanoparticles as well as modifying their properties.[21] The most efficient supported NP catalyst for the hydrolysis of sodium borohydride is based on ruthenium NPs confined in zeolite-Y, with a turnover frequency of 550 $mol_{H2}mol_{Ru}^{-1}min^{-1}$.[17]

Ionic liquids have been used to stabilise nanoparticles,[22] but weak electrostatic interactions are often insufficient to prevent aggregation under catalysis conditions.[23] One potential solution is incorporation of a heteroatom donor such as phosphine, amine, nitrile, ether, or thiol to form a covalent interaction with the nanoparticle surface,[24] leading to improved catalyst stability and performance. However, functional ionic liquids are prohibitively expensive as a bulk solvent and leaching can lead to product contamination, making their implementation difficult.

One approach to tackling these issues has involved attaching the ionic liquid to the surface of a support like mesoporous silica, polymer, or MOF.[20] This surface grafted IL would be able to provide weak electrostatic stabilisation of the nanoparticles, as for an ionic liquid, while covalent attachment to the support would prevent the leaching of the ionic liquid, aid in the separation and retrieval of the catalyst, and decrease the volume of the ionic liquid as the catalyst would be confined within the support.[25] Polymers are an attractive choice for supports due to their adaptable nature, allowing the systematic modification of hydrophilicity, ionic microenvironment, charge density, and redox properties, the introduction of additional functionality, and control of the composition and stoichiometry of the metal precursor(s) to facilitate the creation of bi- and trimetallic nanoparticles with synergistic effects. Our research group has recently delved into this concept and formulated heteroatom donor-decorated polymer-immobilised ionic liquids, with the idea that the heteroatom donor could impact the size, size distribution, and morphology of the nanoparticles, supplement the weak electronic stabilisation provided by the IL as well as modify their surface electronic structure and thereby adjust their effectiveness as catalysts.

There have been reports of the beneficial effect of ligands on the performance of heterogeneous nano-catalysts.[26] For example, palladium nanoparticles immobilised on a

polyethene glycol-modified phosphine-decorated PIIL are active catalysts for aqueous phase Suzuki-Miyaura cross-coupling,[27] selective hydrogenation, and transfer hydrogenation, of nitroarenes.[28] Gold and ruthenium nanoparticles stabilised by a phosphine oxide-decorated polymer also exhibit catalytic activity in selective reductions and hydrogenations.[29]

This study explored the efficacy of amine-decorated polymer immobilised ionic liquid stabilised RuNPs for $NaBH_4$ hydrolysis (Scheme 2.1). Results show that RuNPs stabilised by an amino-modified polymer outperform their phosphine oxide-decorated and unmodified counterparts. Kinetic studies and deuterium isotope effects were used to probe the mechanism and confirm competition between β-hydride elimination/re-insertion and reductive elimination during the hydrogenation of 1,1-diphenylethene using hydrogen generated from $NaBH_4$ hydrolysis.

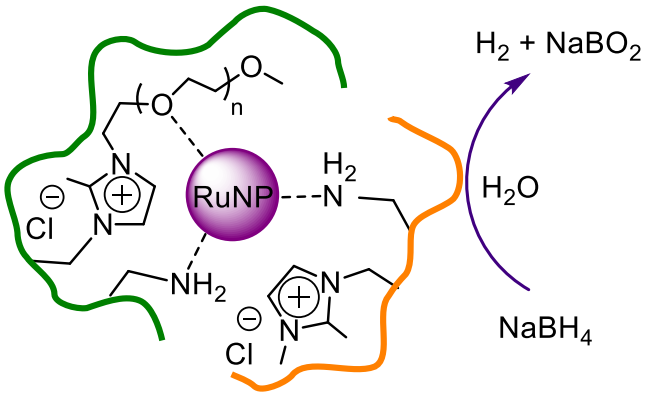

Scheme 2.1 PIIL stabilised RuNPs

2.2 Results and Discussion

The first objective was to prepare the amine-decorated polymer immobilised ionic liquids and investigate the heteroatom donor's effect on the stability and dispersity of noble metal nanoparticles and their performance as catalysts (Sheme 2.2).

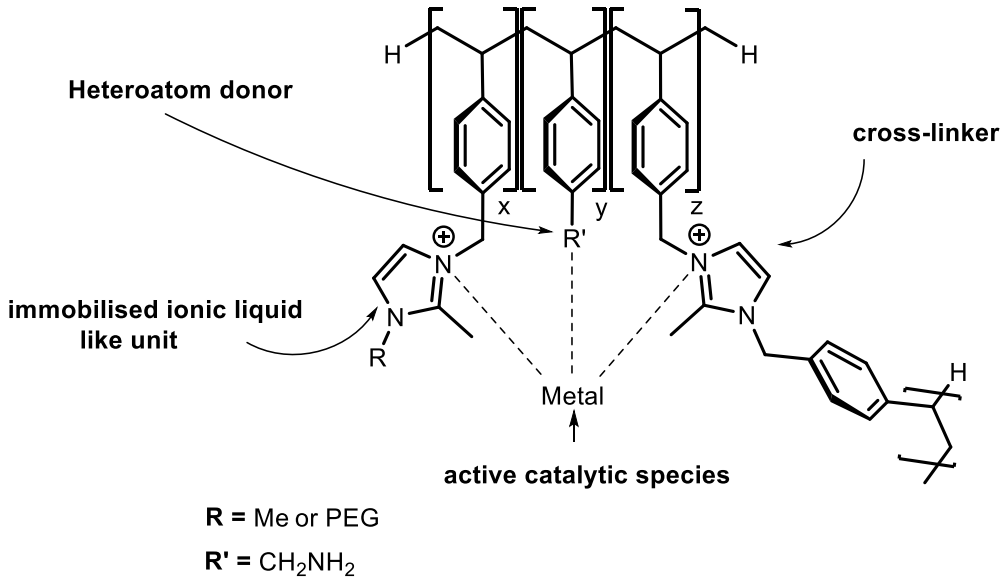

Scheme 2.2 Schematic structure of the prepared catalysts.

2.2.1 Synthesis of Monomers

Four styrene-based monomers **2.1**, **2.3**, **2.5** and **2.9** (Scheme 2.3), were required to prepare the two PIILP materials NH_2-PIILS (**2.10**) and NH_2-PEGPIILS (**2.11**).

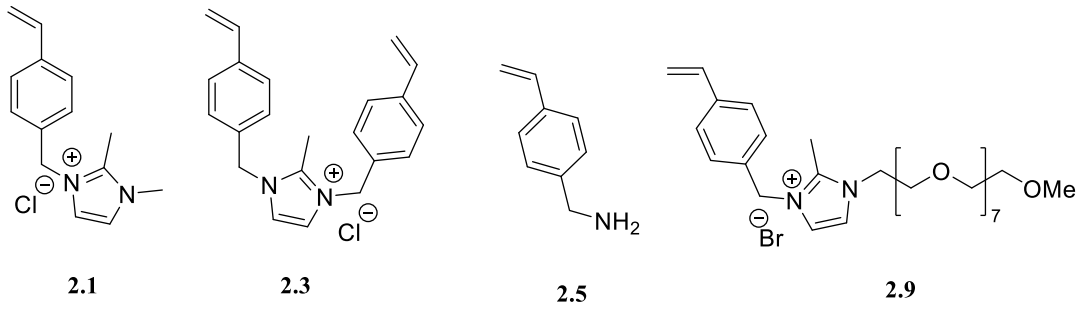

Scheme 2.3 Monomer structures: dimethylimidazolium monomer **2.1**, dibenzylimidazolium crosslinking monomer **2.3**, amino functionalised monomer **2.5**, and PEGylated imidazolium monomer **2.9**.

The imidazolium co-monomer 1,2-dimethyl-3-(4-vinylbenzyl)-1H-imidazolium chloride **2.1** was synthesised following a procedure previously developed by the Doherty-Knight group (Scheme 2.4). This monomer was prepared by reaction of 1,2-dimethyl imidazole and 1-

chloromethyl-4-vinyl-benzene at 50°C and isolated in 90 % yield. The identity and purity of the product were confirmed by ^{1}H and ^{13}C NMR spectroscopy.

The dibenzylimidazolium crosslinking monomer **2.3** was prepared in two steps. The first step involved the reaction of lithium 2-methyl imidazolide, generated *in situ* by deprotonation of 1,2-dimethylimidazole with sodium hydride, with 1-chloromethyl-4-vinyl-benzene in DMF to generate 1,2-dimethyl-3-(4-vinylbenzyl)-1H-imidazole **2.2**.

In the second step, a further equivalent of 1-chloromethyl-4-vinyl-benzene was reacted with **2.2** to afford 2-methyl-1,3-bis(4-vinylbenzyl)-1H-imidazol-3-ium chloride **2.3**, according to (Scheme 2.4).

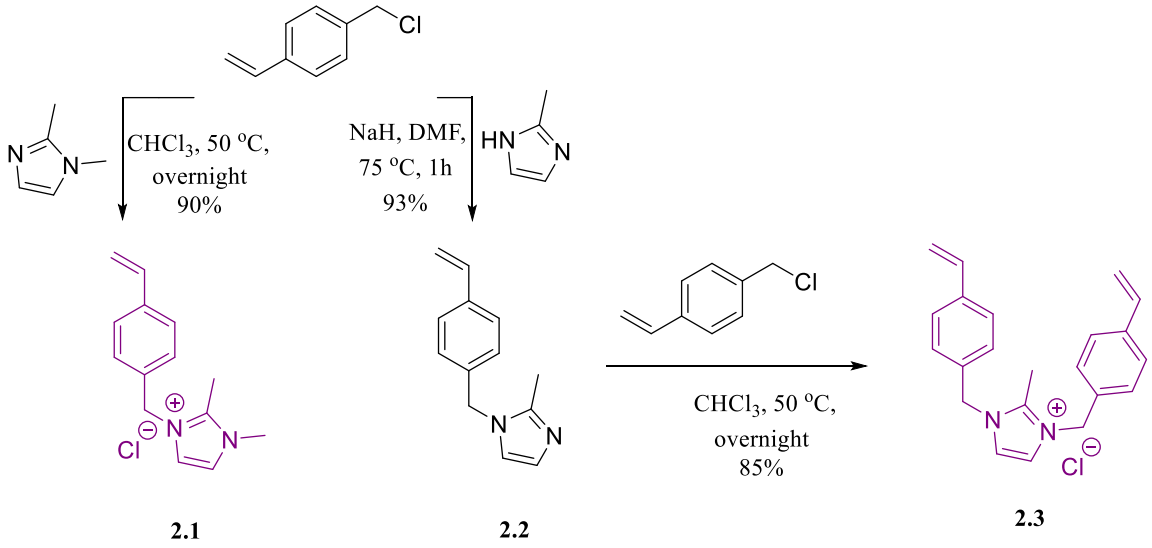

Scheme 2.4 Synthesis of 1,2-dimethyl-3-(4-vinylbenzyl)-1H-imidazolium chloride **2.1** and 2-methyl-1,3-bis(4-vinylbenzyl)-1H-imidazol-3-ium chloride **2.3**.

Monomer **2.5** was prepared by reacting potassium phthalimide with 1-chloromethyl-4-vinyl-benzene to afford *N*-[(4-vinylphenyl) methyl] phthalimide **2.4**, which was then converted to the corresponding amine monomer **2.5** *via* hydrazinolysis according to Scheme 2.5.

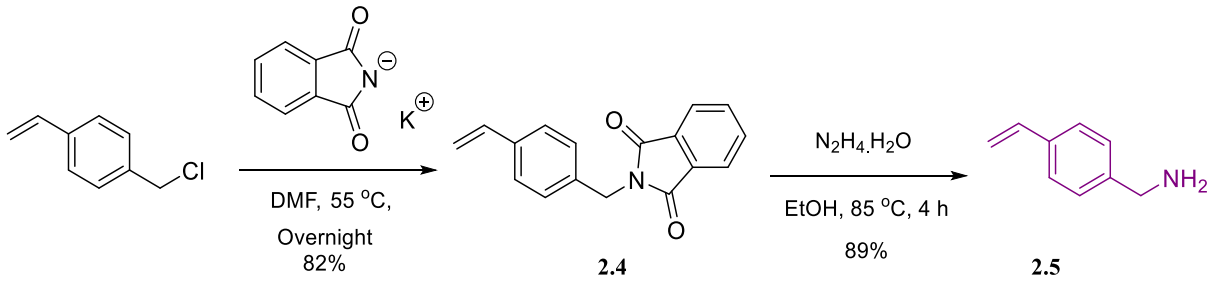

Scheme 2.5 Synthesis of 2-methyl-1-(4-vinylbenzyl)-imidazole **2.5**.

The preparation of the PEG functionalised imidazolium-based ionic liquid, 2-methyl-1-PEG-3-(4-vinylbenzyl) imidazolium bromide (25-chloro-2,5,8,11,14,17,20,23-octaoxapentacosane) **2.9** involved a convergent protocol (Scheme 2.6). This four-step synthesis started with PEG-chloride **2.6**, which was prepared by stirring a poly(ethyleneglycol)monomethyl ether with pyridine in toluene and heated up to 80 °C before adding thionyl chloride.

The reaction mixture was left to reflux for two days to afford **2.6** as a spectroscopically pure product in 86% yield. The next step involved deprotonation of 2-methylimidazole by NaH in THF to afford lithium 2-methylimidazolide, which was reacted with **2.6**, at 75°C overnight to afford PEG-imidazole **2.7** as oil in 88% yield.

A Finkelstein reaction was required to prepare 4-vinylbenzyl bromide **2.8** by exchanging chloride in 4-chloromethylstyrene for bromide. A mixture of 4-vinylbenzyl chloride and sodium bromide in acetonitrile at 85°C was allowed to stir overnight to afford 4-vinylbenzyl bromide **2.8** as oil in 85% yield. The extent of halide exchange was determined to be greater than 90% according to ^{1}H NMR spectroscopy.

The last step in the preparation of 2-methyl-1-(2,5,8,11,14,17,20,23-octaoxapentacosan-25-yl)-3-(4-vinylbenzyl)-1H-imidazol-3-ium bromide **2.9** (Scheme 2.6), involved quaternisation of **2.7** with **2.8** in dichloromethane at 35°Cto produce the PEG functionalised monomer as a pale-yellow oil in 91% yield.

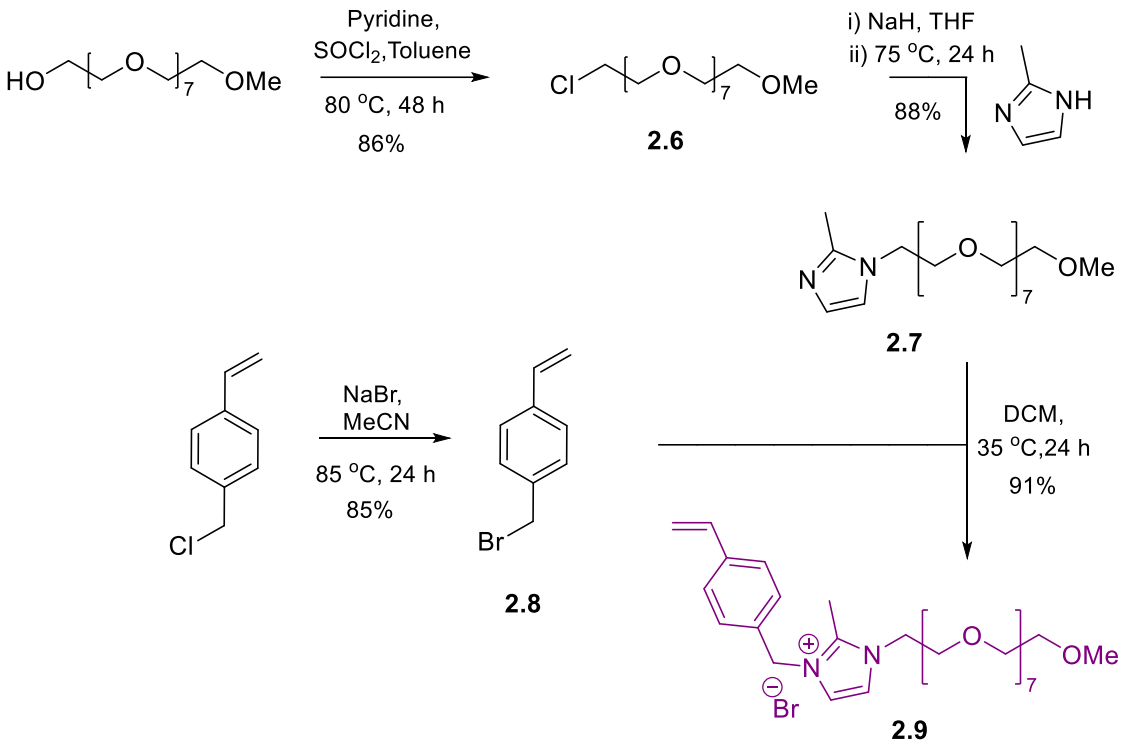

Scheme 2.6 Synthesis of PEGylated monomer **2.9**

2.2.2 Synthesis and Characterisation of Polymers NH_2-PIIL and NH_2-PEGPIIL

Using PIIL to stabilise the NPs has several significant advantages. It has steric and electrostatic effects that help immobilise the NPs.

In this project, two polymer immobilised ionic liquids NH_2-PIILP **2.10** and NH_2-PEGPIILP **2.11**, were prepared by AIBN initiated random copolymerisation of three monomers **2.1**:**2.5**:**2.3** for NH_2-PIILP and **2.9**:**2.5**:**2.3** for NH_2-PEGPIILP in the ratio **2.1** and **2.9** = 1.86, **2.5** = 1 and **2.3** = 0.14 (Scheme 2.7). Thus overall, the repeat unit contains two ionic liquid units (x = 1.86 + z = 0.14) and one amine (y = 1) with an overall cationic charge of 2; the same ratio has been used previously by the Doherty research group for phosphine, nitrile and ether modified PIILs and as such was used here for consistency.[27–29]

The preparation by the free radical polymerisation was carried out by dissolving the three monomers in dry ethanol and adding 5 mol% AIBN to the reaction mixture. A freeze-pump-thaw technique was required to remove all the oxygen from the system, and the reaction

mixture was allowed to stir for two days at 85°C. After this, a further portion of AIBN 5 mol% was added, and the degassing process was repeated. The mixture was then heated again to 85°C for three days to ensure that the polymerisation reached completion. After work up, NH_2-PIILP **2.10** and NH_2-PEGPIILP **2.11** were obtained in 93% and 89% yield, respectively.

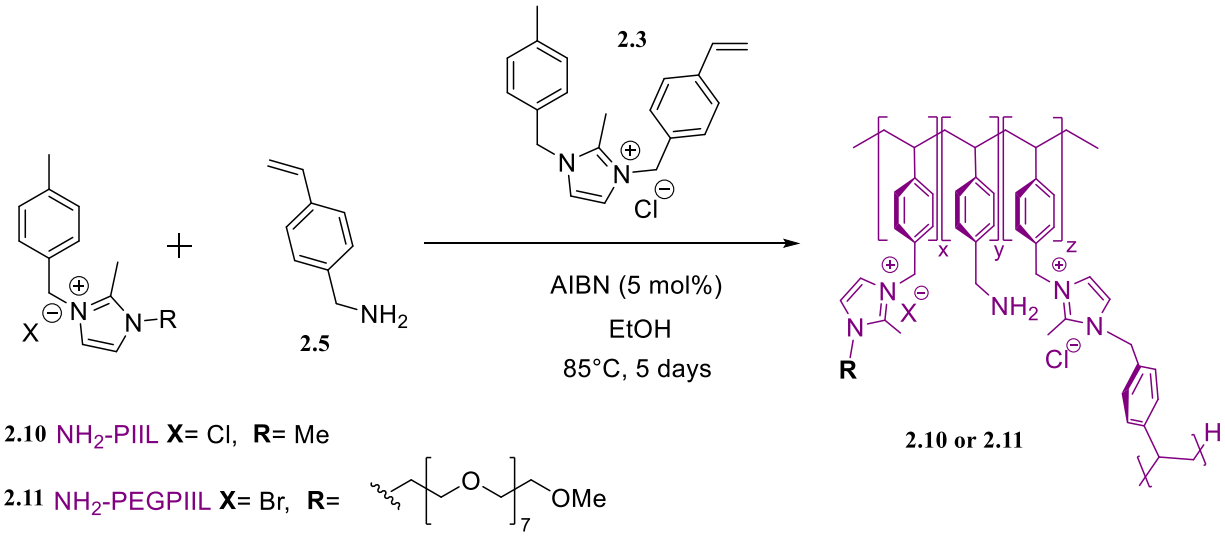

Scheme 2.7 Synthesis of NH_2-PIIL (**2.10**) and NH_2-PEGPIIL (**2.11**) via radical-initiated polymerisation.

The ^{1}H NMR spectrum of NH_2-PIIL (Figure 2.1) shows broad peaks resulting from the random structure of the polymer and limiting tumbling effects. Moreover, there is an absence of peaks corresponding to vinyl protons. The protons from the aromatic and imidazolium groups were identified in the chemical shift range at δ 6.65-7.55 ppm. It should be noted that the polymer composition is undefined with respect to the precise sequence of monomer units along the chain, reflecting the statistical nature of the copolymerisation. The CH_2 adjacent to the imidazolium ring appeared at δ 5.50 ppm. The chemical shift at 4.40 ppm on the NMR spectrum (Figure 2.1 bottom) determined the presence of the methoxy protons in the PEG functionalised monomer, and the peak at δ 2.78 ppm was identified as belonging to the methyl groups on the two imidazolium rings in both polymers. The ^{1}H NMR spectra clearly show that the polymerisations reached completion, and integration of the CH_2 to the aromatic region confirmed that the imidazolium to amine co-monomer ratio was 2:1.

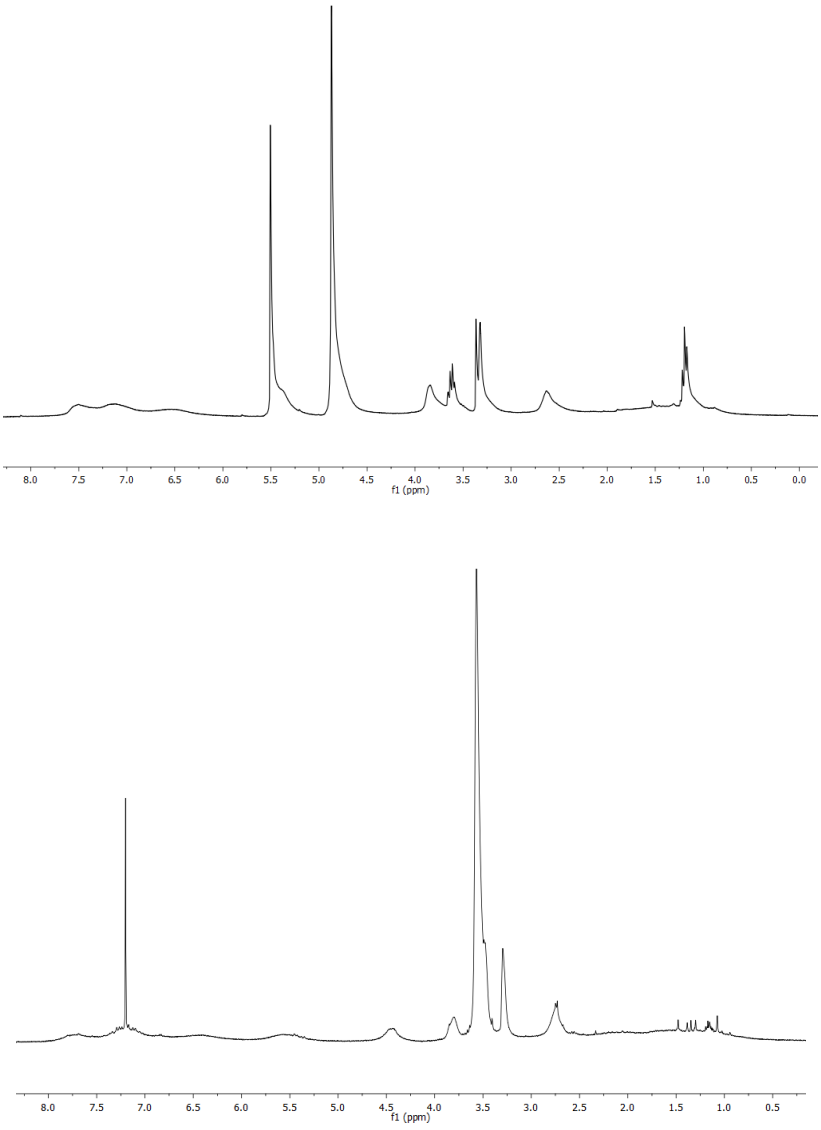

Figure 2.1 Solution state ^{1}H NMR spectrum of **2.10** in d_4-MeOH (top), and **2.11** in $CDCl_3$ (bottom)

The spectrum in Figure 2.2 depicts the solid state ^{13}C {^{1}H} NMR spectrum of NH_2-PIIL **2.10** and its PEGylated variant **2.11**. Both spectra indicate that the main component of the product, approximately at ~δ 130 and 145 ppm, is accompanied by spinning sidebands, which correspond to the aromatic carbon atoms of polystyrene and the carbon atoms of the imidazolium ring, as well as signals between δ 10 and 51 ppm which belong to the methylene carbon atoms of the polystyrene backbone and the methyl group attached to the imidazolium ring.

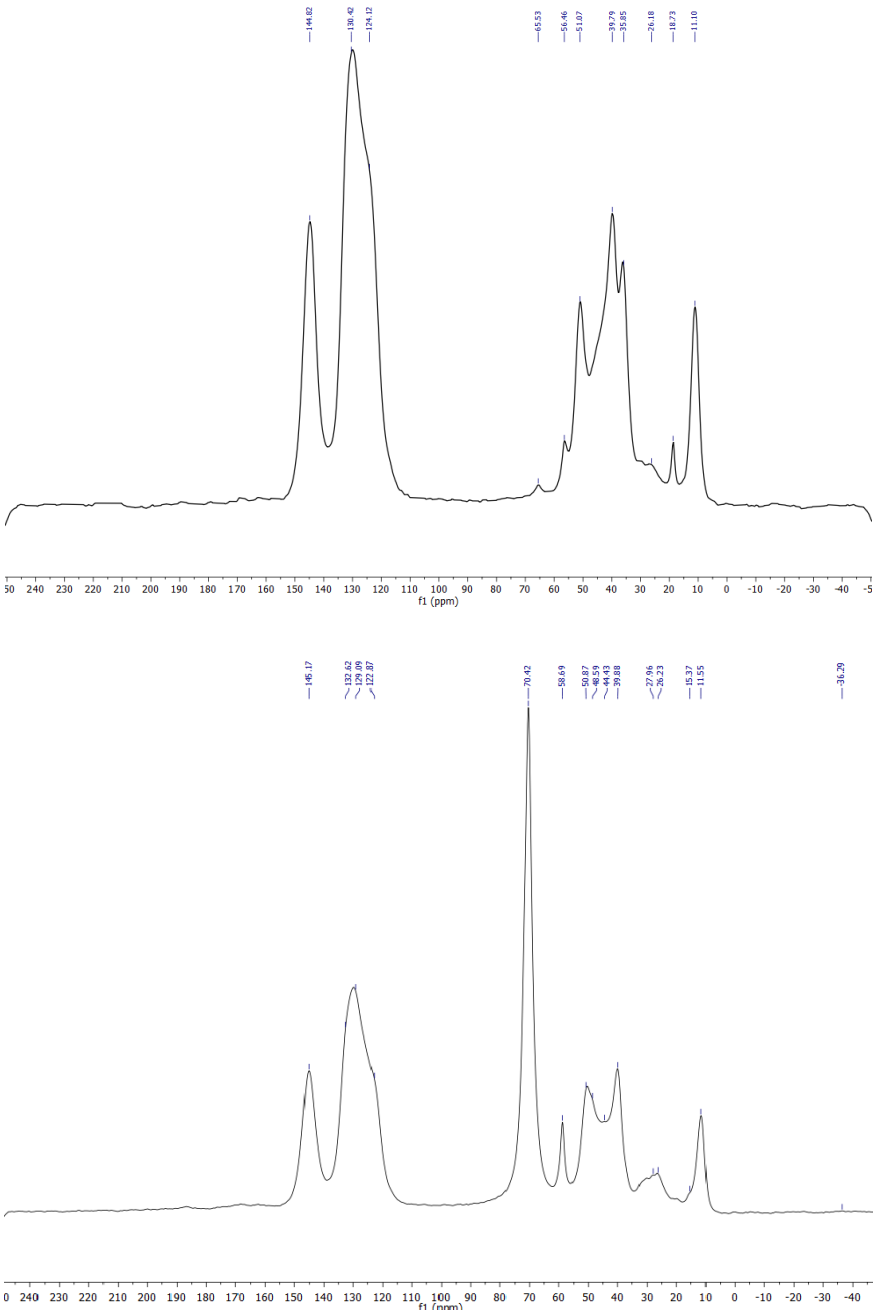

Figure 2.2 Solid state $^{13}C\{^{1}H\}$ NMR spectrum of **2.10** (top), and **2.11** (bottom)

SEM analysis was performed to study the surface structure of the polymers of NH_2-PIIL **2.10** and NH_2-PEGPIIL (**2.11**) (Figure 2.3). The investigation showed that both polymers have mainly even surfaces with sporadic small regions showing irregular porous characteristics. While the overall surface morphologies are broadly similar, subtle differences in pore distribution and size were observed upon closer examination. This finding indicates that the hydrophilic properties of the polymer-immobilised ionic liquid composites might cause some level of

moisture or solvent absorption, possibly due to the uptake of alcohol solvents during the polymerisation procedure.

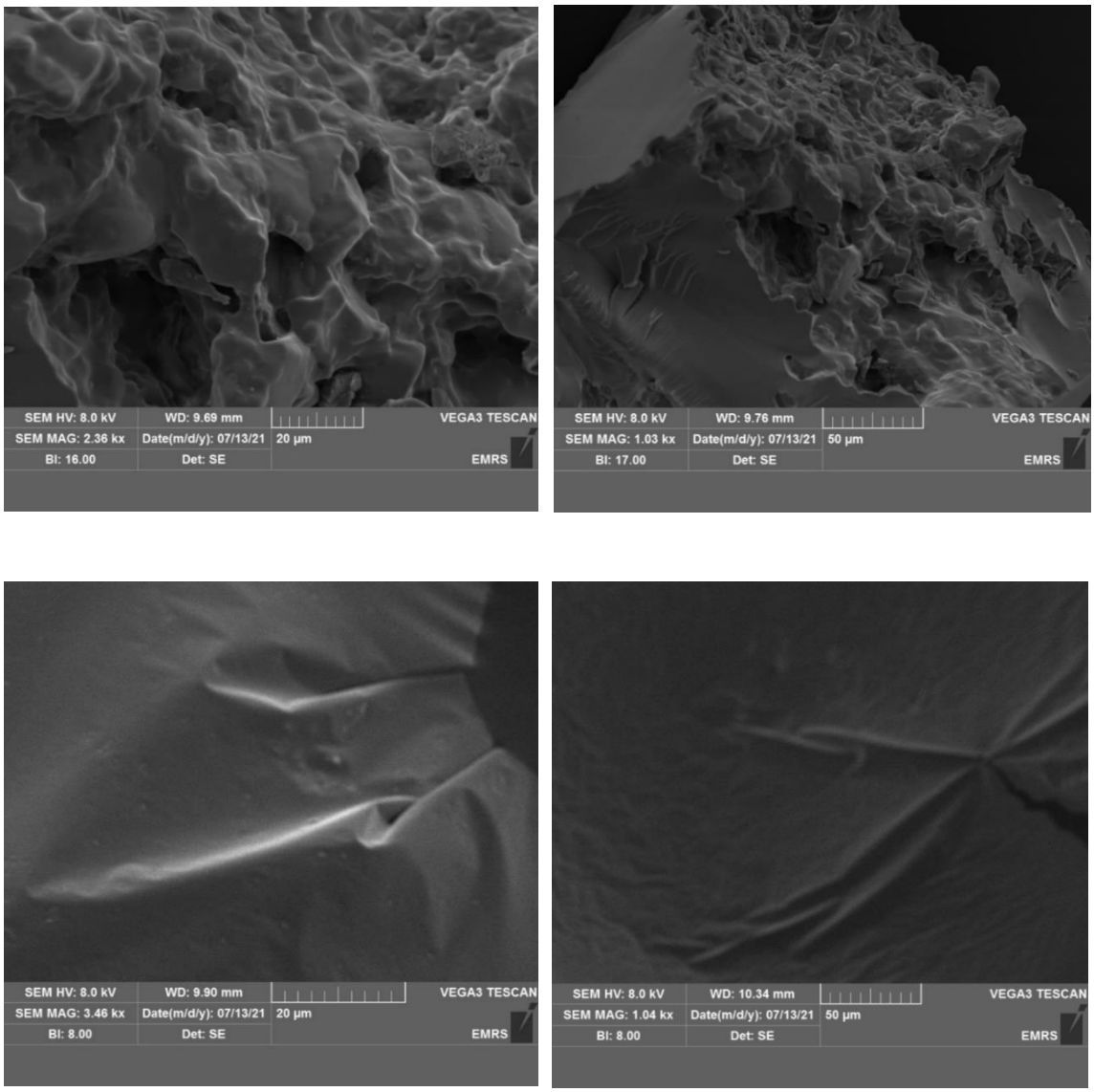

Figure 2.3 SEM images of freshly prepared samples of NH_2-PIIL (**2.10**) (top) NH_2-PEGPIIL (**2.11**) (bottom)

Thermogravimetric analysis was utilised to examine the thermal stability of the polymers. The initial minor degradation process close to 100°C is caused by the evaporation of water or solvent adsorbed on the support, indicating a low level of solvent absorption. However, a slight mass loss observed before the main degradation stages, particularly in Figure 2.4 (top), may also suggest the presence of trace amounts of trapped monomers or other low-molecular-weight species that were not fully removed during purification. Following the

removal of the remaining solvent, both polymers experience two similar stages of degradation. According to the literature, the degradation of the polystyrene backbone occurs at approximately 450°C;[30] this is noticeable in both TGA spectra (Figure 2.4). The first stage is linked to the breakdown of the imidazolium fragment at around 340°C, which has been observed to occur through dealkylation and carbene formation.[31] Since the initial degradation of the two polymers does not occur until ~330°C, which is significantly higher than the temperatures needed for liquid-phase catalysis, NH_2-PIIL **2.10** and NH_2-PEGPIIL **2.11** are stable enough to be used as catalyst supports.

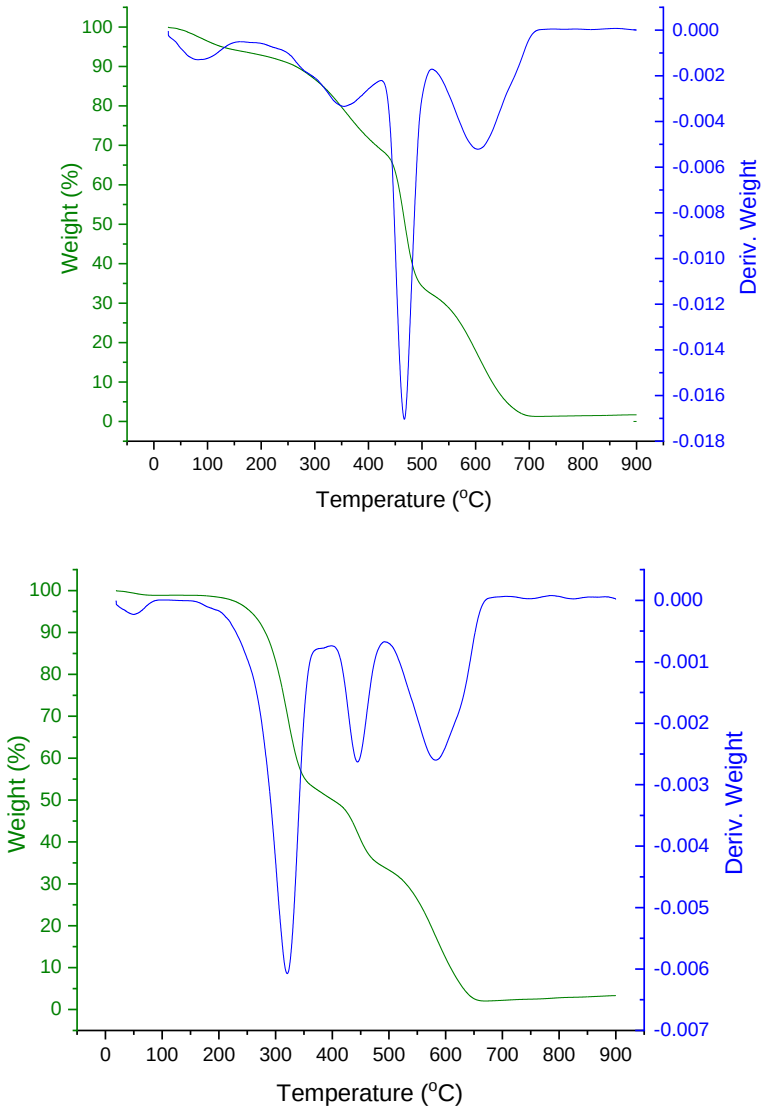

Figure 2.4 TGA curve for NH_2-PIIL (**2.10**) (top) NH_2-PEGPIIL (**2.11**) (bottom); wt% v temperature. Heating rate of 10 °C min^{-1} in air.

2.2.3 Synthesis and Characterisation of NH_2-PIILS and NH_2-PEGPIILS supported Ruthenium Nanoparticles

Catalysts **2.14** and **2.15** were synthesised in a one-pot reaction (Scheme 2.8). The polymers were impregnated with commercial ruthenium trichloride in ethanol with a 1:1 ratio of ruthenium to neutral monomer and stirred overnight to give precatalysts **2.12** and **2.13,** which were subsequently reduced in situ with sodium borohydride to afford RuNP@NH_2-PIILP (**2.14**) and RuNP@NH_2-PEGPIILP (**2.15**) as black powders in 79% yield. The ruthenium loadings in **2.14** and **2.15** were determined to be 0.34 and 0.69 $mmolg^{-1}$, respectively, using ICP-OES. (see the appendix for details on the yield and ICP-OES calculations).

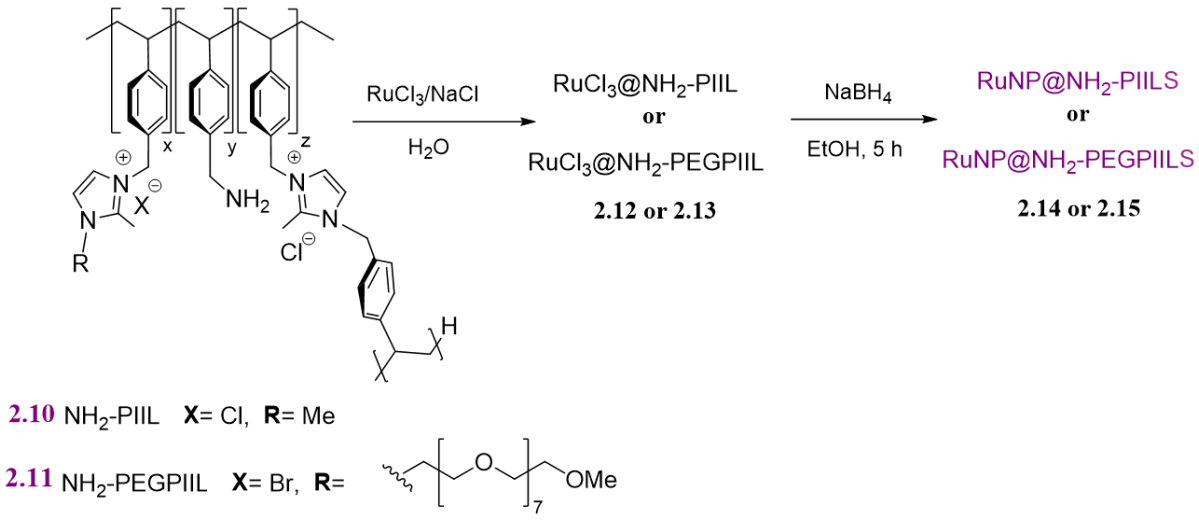

Scheme 2.8 Synthesis of RuNP@NH_2-PIILS (**2.14**) and RuNP@NH_2-PEGPIILS (**2.15**).

The data shown in Figure 2.5 illustrates the solid state $^{13}C\{^1H\}$ NMR spectra of RuNP@NH_2-PIILS **2.14** and RuNP@NH_2-PEGPIILS **2.15**. Both data sets indicate that the main part of the compound is found around δ 121 and 149 ppm, which corresponds to the imidazolium ring and the aromatic carbon atoms, as well as signals between δ 10 and δ 51 ppm associated with the methyl group attached to the imidazolium ring and the aliphatic carbon atoms of the polystyrene backbone. Additional signals specific to the polymer at δ 71 and δ 59 ppm for **2.15** are belong to the carbon atoms of the PEG chain and terminal OMe, respectively, and a signal at δ 51 ppm for **2.14** and **2.15** is associated with the CH_2NH_2.

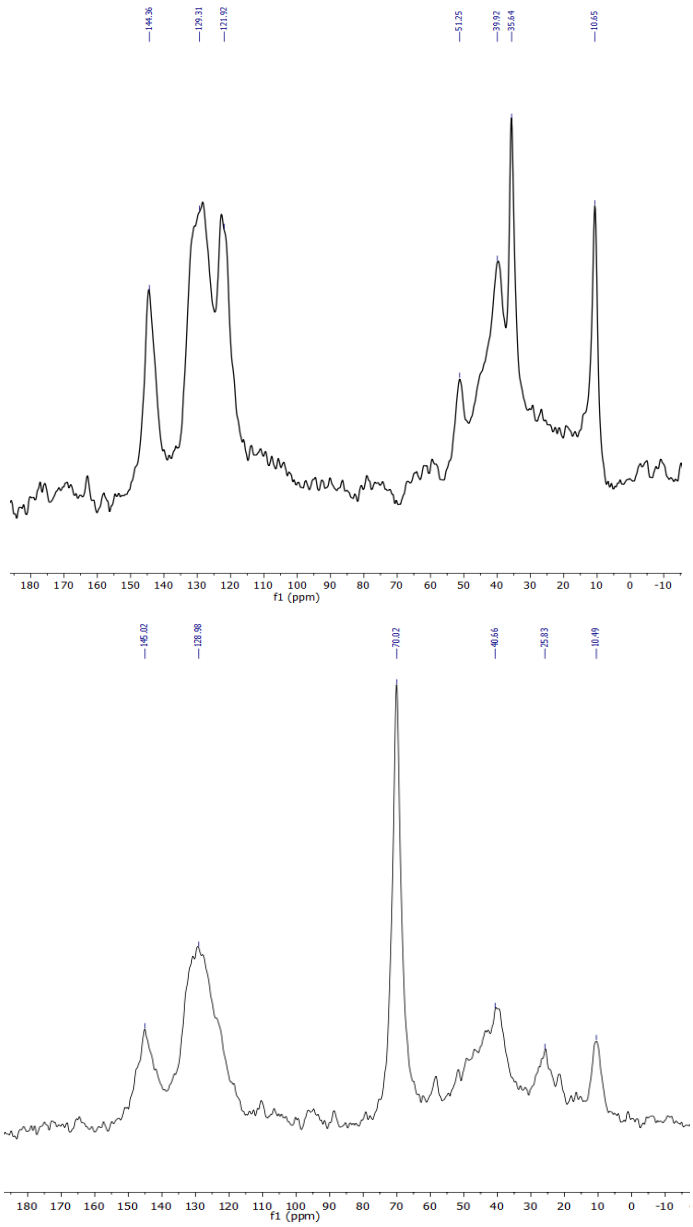

Figure 2.5 Solid state $^{13}C\{^{1}H\}$ NMR spectrum of RuNP@NH_2-PIILS (**2.14**) (top) RuNP@NH_2-PEGPIILS (**2.15**) (bottom)

The SEM analysis of the RuNP materials revealed significant differences in the surface structure between the polymers containing $RuCl_3$ and the unaltered polymers (Figure 2.6). The catalyst materials appeared much more granular than the smooth surface of the unmodified polymers. This suggests that additional treatment steps during impregnation and reduction led to the grainy appearance of the specimens. Therefore, the altered surface characteristics are likely a result of these additional processes.

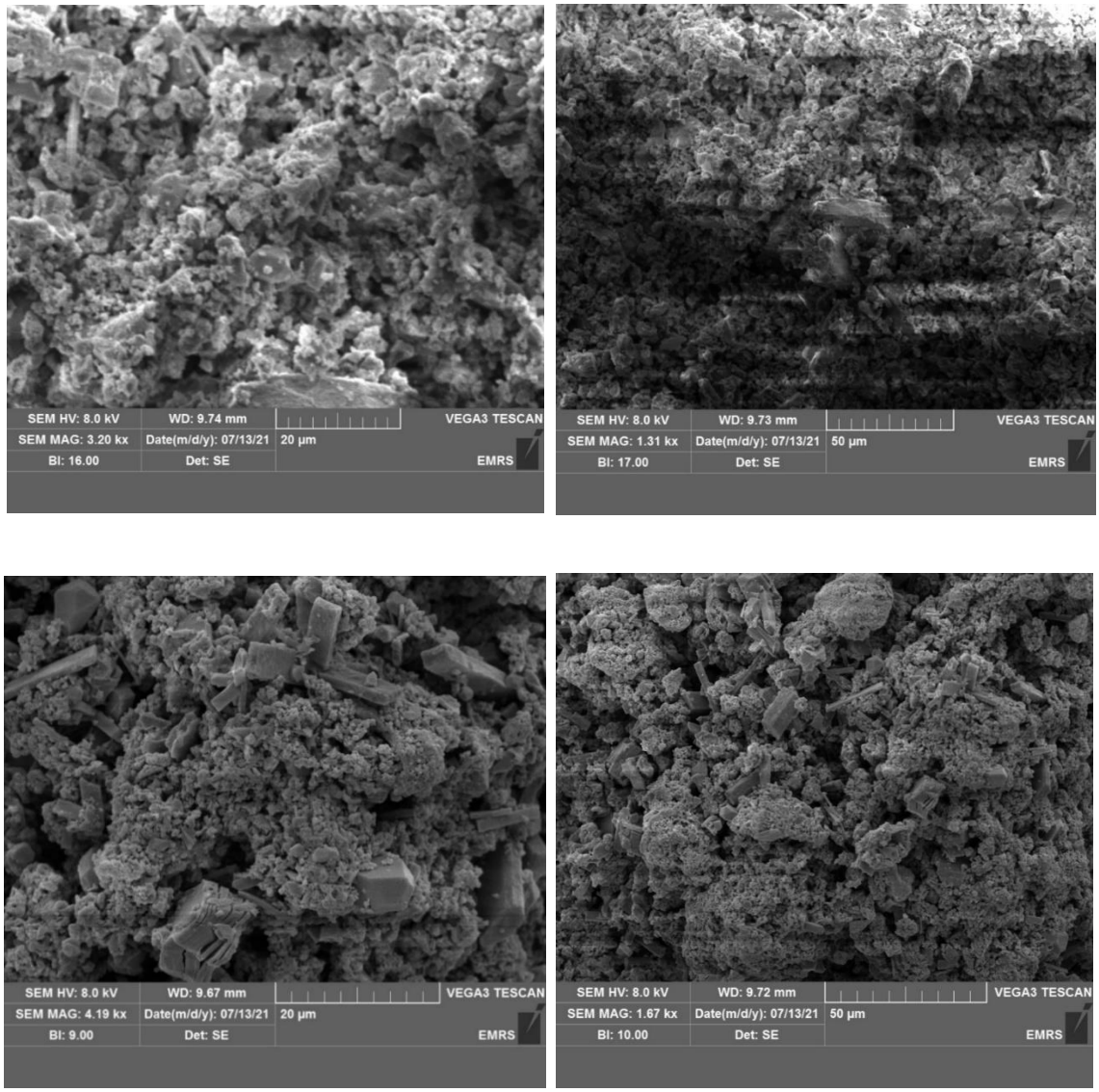

Figure 2.6 SEM images of a freshly prepared sample of RuNP@NH_2-PIILS (**2.14**) (top) RuNP@NH_2-PEGPIILS (**2.15**) (bottom)

X-ray photoelectron spectroscopy (XPS) was carried out for surface characterisation of the RuNP-based catalysts with analysis of the Ru 3p region due to the overlap of the C 1s and Ru 3d regions. For catalysts **2.14** and **2.15**, the Ru $3p_{3/2}$ peak position was shifted to lower binding energies (462.56 eV and 461.89 eV) as compared to the Ru $3p_{3/2}$ binding energy of 463.19 eV for catalyst stabilised unmodified imidazolium-based polymer RuNP@PIILS.[32] TEM micrographs of **2.14** and **2.15** revealed that the ruthenium nanoparticles were ultrafine and near monodisperse with diameters 1.8 and 1.6 nm (Figure 2.7c-d).

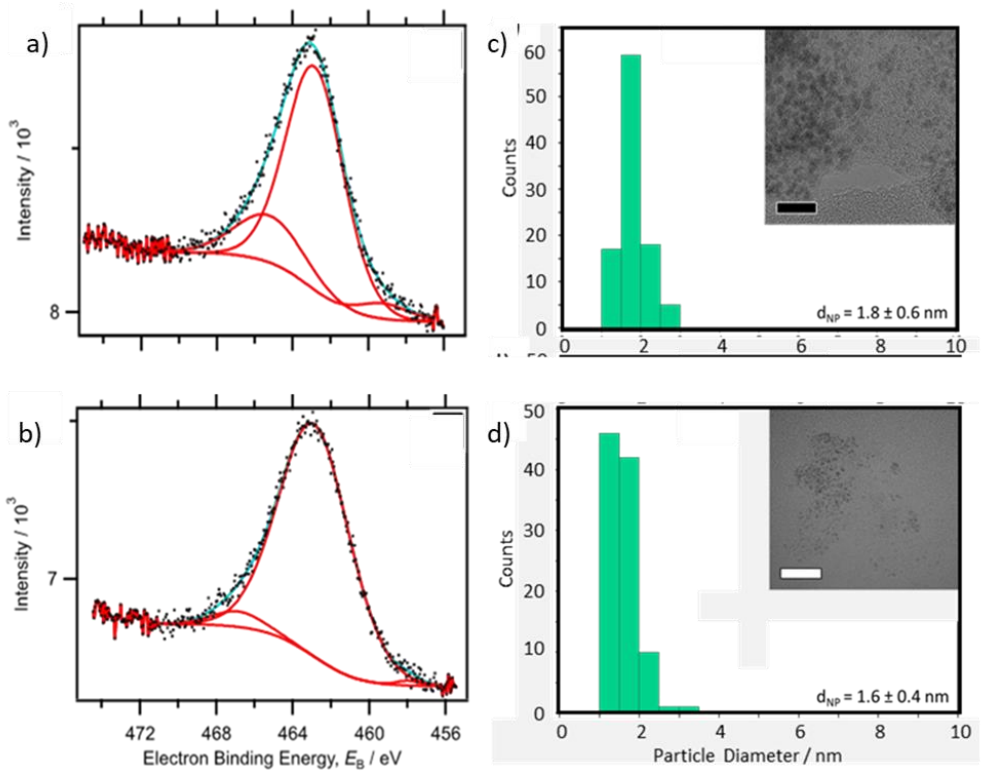

Figure 2.7 a-b) XPS data showing the Ru $3p_{3/2}$ region of PIIL-stabilised ruthenium nanoparticles **2.14** and **2.15**, respectively; c-d) Sizing data and TEM micrographs (inset) of PIIL-stabilised ruthenium nanoparticles **2.14** and **2.15.** Scale bars are 20 nm (white) and 10 nm (black).

In chapters 3 and 4, a further characterisation for both catalysts RuNP@NH_2-PEGPIILS (**2.14**) and the corresponding PEG-modified catalyst RuNP@NH_2-PEGPIILS (**2.15**), will be presented.

2.2.4 RuNP Catalysed Hydrolysis of Sodium Borohydride

The hydrolysis of sodium borohydride was identified to investigate the efficacy of catalysts **2.14** and **2.15** on the basis that PEG-modified 'click'-dendrimer stabilised noble and bimetallic metal nanoparticles have been reported to catalyse this reaction with promising initial TOFs and, as such, would provide a formative benchmark for comparative evaluation. The following methods were used to determine Turn Over Frequencies (TOF).

(a) Turn over frequencies based on the total metal content were determined using the following equation:

$$TOF\ (h^{-1}) = \frac{n_{H2\ liberated}}{n_{catalyst}\ x\ \ time\ (\text{min})}\ x\ 60$$

(b) Turn over frequencies based on the available surface metal atoms were determined using the following equation:

$$TOF\ (h^{-1}) = \frac{n_{H2\ liberated}}{n_{catalyst}\ x\ \%\ surface\ atoms}\ x\ 100\ x\ 60$$

The following assumptions were made to calculate the % of the metal atoms at the surface:

I. The nanoparticles were assumed to be spherical and the distribution of surface metal atoms on the surface is symmetric in all directions.
II. The average nanoparticle diameters were used for the calculation.
III. The surface was assumed to be metallic without oxidised species or interactions with the support and/or heteroatom donors.

Preliminary catalyst testing was conducted using recent literature protocols,[33,34] reactions were initially conducted at 30 °C using 0.2 mol% of **2.14** and **2.15** to catalyse the hydrolysis of a 0.28 M sodium borohydride solution (Figure 2.8). The reaction was monitored by measuring the volume of hydrogen liberated as a function of time using water displacement from a burette assembly, and all data were corrected by subtracting the background hydrogen gas generated under the same conditions. Hydrogen evolution started immediately with no induction period, which is consistent with the metallic state of the ruthenium. Under these conditions, RuNP@NH_2-PIILS (**2.14**) gave the highest initial TOF of 134 $mole_{H2}.molcat^{-1}.min^{-1}$ and reached 92% conversion after 20 min, whereas its PEGylated counterpart RuNP@NH_2-PEGPIILS (**2.15**) was less active with a slightly lower initial TOF of 107 $mole_{H2}.molcat^{-1}.min^{-1}$. In contrast, under the same conditions, RuNP@PIILS and RuNP@PEGPIILS, which are similar to **2.14** and **2.15** but lack the amine group were less active with initial TOFs of 121 $mole_{H2}.molcat^{-1}.min^{-1}$ and 89 $mole_{H2}.molcat^{-1}.min^{-1}$, respectively (Figure 2.8). These two non-amine based catalysts were prepared by Reece Paterson, a PhD researcher in the Doherty group.

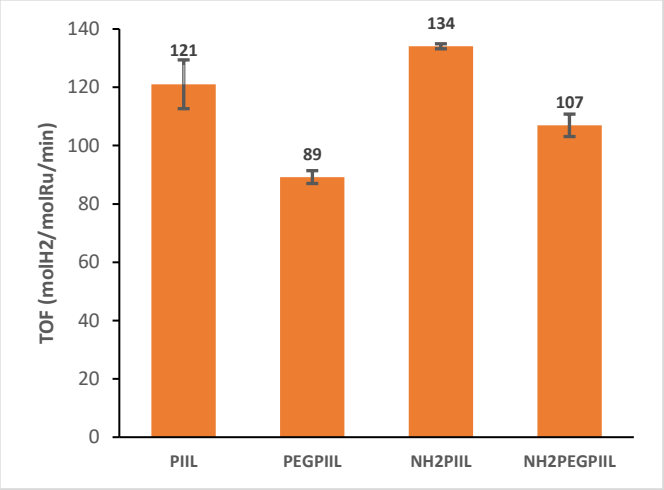

Figure 2.8 TOFs for the catalytic reactions of RuNP@PIILS, RuNP@PEG-PIILS, RuNP@NH_2-PIILS (**2.14**) and RuNP@NH_2-PEGPIILS (**2.15**).

For comparison, 0.2 mol% Ru/C (5 wt%) catalysed this hydrolysis under the same conditions but only reached 57% conversion after 25 min with a TOF of 69 $mole_{H2}.molcat^{-1}.min^{-1}$. The initial TOF for **2.14** improved to 177 $mole_{H2}.molcat^{-1}.min^{-1}$ when the reaction was conducted in a dilute solution (10 mL) with a reduced catalyst loading of 0.08 mol%. A series of baseline hydrolysis reactions conducted on their polymers **2.10** and **2.11** confirmed that the RuNPs were essential for catalysis, as the gas evolution did not exceed the background reaction under the same conditions.

The relationship between the effectiveness of catalysts **2.14** and **2.15** and the size of the nanoparticles is not clearly understood and further research will need to be conducted to examine the electron density on the surface of the RuNPs in relation to the support and to determine if the amine has an impact on the surface ensemble that activates the substrate or enhances the dispersion of the catalyst in the reaction mixture, providing access to the active site. Amine-modified supports have been previously reported to enhance the effectiveness of nanoparticle catalysts when compared to their unmodified counterparts. For instance, ruthenium nanoparticles stabilised within the pores of amine-modified MIL-53 (MIL-53(Al)-NH_2) are significantly more active catalysts for the dehydrogenation of amine borane than unmodified MIL(Al)-53. This enhancement was attributed to the creation and stabilisation of ultra-small RuNPs.[35] Incorporating an amine onto the surface of a catalyst support has been reported to have beneficial effects on catalyst performance. Examples include the significant improvement in both activity and selectivity of platinum nanowires for the partial

hydrogenation of nitroarenes to N-phenylhydroxylamine,[36] increased activity of RuNPs in the aqueous phase hydrogenation of levulinic acid to γ-valerolactone,[37] enhanced activity for the transfer hydrogenation of nitroarenes catalysed by RuNP confined in an amine-modified porous organic polymer,[38] heightened activity in the PtNP-catalysed hydrogenation of quinoline,[39] and improved activity and selectivity for Pt/Co and PdNP-catalysed semi-hydrogenation of alkynes.[40,41] Influence of Sodium Hydroxide

When comparing the effectiveness of **2.14** and **2.15** with previous studies on other supported ruthenium nanoparticles, it is important to approach the comparison with caution due to the significantly different experimental conditions and data collection protocols used. The turnover frequency (TOF) of 177 $mole_{H2}.molcat^{-1}.min^{-1}$ is higher than the TOF of 80 $mole_{H2}.molcat^{-1}.min^{-1}$ achieved with PEGylated dendrimer-stabilised RuNPs,[34] and 105 $mole_{H2}.molcat^{-1}.min^{-1}$ with ruthenium electrodeposited on nickel foam.[42] It also represents a significant improvement over the TOF of 67 $mole_{H2}.molcat^{-1}.min^{-1}$ obtained in 5% wt NaOH with RuNPs nanoclusters stabilised by confinement in the framework of Zeolite-Y,[17] 16 $mole_{H2}.molcat^{-1}.min^{-1}$ for RuNP@ZIF-67,[43] and 35 $mole_{H2}.molcat^{-1}.min^{-1}$ for carbon-supported bimetallic RuCo nanoparticles.[44] However, it is lower than the TOF of 550 $mole_{H2}.molcat^{-1}.min^{-1}$ obtained with RuNPs stabilised in Zeolite-Y[17] and 505 $mole_{H2}.molcat^{-1}.min^{-1}$ with nanoporous ruthenium prepared by chemical dealloying Ru-Al.[45] To the best of our knowledge, these latter systems are the most active ruthenium-based catalysts to be reported for this reaction.

The highest TOF achieved was for RuNP@NH_2-PIILP (**2.14**), and to explore further the reaction kinetics studies, deuterium isotope effects and recycling experiments were conducted. The corresponding experiments with catalysts **2.15** are reported for comparison. Multiple reports indicate increased activity for the metal nanoparticle-catalysed hydrolysis of sodium borohydride and amine borane when an additional base is present. Astruc, for instance, documented a significant rise in the initial turnover frequency (TOF) for the hydrolysis of $NaBH_4$ catalysed by dendrimer-supported RuNPs from 80 $mole_{H2}.molcat^{-1}.min^{-1}$ to 186 $mole_{H2}.molcat^{-1}.min^{-1}$ in the presence of 0.2 M NaOH. An increase in TOF was also observed for various other catalysts, including Rh, Au, Pd, Co, Ni, Fe, and Co nanoparticles, except for PtNPs, which experienced a distinctly negative effect.[34]

This increase in activity has been suggested to be caused by the hydroxide coordinating to the surface of the nanoparticle, boosting the electron density and facilitating activation of the O-H bond. In contrast, Pt is a metal with high electron density and is extremely reactive toward oxidative addition. Consequently, the hydroxide ions occupy active sites on the platinum surface, preventing substrate coordination and activation. The significant increase in activity of a dendrimer-stabilised RuNP-based catalyst led us to investigate the efficiency of **2.14** for the catalytic hydrolysis of $NaBH_4$ based on the concentration of sodium hydroxide. Reactions were conducted using 0.16 mol% of **2.14** to catalyse the hydrolysis of alkaline solutions of 0.28 M $NaBH_4$ with sodium hydroxide concentrations ranging from 0.05 mM to 100 mM (Figure 2.9). At low concentrations of NaOH (< 0.05 mM), there was no observable change in the initial TOF, but the TOFs gradually decreased with increasing NaOH concentration. This decrease became more significant when the concentration of sodium hydroxide reached 5 mM. The initial TOF dropped from 177 $mole_{H2}.molcat^{-1}.min^{-1}$ in the absence of sodium hydroxide to 85 $mole_{H2}.molcat^{-1}.min^{-1}$ in a 100 mM NaOH solution of $NaBH_4$. Several studies have reported a reduction in the rate of hydrogen generation with increasing NaOH concentration (1-10 wt% NaOH) for the ruthenium-catalysed hydrolysis of $NaBH_4$.[46,47] This has been attributed to the strong interactions between hydroxide ions and water, which decreases the available free water required for the hydrolysis of $NaBH_4$.[46] It is worth mentioning that elevated levels of NaOH have been proven to increase the rate of hydrogen production for the non-noble metal catalysed hydrolysis of $NaBH_4$. In other words, these systems can handle high hydroxide concentrations, and the bonding of OH- to the surface does not seem to hinder substrate binding.[48,49] The decrease in hydrogen generation rate for **2.14**, even with a low NaOH concentration of 0.001 wt% (0.28 mM), is unlikely to be due to reduced water activity. The high rate in the absence of NaOH may reflect the natural ability of ruthenium to facilitate oxidative addition. However, the presence of even a small amount of NaOH may reduce activity due to the hydrophilic nature of ruthenium, obstructing substrate coordination and activation. At these concentrations, there would be enough OH^- ions to disrupt the hydrogen-bonded $NaBH_4$---H_2O ensemble involved in the rate-limiting O-H bond activation step.

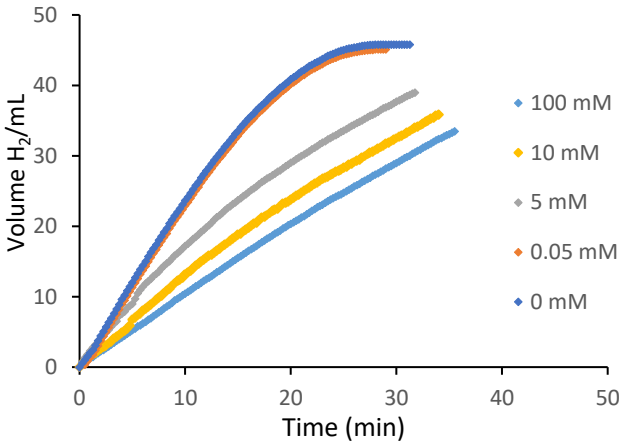

Figure 2.9 Plot of the volume of hydrogen generated against time for the hydrolysis of 2 mL of alkaline 0.28 M $NaBH_4$ as a function of sodium hydroxide concentration between 0.035 mM and 100 mM catalysed by 0.16 mol% **2.14**.

2.2.5 Comparative kinetic study as a function of temperature, catalyst concentration and $NaBH_4$ concentration.

Studies involving the rate of reaction at various temperatures and the activation parameters for the release of hydrogen from $NaBH_4$ were conducted to compare with similar systems in the literature. A sequence of experiments was carried out to observe the hydrolysis of a 0.28 M $NaBH_4$ solution over time and determine the initial rates at temperatures ranging from 294 K to 313 K (Figure 2.10 a-b). The calculated activation energies (E_a) for the hydrolysis of $NaBH_4$ catalysed by **2.14** and **2.15**, as determined from an Arrhenius plot of lnk versus 1/T (lnk = lnA - E_a/RT) using the initial rates obtained from the linear portion of the graph, were 38.9 kJ mol^{-1} and 46.4 kJ mol^{-1}, respectively (Figure 2.10 c-d). These values fall within the reported range for the hydrolysis of $NaBH_4$ using other RuNP-based catalysts, including 35 kJ mol^{-1} for RuNPs stabilised within Zeolite-Y,[17] 41 kJ mol^{-1} for acetate-stabilised water-dispersible RuNPs,[17] 36 kJ mol^{-1} for RuNPs confined in ZIF-67,[43] 47 kJ mol^{-1} for RuNPs immobilised by anion exchange resin IRA-400,[46] and 41.8 kJ mol^{-1} for ruthenium immobilised on Al_2O_3 pellets.[50] These values are slightly lower than 61.1 kJ mol^{-1} for RuNPs supported on amine-modified graphite,[51] 56.0 kJ mol^{-1} for RuNP@IRA-400,[46] and 66.9 kJ mol^{-1} for ruthenium supported on carbon.[52] No apparent correlation exists between the activation energies and the initial rates, which may be attributed to variations in the number of active sites or their availability, as these factors determine the pre-exponential factor (A).[35,53]

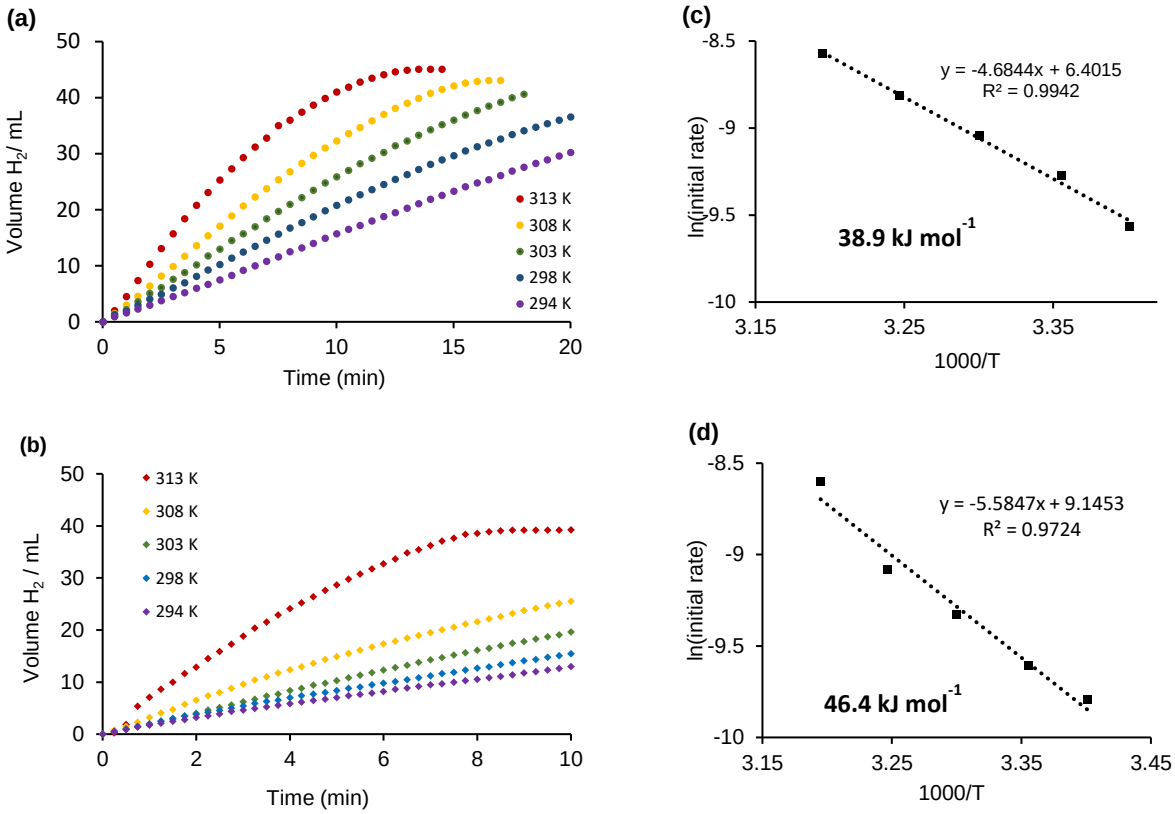

Figure 2.10 (a,b) a plot of the volume of hydrogen generated against time for the hydrolysis of 2 mL of 0.28 M $NaBH_4$ at various temperatures catalysed by 0.16 mol% **2.14** and 0.32 mol% **2.15**; (c,d) corresponding Arrhenius plot for the data

The release of hydrogen was then studied based on the concentration of **2.14** with catalyst loadings ranging from 0.12 mol% to 0.28 mol%, in 0.28 M $NaBH_4$ (0.021 g in 2 mL) at 298 K (Figure 2.11 a). The plot of the initial hydrogen generation rate versus catalyst concentration resulted in a straight line with a slope of 1.04 when plotted on a logarithmic scale (Figure 2.11 c), which suggests that the hydrolysis of $NaBH_4$ follows first-order kinetics with respect to the catalyst. Likewise, the slope obtained from the logarithmic plots using catalyst **2.15** with loadings between 0.25 mol% and 0.64 mol% was 1.0197, also indicating first-order kinetics (Figure 2.11 b, d).

This data is also in line with recent accounts of noble metal nanoparticle-catalysed production of hydrogen from hydrogen rich boron compounds, with a slope of 0.73 for RuNPs confined in

Zeolite-Y,[17] 0.94 for RuNPs stabilised by polyvinylpyrrolidinone,[54] 1.06 for $Ru(acac)_3$,[55] 1.17 for RuNPs stabilised by porphyrin,[56] 0.85 for PtCoNP@dendrimer,[34] and 0.82 for Ni2Pt@ZIF-8 .[57] RuNPs stabilised by polyvinylpyrrolidinone,[54] 1.06 for $Ru(acac)_3$,[55] 1.17 for porphyrin-stabilised RuNPs,[54] 0.85 for PtCoNP@dendrimer,[34] and 0.82 for Ni_2Pt@ZIF-8.[57]

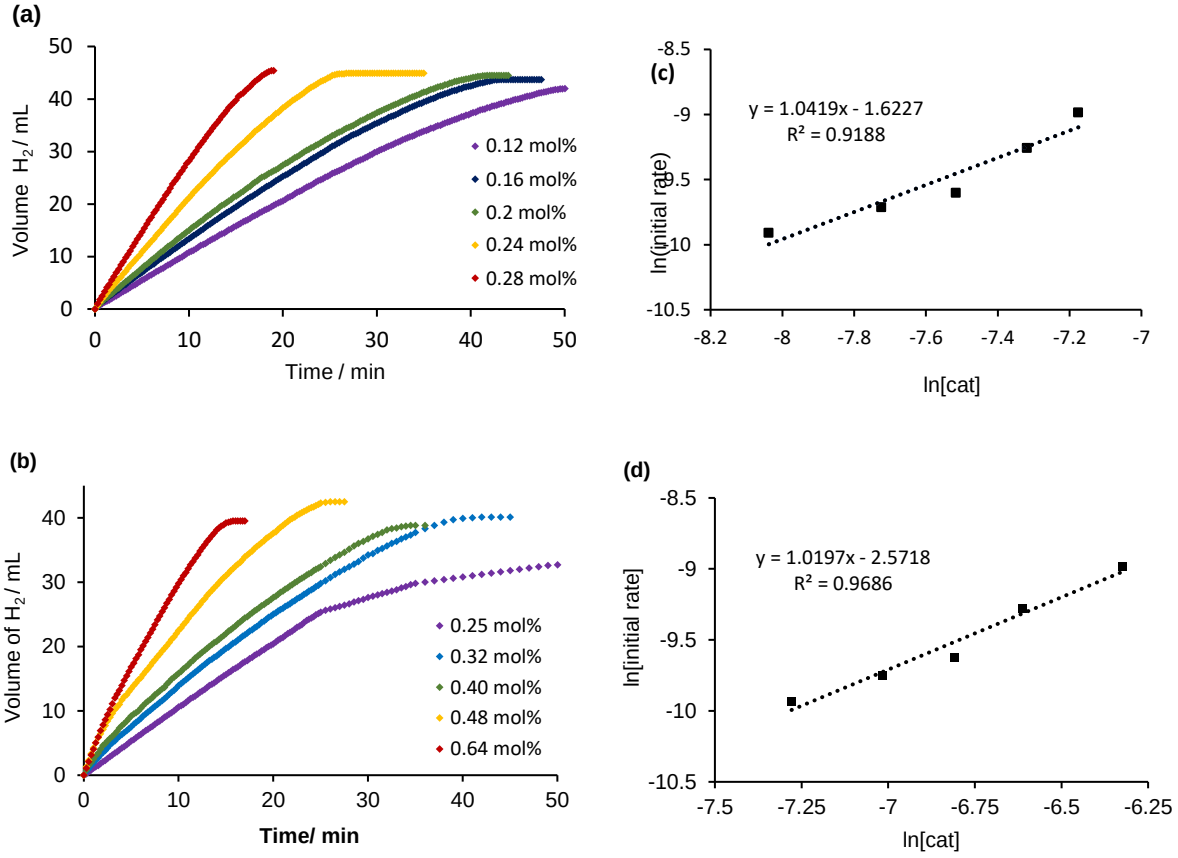

Figure 2.11 (a,b) Plots of the volume of hydrogen generated against time for the hydrolysis of 2 mL of 0.28 M $NaBH_4$ catalysed by various concentrations of **2.14** and **2.15**; (c,d) corresponding plots of the initial hydrogen generation rate against catalyst concentration in logarithmic scale.

Furthermore, an analysis was carried out to study how the rate of hydrolysis of $NaBH_4$ varied with the substrate concentration using catalyst **2.14.** The reaction order with respect to $NaBH_4$ has been reported to depend on the amount of $NaBH_4$ in solution ($NaBH_4$:catalyst ratio), changing from 1 to 0 as the concentration of $NaBH_4$ increases.[58]

To obtain kinetic data, a series of reactions were conducted using 0.026 mmol of catalyst **2.14** in 200 mL of water, while varying the initial concentration of $NaBH_4$ from 0.066 mM to 0.53 mM. These concentrations correspond to catalyst:hydride ratios between 2:1 and 1:4 (Figure 2.12). Low catalyst/hydride mole ratios were employed to prevent the BH_4 --induced dynamic saturation of the active sites on the catalyst surface during the reaction and avoid zero-order kinetics. These ratios ensured that the catalyst surface was not fully covered by $NaBH_4$ under these conditions, leaving active sites available. The slope of 1.02 derived from the logarithmic graph showing the relationship between hydrogen production rate and $NaBH_4$ concentration verifies that the hydrolysis follows first-order kinetics with respect to the substrate, indicating that the rate-limiting step involves activation of the substrate on the catalyst surface. Under identical conditions, a slope of 1.01 was also observed with catalyst **2.15**, which also aligns with first-order kinetics (Figure 2.12 c,d).

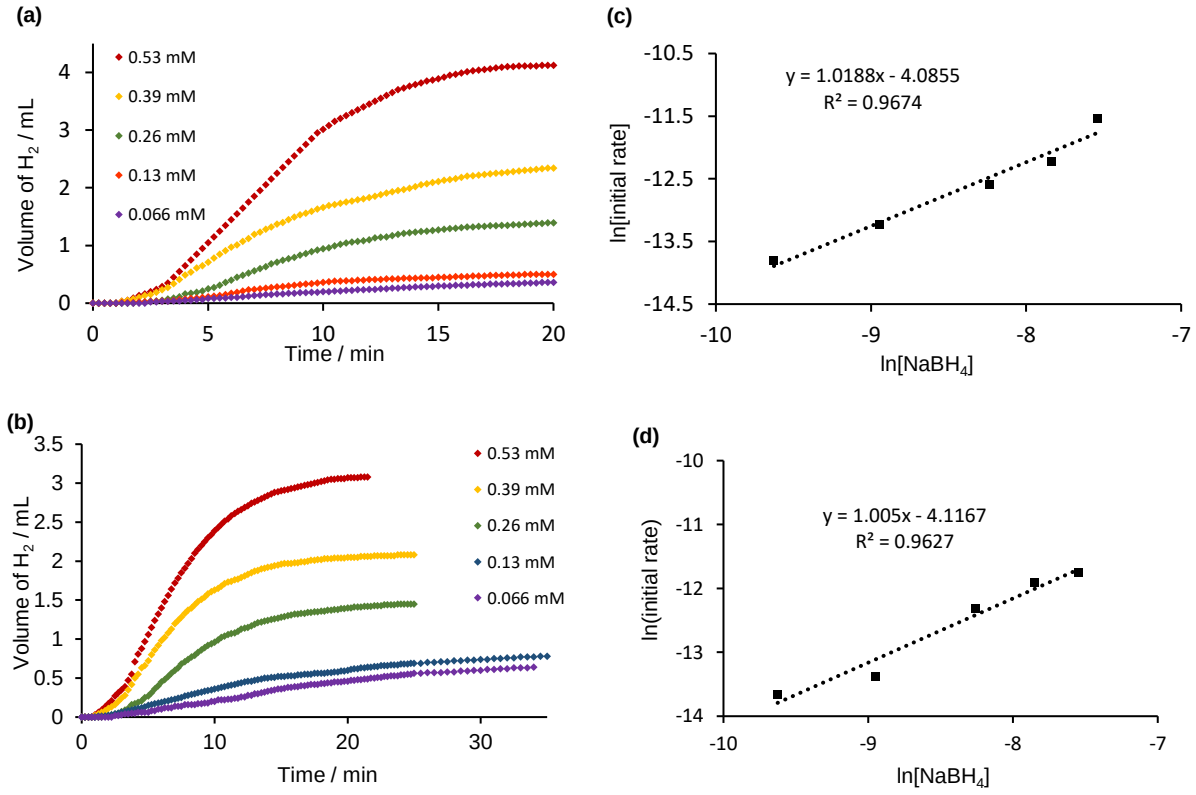

Figure 2.12 (a,b) Plot of the volume of hydrogen generated against time for the hydrolytic dehydrogenation of $NaBH_4$ at 298 K catalysed by 0.026 mmol of **2.14** (0.0764 g) and **2.15** (0.0376 g); (d-f) the corresponding plots of the initial hydrogen generation rate against the concentration of sodium borohydride in logarithmic scale.

The reaction kinetics with respect to $NaBH_4$ have been previously documented as first-order for ruthenium on carbon,[47] palladium on carbon[59], and Pd and Pt dispersed on functionalised surfaces of carbon nanotubes when the reactions were carried out at low concentrations of $NaBH_4$.[60] A similar investigation was completed using catalyst **2.14** with significantly higher catalyst/hydride mole ratios. The reaction was performed in 2 mL of water, and the initial concentration of sodium borohydride varied from 0.28 M to 1.11 M, corresponding to catalyst:hydride ratios between 1:625 and 1:2500. This resulted in a slope of 0.26, which is more consistent with zero-order kinetics due to saturation of the active sites on the catalyst surface during the reaction, as demonstrated by Patel[58] (Figure 2.13).

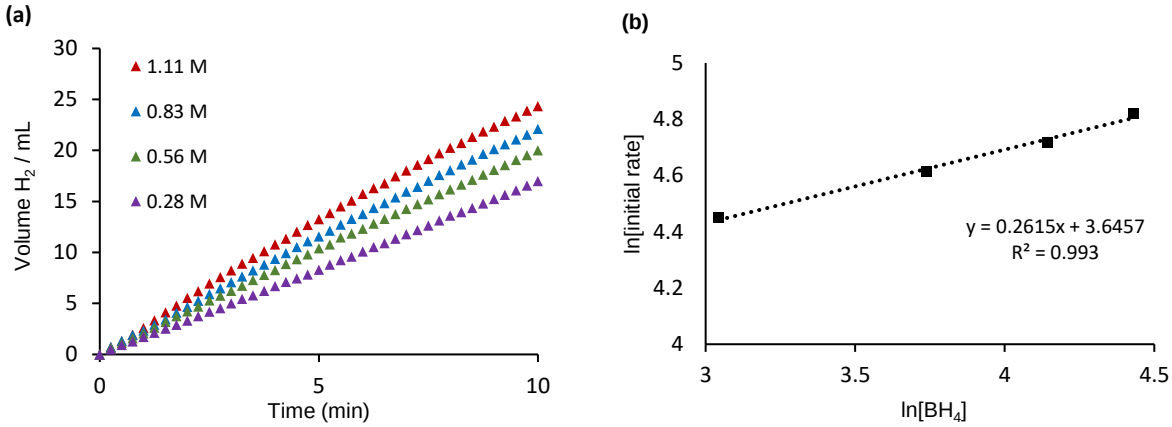

Figure 2.13 (a) Plot of volume of hydrogen generated against time for the hydrolytic dehydrogenation of $NaBH_4$ at 298 K catalysed by **2.14** (0.0026 g, 0.884 μmol); (b) the corresponding plot of the initial hydrogen generation rate against concentration of sodium borohydride in logarithmic scale.

2.2.6 Kinetic Isotope Effects (KIE)

The kinetic isotope effect (KIE) provides valuable information about the rate-limiting step (RLS) of a reaction. It has been commonly employed to investigate the catalytic liberation of hydrogen from borohydride and amine borane (AB).[61,62] Although the mechanism of the reaction is still not fully understood,[10] it is evident that both $NaBH_4$ and AB act as hydride donors, contributing one of the two hydrogen atoms in the resulting hydrogen. Meanwhile, water provides the other hydrogen atom in the form of a proton.[63,64] The rate-limiting step involves the activation of the O-H bond of water, which is indicated by the significant primary

kinetic isotope effect (KIE) observed when the hydrolysis is conducted in D_2O rather than H_2O.[34,59,61] Activation of the O-H bond may occur through oxidative addition by forming a hydrogen-bonded ensemble between a borohydride coordinated to the surface and a water proton. The liberated hydrogen could result from reductive elimination between a borohydride-derived NP-H and a water-derived NP-H or from a simultaneous σ-bond metathesis-like process involving a surface-coordinated $[BH_4]^-$ and the water-derived NP-H, possibly facilitated by hydroxide (Figure 2.14, pathways a-c). Alternatively, both the protonic and hydridic hydrogen atoms could be transferred to the nanoparticle surface through the oxidative addition of the O-H and B-H bonds, respectively, resulting in a dihydride that produces hydrogen and BH_3-OH via reductive elimination (Figure 2.14, pathway d-e), as suggested by Astruc for the CoNP@ZIF-8 catalysed hydrolysis of $NaBH_4$.[33] While the pathways in Figure 2.14 f-g initiate through the oxidative addition of the O-H bond of water in a hydrogen-bonded ensemble between water and a surface-coordinated borohydride, Jagirdar[65] and Ma[66] have proposed that the activation of the O-H bond and the generation of H_2 could occur through a hydrogen-bonding interaction between surface adsorbed water and a surface hydride produced by facile hydride transfer from $NaBH_4$ to the NP surface.

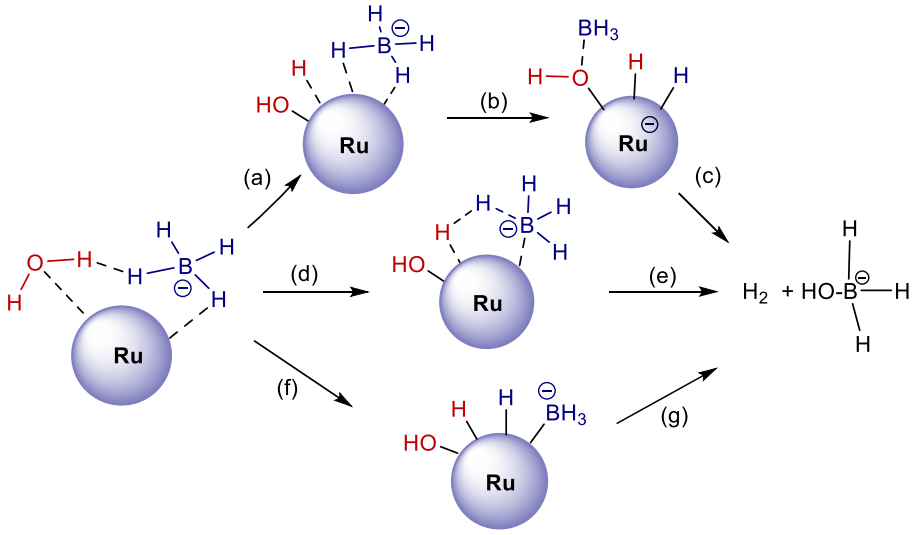

Figure 2.14 Proposed pathways for RuNP-catalysed hydrolytic hydrogen evolution involve (**a-c**) oxidative addition of an O-H and hydride transfer followed by reductive elimination of H_2, (**d-e**) oxidative addition of an O-H bond followed by σ -bond metathesis, or (**f-g**) oxidative addition of the O-H and B-H bonds followed by reductive elimination of H_2 and $[HO\text{-}BH_3]^-$.

The involvement of H_2O in the breakdown of $NaBH_4$ triggered by **2.14** was investigated by carrying out reactions in D_2O and observing the release of hydrogen over time to determine the KIE. Experiments were carried out under catalytic conditions, with 0.16 mol% of **2.14** and 2 mL of a 0.28 M $NaBH_4$ solution at 30 °C. A comparison of the effectiveness of **2.14** as a catalyst for the hydrolysis of $NaBH_4$ in H_2O and D_2O demonstrated that the reaction was faster in H_2O than in D_2O, exhibiting a primary kinetic isotope effect (k_H/k_D) of 2.31 (Figure 2.14a). This value aligns with the solvent isotope effect of 2.25 reported by Astruc for the visible light-accelerated hydrolytic dehydrogenation of $NaBH_4$ and amine borane catalysed by gold-ruthenium nanoalloys,[67] as well as the value of 1.8 obtained from a kinetic analysis of the alkaline media-mediated hydrolysis of $NaBH_4$ catalysed by platinum.[59] Furthermore, values of 2.3 were observed for dendrimer-stabilized RhNPs,[61] 2.4 for PtCo@dendrimer,[62] and 2.49 for NiNP@ZIF-8,[68] thus supporting a mechanism involving the rate-limiting cleavage of an O-H bond of water in a surface-coordinated hydrogen-bonded ensemble similar to the one depicted in Figure 2.14.

The initial reaction rates of H_2O and D_2O under stoichiometric conditions were also compared using 26 μmol of catalyst for the catalytic hydrolysis of 200 mL of a 0.13 mM solution of $NaBH_4$ at 30 °C, which corresponds to a catalyst:$NaBH_4$ ratio of 1:1. Comparison of the initial rates yielded a primary kinetic isotope effect of 1.7, as illustrated in Figure 2.14b. This effect is consistent with the rate-limiting oxidative addition of water. The KIE does not distinguish between a rate-limiting step where a surface-coordinated $NaBH_4$-HOH ensemble activates an O-H bond to afford a water-derived metal hydride and a surface-coordinated borohydride and concerted activation of both the B-H and O-H bonds in a similar hydrogen-bonded ensemble (Figure 2.14f).

To further investigate the mechanism, a comparison of the initial rates of hydrolysis of 0.13 mM solutions of $NaBD_4$ and $NaBH_4$ catalysed by 26 μmol of **2.14** at 30 °C was undertaken as this stoichiometry corresponds to a substrate/catalyst ratio of 1. The primary kinetic isotope effect (k_H/k_D) of 2.72 (Figure 2.15 c) similar to that obtained for the visible light-accelerated H_2 evolution from $NaBH_4$ catalysed by a gold-ruthenium nanoalloy, which, together with a KIE of **2.14** obtained for the hydrolysis of $NaBH_4$ in D_2O, suggests that both the O-H and B-H bonds are activated by the ruthenium atoms in the rate-limiting step, most likely through concerted

oxidative addition-hydride transfer via the surface-coordinated hydrogen-bonded [BH_3H^-]----- H-OH ensemble, rather than oxidative addition of both the O-H and B-H bonds.[33] Interestingly, when comparing the rates obtained under the conditions of catalysis using **2.14** to catalyse the hydrolysis of 2 mL of 0.28 M solutions of $NaBH_4$ and $NaBD_4$ at 30 °C, a KIE of 0.65 was obtained (Figure 2.15 d). This inverse kinetic isotope effect is consistent with a surface-coordinated borohydride participating in the activation of an O-H bond of water in the hydrogen-bonded ensemble before hydride transfer.

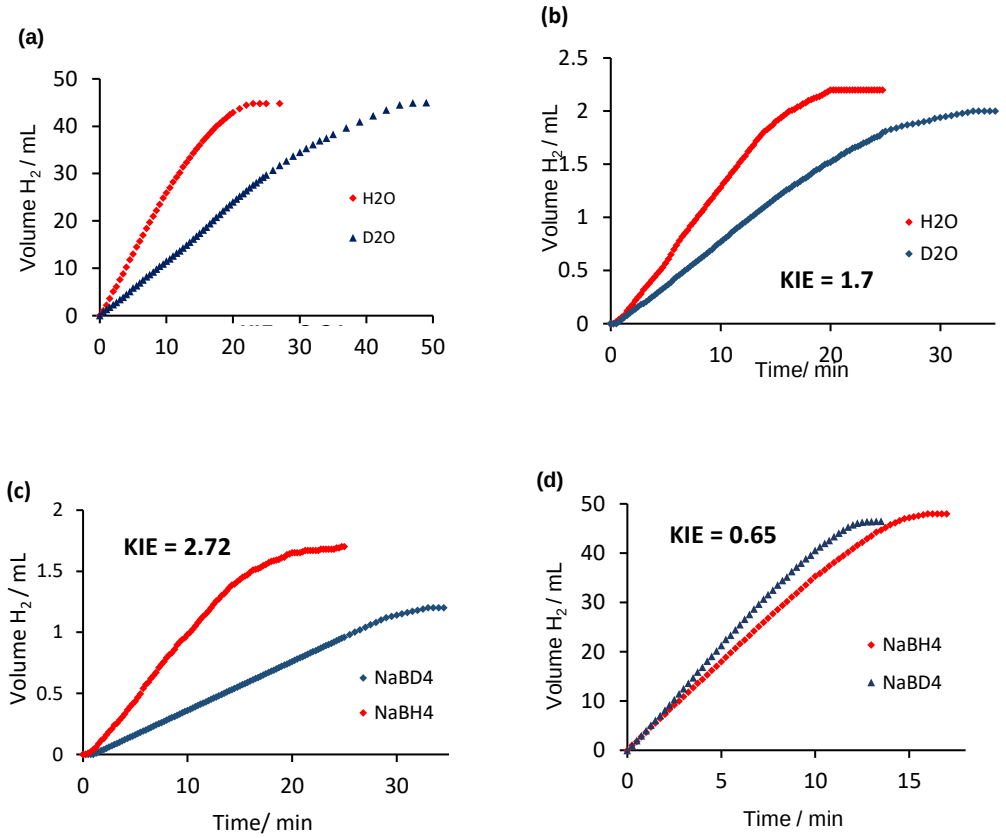

Figure 2.15 (a) Hydrogen release from 2 mL of 0.28 M $NaBH_4$ in H_2O (red line) and D_2O (blue line) catalysed by 0.16 mol% **2.14**; (b) Hydrogen release from 200 mL of 0.13 mM solutions of $NaBH_4$ in H_2O (red) and D_2O (blue) at 303 K using a stoichiometric amount of **2.14** (26 μmol); (c) hydrogen release from 200 mL of 0.13 mM solutions of $NaBH_4$ (red line) and $NaBD_4$ (blue line) in H_2O using a stoichiometric amount of catalyst **2.14** (26 μmol); (d) hydrogen release from 2 mL of a 0.28 M solution of $NaBH_4$ (red line) and $NaBD_4$ (blue line) in H_2O catalysed by 0.2 mol% **2.14**.

2.2.7 Catalyst Recycle and Poisoning Studies

Experimental investigations were conducted to analyse the performance of catalyst **2.14** upon multiple usages, to assess its durability, stability, and applicability in a continuous flow system at an expanded scale. Conventional recycling was unfeasible due to the challenges associated with separating and recovering the small quantity of catalyst via filtration without encountering loss of material after each cycle. Thus, an observational reusability study was conducted by monitoring the hydrolysis until the gas production was complete, after which additional NaBH4 was introduced to the liquid reaction mixture, and the ensuing gas production was monitored. This iterative process was replicated to monitor the catalyst's performance as a function of reaction time and the frequency of reuses. Complete conversions were achieved within 4 minutes for each experiment. Analysis of the gas evolution-time profile and corresponding conversion-cycle number profile in (Figure 2.16 a-b) shows a gradual decrease in conversion over five reuses, with the conversion dropping slightly from 89% after 2 minutes in the first run to 69% after the same duration in the fifth run.

The decrease in catalyst activity in successive runs, which is calculated as the percentage reduction in the initial TOF and determined from the slope of the linear section of the graph of volume versus time, indicates that **2.14** maintains 77% of its effectiveness after being reused five times (Figure 2.16 c, blue line). This is similar to the results of recycling studies conducted on other systems based on noble and non-noble metal nanoparticle catalysts, such as RuNPs immobilised in ZIF-67,[43] ruthenium nanoparticles immobilised within the pores of amine-functionalised MIL-53,[35] ruthenium supported on graphite,[51] RuNP stabilised by polyvinylpyrrolidone, zeolite-confined RuNPs,[17] dendrimer-stabilized PtCo, Rh and Pt nanoparticles and gold-transition metal nanoalloys.[34,61,67,68]

The results from the ICP-OES analysis of the liquid reaction mixture obtained after the fifth cycle indicated that the amount of ruthenium present was below the detection limit (< 0.1 mg L-1), indicating that the decrease in activity was probably not caused by the ruthenium leaching out to form a less active species.

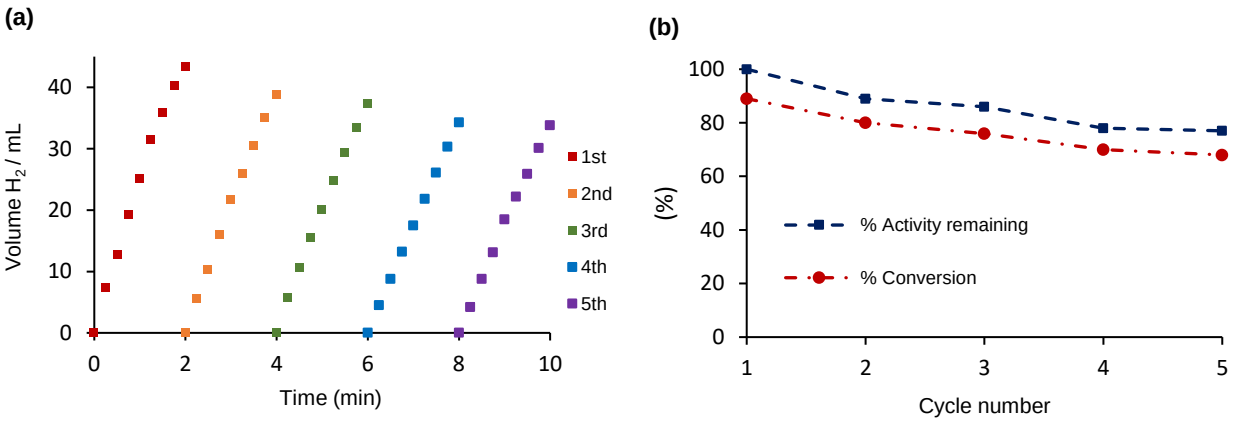

Figure 2.16: (a) Plots of volume versus time for the hydrolysis of 20 mL of a 0.028 M solution of $NaBH_4$ catalysed by 2 mol% **2.14** at 30 °C across five runs; (b) conversion reached in each run (red line) and percentage of initial activity remaining after each successive reuse (blue line). Volumes measured are an average of three runs.

Hot filtration experiments were also carried out to investigate if soluble ruthenium compounds could be causing the release of gas. Using a standard procedure, a hydrolysis of a 0.028 M solution of $NaBH_4$ catalysed by 2 mol% **2.14** was allowed to achieve around 50% conversion. Afterwards, the reaction mixture was filtered using a 45-micron syringe filter to remove the catalyst and the hydrogen evolution from the filtrate was monitored. The hydrogen produced from this filtrate was equivalent to the hydrolysis that occurs without any catalyst present (Figure 2.17, blue line). This strongly suggests that the active catalyst is not soluble in the solution and that leaching does not create active soluble ruthenium compounds. Under identical conditions, a complimentary hydrolysis was allowed to reach completion. The resulting mixture was filtered using a syringe filter with a pore size of (0.45 µm), and an extra amount of $NaBH_4$ was introduced into the filtered solution. The released hydrogen corresponded to the non-catalysed background hydrolysis, which further supports that the catalysis involves a heterogeneous system (Figure 2.17, orange line). After the fifth run, transmission electron microscopy analysis of the catalyst showed that the ruthenium nanoparticles remained almost uniformly dispersed, with an average diameter of 1.8 ± 0.5 nm (Figure 2.17b). This was similar to the 1.8 ± 0.6 nm diameter for the freshly prepared catalyst (Figure 2.7 c), indicating that the decrease in conversion with repeated use is unlikely to be due to aggregation.

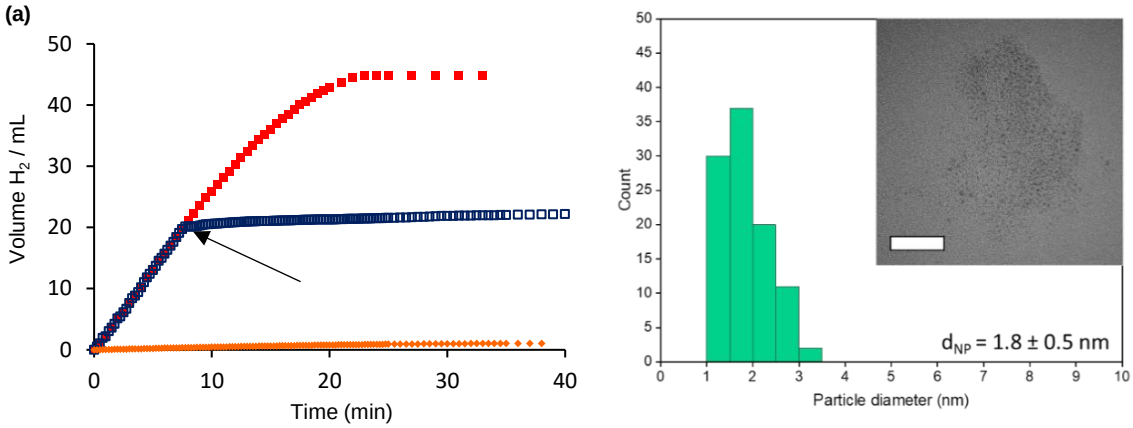

Figure 2.17 (a) Hot filtration experiment for $NaBH_4$ catalysed by 2 mol% **2.14** shows the reaction quenched after filtration. Red line – hydrogen evolution in the presence of **2.14**; blue line in the presence of **2.14** with filtration at t = 7.75 min; (b) sizing histogram of RuNPs for **2.14** after five experimental cycles. A TEM image of the material is shown in the inset.

There have been multiple reports that the by-product sodium metaborate dihydrate, which is produced during the hydrolysis of $NaBH_4$, deactivates the catalyst by adsorbing on the surface.[35,44,62] However, Wie has shown that the deactivated Ru on nickel foam catalyst can be partially regenerated by rinsing the catalyst with deionised water and fully regenerated by rinsing with HCl to eliminate the $NaBO_2$.[42] To investigate this possibility, a series of poisoning studies were conducted to establish if the build-up of $NaBO_2$ modified catalyst performance. In these studies, solutions of **2.14** were mixed with 100 equivalents of sodium metaborate across a range of pre-stirring times from 0 min to 60 min before the addition of $NaBH_4$. The gas released during the reaction was then observed over time. A ^{11}B NMR spectrum of the reaction mixture confirmed that the tetrahydroxyborate anion $[B(OH)_4]^-$ was the only by-product produced. The spectrum showed a distinct peak at δ 2.2 ppm,[59] and no partially hydrolysed intermediates or other species were detected. The comparison of hydrogen evolution (Figure 2.18 a-b) demonstrates that the catalyst is passivated by the addition of $NaBO_2$, as indicated by the decrease in conversion and initial TOF with increasing pre-stirring time. The passivation effect is immediate, with the TOF decreasing from 84 $mole_{H2}.molcat^{-1}.min^{-1}$ to 80 $mole_{H2}.molcat^{-1}.min^{-1}$ upon the addition of $NaBO_2$ without pre-stirring (time = 0 min). Subsequently, the TOFs gradually decrease to 57 $mole_{H2}.molcat^{-1}.min^{-1}$ with a pre-stirring time of 60 min.

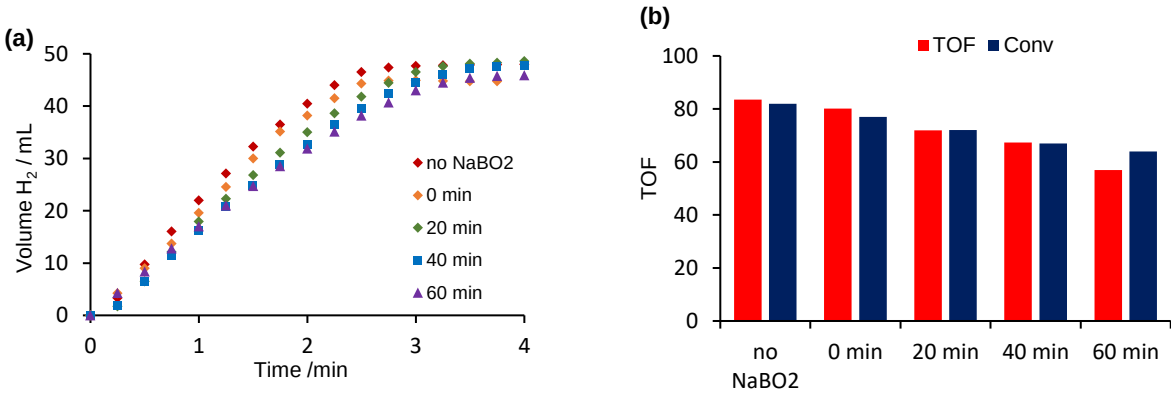

Figure 2.18 (a) A plot of the volume of hydrogen against time for hydrolysis of 20 mL of 0.028 M solution of $NaBH_4$ catalysed by 2 mol% **2.14** as a function of pre-stirring time with added $NaBO_2$; (b) the corresponding conversions obtained and TOFs as a function of $NaBO_2$ pre-stirring time.

The formation of $NaBO_2$ can also be observed by tracking the pH of the reaction solution as a function of time during the catalytic hydrolysis of a 0.028 M $NaBH_4$ solution using 2 mol% of **2.14.** As shown in Figure 2.19, the pH of the reaction solution corresponds to the conversion, starting at pH 8.3 at time = 0 min, which was measured immediately after adding the $NaBH_4$ and increasing to pH = 11.1 after approximately 2.5 min when the gas evolution had ended. For comparison, a 0.028 M solution of $NaBO_2$ without a catalyst or $NaBH_4$ has a pH of 11.30, which gratifyingly is similar to the pH of a hydrolysis reaction at high conversion.

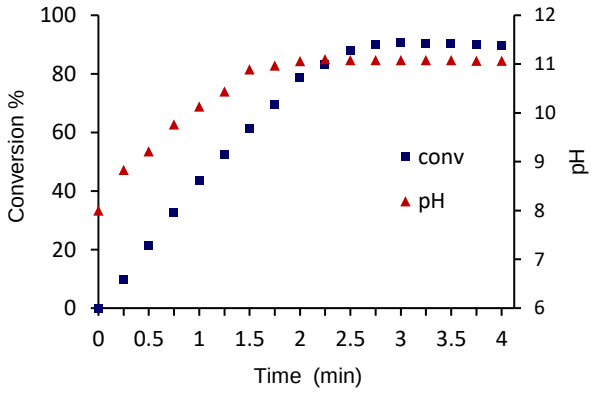

Figure 2.19 A plot of pH and conversion against time for the hydrolysis of a 0.028 M solution of $NaBH_4$ (20 mL) at 30 °C catalysed by 2 mol% **2.14**

2.3 Conclusions

Ruthenium nanoparticles stabilised by ionic liquids immobilised on a polymer catalyse the hydrolytic release of hydrogen from sodium borohydride. The catalyst, which is stabilised by an amino-modified imidazolium-based polymer, exhibited the highest level of activity, with an initial turnover frequency (TOF) of 171 $mole_{H2}.mol_{cat}^{-1}.min^{-1}$, one of the highest reported for a ruthenium nanoparticle-based system. The kinetics of the reaction showed that, at low hydride/catalyst mole ratios, the reaction was first order with respect to the catalyst and sodium borohydride, but at high hydride/catalyst mole ratios, it was zero order with respect to $NaBH_4$ concentration. The observed activation energies of 38.9 kJ mol^{-1} to 51.8 kJ mol^{-1} for RuNP@NH_2-PIILS and RuNP@NH_2-PEGPIILS, respectively, are typical for 'the hydrolysis of hydrogen-rich boron compounds catalysed by platinum group metal nanoparticles. The activation energy of 38.9 kJ mol^{-1} for RuNP@NH_2PIILS is lower than the other catalysts tested and aligns with its higher initial TOF. A kinetic isotope effect (k_H/k_D) of 2.31 was determined for reactions in H_2O and D_2O, and a k_H/k_D of 2.72 for reactions with $NaBH_4$ and $NaBD_4$ at a low catalyst/hydride mole ratio. These values suggest that the O-H and B-H bonds are activated by surface ruthenium atoms in the rate-limiting step, most likely through a concerted oxidative addition-hydride transfer involving the surface-coordinated [BH_3H^-]-----H-OH ensemble. Interestingly, the k_H/k_D of 0.67 obtained from comparing the initial rates for the hydrolysis of $NaBH_4$ and $NaBD_4$ under catalytic conditions shows an inverse KIE, which supports the idea of a surface-coordinated borohydride activating an O-H bond of water prior to rapid hydride transfer. Recycle studies revealed that RuNP@NH_2-PIILS retains 79% of its activity over five runs, and poisoning studies with $NaBO_2$ suggest that catalyst deactivation may result from the absorption of the metaborate by-product on the surface of the nanoparticle. To this end, PIILs can effectively be used to explore how polymer characteristics such as charge density, the quantity and type of heteroatom donor and functionality, porosity, and hydrophilicity impact the size, shape, and effectiveness of the nanoparticles. Additionally, they can be used to customise catalyst-support interactions to improve effectiveness. Ultimately, this catalyst technology will be expanded to encompass the hydrogen evolution reaction to create durable, stable, highly active, and cost-efficient catalysts for application in fuel cells.

2.4 References

1. P. Poizot and F. Dolhem, *Energy Environ. Sci.*, 2011, **4**, 2003–2019.

2. L. Schlapbach and A. Züttel, *Nature*, 2001, **414**, 353–358.

3. T. He, P. Pachfule, H. Wu, Q. Xu and P. Chen, *Nat. Rev. Mater.*, 2016, **1**, 1–17.

4. U. Eberle, M. Felderhoff and F. Schüth, *Angew. Chem. Int. Ed.*, 2009, **48**, 6608–6630.

5 A. F. Dalebrook, W. Gan, M. Grasemann, S. Moret and G. Laurenczy, *Chem. Commun.*, 2013, **49**, 8735–8751.

6. U. B. Demirci, *Int. J. Hydrog. Energy*, 2017, **42**, 21048–21062.

7. P. Brack, S. E. Dann and K. G. U. Wijayantha, *Energy Sci. Eng.*, 2015, **3**, 174–188.

8. T. Shimbayashi and K. Fujita, *Tetrahedron*, 2020, **76**, 130946.

9. L. Luconi, G. Tuci, G. Giambastiani, A. Rossin and M. Peruzzini, *Int. J. Hydrog. Energy*, 2019, **44**, 25746–25776.

10. C. Wang and D. Astruc, *Chem. Soc. Rev.*, 2021, **50**, 3437–3484.

11. X.-F. Yang, A. Wang, B. Qiao, J. Li, J. Liu and T. Zhang, *Acc. Chem. Res.*, 2013, **46**, 1740–1748.

12. G. Schmid, *Nanoparticles: From Theory to Application*, John Wiley & Sons, 2011.

13. Z.-M. Huang, A. Su and Y.-C. Liu, *Energy*, 2013, **51**, 230–236.

14. K. Kim, T. Kim, K. Lee and S. Kwon, *J. Power Sources*, 2011, **196**, 9069–9075.

15. L. Yin, T. Zhang, K. Dai, B. Zhang, X. Xiang and H. Shang, *ACS Sustain. Chem. Eng.*, 2021, **9**, 822–832.

16. Q. Sun, N. Wang, Q. Bing, R. Si, J. Liu, R. Bai, P. Zhang, M. Jia and J. Yu, *Chem*, 2017, **3**, 477–493.

17. M. Zahmakiran and S. Özkar, *Langmuir*, 2009, **25**, 2667–2678.

18. Q. Sun, N. Wang, R. Bai, Y. Hui, T. Zhang, D. A. Do, P. Zhang, L. Song, S. Miao and J. Yu, *Adv. Sci.*, 2019, **6**, 1802350.

19. P. Verma, K. Yuan, Y. Kuwahara, K. Mori and H. Yamashita, *Appl. Catal. B Environ.*, 2018, **223**, 10–15.

20. B. Şen, A. Aygün, A. Şavk, C. Yenikaya, S. Cevik and F. Şen, *Int. J. Hydrog. Energy*, 2019, **44**, 2988–2996.

21. G. Lu, S. Li, Z. Guo, O. K. Farha, B. G. Hauser, X. Qi, Y. Wang, X. Wang, S. Han, X. Liu, J. S. DuChene, H. Zhang, Q. Zhang, X. Chen, J. Ma, S. C. J. Loo, W. D. Wei, Y. Yang, J. T. Hupp and F. Huo, *Nat. Chem.*, 2012, **4**, 310–316.

22. C. Hardacre and V. Parvulescu, *Catalysis in Ionic Liquirds: From Catalyst Synthesis to Application*, Royal Society of Chemistry, 2014.

23. A. S. Pensado and A. A. H. Pádua, *Angew. Chem. Int. Ed.*, 2011, **37**, 8683–8687.

24. K. L. Luska and A. Moores, *ChemCatChem*, 2012, **4**, 1534–1546.

25. F. Giacalone and M. Gruttadauria, *ChemCatChem*, 2016, **8**, 664–684.

26. L. Lu, S. Zou and B. Fang, *ACS Catal.*, 2021, **11**, 6020–6058.

27. S. Doherty, J. G. Knight, T. Backhouse, E. Abood, H. Alshaikh, I. J. S. Fairlamb, R. A. Bourne, T. W. Chamberlain and R. Stones, *Green Chem.*, 2017, **19**, 1635–1641.

28. S. Doherty, J. G. Knight, T. Backhouse, A. Bradford, F. Saunders, R. A. Bourne, T. W. Chamberlain, R. Stones, A. Clayton and K. Lovelock, *Catal. Sci. Technol.*, 2018, **8**, 1454–1467.

29. S. Doherty, J. G. Knight, T. Backhouse, T. S. T. Tran, R. Paterson, F. Stahl, H. Y. Alharbi, T. W. Chamberlain, R. A. Bourne, R. Stones, A. Griffiths, J. P. White, Z. Aslam, C. Hardare, H. Daly, J. Hart, R. H. Temperton, J. N. O'Shea and N. H. Rees, *Catal. Sci. Technol.*, 2022, **12**, 3549–3567.

30. S. Montolio, C. Vicent, V. Aseyev, I. Alfonso, M. I. Burguete, H. Tenhu, E. García-Verdugo and S. V. Luis, *ACS Catal.*, 2016, **6**, 7230–7237.

31. S. D. Chambreau, A. C. Schenk, A. J. Sheppard, G. R. Yandek, G. L. Vaghjiani, J. Maciejewski, C. J. Koh, A. Golan and S. R. Leone, *J. Phys. Chem. A*, 2014, **118**, 11119–11132.

32. R. Paterson, A. A. Alharbi, C. Wills, C. Dixon, L. Šiller, T. W. Chamberlain, A. Griffiths, S. M. Collins, K. Wu, M. D. Simmons, R. A. Bourne, K. R. J. Lovelock, J. Seymour, J. G. Knight and S. Doherty, *Mol. Catal.*, 2022, **528**, 112476.

33. C. Luo, F. Fu, X. Yang, J. Wei, C. Wang, J. Zhu, D. Huang, D. Astruc and P. Zhao, *ChemCatChem*, 2019, **11**, 1643–1649.

34. N. Kang, R. Djeda, Q. Wang, F. Fu, J. Ruiz, J.-L. Pozzo and D. Astruc, *ChemCatChem*, 2019, **11**, 2341–2349.

35. S. Zhang, L. Zhou and M. Chen, *RSC Adv.*, 2018, **8**, 12282–12291.

36. G. Chen, C. Xu, X. Huang, J. Ye, L. Gu, G. Li, Z. Tang, B. Wu, H. Yang, Z. Zhao, Z. Zhou, G. Fu and N. Zheng, *Nat. Mater.*, 2016, **15**, 564–569.

37. J. Tan, J. Cui, G. Ding, T. Deng, Y. Zhu and Y. Li, *Catal. Sci. Technol.*, 2016, **6**, 1469–1475.

38. J. Mondal, S. K. Kundu, W. K. Hung Ng, R. Singuru, P. Borah, H. Hirao, Y. Zhao and A. Bhaumik, *Chem. – Eur. J.*, 2015, **21**, 19016–19027.

39. M. Guo, C. Li and Q. Yang, *Catal. Sci. Technol.*, 2017, **7**, 2221–2227.

40. S. G. Kwon, G. Krylova, A. Sumer, M. M. Schwartz, E. E. Bunel, C. L. Marshall, S. Chattopadhyay, B. Lee, J. Jellinek and E. V. Shevchenko, *Nano Lett.*, 2012, **12**, 5382–5388.

41. F. P. da Silva, J. L. Fiorio and L. M. Rossi, *ACS Omega*, 2017, **2**, 6014–6022.

42. Y. Wei, Y. Wang, L. Wei, X. Zhao, X. Zhou and H. Liu, *Int. J. Hydrog. Energy*, 2018, **43**, 592–600.

43. D. D. Tuan and K.-Y. A. Lin, *Chem. Eng. J.*, 2018, **351**, 48–55.

44. R. Fiorenza, S. Scirè and A. m. Venezia, *Int. J. Energy Res.*, 2018, **42**, 1183–1195.

45. L. Semiz, N. Abdullayeva and M. Sankir, *J. Alloys Compd.*, 2018, **744**, 110–115.

46. S. C. Amendola, S. L. Sharp-Goldman, M. S. Janjua, N. C. Spencer, M. T. Kelly, P. J. Petillo and M. Binder, *Int. J. Hydrog. Energy*, 2000, **25**, 969–975.

47. Y. Shang and R. Chen, *Energy Fuels*, 2006, **20**, 2149–2154.

48. J. C. Ingersoll, N. Mani, J. C. Thenmozhiyal and A. Muthaiah, *J. Power Sources*, 2007, **173**, 450–457.

49. J. Lee, K. Y. Kong, C. R. Jung, E. Cho, S. P. Yoon, J. Han, T.-G. Lee and S. W. Nam, *Catal. Today*, 2007, **120**, 305–310.

50. C.-C. Su, M.-C. Lu, S.-L. Wang and Y.-H. Huang, *RSC Adv.*, 2012, **2**, 2073–2079.

51. Y. Liang, H.-B. Dai, L.-P. Ma, P. Wang and H.-M. Cheng, *Int. J. Hydrog. Energy*, 2010, **35**, 3023–3028.

52. J. S. Zhang, W. N. Delgass, T. S. Fisher and J. P. Gore, *J. Power Sources*, 2007, **164**, 772–781.

53. X. Xie, Y. Li, Z.-Q. Liu, M. Haruta and W. Shen, *Nature*, 2009, **458**, 746–749.

54. Y. Karataş, A. Aygun, M. Gülcan and F. Şen, *J. Taiwan Inst. Chem. Eng.*, 2019, **99**, 60–65.

55. E. Keçeli and S. Özkar, *J. Mol. Catal. Chem.*, 2008, **286**, 87–91.

56. N. Zhang, G. Liu, Y. Sun, Y. Wang, J. Yan and X. Liu, *Catal. Lett.*, 2021, **151**, 2272–2278.

57. F. Fu, C. Wang, Q. Wang, A. M. Martinez-Villacorta, A. Escobar, H. Chong, X. Wang, S. Moya, L. Salmon, E. Fouquet, J. Ruiz and D. Astruc, *J. Am. Chem. Soc.*, 2018, **140**, 10034–10042.

58. N. Patel, R. Fernandes and A. Miotello, *J. Power Sources*, 2009, **188**, 411–420.

59. G. Guella, C. Zanchetta, B. Patton and A. Miotello, *J. Phys. Chem. B*, 2006, **110**, 17024–17033.

60. R. Peña-Alonso, A. Sicurelli, E. Callone, G. Carturan and R. Raj, *J. Power Sources*, 2007, **165**, 315–323.

61. Q. Wang, F. Fu, A. Escobar, S. Moya, J. Ruiz and D. Astruc, *ChemCatChem*, 2018, **10**, 2673–2680.

62. Q. Wang, F. Fu, S. Yang, M. Martinez Moro, M. de los A. Ramirez, S. Moya, L. Salmon, J. Ruiz and D. Astruc, *ACS Catal.*, 2019, **9**, 1110–1119.

63. W.-W. Zhan, Q.-L. Zhu and Q. Xu, *ACS Catal.*, 2016, **6**, 6892–6905.

64. C. Wang, Q. Wang, F. Fu and D. Astruc, *Acc. Chem. Res.*, 2020, **53**, 2483–2493.

65. S. Babu Kalidindi, U. Sanyal and B. R. Jagirdar, *Phys. Chem. Chem. Phys.*, 2008, **10**, 5870–5874.

66. H. Ma and C. Na, *ACS Catal.*, 2015, **5**, 1726–1735.

67. N. Kang, Q. Wang, R. Djeda, W. Wang, F. Fu, M. M. Moro, M. de los A. Ramirez, S. Moya, E. Coy, L. Salmon, J.-L. Pozzo and D. Astruc, *ACS Appl. Mater. Interfaces*, 2020, **12**, 53816–53826.

68. C. Wang, J. Tuninetti, Z. Wang, C. Zhang, R. Ciganda, L. Salmon, S. Moya, J. Ruiz and D. Astruc, *J. Am. Chem. Soc.*, 2017, **139**, 11610–11615.

Chapter 3: Application of RuNP@NH_2-PEGPIILS Catalyst to the Partial and Complete Reduction of Quinolines

3.1 Introduction

Quinoline was discovered by Runge in 1834 and is naturally found in bone oil, coal tar, and the bark of the Angostura plant. The name "quinoline" comes from heating the famous antimalarial alkaloid quinine with alkali. While quinoline itself is not very useful, its reduction to 1,2,3,4-tetrahydroquinoline has been a significant discovery as this motif is present in a range of bioactive compounds with antimalarials, anti-inflammatory, antibacterial and antitumor properties as well as agrochemicals with insecticidal and herbicidal activity[1] for example, benzastatin, aflaquinolones and aspoquinolon.[2,3] Additionally, quinoline has been used to make photovoltaic cells, organic light-emitting diodes (OLEDs), solvents for terpenes and resins, and quinoline-based dyes used in photographic plates.[4] Moreover, quinoline could be used as a liquid organic hydrogen storage substance.[2,5] Catalytic reduction of quinoline and its derivatives presents an appealing method for producing this motif, as it is more effective and uncomplicated compared to other complex processes involving metal-catalysed intramolecular N-C and C-C bond-forming cyclisations, cycloadditions, and rearrangements.[6]

Although homogeneous catalysts using precious metals such as Rh, Ru, Pt and Pd have been established,[2] these catalysts are expensive and challenging to recover and reuse, the use of a stoichiometric amount of co-catalyst makes reuse difficult and reduces environmental friendliness, and they are not suitable for integration into a continuous flow system. On the other hand, supported metal nanoparticles seem to be much more adaptable with various benefits, as they can be recovered and reused using a straightforward filtration process.

The use of heterogeneous catalysts for the reaction of quinoline has gained popularity, and nanoparticles play an essential role in this regard. Several studies have shown that utilising supported metal nanoparticles proves to be highly adaptable, bringing numerous benefits such as enabling simple recovery and reuse through filtration. Furthermore, the catalyst is frequently compatible with environmentally friendly solvents and can be seamlessly integrated into continuous flow processes for scale up.[7]

Additionally, the efficiency of the catalyst can be adjusted by controlling the growth and size of the nanoparticles.[7] In this regard, nanoparticle-support systems such as RuNP/hydroxyapatite,[8] RuNP/ionic liquids,[9] RuNP/N-doped carbon,[10] AuNP supported on

TiO_2,[11] PEG-stabilised RhNPs,[12] have been employed for the selective reduction of quinoline to 1,2,3,4-THQ. Many of these systems show high activity and good selectivity profiles, but harsh conditions are sometimes needed. There is interest in developing more active systems that can operate under mild conditions and that are tolerant towards poisoning by heteroatom donors. Evidence suggests that the activity and selectivity of nanoparticle-based catalysts for hydrogenations can be improved by incorporating organic modifiers onto the support[13] or by tuning metal-support interactions.[14]

Numerous reports indicate that stabilising NPs with modified supports improves their activity and selectivity as catalysts for hydrogenation. This enhancement has been attributed to high surface electron density, ultra-small nanoparticle size, and effective dispersion. For example, palladium nanoparticles supported on amine-rich silica hollow nanospheres showed a significant increase in the turnover frequency for the selective hydrogenation of quinoline compared to their unmodified counterparts; this was attributed to ultra-small particle size and high surface electron density resulting from coordination of the amine to the NP surface.[9] Additional pertinent examples include a significant increase in selectivity and/or efficacy for palladium nanoparticles supported by an amino-polymer silica composite[15] or an amine-modified silica surface[16] for the semi-hydrogenation of alkynes to alkenes; in both cases, the unmodified versions displayed significantly lower selectivity. Platinum nanoclusters confined in the cavities of UiO-66-NH_2 obtained high chemoselectivity for the hydrogenation of the C=O bond in cinnamaldehyde, whereas Pt nanoclusters supported on the external surface of the MOF and a commercial catalyst 5% Pt/C were much less selective.[14,17]

The Doherty group has been investigating the effect of incorporating heteroatom donors into polymer-immobilised ionic liquid (PIIL) to improve catalyst performance. They aim to stabilise nanoparticles by using a covalently grafted ionic liquid for weak electrostatic interactions and incorporating heteroatom donors to supplement this weak stabilisation, prevent aggregation during catalysis, and modify the surface electronic properties and, thereby, catalyst performance.

The initial foray demonstrated a beneficial effect as PdNP supported on polyethyleneglycol-modified phosphine-decorated PIIL is a highly selective catalyst for hydrogenation of the C-C double bond in α,β-unsaturated ketones, nitriles, esters and amides in water,[18] the aqueous

phase reduction of nitroarenes[19] and the Suzuki-Miyaura cross-coupling.[20] Related studies include the partial selective reduction of nitroarenes to *N*-arylhydroxylamines and azoxyarenes using Ru and Au nanoparticles stabilised by a phosphine oxide-decorated PIIL.[21] An increase in the number of reports about improved catalyst performance for nanoparticles supported by amino-modified support prompted the group to expand the program to explore whether the effectiveness of nanoparticles catalysts can be affected by varying the density and type of amine donor in amine-decorated polymer immobilised ionic liquid supports.[52]

This chapter reports that RuNPs stabilised by an amine-decorated polymer immobilised ionic liquid catalyses the selective reduction of quinoline and its derivatives under mild conditions using dimethylamine borane (DMAB) as the hydrogen source to afford the corresponding 1,2,3,4-tetrahydroquinolines in high yields with TOFs that are among the highest to be reported for the RuNP catalysed transfer hydrogenation of this class of substrate. This reduction was shown to occur stepwise via the reversible formation of the 1,2-DHQ, which was subsequently reduced to the 1,2,3,4-THQ (Scheme 3.1).

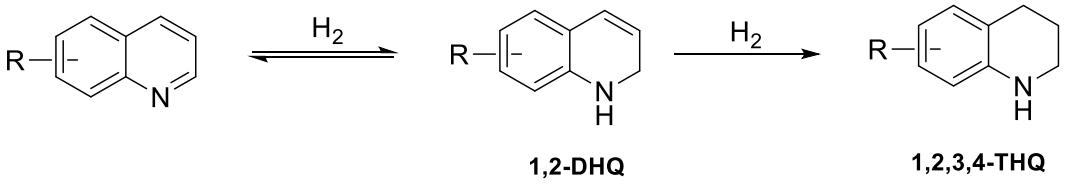

Scheme 3.1 RuNP–catalysed reduction of quinolines via reversible formation of the 1,2-DHQ and its subsequent reduction to the corresponding 1,2,3,4-THQ.

Moreover, the transfer hydrogenation of 3-substituted quinolines demonstrates complete selectivity for the partially reduced 1,2-dihydroquinoline (Figure 3.1), which can serve as versatile building blocks for chiral tetrahydroquinolines and as reducing agents for use in hydrogen transfer reactions. This marks the first report of NP-catalysed hydrogenation of quinoline using dimethylamine borane as the hydrogen source. While there has been a previous report of the metal NP-catalysed reduction of quinoline with amine borane, the turnover frequencies were relatively low and a large excess of the hydrogen donor was required.[22]

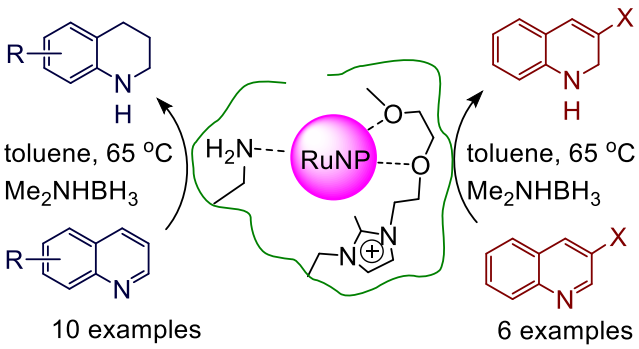

Figure 3.1 Hydrogenation of quinoline

3.2 Result and Discussion

3.2.1 Synthesis and Characterisation of RuNP@NH_2-PEGPIILS

RuNPs stabilised by an amine-decorated imidazolium-based polymer immobilised ionic liquid were prepared by impregnating the corresponding polymer NH_2-PEGPIIL (**3.1**) with ruthenium trichloride as described in Chapter **2** (catalyst **2.15**), to afford a precursor with ruthenium to amine ratio of one; this was subsequently reduced in situ by addition of an excess $NaBH_4$ to afford RuNP@NH_2-PEGPIILS (**3.2**) (Scheme 3.2).

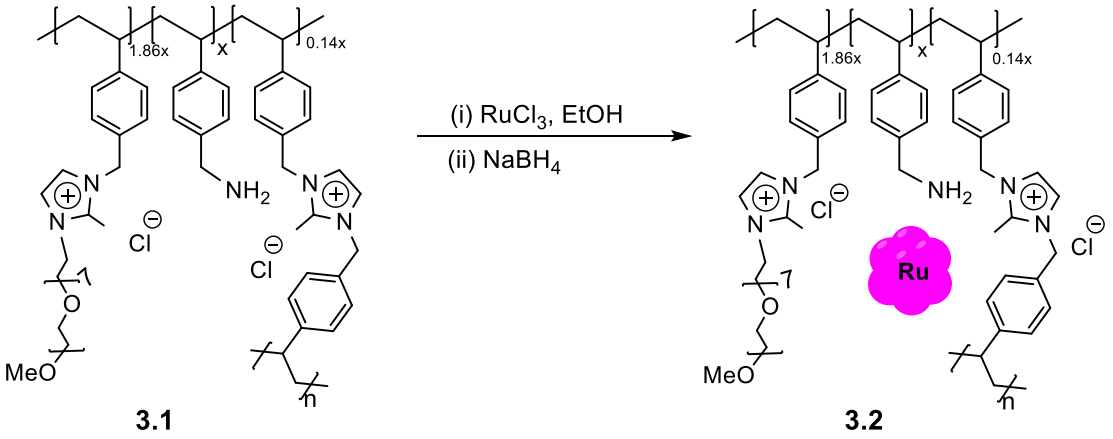

Scheme 3.2 Synthesis and composition of NH_2-PEGPIIL **3.1** stabilised ruthenium nanoparticles **3.2.**

The catalyst underwent characterisation through solid-state NMR spectroscopy, IR spectroscopy, SEM, TEM, EDX, and XPS. Using ICP-OES, the analysis revealed a ruthenium loading of 0.69 mmol g^{-1}.

The NMR data of RuNP@NH_2-PEGPIILS (**3.2**) is similar to other data for catalyst **2.15** described in Chapter 2.

The IR spectra of the RuNP@NH_2-PEGPIIL (**3.2**) (Figure 3.) contain bands at *ca*. 1580 cm^{-1} and 1605 cm^{-1} characteristic of C=C and C=N stretching vibrations of the imidazolium ring and a band at *ca*. 1350 cm^{-1} due to the C-N (imidazolium or amine) stretching vibration, confirming that the ionic liquid monomer was incorporated into the polymer.

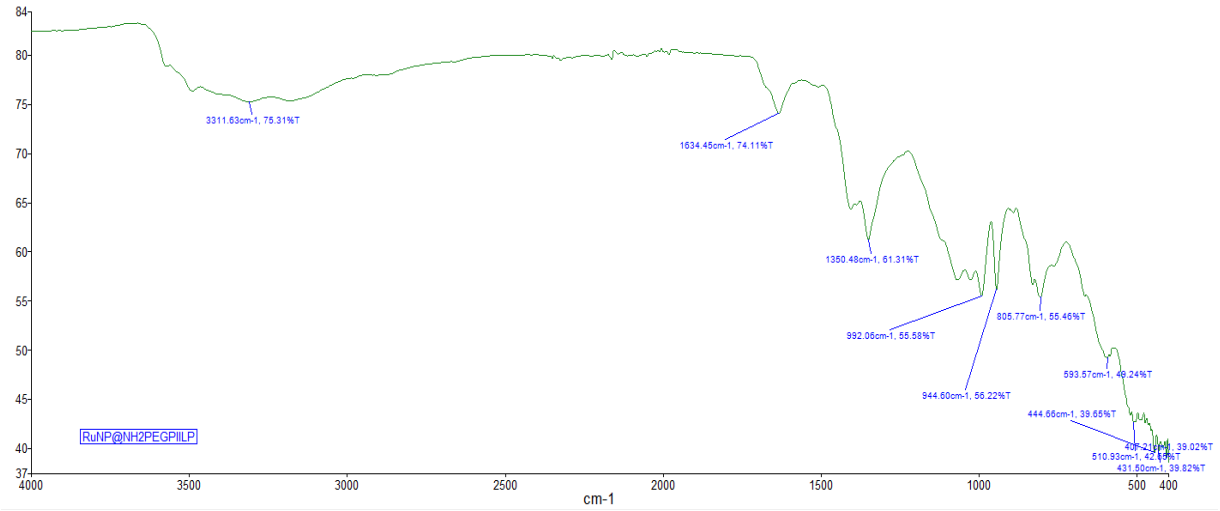

Figure 3.2 FT-IR spectrum of RuNP@NH_2-PEGPIILS

The surface of catalyst **3.2** was characterised by X-ray photoelectron spectroscopy (XPS) by analysing the Ru 3p region. This was analysed due to the overlap of the C 1s and Ru 3d regions (see Figure 3.). Peaks for the Ru $3p_{3/2}$ and $3p_{1/2}$ for catalyst **3.2** were observed at 463.2 eV and 485.3 eV, respectively. These values are higher compared to those reported for metallic Ru(0) (461.3 eV and 483.5 eV) and are consistent with RuO_2, which has reported binding energies of 463.0 eV and 485.2 eV.[23] The presence of RuO_2 species most likely results from the surface oxidation of the preformed metallic Ru nanoparticles.[52]

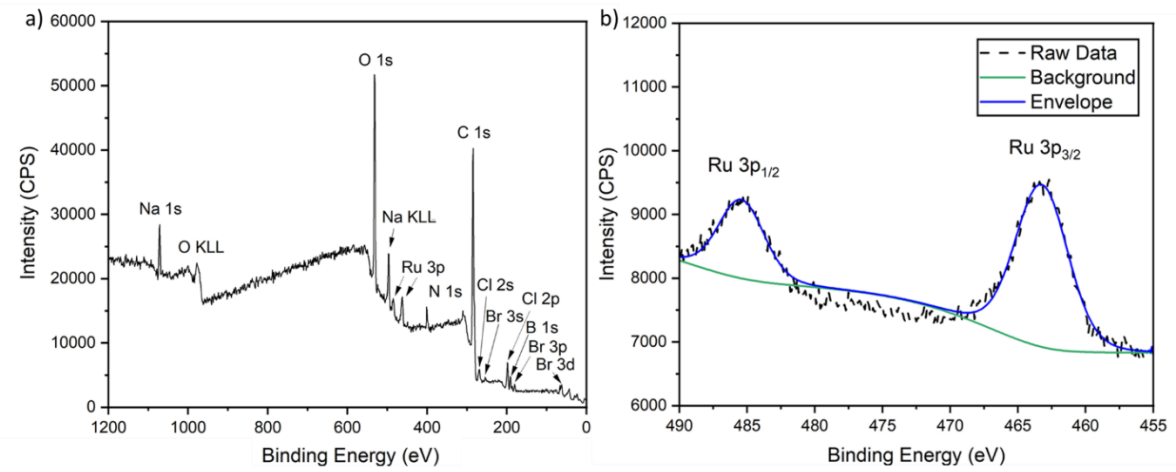

Figure 3.3 XPS data showing (a) the overall survey scan and (b) the Ru $3p_{3/2}$ region of 3.1

The nanoparticle size was determined based on TEM images. The TEM micrograph of **3.1** showed that the ruthenium nanoparticles were extremely small and almost uniformly sized with an average diameter of 1.8 ± 0.5 nm (Figure 3. a). An EDX elemental mapping image (Figure 3. b) indicated a uniform distribution and effective dispersal of the RuNPs within the support, resembling the structure of previously reported RuNP@PIILS catalysts.[24]

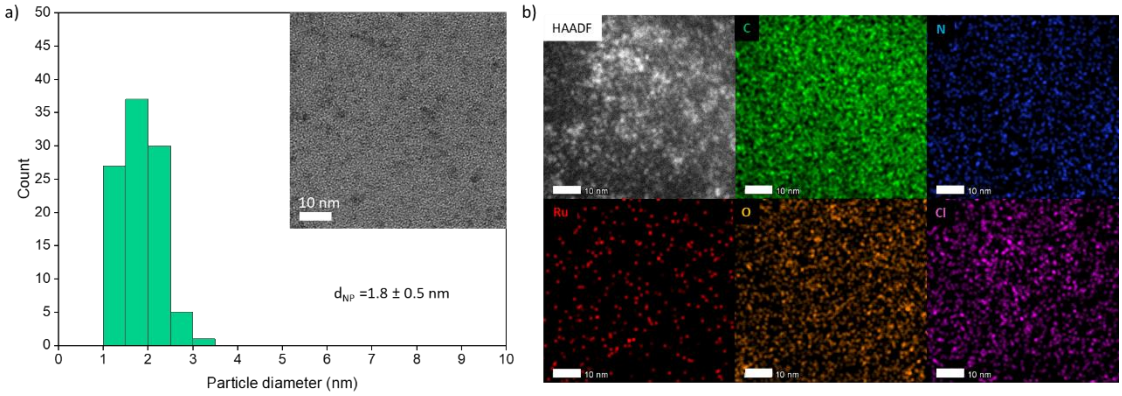

Figure 3.4 (a) Size distribution of NPs in 3.2 determined by counting >100 particles with HRTEM image inset and (b) HAADF image and EDX mapping of **3.2**. All scale bars are 10 nm (white).

3.2.2 Catalytic hydrogenation of quinoline

The tetrahydroquinoline motif is present in various bioactive compounds and agrochemicals, making it a suitable transformation for testing the efficiency of RuNP@NH_2-PEGPIILS. Additionally, ruthenium nanoparticles have previously been reported to be effective catalysts for this reduction.[8]

The reduction of quinoline to 1,2,3,4-tetrahydroquinoline occurs stepwise through the reversible formation of 1,2-dihydroquinoline. Initial studies investigated the influence of solvent and reducing agent in order to optimise the reaction parameters. The conversion and selectivity of different reactions were evaluated by adjusting the temperature, time, solvent, reducing agent, and mole ratio.

Following the procedures outlined in recent literature as a lead,[8,25,26] a preliminary experiment was conducted in the water at 40°C under a nitrogen atmosphere using a catalyst loading of 0.1 mol% **3.2** and 2.5 mole equivalents of $NaBH_4$, the result was a 47% conversion to 1,2,3,4-

tetrahydroquinoline. This conversion only increased to 54% when using 5 mole equivalents of $NaBH_4$ (Table 3.1, entries 1-2). When the hydrogen donor was varied under the same conditions, it was found that the conversion improved to 61%, with 100% selectivity for 1,2,3,4-tetrahydroquinoline when dimethylamine borane was used as the hydrogen donor. In contrast, reductions with ammonia borane, hydrazine hydrate and formic acid triethylamine azeotrope gave either low or negligible conversions (Table 3.1, entries 3-6). Thus, dimethylamine borane was chosen as the preferred hydrogen donor for further optimisation studies.[52]

Table 3.1 Selective reduction of quinoline to 1,2,3,4-tetrahydroquinoline as a function of hydride source.[a]

Entry	Catalyst (mol %)	Hydride (equiv.)	Temp (°C)	solvent	Conv. (%)[b]	Selectivity (%)[c]
1	**3.2** (0.1)	$NaBH_4$ (2.5)	40	H_2O	47	100
2	**3.2** (0.1)	$NaBH_4$ (5)	40	H_2O	54	100
3	**3.2** (0.1)	N_2H_4 (3)	40	H_2O	3	100
4	**3.2** (0.1)	$Me_2NH.BH_3$ (5)	40	H_2O	61	100
5	**3.2** (0.1)	$NH_3.BH_3$ (5)	40	H_2O	19	100
6	**3.2** (0.1)	$HCO_2H.NEt_3$ (5)	40	H_2O	0	-

[a] *Reaction conditions*: Conducted under a nitrogen atmosphere, 1 mmol quinoline, 0.1 mol% catalyst, 3 mL solvent, hydride source, 4h, temperature. [b] % Conversion was determined by ^1H NMR spectroscopy using dioxane as the internal standard—an average of at least three runs. [c] Selectivity for 1,2,3,4-tetrahydroquinoline = [% 1,2,3,4-tetrahydroquinoline/(% 1,2,3,4-tetrahydroquinoline + % 1,2-dihydroquinoline)] x 100%. [d] Selectivity for 1,2-dihydroquinoline.

3.2.3 Solvent optimisation of reactions for Ru@NH_2-PEGPIILS catalysed hydrogenation of quinoline

Given that the activity and selectivity of a heterogeneous catalyst can be influenced by the choice of solvent,[8,27] a study was conducted to assess the conversion and selectivity as a function of the solvent for the dimethylamine borane-mediated reduction of quinoline at 40°C using a 0.1 mol% loading of **3.2.** As illustrated in (Table 3.2), hydrogenation was conducted in three different organic solvents and water under the same conditions. The reactions conducted in methanol and ethanol resulted in slightly reduced yields of 31% and 24%, respectively, compared to 61% in water (Table 3.2, entries 2-3). When toluene was used as the solvent, the yield increased slightly to 68%, but there was a significant change in the primary product, resulting in 43% of 1,2-dihydroquinoline and 25% of 1,2,3,4-tetrahydroquinoline, corresponding to 37% selectivity for the latter. The identity of the former was verified by comparing its distinct ^{1}H NMR signals with those of an authentic sample. It was surprising to observe such a drastic change in selectivity based on the solvent, as the reactions carried out in water, ethanol, and methanol all produced 1,2,3,4-tetrahydroquinoline as the exclusive product, regardless of the yield. The noticeable difference in selectivity between reactions conducted in water or a protic solvent compared to toluene might be related to the distinct pathways for hydrogen release, where reactions in a protic solvent involve hydrolysis and release three equivalents of hydrogen, while reactions in toluene involve catalytic dehydrogenation and only release one equivalent or the hydrophobic environment created by the toluene may facilitate the liberation of the 1,2-dihydroquinoline from the surface of the nanoparticle thereby preventing a second hydrogenation.

The reaction under biphasic conditions in a 1:1 mixture of toluene and water resulted in only 16% conversion after 4 hours, with 100% selectivity for 1,2,3,4-tetrahydroquinoline. While THF has been reported to be the preferred solvent for the NP-catalysed reduction of quinoline,[28,29] a reduction using 0.1 mol% **3.2** only achieved 24% conversion after 4 hours, albeit with complete selectivity for 1,2,3,4-tetrahydroquinoline (Table 3.2, entry 5). A reduction was also performed in toluene using 5 equivalents of sodium borohydride to compare its efficiency with dimethylamine borane. Under identical conditions, the conversion only reached 3% compared to 54% in water, likely due to limited reduction caused by the low

solubility of sodium borohydride in toluene (Table 3.2, entry 6). Similarly, ammonia borane was found to be a poor hydrogen donor in toluene, as the reduction of quinoline only reached 6% conversion to a mixture of 1,2-dihydroquinoline and 1,2,3,4-tetrahydroquinoline (Table 3.2, entry 7). Analysis of the reaction mixture revealed that the low conversion was probably due to the formation of the quinoline-borane adduct, as indicated by a characteristic signal at δ -13.8 ppm in the ^{11}B NMR ($^{1}J_{B\text{-}H}$ = 96 Hz) spectrum and an additional set of resonances in the ^{1}H NMR spectrum consistent with those reported in the literature.[30,52]

Table 3.2 Optimisation of reaction solvent for the reduction of quinoline to 1,2,3,4-tetrahydroquinoline.

Entry	Catalyst (mol %)	Hydride (equiv.)	Temp (°C)	Solvent	Conv. (%)[b]	Selectivity (%)[c]
1	**3.2** (0.1)	$Me_2NH.BH_3$ (5)	40	H_2O	61	100
2	**3.2** (0.1)	$Me_2NH.BH_3$ (5)	40	EtOH	24	100
3	**3.2** (0.1)	$Me_2NH.BH_3$ (5)	40	MeOH	31	100
4	**3.2** (0.1)	$Me_2NH.BH_3$ (5)	40	Toluene	68	63[d]
5	**3.2** (0.1)	$Me_2NH.BH_3$ (5)	40	THF	24	100
6	**3.2** (0.1)	$NaBH_4$ (5)	40	Toluene	3	100
7	**3.2** (0.1)	$NH_3.BH_3$ (5)	40	Toluene	6	50

[a] Reaction conditions: Conducted under a nitrogen atmosphere, 1 mmol quinoline, 0.1 mol% catalyst, 3 mL solvent, hydride source, 4h, temperature. [b] % Conversion was determined by ^{1}H NMR spectroscopy using dioxane as the internal standard—an average of at least three runs. [c] Selectivity for 1,2,3,4-tetrahydroquinoline = [% 1,2,3,4-tetrahydroquinoline/(% 1,2,3,4-tetrahydroquinoline + % 1,2-dihydroquinoline)] x 100%. [d] Selectivity for 1,2-dihydroquinoline.

3.2.4 The efficiency of RuNP@NH_2-PEGPIILS as a catalyst for the reduction of quinoline

When toluene was used as the solvent and dimethylamine borane as the hydrogen donor, the conversion rose from 68% at 40 °C to 72% at 50 °C and eventually reached 82% with 84% selectivity for 1,2,3,4-tetrahydroquinoline when the reaction temperature was increased to 65 °C (Table 3.3, entry 1). Considering that near complete conversion with high selectivity for 1,2,3,4-tetrahydroquinoline could be achieved by adjusting the reaction time accordingly, this temperature was chosen for further optimisation studies and to assess the range of substrates (as discussed later).

The conversion increased to 96% with 99% selectivity for 1,2,3,4-tetrahydroquinoline after 4 hours at 65 °C when the catalyst loading was increased to 0.25 mol%, and this was confirmed by ^{1}H NMR and ^{13}C NMR (Appendix). However, when the catalyst loading was further increased to 0.5 mol%, the conversion only improved to 97% under the same conditions (Table 3.3, entries 2-3), indicating that the reaction is limited by mass transfer under these conditions. The effectiveness of **3.2** was also tested by reducing the catalyst loading to 0.05 mol%, which resulted in a corresponding decrease in the conversion to 61% with 54% selectivity for 1,2,3,4-tetrahydroquinoline after 4 h (Table 3.3, entry 4).

A large excess of reducing agents is often necessary when aiming for efficient transfer hydrogenation. The study investigated the conversion in relation to the mole ratio of dimethylamine borane to quinoline. The conversion dropped quite dramatically from 94% with five equivalents of dimethylamine borane to 68% with 2.5 equivalents. However, increasing to 10 equivalents improved the conversion to 97%, with 99% selectivity for 1,2,3,4-tetrahydroquinoline (Table 3.3, entries 5-6).

A background reduction of quinoline in toluene in the absence of catalyst **3.2** but with five equivalents of dimethylamine borane gave no conversion after 4h, indicating the important role of the catalyst. The impact of the polymer's composition, specifically the amine and PEG components, on catalyst performance was studied by comparing catalysts with different compositions, including RuNP@PEGPIILS, RuNP@PIILS, and RuNP@NH_2-PIILS which either lack the hydrophilic PEG chain the amine of both.[31]

The data in Table 3.3 (entries 7-9) shows that removing the surface-grafted amine significantly affected the conversion as a reduction catalysed by 0.25 mol% RuNP@PEGPIILS only reached 65% conversion with 86% selectivity for 1,2,3,4-tetrahydroquinoline after 4 hours, compared with 96% conversion and 99% selectivity for **3.2**. Similarly, using RuNP@PIILS as the catalyst under the same conditions resulted in an even larger drop in conversion to 43%. This suggests that both the PEG and the amino group are necessary for optimal efficiency.

The performance of the RuNP@NH_2-PIILS catalyst, which achieved 71% conversion with 89% selectivity for 1,2,3,4-THQ, represents a significant improvement compared to the conversion of 43% achieved with RuNP@PIILS. This improvement can be attributed to the influence of the amine on catalyst performance. It has been shown through these modifications that each constituent directly and substantially affects the efficacy of the catalyst. However, further investigation will be necessary to fully comprehend the specific role of the PEG and the amine.

This research will seek to determine whether the enhanced performance of RuNPs supported on PEG-amine modified polymer is due to strong metal molecular support interactions (SMSSI), as previously described by Yadav et al.,[32,33] NP size, distribution, dispersion,[34] hydrophilicity/hydrophobicity balance and access to the active site, surface electronic structure or a cooperative role of the amine in the catalytic cycle's elementary steps.[35,53]

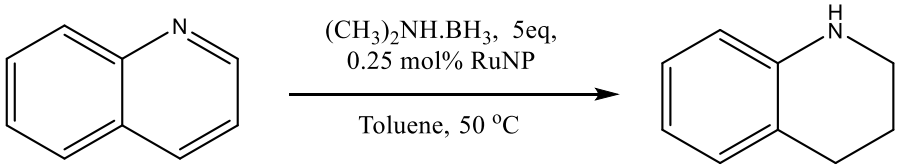

Scheme 3.3 Hydrogenation of quinoline using $(CH_3)_2NH.BH_3$ (5mmol)

The effectiveness of **3.2** as a catalyst for the reduction of quinoline was also compared to that of commercially available Ru/C (5 wt%). Under the same conditions, only 11% conversion was achieved after 4 hours, but with 100% selectivity for 1,2,3,4-tetrahydroquinoline (Table 3.3, entry 10). As there have been multiple reports of efficient and selective hydrogenation or reduction of quinoline catalysed by PtNP-based systems, including PtNP stabilised by G_4OH PAMAM dendrimers supported in SBA-15,[36] as well as PtNPs stabilised by bulky terphenylphosphines,[26] the efficiency of **3.2** was also compared to its platinum counterpart PtNP@NH_2-PEGPIILS. Surprisingly, under the optimal conditions described previously, the reduction of quinoline catalysed by 0.25 mol% PtNP@NH_2-PEGPIILS only reached 13% conversion after 4 hours, while **3.2** reached 96% at the same time (Table 3.3, entry 11).[52]

Table 3.3 Selective reduction of quinoline to 1,2,3,4-tetrahydroquinoline as a function of catalyst and the amount of hydride source.[a]

Entry	Catalyst (mol %)	Hydride (equiv.)	Temp (°C)	solvent	Conv. (%)[b]	Selectivity (%)[c]
1	**3.2** (0.1)	$Me_2NH.BH_3$ (5)	65	toluene	82	84
2	**3.2** (0.25)	$Me_2NH.BH_3$ (5)	65	toluene	96	99
3	**3.2** (0.5)	$Me_2NH.BH_3$ (5)	65	toluene	97	99
4	**3.2** (0.05)	$Me_2NH.BH_3$ (5)	65	toluene	61	54
5	**3.2** (0.25)	$Me_2NH.BH_3$ (2.5)	65	toluene	68	79
6	**3.2** (0.25)	$Me_2NH.BH_3$ (10)	65	toluene	98	99
7	RuNP@PEGPIILS (0.25)	$Me_2NH.BH_3$ (5)	65	toluene	65	86
8	RuNP@PIILS (0.25)	$Me_2NH.BH_3$ (5)	65	toluene	43	75
9	RuNP@NH_2PIILS (0.25)	$Me_2NH.BH_3$ (5)	65	toluene	71	89
10	Ru/C (0.25)	$Me_2NH.BH_3$ (5)	65	toluene	11	100
11	PtNP (0.25)	$Me_2NH.BH_3$ (5)	65	toluene	13	100
12	**3.2** (0.25)	H_2 (1 atm)	65	toluene	14	100

[a] Reaction conditions: Conducted under a nitrogen atmosphere, 1 mmol quinoline, x mol% catalyst, 3 mL solvent, hydride source, 4h, temperature. [b] % Conversion was determined by ^{1}H NMR spectroscopy

using dioxane as the internal standard. Average of at least three runs. [c] Selectivity for 1,2,3,4-tetrahydroquinoline = [% 1,2,3,4-tetrahydroquinoline/(% 1,2,3,4-tetrahydroquinoline + % 1,2-dihydroquinoline)] x 100%. [d] Selectivity for 1,2-dihydroquinoline

Although the poor conversion was unexpected, a comparison of the hydrolytic evolution of hydrogen from $NMe_2H.BH_3$ using 0.1 mol% **3.2** and PtNP@NH_2-PEGPIILS revealed that the former is a significantly more efficient catalyst, achieving near quantitative liberation of hydrogen after only 28 minutes, with an initial turnover frequency (TOF) of 3,100 h^{-1}, while its platinum counterpart PtNP@NH_2-PEGPIILS only liberated 11% hydrogen at the same time, with an initial TOF of 320 h^{-1} (Figure 3. a).

Likewise, **3.2** also proved to be a more effective catalyst for the dehydrocoupling of $NMe_2H.BH_3$ in toluene compared to its platinum counterpart (Figure 3. b). Although the difference is not as significant as in the case of hydrolysis, it is still appreciable. The low conversion observed in the reduction of quinoline using PtNP@NH_2-PEGPIILS as the catalyst may be attributed to the limited availability of hydride species at the NP surface, resulting from the slow release of hydrogen from the dimethylamine borane adduct. To investigate if the reduction involving dimethylamine borane occurred with molecular hydrogen liberated from the donor or directly through borane-derived surface hydride species, a catalytic reduction was carried out under 1 atmosphere of hydrogen, under the optimum conditions identified above. It was expected that a high conversion would be achieved if the reduction involved molecular hydrogen. However, under identical conditions, the conversion only reached 14%, with 100% selectivity for 1,2,3,4-tetrahydroquinoline (Table 3.3, entry 12).

This is significantly lower than the 96% conversion obtained with dimethylamine borane, indicating that the reduction most likely occurs via a heterolytic pathway involving a surface-mediated hydride transfer rather than the activation of molecular hydrogen released from the surface (further discussed later).

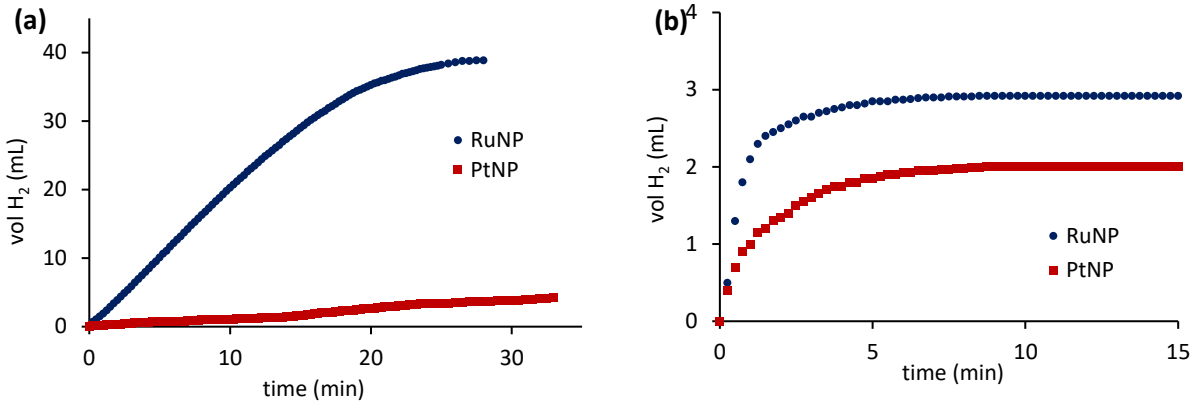

Figure 3.5 Volume of hydrogen generated against time for the release of hydrogen from a 0.28 M aqueous solution of $NMe_2H.BH_3$ as a function of time at 303 K catalysed by 0.1 mol% RuNP@NH_2-PEGPIILS **3.2** (blue) and 0.1 mol% PtNP@NH_2-PEGPIILS (red) (a) hydrolytic evolution conducted in water (b) dehydrocoupling conducted in toluene.

3.2.5 Time profile and comparative test

After establishing the optimal conditions for achieving high conversion and selectivity for 1,2,3,4-tetrahydroquinoline, the composition was monitored as a function of time in d_8-toluene at 65 °C to analyse the reaction profile and calculate the initial turnover frequency (TOF) to compare with previously documented systems. A series of simultaneous reactions were conducted at various time intervals, and ^{1}H NMR spectroscopy was used to quantify the resulting composition. The composition-time profile in Figure 3. demonstrates the rapid depletion of quinoline and the production of 1,2,3,4-tetrahydroquinoline in the initial phase of the reaction (15 minutes). Subsequently, there was a gradual accumulation of 1,2-dihydroquinoline up to 17% within the first two hours, which then decreased over longer reaction times, leading to the exclusive formation of 1,2,3,4-tetrahydroquinoline after 10 hours.

A similar pattern was observed with a catalyst loading of 0.25 mol%; however, the maximum concentration of 1,2-dihydroquinoline only reached 6%, and complete conversion to 1,2,3,4-tetrahydroquinoline was achieved after approximately 4 hours (as shown in Figure 3.2). These observations align with the facile reduction of the 1,2-dihydroquinoline formed early in the early stages of the reaction, which explains the low selectivity for the partial reduction of quinoline.[52]

When the effectiveness of **3.2** as a catalyst for the transfer hydrogenation of quinoline to 1,2,3,4-tetrahydroquinoline was compared with other nanoparticle-based systems, **3.2** was found to be one of the most active catalysts reported. For instance, the initial turnover frequency of 610 moles of quinoline converted per mole of Ru per hour at 65 °C is significantly higher than the 12 moles of product per mole of Ru per hour obtained at 60 °C with RuNPs intercalated in hectorite,[8] 13 moles of product per mole of Pd per hour obtained with PdNPs stabilised in an ethyl methacrylate and ethylene glycol dimethacrylate based co-polymer,[25] 51 moles of product per mole of Au per hour for AuNP supported on amino-modified SAB-15,[37] 2 moles of product per mole of Pt per hour for phosphine-decorated platinum nanoparticles,[26] Ni dispersed in porous carbon NiNPs@PC (turnover frequency of 310 moles of product per mole of Ni per hour in water/alcohol at room temperature),[38] and even comparable to that of 600 moles of product per mole of Au per hour obtained at 130°C with AuNPs supported on rutile.[37]

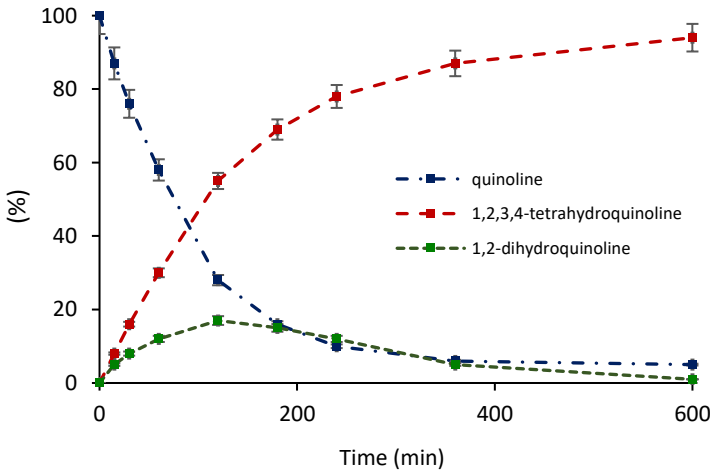

Figure 3.6 Reaction composition as a function of time for the dimethylamine borane-mediated reduction of quinoline in toluene at 65 °C catalysed by 0.1 mol% **3.2.**

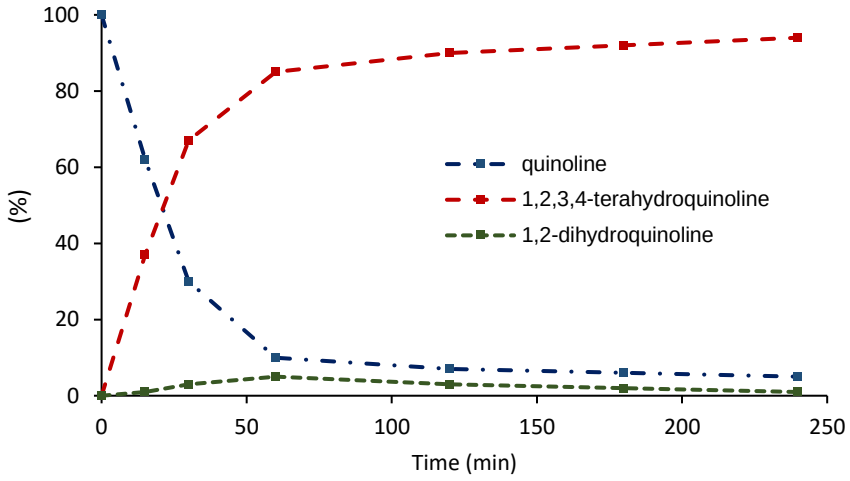

Figure 3.2 Reaction composition as a function of time for the dimethylamine borane-mediated reduction of quinoline in toluene at 65 °C catalysed by 0.25 mol% **3.2.**

There are not many reports of the use of nanoparticle-based systems as catalysts for the transfer hydrogenation of quinoline to tetrahydroquinoline. Therefore, the comparison was expanded to encompass hydrogenation catalysed by nanoparticle-based systems. Gratifyingly, the TOF achieved with **3.2** is comparable to or better than most of these systems, including RuNPs dispersed in 3D-interconnected hierarchical porous N-doped carbon (TOF of 654 h^{-1} in EtOH at 100 °C),[39] a well-dispersed core-shell nanocatalyst, Ru-SiO_2@mSiO_2 (TOF of 30 h^{-1} in water at 90 °C),[40] thermoregulated phase-transfer Pt nanoparticles (TOF of 193 h^{-1} in water at 80 °C),[41] RuNPs stabilised by a diol functionalised ionic liquid (TOF of 10 h^{-1} in [BMMIM]NTf_2 at 80 °C),[9] polymer supported PdNPs (TOF of 22 h^{-1} in MeOH/water at 80 °C),[25] phosphine-functionalised ionic liquid-stabilised rhodium and ruthenium NPs (TOF of 20 h^{-1} in [BMIM][PF_6] at 50 °C and 71 h^{-1} in water at 50 °C, respectively)[27,42] and RuNPs supported on biomass-derived N-doped porous 2D-carbon nanosheets (TOF of 96 h^{-1} in ethanol at 40 °C).[43] Other relevant comparisons include PdNPs supported on amine-rich hollow silica nanospheres (TOF of 135 h^{-1} in cyclohexane at 50 °C),[44] NHC-stabilised RhNPs (TOF of 496 h^{-1} in THF at 60 °C),[29] Ru clusters confined in hydrogen-bonded organic frameworks (TOF of 3 h^{-1} in water at 80 °C),[45] PdNPs stabilised by carbon-metal covalent bonds (TOF of 6 h^{-1} in water at room temperature),[46] RuNPs supported on nitrogen-doped carbon (TOF of 20 h^{-1} in ethanol at 30 °C),[47] and isolated single ruthenium atoms anchored on the amine-modified MOF UiO-66-NH_2

(TOF of 25 h^{-1} in THF at 100 °C).[48] A significantly higher TOF of 3,400 h^{-1} has been reported for the hydrogenation of quinoline using RuNPs immobilised on magnesium oxide, however, reactions were conducted at 150 °C under 50 atm of hydrogen.[28,52]

3.2.6 Catalytic hydrogenation of quinoline derivatives (substrate screening)

Since it has been found that RuNP@NH_2PEGPIILP is active for the reduction of quinoline to 1,2,3,4-tetrahydroquinoline, the same optimised conditions were used for the hydrogenation of a range of substituted quinolines to assess the efficiency and scope of **3.2** and to evaluate its performance against existing systems, as shown in Table 3.4. The reactions were initially carried out at 65 °C in toluene for 4 hours to gather comparative performance data based on the substrate. Subsequently, the reaction times were modified to examine the impact of reaction time on the conversion and selectivity for either the 1,2-dihydroquinoline or the 1,2,3,4-tetrahydroquinoline.[52]

The identity of the product was verified for every substance studied by comparing the NMR spectroscopic data with an authentic sample and the mass spectrum. 6-Bromoquinoline underwent a significant transformation, resulting in a mixture of 6-bromo-1,2-dihydroquinoline as the primary component (60%) and 6-bromo-1,2,3,4-tetrahydroquinoline (40%) after 4 hours, with no signs of competitive hydrodehalogenation to quinoline or its reduction products. Nanoparticle-based catalysts, such as metal-carbon stabilised PdNPs,[46] [39]RuNPs supported on N-doped porous carbon nanosheets derived from biomass,[43] and amine-modified silica-supported AuNPs,[37] have previously been reported to facilitate facile hydrodehalogenation of bromo- and chloro-substituted substrates. Therefore, the distinctive advantage of catalyst **3.2** for its application in synthesis lies in the selective reduction of bromo-substituted quinolines without cleaving the C-Br bond.

Notably, prolonging the reaction time to 24 hours caused only a slight increase in the yield of 6-bromo-1,2,3,4-tetrahydroquinoline to 51%, accompanied by a reduction in the amount of 6-bromo-1,2-dihydroquinoline. A similar result in conversion and composition-time profile was observed in the reduction of 5-bromoquinoline, which gave high conversion to a 70:30 mixture of the corresponding dihydroquinoline and tetrahydroquinoline after 4 hours;

moreover, this ratio remained relatively unchanged even when the reduction was carried out in the presence of ten equivalents of $NMe_2H.BH_3$ (Table 3.4, entries 2-3).

Under the same conditions, 6-methoxyquinoline, a representative electron rich substate, achieved 39% conversion after 4 hours with 100% selectivity for 6-methoxy-1,2,3,4-tetrahydroquinoline. The conversion improved to 76%, to afford 6-methoxy-1,2,3,4-tetrahydroquinoline as the only product when the reaction time was extended to 24 hours. In contrast, 6-methylquinoline reached 87% conversion, to afford a mixture of 6-methyl-1,2-dihydroquinoline (22%) and 6-methyl-1,2,3,4-tetrahydroquinoline (78%) after 4 hours. When the reaction time was extended to 16 hours, 100% conversion was obtained with 98% selectivity for 6-methyl-1,2,3,4-tetrahydroquinoline (Table 3.4, entries 4-5).

Decent conversions were also achieved for the reduction of 5- and 6-aminoquinoline after 4 hours, although with low selectivity for the corresponding 1,2,3,4-tetrahydroquinoline. However, the conversion and the selectivity for the corresponding tetrahydroquinoline improved when the reaction time was increased to 24 hours (Table 3.4, entries 6-7).

The sterically crowded 8-methylquinoline proved to be considerably more difficult to reduce, achieving only 11% conversion to 8-methyl-1,2,3,4-tetrahydoquinoline after 24 hours at 80°C (Table 3.4, entry 8).[52]

This substrate has been known to pose significant challenges, with low conversions reported when using nanoparticle-based catalysts. The transfer hydrogenation of *N*-ethyl quinolinium bromide proceeded smoothly, resulting in good conversion to *N*-ethyl-1,2,3,4-tetrahydroquinoline as the sole product in just 4 hours, with complete conversion after 16 hours (Table 3.4, entry 9). Similarly, the reduction of quinoline N-oxide led to deoxygenation, achieving complete conversion with 97% selectivity for tetrahydroquinoline after 24 hours (Table 3.4, entry 10).

Recently, activating quinolines as their *N*-oxides has been reported to trigger the addition of hydrogen, allowing for catalytic transfer hydrogenation using ethanol as a renewable hydrogen source.[49] Additionally, pyridines and quinolines have been activated for nucleophilic addition by *N*-alkylation to the corresponding pyridinium bromide, which successfully prevents undesired re-aromatisation.[49] In this study, dihydroquinolines were identified as

intermediates during the hydrogenation of substituted quinolines and were found to be the major species in the early stages of the reaction in some cases. However, selectively reducing quinolines to the corresponding dihydroquinolines is extremely challenging due to the high reactivity of the dihydroquinoline towards further reduction to the tetrahydroquinoline.

Table 3.4 Reduction of quinolines to the corresponding 1,2-dihydroquinoline and 1,2,3,4-tetrahydroquinoline catalysed by 0.25 mol% 3.2.[a]

Entry	Substrate	Product	Time (min)	Conv. (%)[b,c]	Selectivity (%)[c,d]
1	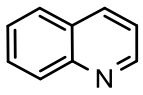	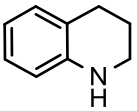	240	96	99
2	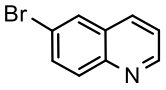	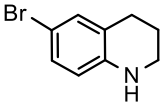	240/600	94/93	40/51
3	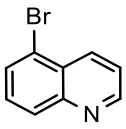	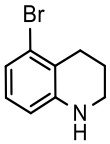	240/600	91/91	30/40
4	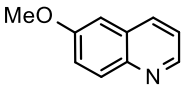	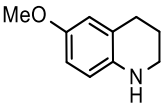	240/1440	39/76	100/100
5	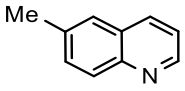	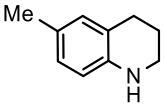	240/960	87/100	78/98

Entry	Substrate	Product	Time (min)	Conv. (%)[b,c]	Selectivity (%)[c,d]
6	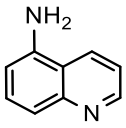	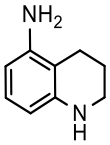	240/1440	91/98	54/80
7	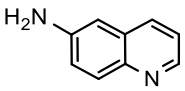	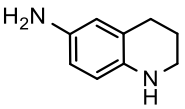	240/1440	71/88	68/82
8	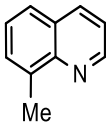	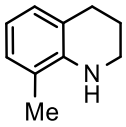	1440	12	100
9	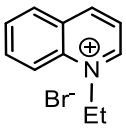	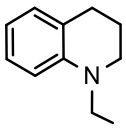	240/960	65/99	100/100
10	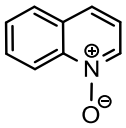	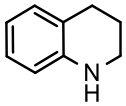	240/1980	47/100	62/97

[a] Reaction conditions: Conducted under nitrogen, 1.0 mmol substrate, 0.25 mol% **3.2**, 3 mL toluene, 5.0 mmol dimethylamine borane, 65 °C, time. [b] % Conversion determined by ^{1}H NMR spectroscopy using dioxane as the internal standard. Average of three runs. [c] Reactions were initially run for either 60 min or 240 min to obtain comparative conversion data for each substrate, and where required, a second reaction was conducted for an appropriate time to reach high conversion; the corresponding reaction times, conversions and selectivities are separated by the / symbol. [d] Selectivity for either 1,2-DHQ or 1,2,3,4-THQ = [% 1,2-DHQ or % 1,2,3,4-THQ / (% 1,2,3,4-tetrahydroquinoline + % 1,2-dihydroquinoline)] x 100%.

Remarkably, when using the optimal conditions mentioned earlier, the reduction of quinolines substituted at the 3-position took place quickly and resulted in the complete conversion to afford the corresponding 1,2-dihydroquinoline as the sole product Specifically, both 3-bromoquinoline and 3-methylquinoline were reduced with 100% selectivity to the respective 3-substituted dihydroquinoline in near complete conversion (Table 3.5, entries 1-2).[52]

The selective partial reduction of 3-acetylquinoline and 3-quinolinecarboxaldehyde under the same conditions resulted in the reduction of the carbonyl group, producing 1-(1,2-dihydroquinolin-3-yl)ethan-1-ol and (1,2-dihydroquinolin-3-yl)methanol as the sole product at complete conversion, with no evidence for the tetrahydroquinoline (Table 3.5, entries 3-4).

Conducting the transfer hydrogenation of 3-acetylquinoline and 3-quinolinecarboxaldehyde at room temperature under otherwise identical conditions led to the rapid and quantitative reduction of the acyl and aldehyde groups, respectively, yielding 1-(quinolin-3-yl)ethan-1-ol and quinolin-3-ylmethanol after only 60 minutes. Subsequently, the selective partial reduction to the corresponding dihydroquinoline was achieved by adding an additional five equivalents of dimethylamine borane and increasing the reaction temperature to 65 °C for 6 hours. Although it may be tempting to attribute this specific partial reduction to the steric impact of the substituent, there are relatively few examples of the selective partial reduction of this type of substrate and AuNPs supported on amine-functionalised silica,[28,37] PEG-stabilised rhodium nanoparticles,[12] nickel nanoparticles on porous carbon,[38] and ruthenium nanoparticles stabilised in silica nanospheres coated with a microporous silica layer, $RuSiO_2@mSiO_2$,[40] all these catalyse the reduction of 3-substituted quinolines to afford high yields of the corresponding tetrahydroquinolines with no sign of dihydroquinoline, indicating that the substituent alone is not responsible for the high selectivity achieved with **3.2**.

Moreover, reductions conducted with ten equivalents of dimethylamine borane and extended reaction times also produced the dihydroquinoline as the major species. The transfer hydrogenation of phenanthridine and acridine resulted in rapid partial reduction to afford 5,6-dihydrophenanthridine and 9,10-dihydroacridine, respectively, with 100% selectivity at complete conversion (Table 3.5, entries 5-6). While the partial transfer hydrogenation of quinolines to 1,2-dihydroquinolines has recently been achieved with remarkable selectivity using a homogeneous cobalt(II) phosphinoamido cooperative catalyst and amine borane as

the hydrogen donor,[50] this is the first report of the selective partial reduction of 3-substituted quinolines to the corresponding 1,2-dihydroquinolines with a nanoparticle-based catalyst.[52]

Table 3.5 Reduction of quinolines substituted to the corresponding 1,2-dihydroquinoline catalysed by 0.25 mol% **3.2.**[a]

Entry	Substrate	Product	Time (min)	Conv. (%)[b,c]	Selectivity (%)[c,d]
1	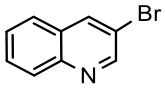	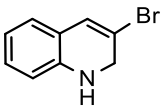	240	97	100
2	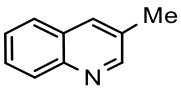	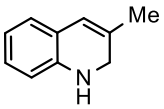	480	94	100
3	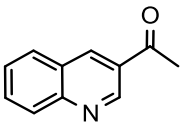	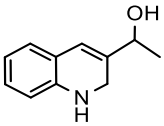	240/360	72/100	100/100
4	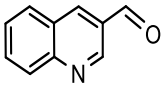	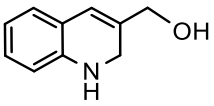	240/360	80/100	100/100
5	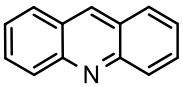	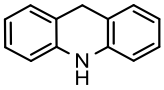	60	100	100
6	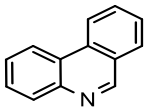	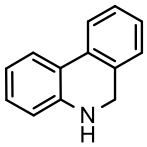	60	100	100

[a] Reaction conditions: Conducted under nitrogen, 1.0 mmol substrate, 0.25 mol% **3.2**, 3 mL toluene, 5.0 mmol dimethylamine borane, 65 °C, time. [b] % Conversion determined by ^{1}H NMR spectroscopy using dioxane as the internal standard. Average of three runs. [c] Reactions were initially run for either 60 min or 240 min to obtain comparative conversion data for each substrate and where required a second reaction was conducted for an appropriate time to reach high conversion; the corresponding reaction times, conversions and selectivities are separated by the / symbol. [d] Selectivity for either 1,2-DHQ or 1,2,3,4-THQ = [% 1,2-DHQ or % 1,2,3,4-THQ / (% 1,2,3,4-tetrahydroquinoline + % 1,2-dihydroquinoline)] x 100%.

In addition to being used as reagents for creating chiral tetrahydroquinolines, 1,2-dihydroquinolines have been found to be effective agents for transferring hydrogen. The efficiency of 3-methyl-1,2-dihydroquinoline as a source of hydrogen was investigated by heating a solution of 3-methyl-1,2-dihydroquinoline in d_8-toluene at 65°C (Scheme 3.4) and tracking the reaction progress over time using ^{1}H NMR spectroscopy to measure the composition (Figure 3.3 for the corresponding NMR spectra).

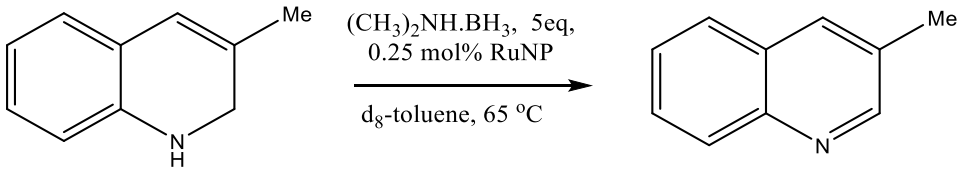

Scheme 3.4 The dehydrogenation of 3-methyl-1,2-dihydroqinoline in d_8-toluene solution.

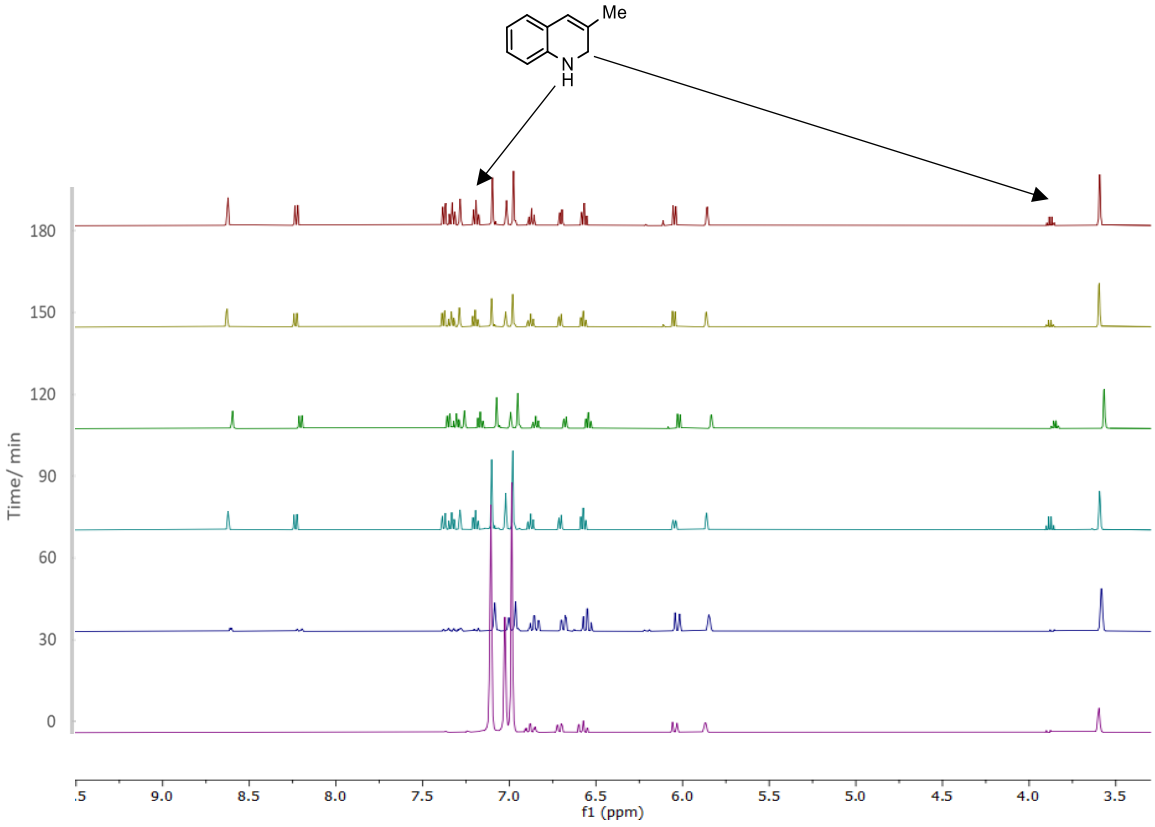

Figure 3.3 Stacked plot of ^{1}H NMR spectra as a function of time to monitor the evolution of hydrogen from 3-methyl-1,2-dihydroqinoline in d_8-toluene solution at 60 °C.

The resulting profile in Figure 3.9 demonstrates that the concentration of 3-methyl-1,2-dihydroquinoline diminishes gradually while 3-methylquinoline is formed as the sole spectroscopically observable product. Moreover, there was no indication of the disproportionation process leading to the production of 3-methyl-1,2,3,4-tetrahydroquinoline, a pathway that has previously been recognised in the formic acid-mediated reduction of 2-methyl quinoline utilising AuNPs supported on amino-modified silica. While deuterium labelling experiments revealed various pathways for the transfer hydrogenation of 2-methylquinoline, the major pathway was confirmed to be the 1,2-addition of hydride followed by subsequent disproportionation of the resulting 2-methyl-1,2-dihydroquinoline.[37,51,52]

Qualitatively, 3-bromo-1,2-dihydroquinoline exhibited a similar composition profile, although the release of hydrogen was observed to be faster than 3-methyl-1,2-dihydroquinoline (Figure 3.4). The release of hydrogen was validated through a transfer hydrogenation experiment involving 3-methyl-1,2-dihydroquinoline and 1,1-diphenylethene in toluene at 60 °C using 5 wt% Pd/C as the catalyst. Following a 2-hour duration, analysis of the crude reaction mixture using ^{1}H NMR spectroscopy indicated the presence of 1,1-diphenylethane, as indicated by characteristic multiples at δ 1.67 (d, J = 7.4 Hz) and δ 4.19 (q, J = 7.4 Hz), consistent with the process of transfer hydrogenation (Scheme 3.5).

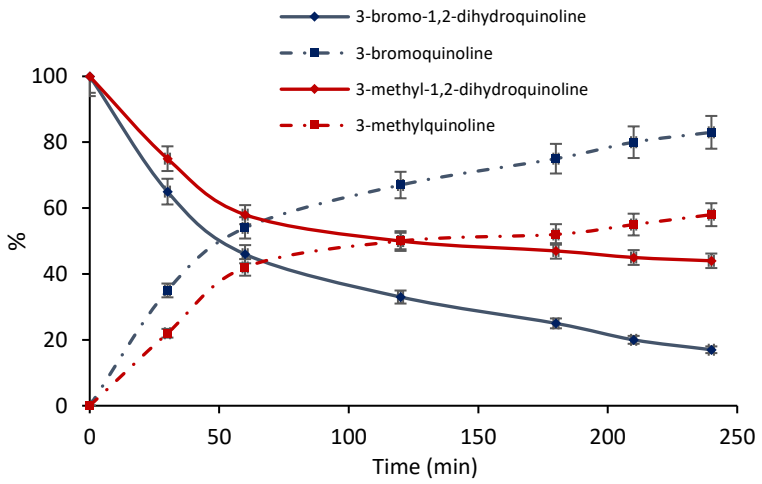

Figure 3.4: Composition of d_8-toluene solutions of 3-methyl-1,2-dihydroquinoline and 3-bromo-1,2-dihydroquinoline heated at 65 °C as a function of time showing the liberation of hydrogen to form 3-methylquinoline and 3-bromoquinoline, respectively.

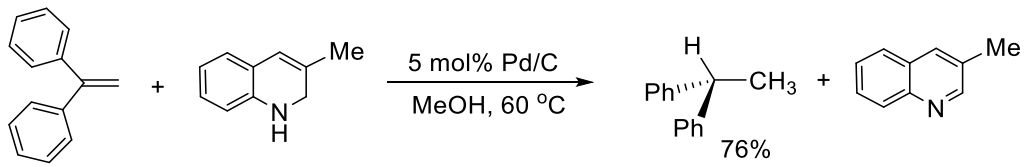

Scheme 3.5: Transfer hydrogenation of 1,1-diphenylethene in methanol using 3-methyl-1,2-dihydroquinoline as the hydrogen donor catalysed by 5 mol% Pd/C.

3.2.7 Hot filtration and Catalyst recyclability

A hot filtration experiment for the transfer hydrogenation of quinoline catalysed by RuNP@NH_2-PEGPIILP was conducted to explore the heterogeneous nature of **3.2**. The process involved running two parallel reactions using 0.1 mol% of **3.2** with five-mole equivalents of dimethylamine borane to catalyse the reduction of quinoline. When the conversion reached about 40%, a 45-micron syringe filter was used to filter one of the reaction mixtures, and the composition of the resulting filtrate was observed over the next 120 minutes. The conversion time profile for the second reaction was taken as a standard for comparison.

A comparison of the composition-time profiles for both reactions (Figure 3.10) clearly shows that the filtration quenches the reduction, indicating that removal of the filtration removed the active species and that the catalyst is either heterogeneous and has been removed or leaching of the ruthenium generates a less active species.[52]

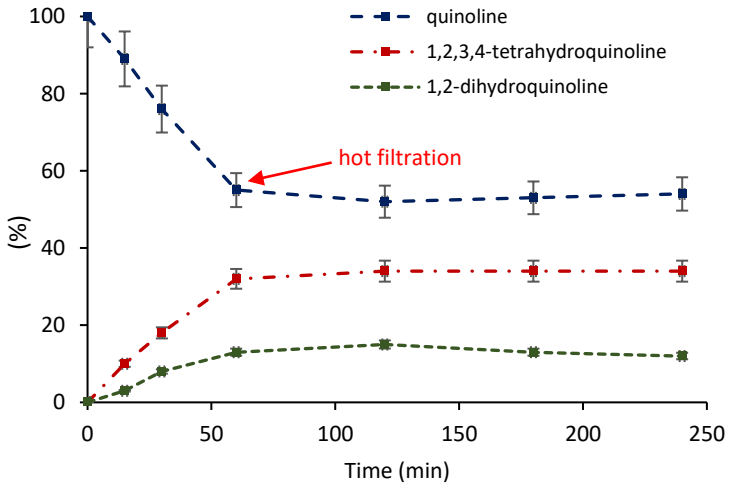

Figure 3.10 Hot filtration experiment for the dimethylamine borane-mediated transfer hydrogenation of quinoline in toluene at 65 °C catalysed by 0.1 mol% **3.2.**

Any slight changes in the composition of the reaction mixture after the hot filtration can be attributed to the release of hydrogen from the 1,2-dihydroquinoline to produce quinoline, as this partial reduction has been demonstrated to be reversible.

Analysis of the organic filtrate collected after the filtration revealed that the ruthenium content was below the detection limit of the ICP-OES, suggesting that the catalyst is most likely heterogeneous and that leaching to less active species is not significant. In a complimentary hot filtration experiment, a reduction was allowed to reach complete conversion, after which the solution was filtered through a 45-micron syringe filter and a fresh portion of quinoline was added to the filtrate and the composition was monitored for a further 4 h. There was no further measurable conversion of quinoline, even after stirring for a further 4 h at 65 °C, which provides additional support that the filtration removed the active species.[52]

A study on recycling was conducted to examine how stable and long-lasting **3.2** is as a catalyst for the transfer hydrogenation of quinoline using dimethylamine borane as the hydrogen source. The performance of the reaction was monitored across multiple uses to assess whether it would be suitable for use in a continuous flow system, similar to that described in a study using PdNP@PPh_2-PEGPIILS as the catalyst for the reduction of nitrobenzene with sodium borohydride.[19]

However, the challenge of retrieving a small amount of catalyst through filtration made it impractical to carry out a standard recycling experiment. To overcome this, the conversion and selectivity profile for the reduction of quinoline using dimethylamine borane was monitored as a function of time and when the reaction was complete, additional portions of quinoline, and dimethylamine borane were introduced without any purification or catalyst treatment. The composition of the resulting mixture was then monitored for a further 4 hours, and this protocol was repeated for three additional cycles to assess the efficiency of **3.2** over time and with repeated use.[52]

The information presented in Figure 3. shows that the catalyst maintains high selectivity during each run and that there is a gradual decrease in conversion, which is most evident in the fourth run. However, the conversion can be improved by extending the reaction time to 8 hours. The decrease in conversion upon reuse could be attributed to several factors, including

the leaching of ruthenium to generate less active soluble species, which could, in turn, reduce the size and alter the morphology of the remaining nanoparticles, aggregation to afford larger less active nanoparticles or deactivation/passivation of the catalyst due to saturation of the surface-active ruthenium sites by the nitrogen donor in the tetrahydroquinoline product.[52]

Analysis of the organic phase after the fourth reuse confirmed that the ruthenium content was below the detection limit of the ICP-OES, indicating that the reduction in conversion is unlikely to be caused by leaching of the catalyst to form a less active homogeneous species. However, this analysis does not differentiate a pathway involving leaching and re-deposition. Furthermore, TEM analysis of the organic phase remaining after the fourth run revealed that the ruthenium nanoparticles remained monodisperse, with no significant change in size, as the mean diameter of 1.7 ± 0.5 nm was comparable to that of 1.8 ± 0.5 nm for a freshly prepared sample of catalyst **3.2**.

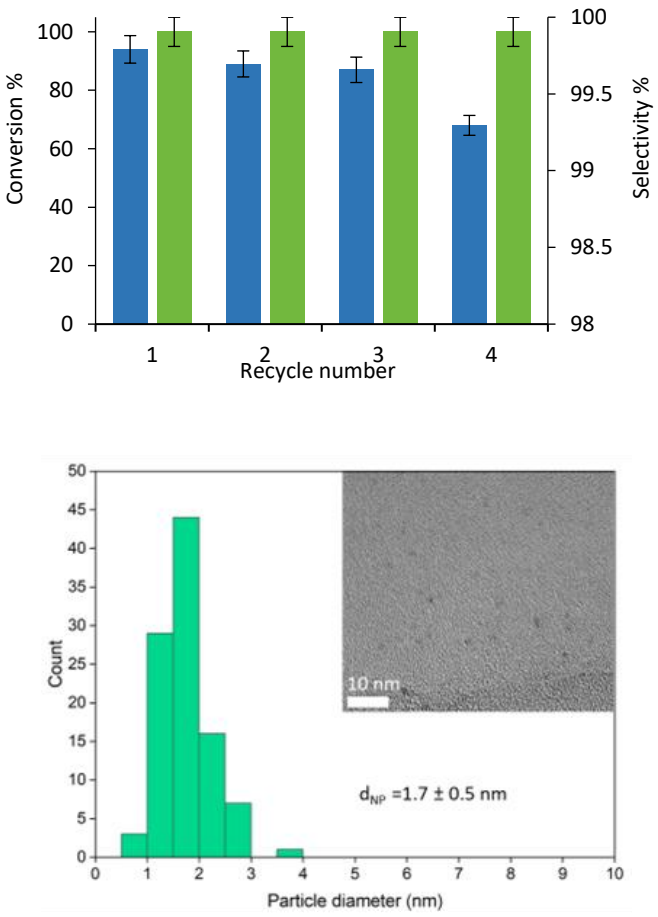

Figure 3.11 (top) Reuse study for the dimethylamine borane-mediated reduction of quinoline to 1,2,3,4-tetrahydroquinoline conducted in toluene at 65 °C blue bars – conversion of quinoline, green bars – selectivity for 1,2,3,4-tetrahydroquinoline and (bottom) sizing histogram of RuNPs for **3.2** after four reuses and a TEM image of the recovered material.

As the decrease in conversion with reuse was not due to leaching or aggregation, an investigation was conducted to determine if the deactivation or passivation was caused by the coordination of the accumulated tetrahydroquinoline to the active surface ruthenium sites. This coordination could potentially block access of the substrate and/or modify the reactivity. To study this, the catalyst was pre-treated with four equivalents of 1,2,3,4-tetrahydroquinoline at 65 °C for various pre-stirring times. The aim was to assess the effect of the potential nitrogen donor group on its activity for the dimethylamine borane-mediated reduction of quinoline. Under the optimum conditions mentioned above, conversions of 92%, 93%, and 92% were obtained after pre-stirring catalyst **3.2** with 1,2,3,4-tetrahydroquinoline for 0 min, 20 min, and 60 min before adding the quinoline.[52]

These conversions were similar to the 94% obtained in the absence of tetrahydroquinoline, which suggests that the product accumulating during each successive run does not passivate or poison the active surface sites.

Finally, XPS analysis of the catalyst recovered after five cycles indicated a significant amount of boron fouling on the surface, which we believe is the most likely explanation for the reduction in activity with reuse (Figure 3.5) and (Figure 3.6).

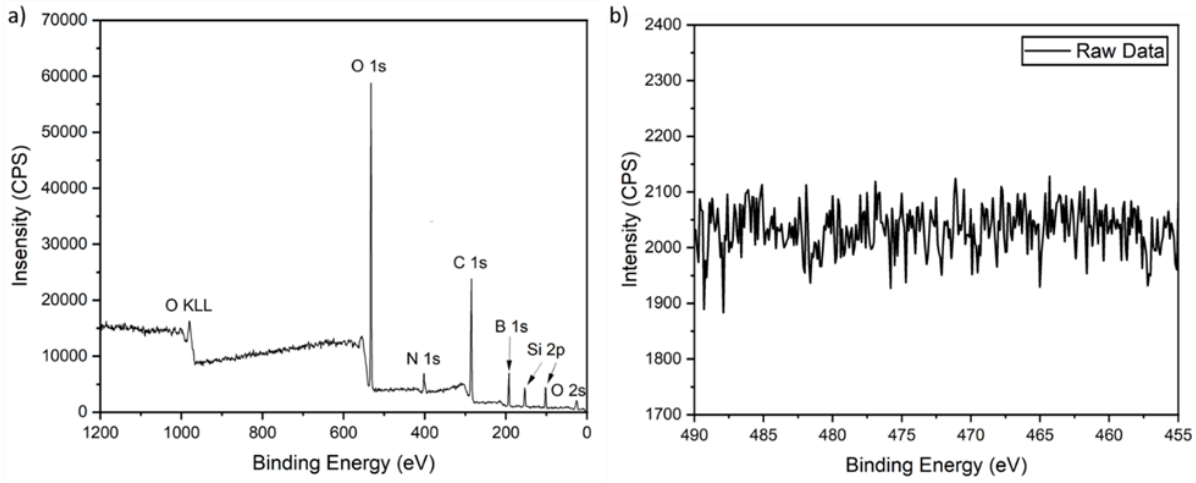

Figure 3.5 (a) XPS survey spectrum of **3.2** after recycling and (b) the corresponding high-resolution Ru 3p core level XPS spectrum referenced to the C 1s alkyl peak at 284.8 eV.

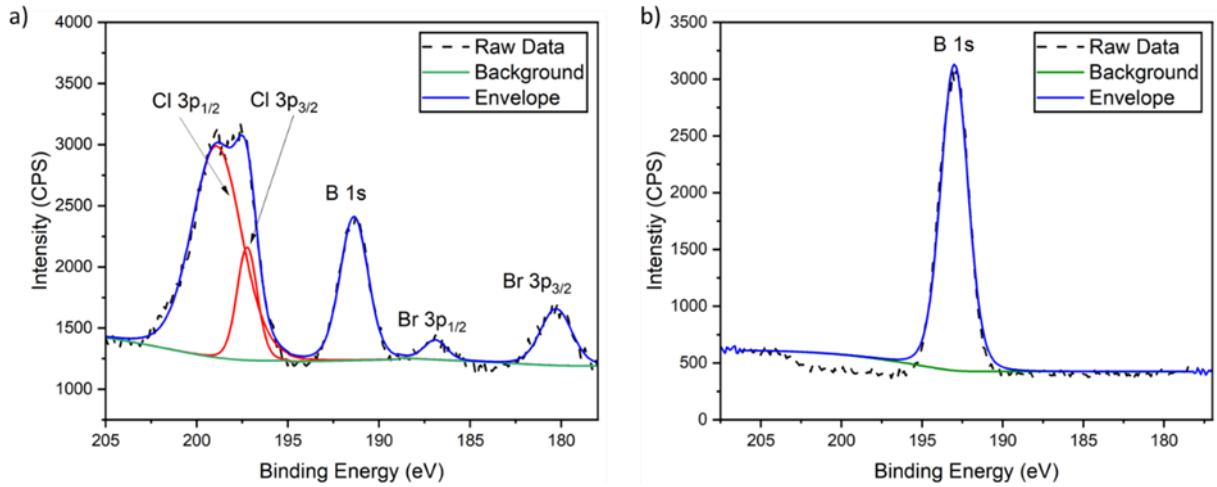

Figure 3.6 High-resolution XPS spectra of the B 1s, Cl 2p and Br 3p region of (a) RuNP@NH_2-PEGPIILS (**3.2**), and (b) **3.2** after recycling experiments, both referenced to the C 1s alkyl peak at 284.8 eV.

3.3 Proposed Mechanism for the Reduction of Quinoline

Given that **3.2** facilitates the liberation of hydrogen from dimethylamine borane in water and toluene, it is possible that quinoline reduction could occur via a heterolytic pathway involving the transfer of a hydride and a proton from the hydrogen donor. This has been previously documented for the reduction of quinoline with sodium borohydride catalysed by hectorite-supported RuNPs,[8] as well as with formic acid/triethylamine catalysed by AuNPs supported on amine-functionalised silica.[37] Alternatively, the reduction could occur through homolytic activation of molecular hydrogen that is produced in situ from the dimethylamine borane. However, given that a catalytic hydrogenation of quinoline performed at 65 °C under 1 atm of hydrogen in the presence of 0.25 mol% **3.2** only achieved 14% conversion after 4 hours, the reduction most likely occurs via a heterolytic pathway involving the transfer of a hydride from the hydrogen donor to the surface of the nanoparticle, leading to the formation of the active hydride. Based on this, we cautiously propose that the amino group present on the polymer's surface serves multiple functions. One of these functions is to enable the heterolytic release of hydrogen from the dimethylamine borane, forming an active surface hydride and an ammonium ion.[52]

This process may occur through a cooperative amine-facilitated concerted deprotonation-hydride transfer pathway, as illustrated in step (i) of Scheme 3.6. However, it is currently uncertain whether a direct transfer of the hydride from the amine borane to the C (2) carbon atom of an activated surface-coordinated quinoline is possible. This transfer may involve a hydrogen-bonded ensemble similar to the one depicted in the inserted image in Scheme 3.6. Additionally, the primary amine grafted to the support could potentially engage in a hydrogen bond with the nitrogen atom of the quinoline, promoting the coordination of the substrate through the nitrogen atom rather than the arene ring.[52]

This interaction has been suggested as a possible explanation for the selective hydrogenation of the N-heterocyclic ring, while adsorption through the phenyl ring results in its hydrogenation to obtain 5,6,7,8-tetrahydroquinoline. Furthermore, the hydrogen bond will activate the quinoline ring and facilitate the hydride transfer to the most electron-deficient atom of the quinoline (C2) while protonation of the nitrogen by the ammonium group would liberate the dihydroquinoline, as illustrated in steps (ii)-(iii) of (Scheme 3.6). Subsequent

hydride addition to C(4) followed by protonation at C(3) would produce the corresponding tetrahydroquinoline. Additionally, the hydrogen bond between the amino group on the support and the nitrogen atom of the reduced product will weaken its interaction with the surface ruthenium atom, aiding in dissociation and preventing catalyst poisoning.

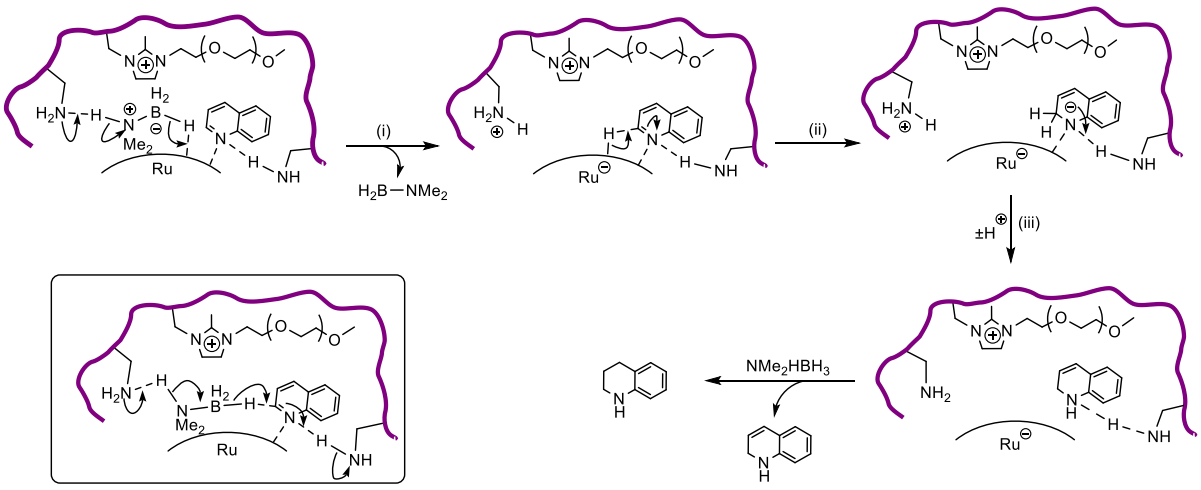

Scheme 3.6: Possible pathway for the dimethylamine borane-mediated reduction of quinoline involving amine-assisted hydride transfer and hydrogen bond-directed coordination and activation of quinoline.

Preliminary studies on how the polymer composition affects catalyst performance suggest that various components primarily affect the conversion as complete selectivity for tetrahydroquinoline is retained for the dimethylamine borane mediated reduction of quinoline when the PEG and amino groups are eliminated. It would be valuable to investigate if this design principle can be used to achieve high selectivity for the hydrogenation of quinoline in aprotic and protic solvents, thus testing the soundness of our current understanding. To achieve this, further modifications to the catalyst, surface investigations, and kinetic and computational studies will need to be conducted to gain a more comprehensive understanding of the factors that impact catalyst performance. This will help in designing more effective catalysts.[52]

3.4 Conclusions

Ruthenium nanoparticles stabilised by amine-decorated imidazolium-based polymer immobilised ionic liquid, RuNP@NH_2-PEGPIILS, is a highly effective catalyst for transfer hydrogenation of quinoline to 1,2,3,4-tetrahydroquinoline (THQ) via 1,2-dihydroquinoline. This catalyst has an initial TOF of 610 mol of quinoline converted per mol of Ru per hour, which is one of the highest reported for a metal nanoparticle-based catalyst.

Under ideal conditions, a broad range of substituted quinolines were transformed to a combination of the respective 1,2-dihydroquinoline and 1,2,3,4-tetrahydroquinoline in short reaction times, while tended reaction times favoured the 1,2,3,4-tetrahydroquinoline as the principal product. Notably, the reduction of 3-substituted quinolines displayed 100% selectivity for the corresponding partially reduced 1,2-dihydroquinolines, which were obtained in near quantitative yields. Achieving complete selectivity for the partial reduction of 3-substituted quinolines to the respective 1,2-dihydroquinolines is unparalleled for a catalyst based on nanoparticles, suggesting that this system could be valuable for synthesising this type of substrate.

Future studies should explore the surface interactions of the reactants and conduct kinetic studies to gain a more comprehensive understanding of the specificity of this process. This marks the first example where a nanoparticle has been used to catalyse the hydrogenation of quinoline with dimethylamine borane as the hydrogen source. The reversible nature of the partial reduction of 3-substituted quinolines was demonstrated, and 8-methyl-1,2-dihydroquinoline acted as an efficient hydrogen donor for the palladium-catalysed reduction of 1,1-diphenylethene.

Studies on catalyst poisoning revealed that the NPs remained active despite the presence of the 1,2,3,4-tetrahydroquinoline product. The declining conversion during reuse was likely caused by fouling from the buildup of boron-containing substances on the nanoparticle surface, as indicated by an XPS analysis of the spent catalyst. Ongoing research will investigate modifications to the polymer to identify the essential components of this NP-polymer system necessary for achieving high activity. Additionally, preparations are proceeding to develop porous ionic liquid polymers aimed at enhancing catalyst reusability and longevity.[52]

3.5 References

1. Y. Wang, B. Dong, Z. Wang, X. Cong and X. Bi, *Org. Lett.*, 2019, **21**, 3631–3634.
2. M. El-Shahat, *J. Heterocycl. Chem.*, 2022, **59**, 399–421.
3. J. D. Scott and R. M. Williams, *Chem. Rev.*, 2002, **102**, 1669–1730.
4. G. A. Ramann and B. J. Cowen, *Molecules*, 2016, **21**, 986.
5. S. P. Verevkin, S. P. Safronov, A. A. Samarov and S. V. Vostrikov, *Appl. Sci.*, 2021, **11**, 11758.
6. V. Sridharan, P. A. Suryavanshi and J. C. Menéndez, *Chem. Rev.*, 2011, **111**, 7157–7259.
7. L. Bai, X. Wang, Q. Chen, Y. Ye, H. Zheng, J. Guo, Y. Yin and C. Gao, *Angew. Chem. Int. Ed.*, 2016, **55**, 15656–15661.
8. B. Sun, D. Carnevale and G. Süss-Fink, *J. Organomet. Chem.*, 2016, **821**, 197–205.
9. H. Konnerth and M. H. G. Prechtl, *Green Chem.*, 2017, **19**, 2762–2767.
10. X. Yu, R. Nie, H. Zhang, X. Lu, D. Zhou and Q. Xia, *Microporous Mesoporous Mater.*, 2018, **256**, 10–17.
11. D. Ren, L. He, L. Yu, R.-S. Ding, Y.-M. Liu, Y. Cao, H.-Y. He and K.-N. Fan, *J. Am. Chem. Soc.*, 2012, **134**, 17592–17598.
12. M. Niu, Y. Wang, P. Chen, D. Du, J. Jiang and Z. Jin, *Catal. Sci. Technol.*, 2015, **5**, 4746–4749.
13. L. Lu, S. Zou and B. Fang, *ACS Catal.*, 2021, **11**, 6020–6058.
14. S. Zhang, Z. Xia, T. Ni, Z. Zhang, Y. Ma and Y. Qu, *J. Catal.*, 2018, **359**, 101–111.
15. W. Long, N. A. Brunelli, S. A. Didas, E. W. Ping and C. W. Jones, *ACS Catal.*, 2013, **3**, 1700–1708.
16. F. P. da Silva, J. L. Fiorio and L. M. Rossi, *ACS Omega*, 2017, **2**, 6014–6022.
17. Y. Cao and T. Mu, *Ind. Eng. Chem. Res.*, 2014, **53**, 8651–8664.
18. S. Doherty, J. G. Knight, T. Backhouse, E. Abood, H. Alshaikh, I. J. S. Fairlamb, R. A. Bourne, T. W. Chamberlain and R. Stones, *Green Chem.*, 2017, **19**, 1635–1641.
19. S. Doherty, J. G. Knight, T. Backhouse, A. Bradford, F. Saunders, R. A. Bourne, T. W. Chamberlain, R. Stones, A. Clayton and K. Lovelock, *Catal. Sci. Technol.*, 2018, **8**, 1454–1467.

20. S. Doherty, J. G. Knight, T. Backhouse, E. Abood, H. Al-shaikh, A. R. Clemmet, J. R. Ellison, R. A. Bourne, T. W. Chamberlain, R. Stones, N. J. Warren, I. J. S. Fairlamb and K. R. J. Lovelock, *Adv. Synth. Catal.*, 2018, **360**, 3716–3731.

21. S. Doherty, J. G. Knight, T. Backhouse, R. J. Summers, E. Abood, W. Simpson, W. Paget, R. A. Bourne, T. W. Chamberlain, R. Stones, K. R. J. Lovelock, J. M. Seymour, M. A. Isaacs, C. Hardacre, H. Daly and N. H. Rees, *ACS Catal.*, 2019, **9**, 4777–4791.

22. C. A. Lawson, A. P. Dominey, G. D. Williams and J. A. Murphy, *Chem. Commun.*, 2020, **56**, 11445–11448.

23. D. J. Morgan, *Surf. Interface Anal.*, 2015, **47**, 1072–1079.

24. S. Doherty, J. G. Knight, T. Backhouse, T. S. T. Tran, R. Paterson, F. Stahl, H. Y. Alharbi, T. W. Chamberlain, R. A. Bourne, R. Stones, A. Griffiths, J. P. White, Z. Aslam, C. Hardare, H. Daly, J. Hart, R. H. Temperton, J. N. O'Shea and N. H. Rees, *Catal. Sci. Technol.*, 2022, **12**, 3549–3567.

25. M. M. Dell'Anna, G. Romanazzi, S. Intini, A. Rizzuti, C. Leonelli, A. F. Piccinni and P. Mastrorilli, *J. Mol. Catal. Chem.*, 2015, **402**, 83–91.

26. P. Lara, K. Philippot and A. Suárez, *ChemCatChem*, 2019, **11**, 766–771.

27. H.-Y. Jiang and X.-X. Zheng, *Appl. Catal. Gen.*, 2015, **499**, 118–123.

28. M. Fang and R. A. Sánchez-Delgado, *J. Catal.*, 2014, **311**, 357–368.

29. F. Martinez-Espinar, P. Blondeau, P. Nolis, B. Chaudret, C. Claver, S. Castillón and C. Godard, *J. Catal.*, 2017, **354**, 113–127.

30. D. E. Minter, C. R. Kelly and H. C. Kelly, *Inorg. Chem.*, 1986, **25**, 3291–3294.

31. R. Paterson, A. A. Alharbi, C. Wills, C. Dixon, L. Šiller, T. W. Chamberlain, A. Griffiths, S. M. Collins, K. Wu, M. D. Simmons, R. A. Bourne, K. R. J. Lovelock, J. Seymour, J. G. Knight and S. Doherty, *Mol. Catal.*, 2022, **528**, 112476.

32. Y. Luo, Q. Yang, W. Nie, Q. Yao, Z. Zhang and Z.-H. Lu, *ACS Appl. Mater. Interfaces*, 2020, **12**, 8082–8090.

33. M. Yadav, T. Akita, N. Tsumori and Q. Xu, *J. Mater. Chem.*, 2012, **22**, 12582–12586.

34. K. Koh, M. Jeon, C. Won Yoon and T. Asefa, *J. Mater. Chem. A*, 2017, **5**, 16150–16161.

35. S. Masuda, K. Mori, Y. Futamura and H. Yamashita, *ACS Catal.*, 2018, **8**, 2277–2285.

36. C. Deraedt, R. Ye, W. T. Ralston, F. D. Toste and G. A. Somorjai, *J. Am. Chem. Soc.*, 2017, **139**, 18084–18092.

37. B. Vilhanová, J. A. van Bokhoven and M. Ranocchiari, *Adv. Synth. Catal.*, 2017, **359**, 677–686.

38. R. Yun, W. Ma, L. Hong, Y. Hu, F. Zhan, S. Liu and B. Zheng, *Catal. Sci. Technol.*, 2019, **9**, 6669–6672.

39. M. Tang, J. Deng, M. Li, X. Li, H. Li, Z. Chen and Y. Wang, *Green Chem.*, 2016, **18**, 6082–6090.

40. L. Zhang, X. Wang, Y. Xue, X. Zeng, H. Chen, R. Li and S. Wang, *Catal. Sci. Technol.*, 2014, **4**, 1939–1948.

41. X. Xue, M. Zeng and Y. Wang, *Appl. Catal. Gen.*, 2018, **560**, 37–41.

42. H. Jiang and X. Zheng, *Catal. Sci. Technol.*, 2015, **5**, 3728–3734.

43. Y. Cao, L. Ding, Z. Qiu and H. Zhang, *Catal. Commun.*, 2020, **143**, 106048.

44. M. Guo, C. Li and Q. Yang, *Catal. Sci. Technol.*, 2017, **7**, 2221–2227.

45. Q. Song, D. Xu, W. David Wang, J. Fang, X. Sun, F. Li, B. Li, J. Kou, H. Zhu and Z. Dong, *J. Catal.*, 2022, **406**, 19–27.

46. Y. Zhang, J. Zhu, Y.-T. Xia, X.-T. Sun and L. Wu, *Adv. Synth. Catal.*, 2016, **358**, 3039–3045.

47. J. Nie, Z. Zhu, Y. Liao, X. Xiao, F. Mauriello and Z. Zhang, *Mol. Catal.*, 2022, **526**, 112381.

48. X. Wang, W. Chen, L. Zhang, T. Yao, W. Liu, Y. Lin, H. Ju, J. Dong, L. Zheng, W. Yan, X. Zheng, Z. Li, X. Wang, J. Yang, D. He, Y. Wang, Z. Deng, Y. Wu and Y. Li, *J. Am. Chem. Soc.*, 2017, **139**, 9419–9422.

49. S. Yadav, D. Chaudhary, N. Kumar Maurya, D. Kumar, K. Ishu and M. Rao Kuram, *Chem. Commun.*, 2022, **58**, 4255–4258.

50. Z. Wang, Y. Liu, M. Han, N. Ma, Q. Lyu, Q. Liu and W.-H. Sun, *Dalton Trans.*, 2022, **51**, 10983–10991.

51. D. Talwar, H. Y. Li, E. Durham and J. Xiao, *Chem. – Eur. J.*, 2015, **21**, 5370–5379.

52. A. A. Alharbi, C. Wills, T. W. Chamberlain, R. A. Bourne, A. Griffiths, S. M. Collins, K. Wu, P. Mueller, J. G. Knight and S. Doherty, *ChemCatChem*, 2023, **15**, e202300418.

Chapter 4: Efficient Hydrogen Evolution from Amine Borane Catalysed by Ru and Pt Nanoparticles Stabilised by an Amine Decorated Polymer Immobilised Ionic Liquid

4.1 Introduction

The world's dependence on depleting fossil fuels has led to an increased focus on finding sustainable and environmentally friendly energy alternatives.[1] Green hydrogen has emerged as a promising option, as its is a clean and sustainable energy carrier properties, has a high energy density, and it can be produced through water electrolysis or splitting.[2,3] However, the safe storage and transportation of this highly flammable gas remains a significant challenge in developing a hydrogen-based economy.[4] Potential solutions to this problem are to store hydrogen as a low molecular weight solid or liquid hydride or absorb it within the channels of a porous material.[5] Amine boranes have gained considerable attention among these materials due to their high hydrogen content, stability, non-toxicity, and water solubility.[6] While ammonia borane (AB) has the highest hydrogen content, it is expensive and challenging to work with. As an alternative, dimethylamine borane (DMAB) has gained popularity as a cost-effective model hydrogen carrier, and research efforts are underway to develop catalysts for the controlled release of hydrogen from DMAB. In summary, green hydrogen is a promising alternative to fossil fuels for energy storage, and amine boranes, especially DMAB, have shown potential for safe hydrogen storage and transportation. Developing efficient catalysts for the controlled release of hydrogen from DMAB could pave the way for a more sustainable energy future.[7–11]

Dimethylamine borane can produce one mole of H_2 per mole of DMAB when dehydrogenated in organic media (Scheme 4.1, Equation1). Although homogeneous catalysts have achieved high rates of hydrogen production under relatively mild conditions, they often suffer from poor long-term stability, require expensive ligands, and are difficult to recover after use.[12,13] In contrast, heterogeneous catalysts provide several benefits, such as good thermal stability, a range of operating temperatures, ease of recovery, and integration into a device.[14,15]

To this end, nanoparticle-based catalysts have garnered significant attention as their activity can be controlled through their size, and thereby surface area to volume ratio and number of active sites, as well as their morphology, however, the high surface area of metal NPs can lead to self-aggregation under the conditions of catalysis, forming larger species that are less active.[15,16]

To avoid aggregation and exploit additional advantages such as control of growth and morphology, significant enhancements in performance, and improvements in activity and selectivity, NPs can be encapsulated in suitable support such as metal oxide, graphene oxide or reduced graphene oxide, polymers or porous organic cages and MOF.[17–19]

There have been many recent example of NPs facilitating the dehydrogenation of DMAB in organic solvents with promising performance characteristics. These include mono-, bi and trimetallic systems encapsulated in PVP,[10,20,21] graphene oxide and reduced graphene oxide,[20,22] Vulcan carbon,[23] ceria, alumina, or titania,[24] MOFs,[25,26] hydrophilic polymers,[27] and multiwalled carbon nanotubes.[28] Additionally, there is increasing evidence that encapsulating NPs has added advantages for catalysis including control over the growth and structure due to confinement,[29] notable improvements in catalyst performance due to strong metal support interactions,[30] and significant enhancements in activity and selectivity by integrating surface functionality or organic modifiers/ligands to adjust the surface electronic structure, steric environment, and reactant solubility.[31] In contrast to the dehydrogenation in an organic solvent, the hydrolytic release of hydrogen from DMAB results in the liberation of three moles of H_2 (Scheme 4.1, Equation 2). However, there have been relatively few reports of the hydrolysis of DMAB catalysed by nanoparticles; as such there is a growing interest in identifying cost-effective NP-based catalysts that can achieve rapid and controlled hydrolysis of DMAB under mild conditions.

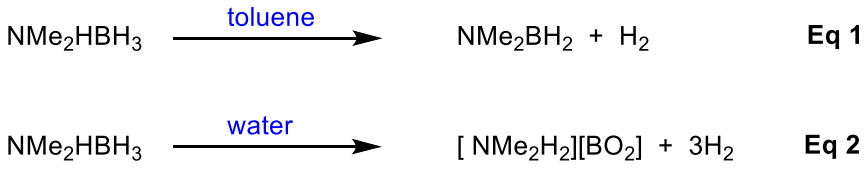

Scheme 4.1 The dehydrogenation of DMAB.

The use of ionic liquids to stabilise metal nanoparticles in various applications has been widely reported.[32] However, there are no reports of using NPs as catalysts for the dehydrogenation of DMAB, even though DMAB has been used as a hydrogen donor in catalytic transfer hydrogenations.[33] It's also noteworthy that ionic liquids facilitate the dehydrogenation of ammonia borane, suggesting a potential cooperative or synergistic relationship with NPs.[34]

Ionic liquids have also been grafted to supports to combine their favourable characteristics with covalent attachment to prevent the leaching of the ionic liquid. However, there are only a handful of reports of their use as supports to stabilise NPs for the hydrolytic release of hydrogen from storage materials. Moreover, ionic liquids have been attached to various supports, including polymers,[35] mesoporous silica,[36] and MOFs,[37] to merge their beneficial properties. This includes the stabilisation of nanoparticles through weak electrostatic interactions, in much the same manner as an IL. Additionally, the covalent bonding to a support prevents leaching of the ionic liquid, enables easier separation and recovery of the catalyst, and reduces the amount of ionic liquid needed, as the catalyst remains within the support.

Additionally, the modular nature of PIILs and their adjustable physical and chemical characteristics should make it possible to modify the charge density and distribution of the ionic microenvironment and the redox properties, introduce extra surface functionality, and regulate the composition of the metal precursor. This could facilitate the creation of synergistic bimetallic and multimetallic nanoparticles with well-defined stoichiometry to enhance catalyst effectiveness and lead to the development of new processes and technologies meeting the standards for commercial applications.

The use of support-grafted ionic liquids for the stabilisation of NPs and molecular catalysts is becoming widespread, but there are only a limited number of reports on their use as supports for stabilizing NPs for the hydrolytic release of hydrogen from storage materials. The first of these reports describes the highly dispersed PdAuNPs stabilised by an imidazolium-based organic polymer, which catalyses the hydrolytic release of H_2 from AB more effectively than its monometallic counterparts.[38] Furthermore, RuNPs supported on a polymeric ionic liquid catalyses the synthesis of benzimidazole from 1,2-diamines and CO_2 through reductive dehydrogenation of DMAB, as well as the DMAB-mediated reduction of olefins and nitroarenes.[39] The Doherty group has been developing heteroatom donor functionalised PIILs as supports for the stabilisation of NPs to explore whether the heteroatom donor can supplement the weak stabilisation provided by the ionic liquid fragment, influence the growth of the NPs or modify the surface electronic/steric properties and thereby exploit the beneficial effects that ligands can have on the performance of heterogeneous nanocatalysts.[40]

To this end, preliminary studies demonstrated that platinum and ruthenium nanoparticles stabilised by a phosphine or amine-decorated polymer-immobilised ionic liquid are highly effective catalysts for the the hydrolytic release of hydrogen from $NaBH_4$.[41,42] In an investigation to enhance the performance of amino-modified PIIL-stabilised Pt and Ru nanoparticles as catalysts for the DMAB-mediated reduction of quinoline, as discussed in Chapter 3, we observed that the efficiency of the catalysts might be linked to varying rates of hydrogen evolution from DMAB, consequently impacting the availability of hydride species at the NP surface.[43] We have now completed a comprehensive comparison of the performance of amino-functionalised PEG-modified polymer-immobilised ionic liquid stabilised ruthenium and platinum NPs as catalysts for the hydrolytic release of hydrogen from DMAB, AB, and $NaBH_4$ and herein report the results of this study.

Remarkably, RuNP@NH_2-PEGPIILS demonstrates significantly higher catalytic activity in hydrolysing DMAB and AB as compared to its platinum counterpart, while both catalysts show similar rates for the hydrolysis of $NaBH_4$.

Moreover, regardless of the catalyst used, the hydrolysis of AB is notably faster than that of DMAB. The differences in apparent activation energies indicate variations in the hydrolysis rates for the substrates and the effectiveness of the two catalysts. Initial kinetic studies involving deuterium isotope effects were conducted to explore the hydrolysis mechanism, and potential pathways were deliberated.

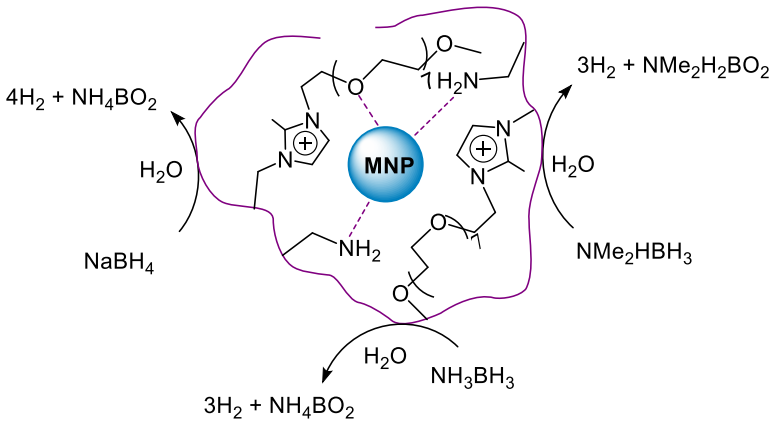

Figure 4.1 Hydrogen evolution from amine borane catalysed by MNPs Stabilised by an amine decorated polymer immobilised ionic liquid.

4.2 Results and Discussion

4.2.1 Synthesis and Characterisation of ($PtCl_4$) Pre-catalyst 4.2 and Nanoparticles 4.3 and 4.4

The preparation of the tetrachloroplatinate loaded precursor [$PtCl_4$]@NH_2-PEGPIILS (**4.2**) and the polymer stabilised platinum and ruthenium nanoparticles **4.3** and **4.4** needed for this research are illustrated in Scheme 4.1. Precursor **4.2** was prepared by impregnation of the NH_2-PEGPIIL polymer **4.1** with tetrachloroplatinate such that complete exchange of all the bromide and chloride would afford an amine to the platinum ratio of one; the resulting precursor **4.2** was isolated as a dark red solid in near quantitative yield. Quantitative analysis of the Cl 2p and Br 3d components of the XPS spectrum of **4.3** revealed that the exchange was not complete as evidenced by the presence of both bromide and chloride, although as expected impregnation of NH_2-PEGPIIL with $[PtCl_4]^{2-}$ resulted in a significant reduction of the bromide content as evidenced by a comparison of the bromide to chloride ratio of 1:0.22 for NH_2-PEGPIIL and 1:1.75 for **4.2**; this was supported by ICP OES analysis of the precursor which gave a bromide to chloride ratio of 1:2.2.

The amine-decorated polymer immobilised ionic liquid-stabilised platinum nanoparticles PtNP@NH_2-PEGPIILS (**4.3**) were produced by reduction of **4.2** with sodium borohydride in ethanol and obtained as a free-flowing black powder. Its ruthenium equivalent **4.4** (Figure 4.2) was prepared as previously described.[41]

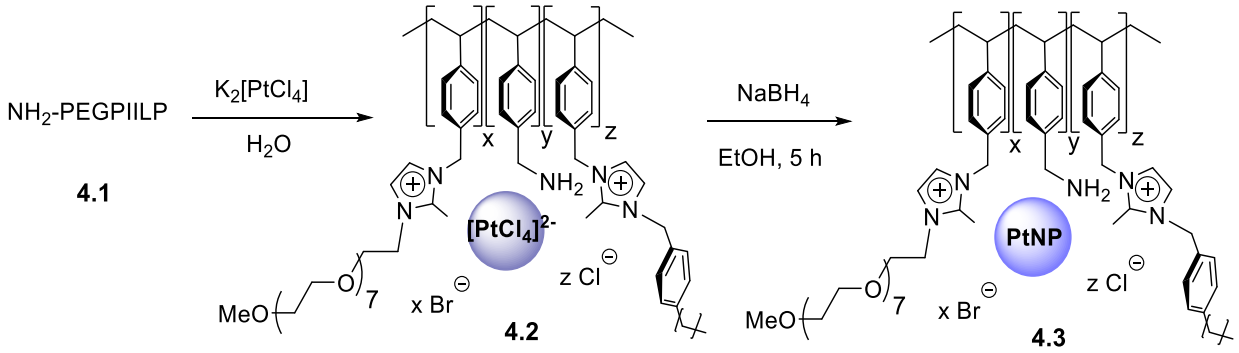

Scheme 4.2: Synthesis of $PtCl_4$@NH_2-PEGPIILS (**4.2**) and PtNP@NH_2-PEGPIILS (**4.3**)

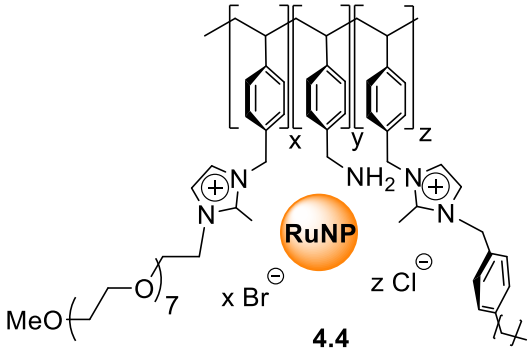

Figure 4.2: The structure of RuNP@NH_2-PEGPIILS (**4.3**)

ICP-OES analysis of $PtCl_4$@NH_2-PEGPIIL (**4.2**), PtNP@NH_2- PEGPIILS **4.3** and RuNP@NH_2-PEGPIILS **4.4** was undertaken to determine their platinum and ruthenium loadings. Moreover, as NH_2-PEGPIIL exists as a combination of bromide and chloride in salt form, and catalysts **4.3** and **4.4** were produced through reduction of the respective metal chloride-impregnated precursors, ICP-OES analysis was utilised to determine the composition of chloride and bromide in **4.3** and **4.4**, considering that the quantity and type of halide could impact their effectiveness.The ratios of chloride-to-bromide in **4.3** and **4.4** were determined to be 6.25:1 and 7.0:1, respectively, confirming that both contain similar amounts of residual bromide. This affirmation is supported by the quantitative analysis of the Cl 2p and Br 3d components of **4.3** and **4.4**, which was used to determine the relative amounts of chloride and bromide remaining after reducing the metal halide-impregnated precursor. The ratios of 7.2:1 and 7.9:1 for **4.3** and **4.4**, respectively, from elemental analysis corroborate those established by ICP-EOS.

The solid-state ^{13}C CP/MAS NMR spectrum of **4.2** shows distinct resonances associated with different chemical environments. Specifically, characteristic resonances are observed for the imidazolium ring and aromatic carbon atoms at chemical shifts between δ 124 and δ 146 ppm, respectively. Additionally, high field signals are present at δ 11–49 ppm, corresponding to the methyl group attached to the imidazolium ring, the methylene groups of the polystyrene backbone, and the methylene of the benzylamine. An intense signal at δ 71 ppm is associated with the carbon atoms of the PEG chain, while a weak signal at δ 58 ppm represents the terminal OMe group, as illustrated in (Figure 4.3). Furthermore, the solid-state ^{13}C CP/MAS NMR spectra of catalysts **4.3** and **4.4** have confirmed the presence of Pt-N and Ru-N interactions.

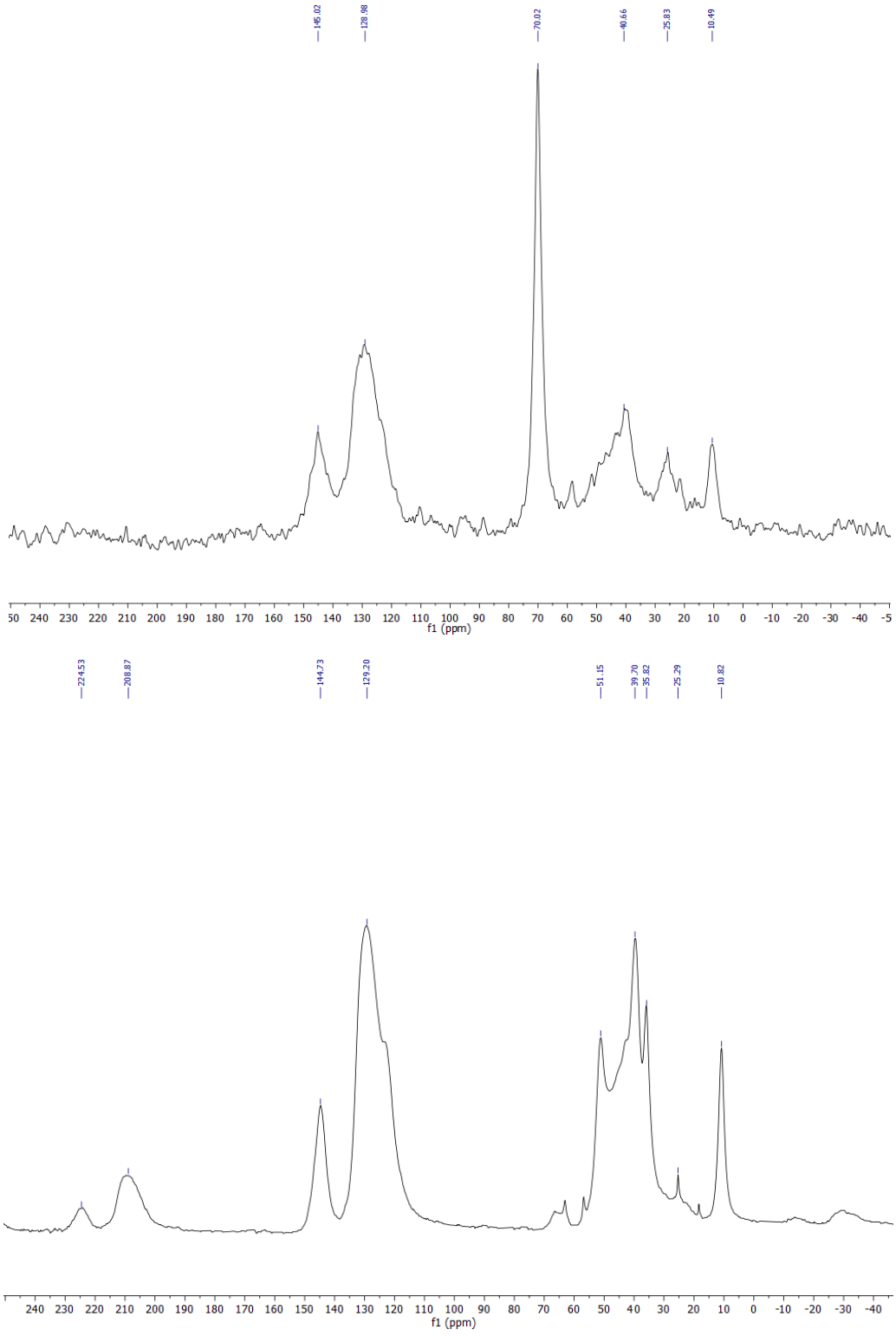

Figure 4.3: Solid state $^{13}C\{^{1}H\}$ CP-TOSS NMR spectrum of $[PtCl_4]@NH_2$-PEGPIILS (**4.2**) (top), $PtNP@NH_2$-PEGPIILS (**4.3**) (bottom).

Comparison of the solid-state ^{15}N NMR spectrum of the polymer support NH_2-PEGPIIL (**4.1**) and precatalyst **4.2** presented convincing proof for a Pt---N interaction. The former showed

three signals at δ-195/-207 and δ-332 ppm for the nitrogen atoms in the imidazolium ring and the amine, while the latter has an additional signal at δ-291 ppm. The 41 ppm shift to a low field is consistent with a platinum-coordinated amine (Figure 4.4).

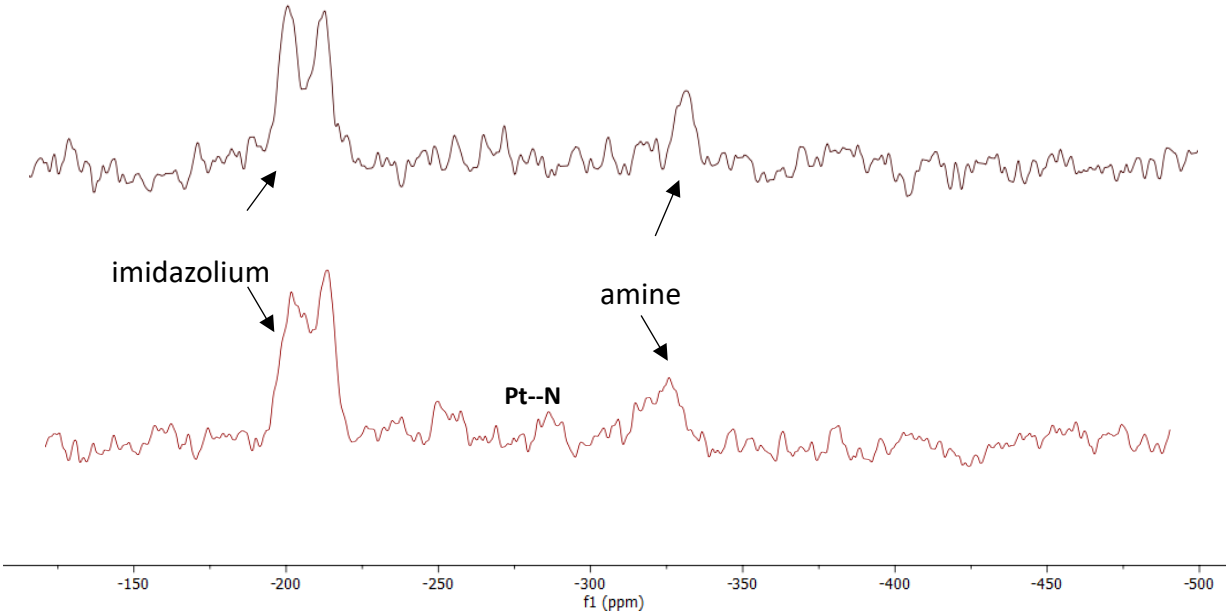

Figure 4.4: Comparison of the CP-MAS ^{15}N NMR spectra of NH_2-PEGPIIL (**4.1**) (top) and [$PtCl_4$]@NH_2-PEGPIILS (**4.2**) (bottom).

The IR spectrum of the polymer, along with those of **4.2** and catalysts **4.3** and **4.4**, exhibit bands at approximately 1580 cm^{-1} and 1600 cm^{-1}, which are indicative of the stretching vibrations of C=C and C=N in the imidazolium ring. Additionally, a band at around 1450 cm^{-1}, attributed to the C-N (imidazolium or amine) stretching vibration, confirms the incorporation of the ionic liquid monomer into the polymer (figure 4.5).

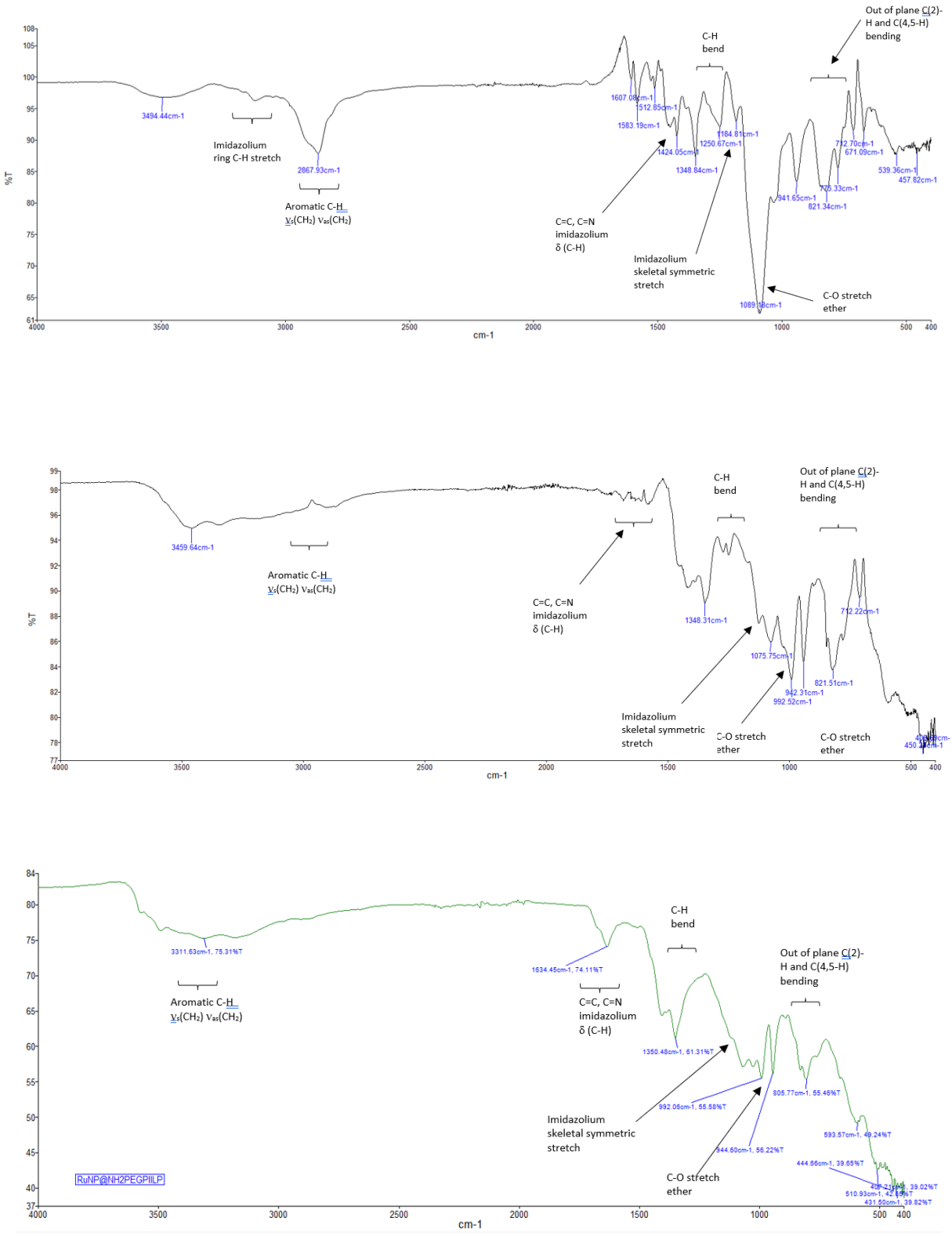

Figure 4.5: FT-IR spectra of freshly prepared [$PtCl_4$]@NH_2-PEGPIILS (**4.2**) (top), PtNP@NH_2-PEGPIILS (**4.3**) (middle) and RuNP@NH_2-PEGPIIL (**4.4**) (bottom).

In the investigation of the heat resilience of catalysts **4.3** and **4.4**, thermogravimetric analysis was applied. The analysis revealed that at approximately 100 °C, there was an initial weight loss, indicating the removal of a small amount of physiosorbed ethanol and/or water. Subsequently, three significant degradation pathways were observed between 260–650 °C, confirming that the catalysts are suitable for hydrolytic dehydrogenation use. Furthermore, the TGA profiles for **4.3** and **4.4** indicate that these catalysts start to decompose at temperatures close to 210 °C, which is notably lower than the temperatures typically needed for the release of hydrogen from storage materials (Figure 4.6).

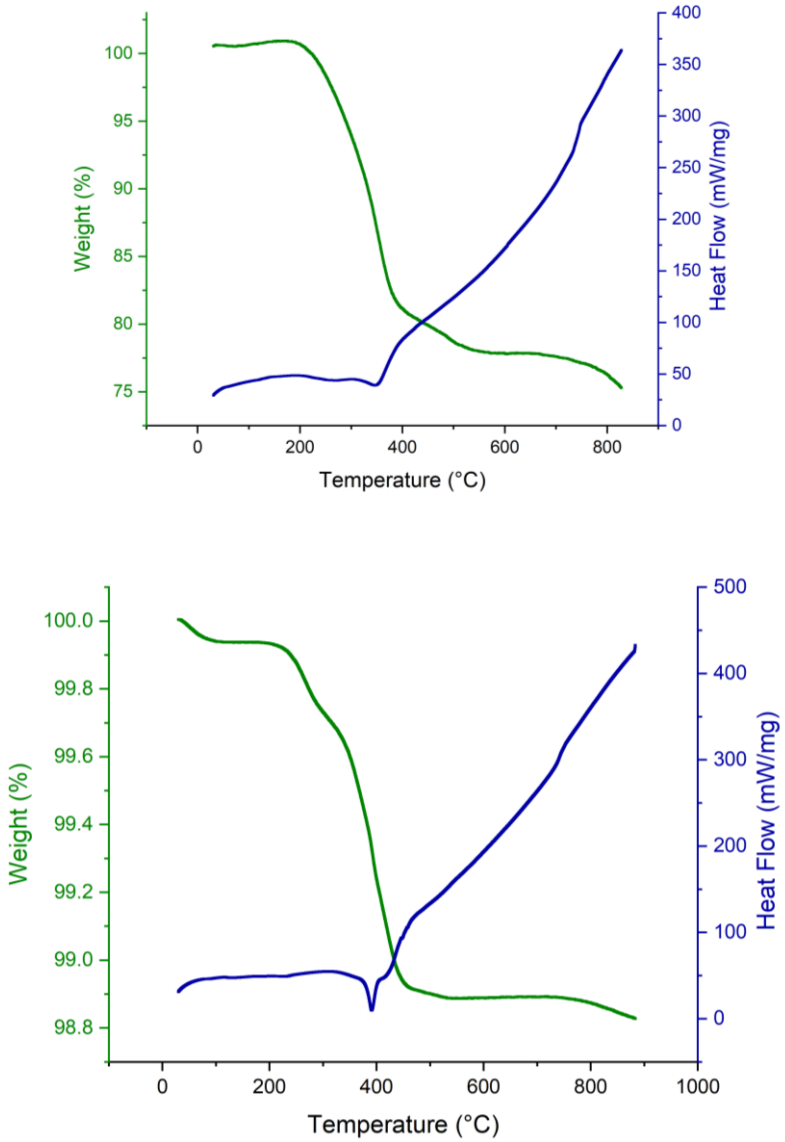

Figure 4.6: TGA/DSC curves for PtNP@NH_2-PEGPIILS **4.3** (top) and RuNP@NH_2-PEGPIILS **4.4** (bottom); wt.% v temperature. Heating rate of 10 °C min^{-1} in air.

Upon conducting a Scanning Electron Microscopy (SEM) examination of the freshly prepared materials, it was observed that there are significant contrasts in the topography and morphology of the $[PtCl_4]^{2-}$ loaded polymer and pre-reduced samples in comparison to polymers **4.1** (Figure 4.7). The texture of the samples in this particular scenario appeared to be powdered, which is believed to be a result of the additional processing stages involved in impregnation and reduction. This suggests that including $[PtCl_4]^{2-}$ and pre-reduction treatments substantially impact the polymers' physical properties.

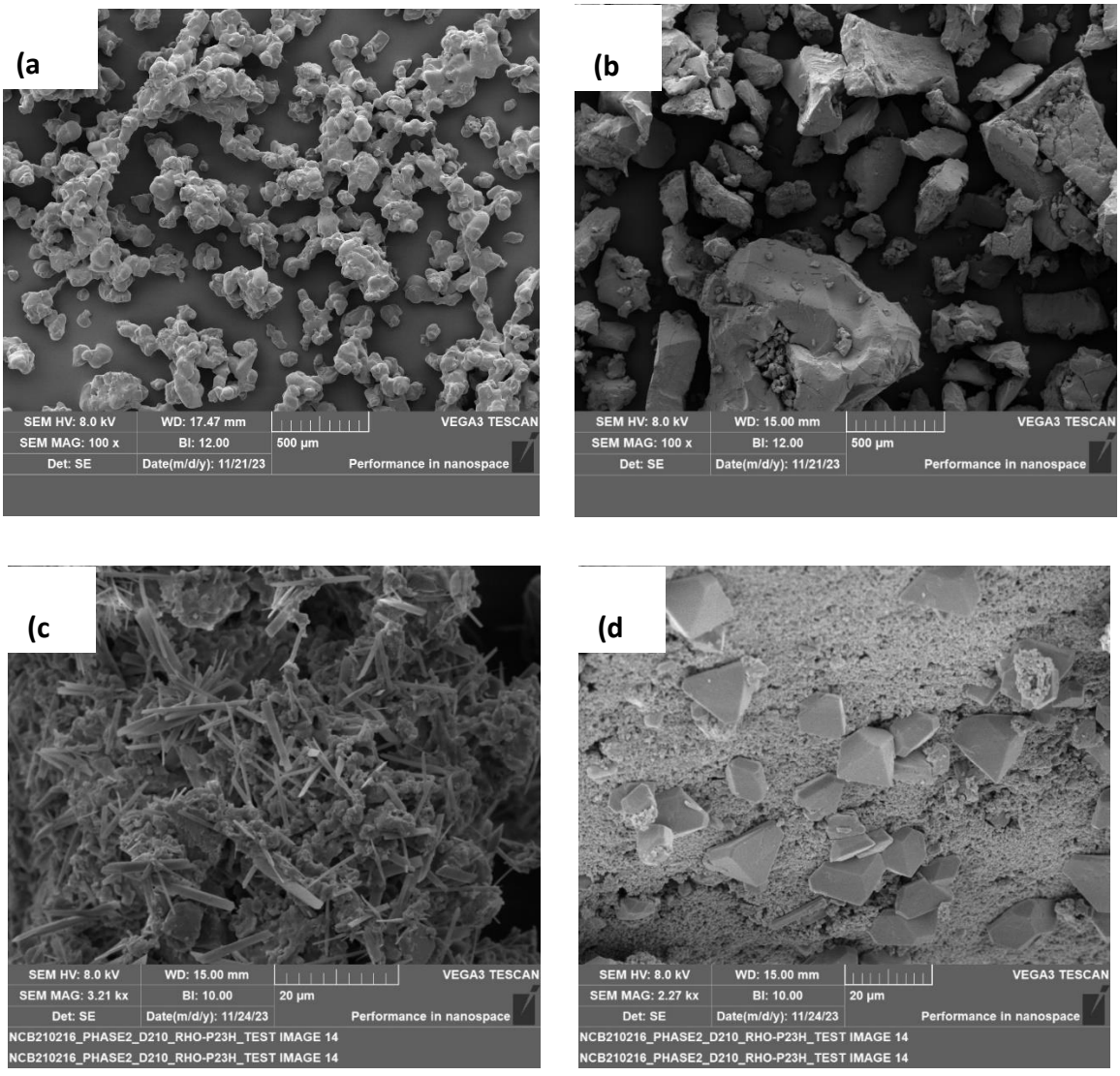

Figure 4.7: Selected SEM images of freshly prepared samples of a) NH_2-PEGPIILS (**4.1**), b) $PtCl_4$@NH_2-PEGPIILS (**4.2**), c) PtNP@NH_2-PEGPIILS (**4.3**) and d) RuNP@NH_2-PEGPIILS (**4.4**).

An examination of the surface of NH_2-PEGPIIL precatalyst **4.2**, and catalysts **4.3** and **4.4** was performed using X-ray photoelectron spectroscopy (XPS). Charge neutralisation was

employed for all samples, and the quoted binding energies (BEs) were not rescaled. Due to the limitations of using advantageous carbon as the reference,[44] peak assignments were determined by considering the characteristic BE separations between the elements. Two peaks at 397.4 eV and 395.6 eV were fitted to the local nitrogen environment of the NH_2-PEGPIIL support, which is indicative of nitrogen in an imidazolium ring and an amine, respectively, as depicted in (Figure 4.8). The N 1s peak of the tetrachloroplatinate-loaded precatalyst **4.2** displayed two main peaks at 397.4 eV and 395.6 eV, which can be attributed to imidazolium and amine species, respectively.[40] These peaks showed no apparent shift compared to those in the polymer, indicating an unchanged chemical environment. Furthermore, a minor component at 395.0 eV was observed, suggesting a potential Pt-N interaction.

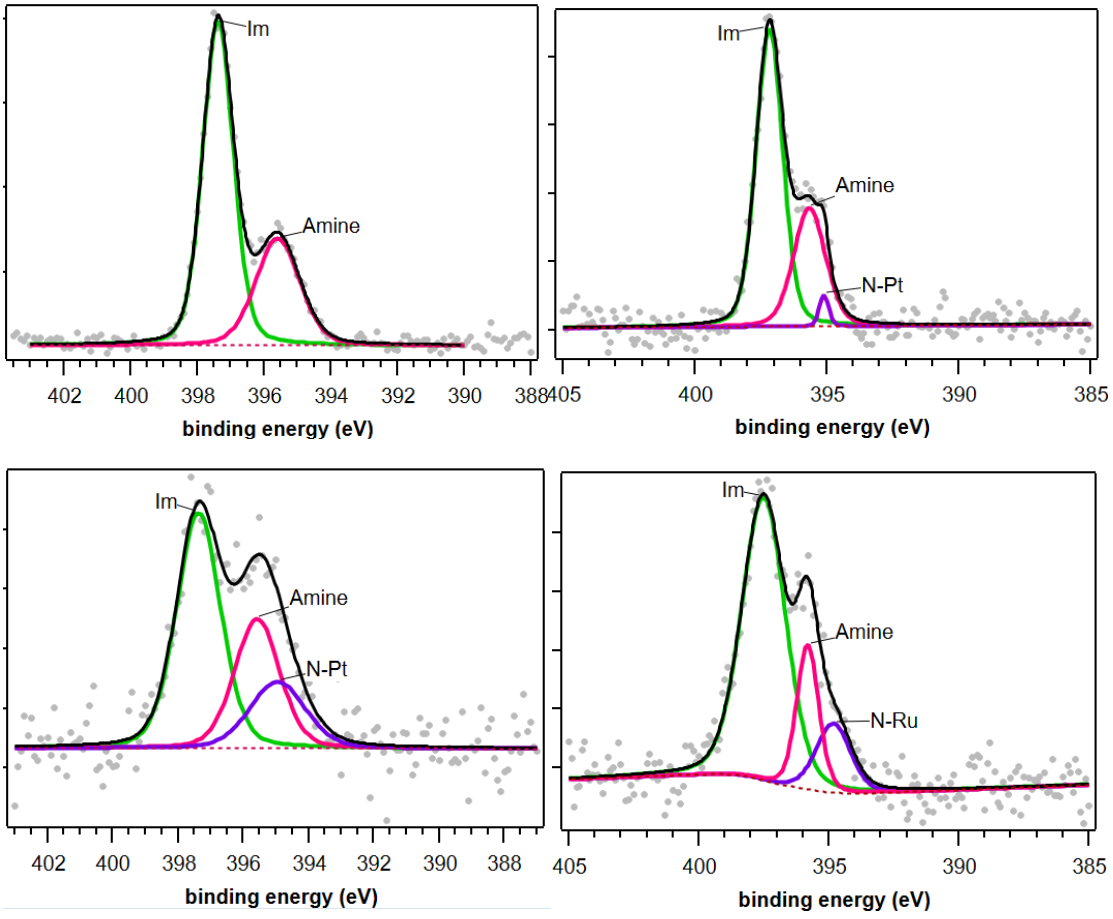

Figure 4.8: N 1s XPS spectrum of NH_2-PEGPIILS (**4.1**) (top left), $PtCl_4$@NH_2-PEGPIILS (**4.2**) (top right), PtNP@NH_2-PEGPIILS (**4.3**) (bottom left) and RuNP@NH_2-PEGPIILS (**4.4**) (bottom right).

In the C 1s region, the polymer composition was also in line with three peaks: one at 280.6 eV for C-C/C-H species, and two at 282.3 eV and 281.2 eV, corresponding to C-O and C-N species, respectively.[40]

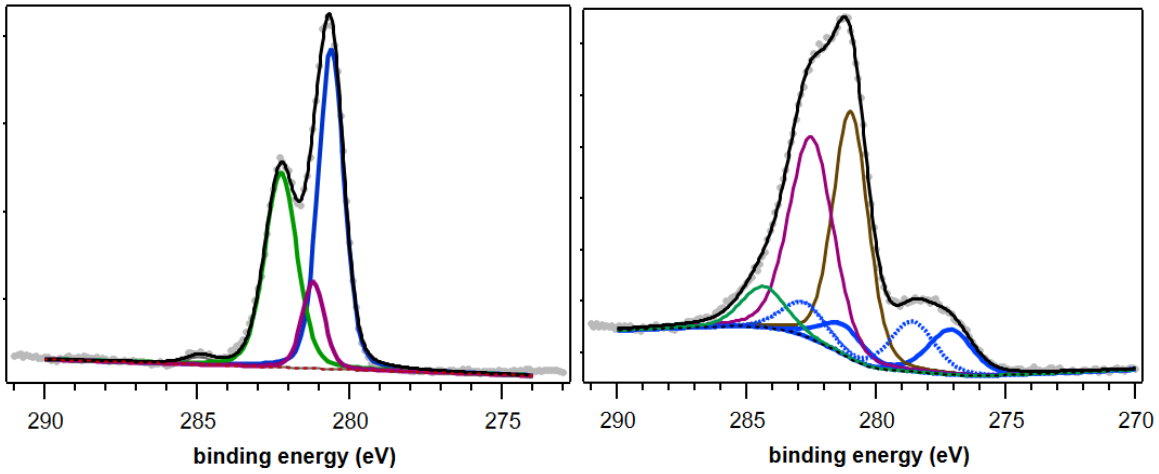

Figure 4.9: C 1s XPS spectrum of NH_2-PEGPIILS **4.1** (left), $PtCl_4$@NH_2-PEGPIILS **4.2** (right), PtNP@NH_2-PEGPIILS **4.3** (bottom left) and RuNP@NH_2-PEGPIILS **4.4** (bottom right).

Analysis of the Pt 4f region of the tetrachloroplatinate loaded precursor revealed two sets of $4f_{7/2}$ and $4f_{5/2}$ spin-orbit doublets, indicating two distinct Pt 4f electronic environments (Figure 4.10 a). The major $4f_{5/2}$ and $4f_{7/2}$ peaks have binding energies of 71.5 eV and 68.2 eV, matching Pt(II) coordinated to chloride, based on literature-reported values for Pt 4f and Cl $2p_{3/2}$ separations (121.3 eV and 124.6 eV).[45,46] The minor $4f_{5/2}$ and $4f_{7/2}$ doublet at 72.8 eV and 69.5 eV likely correspond to platinum coordinated to amine, with a 3.3 eV separation between the peaks and a 326.7 eV difference between the $4f_{7/2}$ state and the N 1s, in line with previous reports of Pt–N interactions.[47,48]

An upward shift in binding energy suggests that the platinum becomes more electron deficient due to the formation of a Pt–N interaction, possibly as a result of the lower negative charge at platinum caused by the substitution of one of the chlorides in $[PtCl_4]^{2-}$ with a neutral amine to afford a $[PtCl_3(amine)]^-$ species.

For catalyst **4.3** data of the Pt 4f region**,** the peak at 64.2 eV in the binding energy spectrum corresponds to residual bromide originating from the PEG-modified imidazolium monomer. It was analysed into two pairs of $3d_{5/2}$ and $3d_{3/2}$ doublets, likely representing the bromide anion and Pt-coordinated bromide.[49] In the XPS spectrum of catalyst **4.3** (Figure 4.10 b), the Pt 4f

region was resolved into two pairs of $4f_{7/2}$ and $4f_{5/2}$ doublets. The energy separation between the Pt $4f_{7/2}$ peaks and the O 1s peak (465.4 eV and 463.8 eV) indicates Pt metal and PtO_2, respectively.[50,51] The analysis of catalyst **4.4** involved the examination of the Ru 3p region because of the overlap between the C 1s and Ru 3d regions. A broad peak at 459.5 eV was analysed and fitted to two Ru $3p_{3/2}$ peaks. The peak with a higher binding energy (BE) was identified as RuO_2, while the peak with a lower BE was linked to Ru(0) (Figure 4.10 c). This task focused on the differentiation between these peaks and the aliphatic C 1 s peak because the values of 177.7 eV and 180.2 eV for this difference align with previously documented values for metallic ruthenium and RuO_2, respectively.[52,53] The peaks associated with RuO_2 species most likely result from surface oxidation of the preformed ruthenium nanoparticles. Lastly, the presence of a borate salt such as $NaBO_2$ or $NaB(OH)_4$ was confirmed by the presence of Na and B 1s peaks in the XPS spectra for **4.3** and **4.4** but these were subsequently eliminated through extraction with water.

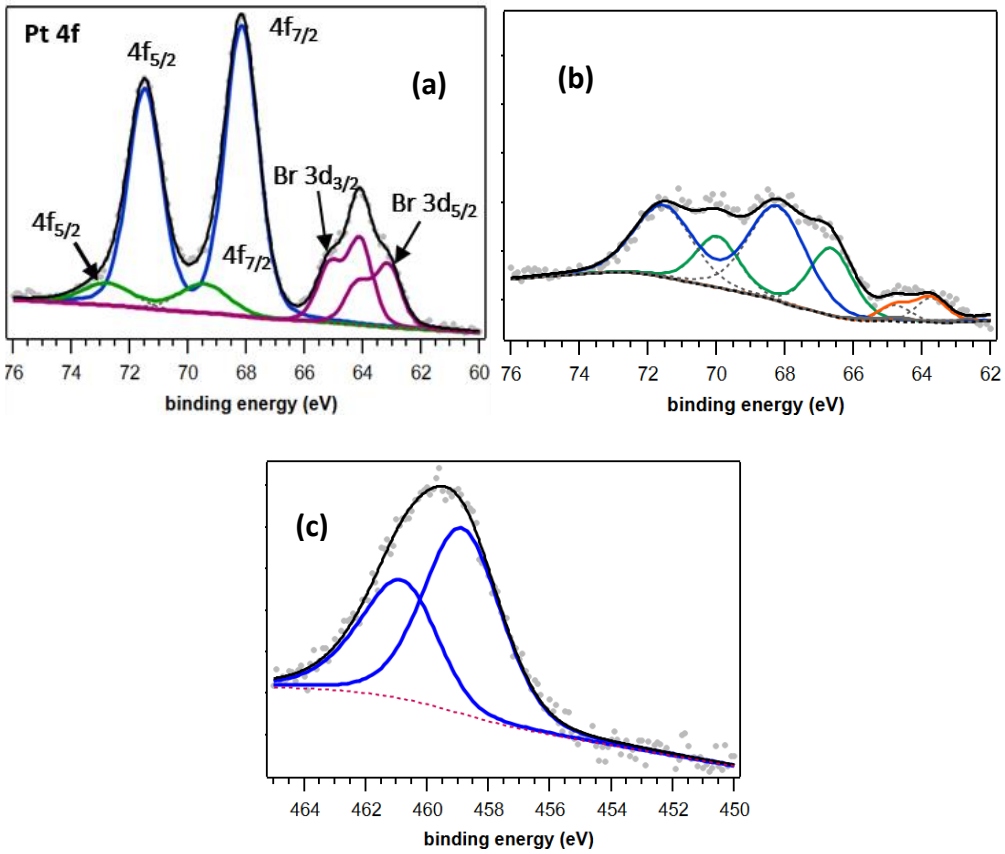

Figure 4.10: Pt 4f core level XPS spectra of (a) **4.2** and (b) **4.3** and (c) Ru 3p XPS spectrum of **4.4**

Table 4.1: Summary of Pt 4f, C 1s, N 1s, O 1s, Br 3d, Cl 2p and B 1s Binding Energies (eV) for PtNP@NH_2-PEGPIILS **4.3.**

Pt 4f	$4f_{5/2}$ Pt(II)	$4f_{5/2}$ Pt(0)	$4f_{7/2}$ Pt(II)	$4f_{7/2}$ Pt(0)
Binding energy (eV)	71.5	69.2	68.2	66.6
C 1s	C-O	C-N	C-C	
Binding energy (eV)	282.7	282.04	280.5	
N 1s	Imidazolium	Amine	Pt---N	
Binding energy (eV)	397.4	395.6	394.9	
O 1s	Pt-O	C-O	C-O	
Binding energy (eV)	532.0	528.6	527.5	
Br 3d	$3d_{3/2}$	$3d_{5/2}$	$3d_{3/2}$	$3d_{5/2}$
Binding energy (eV)	64.5	63.5	62.7	61.7
Cl 2p	$2p_{3/2}$	$2p_{1/2}$		
Binding energy (eV)	196.3	194.7		
B 1s	1s			
Binding energy (eV)	188.0			

Table 4.2: Summary of Ru 3p, C 1s, N 1s, O 1s and Ru 3d Binding Energies (eV) for RuNP@NH_2-PEGPIILS **4.4.**

Ru 3p	$3p_{3/2}$ RuO_2	$3p_{3/2}$ Ru(0)		
Binding energy (eV)	461.1	458.5		
C 1s	C-O	C-N	C-C	
Binding energy (eV)	284.36	282.5	280.9	
N 1s	Imidazolium	Amine	Ru---N	
Binding energy (eV)	397.5	395.8	394.8	
O 1s	O-H	C-O	C-O	O-Ru-O
Binding energy (eV)	532.0	529.8	528.4	527.35
Ru 3d	$3d_{3/2}$ RuO_2	$3d_{3/2}$ Ru(0)	$3d_{5/2}$ RuO_2	$3d_{5/2}$ Ru(0)
Binding energy (eV)	282.7	281.3	278.6	277.1
Br 3d	$3d_{3/2}$	$3d_{5/2}$		
Binding energy (eV)	64.8	63.8		
Cl 2p	$2p_{1/2}$	$2p_{3/2}$		
Binding energy (eV)	196.8	195.0		
B 1s	1s			
Binding energy (eV)	188.3			

The powder X-ray diffraction pattern of RuNP@NH_2-PEGPIILS **4.4** displayed diffraction peaks at 2θ = 28.1°, 35.2°, 40.3°, 54.5°, 58.1°, 59.6°, 65.8°, 67.2°, 69.8°, and 74.3°, corresponding to the (110), (101), (200), (210), (211), (220), (002), (310), (112), (301), and (202) lattice planes

of the tetragonal phase of RuO_2 with the P42/mmm space group (ICDD No. 00–040-1290), in line with existing literature. The lack of diffraction peaks for metallic ruthenium implies that the nanoparticles are either very small in size and/or well dispersed in the polymer (Figure 4.11a). Similarly, the powder XRD pattern for **4.3** contained characteristic diffraction peaks at 2θ=27.9°, 34.7°, 34.8°, 39.6°, 40.2°, 40.3°, 53.8°, 57.7°, 58.8°, 65.0°, 65.6° which index to (110), (011), (101), (020), (200), (111), (121), (220), (002), (130), (221) lattice planes for the orthorhombic phase of β-PtO_2 (ICDD No. 01–073- 2361) and the absence of diffraction peaks associated with metallic PtNPs is also consistent with their small size and high dispersion (Figure 4.12b).

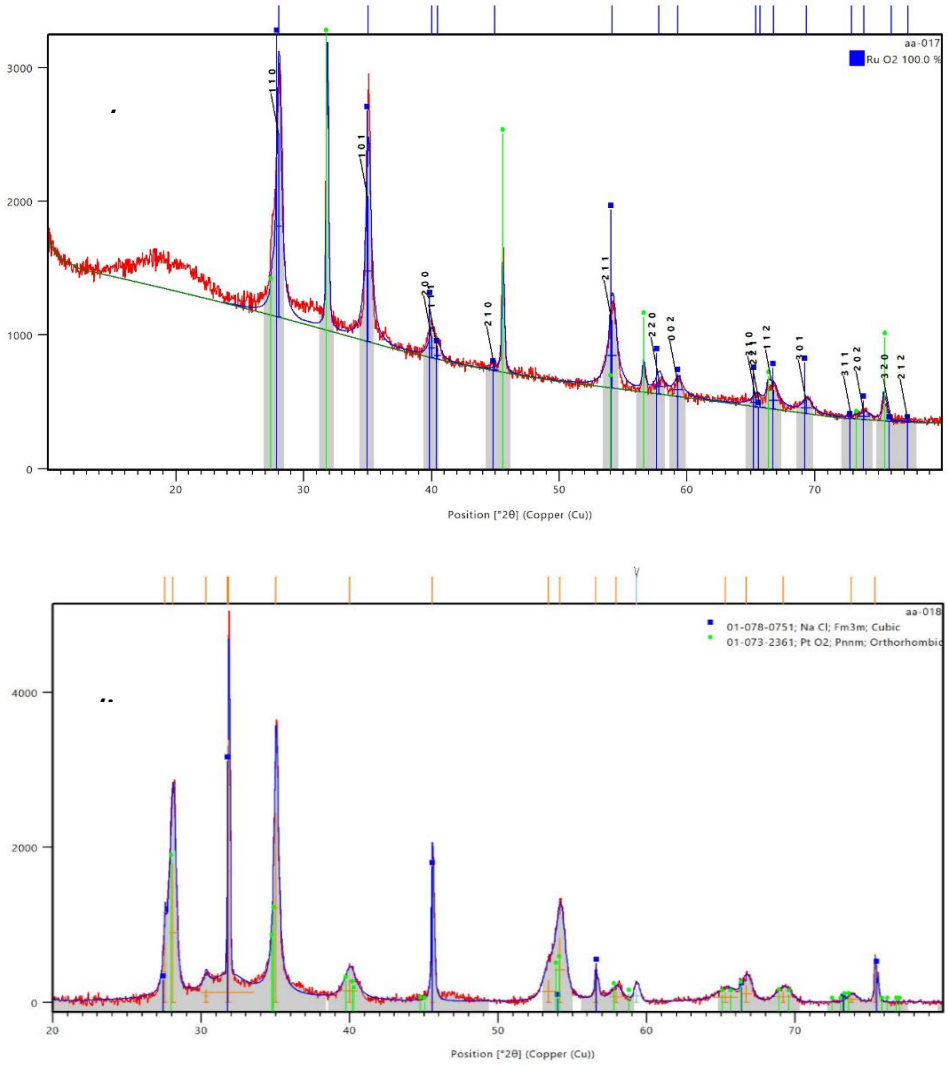

Figure 4.11: Powder XRD spectra of RuNP@NH_2-PEGPIILS(**4.4**) (top) and PtNP@NH_2-PEGPIILS (**4.3**) (bottom)

TEM images of **4.3** and **4.4** indicated that the platinum and ruthenium nanoparticles were extremely small and relatively monodisperse, with average sizes of 1.70 ± 0.5 nm and 1.60 ± 0.3 nm, respectively. Figure 4.12 displays representative images and the corresponding distribution histograms based on the measurement of >100 particles. Additionally, EDX elemental mapping of **4.4** demonstrated an even distribution and excellent dispersion of the RuNPs within the support, as shown in (Figures 4.12 a-g).

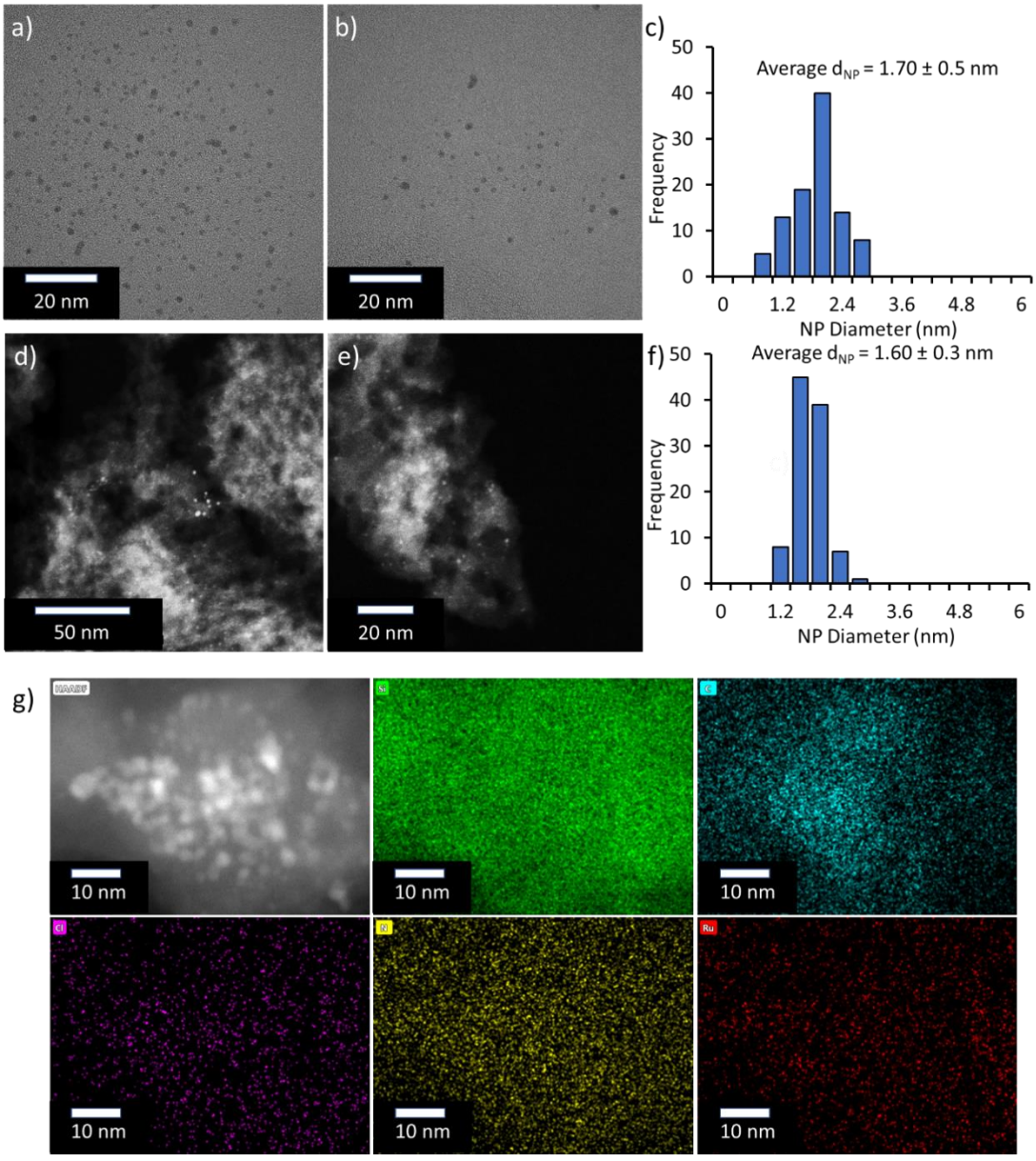

Figure 4.12: TEM images and corresponding sizing histograms of PtNPs for **4.3** (a-c) and (d-f) RuNPs for **4.4** determined by counting >100 particles. (g) HAADF image (grey) and individual EDX elemental maps for **4.4**, showing the distribution of Si (green), C (blue), Cl (purple), N (yellow) and Ru (red).

4.2.2 Preliminary Evaluation of PtNP@NH_2-PEGPIILS and RuNP@NH_2-PEGPIILS as Catalysts for the Evolution of hydrogen from Dimethylamine Borane, Ammonia Borane and $NaBH_4$

The Doherty group has recently conducted a groundbreaking study that reported that platinum nanoparticles (PtNPs) and ruthenium nanoparticles (RuNPs), stabilised by a heteroatom donor-modified polymer immobilised ionic liquids (PIIL), are highly effective catalysts for the hydrolytic evolution of hydrogen from sodium borohydride.[42] This study was subsequently extended to investigate the effectiveness of amino-decorated PIIL-stabilised Pt and Ru nanoparticles as catalysts for the hydrolysis of dimethylamine borane (DMAB), a cost-effective model substrate for ammonia borane. The findings revealed that RuNP@NH_2-PEGPIILS **4.4** exhibited significantly higher catalytic efficiency than its platinum counterpart **4.3**. Preliminary experimentation was performed using 0.25 mol% of **4.3** or **4.4** to catalyse the hydrolytic release of hydrogen from a 0.27 M solution of DMAB, AB and/or $NaBH_4$ at 313 K as shown in (Figure 4.13 a-c). Progress of the reactions was tracked by measuring the quantity of hydrogen released over time by pushing out water from an inverted burette; subsequently, the data was adjusted by compensating for the baseline quantity of hydrogen released under the same conditions at the same time but in the absence of a catalyst.

The % (surface metal atoms) were estimated for each catalyst by calculating the volume of the metal NPs and the volume of the shell containing the first layer of metal atoms.

Volume of nanoparticles:

$$V_{NPs} = \frac{4}{3}\,\pi \text{ x } r_{NPs}^3$$

Volume of the first layer of metal atoms:

$$V_{shell} = \frac{4}{3}\,\pi\, x\, (r_{NPs}^3 - (r_{NPs} - r_{at(M)})^3$$

Calculation for the % surface metal atoms

$$\%_{surface\ metal} = \frac{V_{shell}}{V_{NPs}}$$

Atomic radius of Ru = 0.130 nm

Atomic radius of Pt = 0.135 nm

Table 4.3: Calculation of the % of surface metal atoms for catalysts **4.3** and **4.4**

Entry	Catalyst	NP size (nm)	V_{NPs} (nm^3)	V_{shell} (nm^3)	Surface M (%)
1	**4.3**	1.70	2.57	1.04	40.4
2	**4.4**	1.60	7.79	2.22	28.5

The information presented in Figure 4.13 a indicates that RuNP@NH_2-PEGPIILS (**4.4**) is a significantly more active catalyst for the hydrolysis of DMAB compared to its platinum counterpart **4.3**. The former achieved approximately 99% completion within 20 minutes with an initial total turnover frequency (TOF) of 8,300 $mole_{H2}.mol_{Ru}^{-1}.h^{-1}$, whereas the latter only reached 22% conversion within the same time and 38% conversion when the reaction time was extended to 60 minutes, displaying an initial total TOF of 3,050 $mole_{H2}.mol_{Pt}^{-1}.h^{-1}$.

The difference in efficiency between **4.3** and **4.4** becomes even more apparent when the initial TOFs are determined based on the estimated surface metal atoms (Table 4.4). When comparing, catalytic hydrolysis carried out with 0.25 mol% Ru/C (5 wt%) only achieved 46% conversion after 20 minutes with an initial TOF of 2,800 $mole_{H2}.mol_{Ru}^{-1}.h^{-1}$, while 0.25 mol% Pt/C (5 wt%) only reached 24% conversion after 35 minutes with an initial TOF of 2,200 $mole_{H2}.mol_{Pt}^{-1}.h^{-1}$ (Figure 4.14a). Additionally, stirring the Ru/C and Pt/C with a homogeneous solution of NH_2-PEGPIIL in water for 12 hours before conducting the hydrolysis only led to a slight improvement in the initial TOF to 3,050 $mole_{H2}.mol_{Ru}^{-1}.h^{-1}$ and 2,300 $mole_{H2}.mol_{Pt}^{-1}.h^{-1}$, respectively. An experiment replacing the catalyst with 0.25 mol% NH_2PEG-PIIL confirmed that the metal nanoparticles were essential for the catalysis.

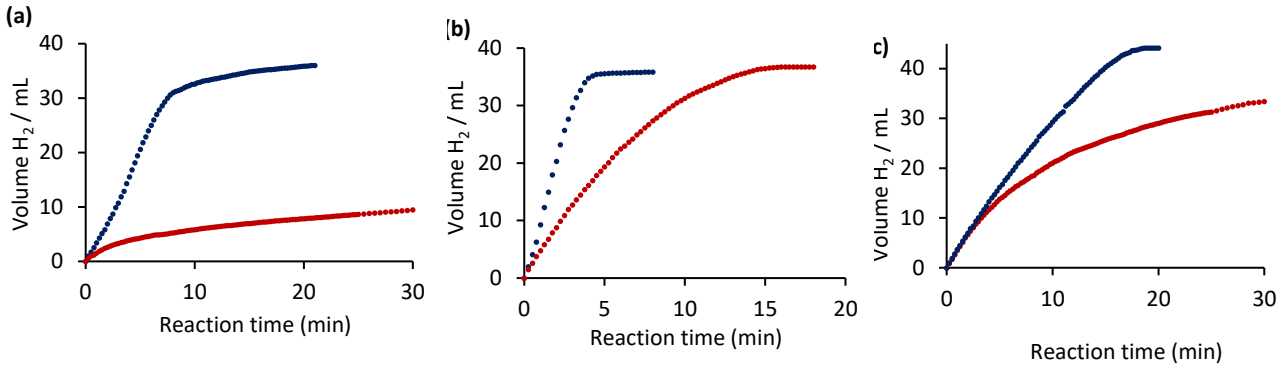

Figure 4.13: (a) Hydrolytic release of hydrogen from a 0.27 M solution of DMAB as a function of time at 313 K catalysed by 0.25 mol% **4.3** and **4.4**, (b) hydrolytic release of hydrogen from a 0.27 M solution of AB as a function of time at 313 K catalysed by 0.25 mol% **4.3** and **4.4**, (c) hydrolytic release of hydrogen from a 0.27 M solution of $NaBH_4$ as a function of time at 313 K catalysed by 0.25 mol% **4.3** and **4.4**. (**4.3** red, **4.4** blue).

The hydrolysis of DMAB (dimethylamine borane) was catalysed by **4.3** and **4.4**, and the same procedure was used to compare the hydrolysis of a 0.27 M solution of ammonia borane (AB). This was done in order to analyse the effectiveness and performance of the catalysts with different substrates. It was observed that catalyst **4.4** was also more active than **4.3** under the same conditions. This conclusion was drawn based on the volume of hydrogen released in the initial stages of the reaction and the initial turnover frequencies (TOFs) of 21,200 $mole_{H2}.mol_{Ru}^{-1}.h^{-1}$and 8,500 $mole_{H2}.mol_{Pt}^{-1}.h^{-1}$, respectively (Figure 4.13b). The ratio of these TOFs showed a similar relative difference to that observed in the hydrolysis of DMAB (Table 4.4). Additionally, the hydrolysis of AB using catalysts **4.3** and **4.4** are significantly faster than the hydrolysis of DMAB, as indicated by comparison of their initial TOFs provided in Table 4.4. Furthermore, both catalysts showed markedly higher efficiency in the hydrolysis of AB compared to the commercially available 5 wt% Ru/C and Pt/C, as both reached 93% conversion, with initial TOFs of 7,750 $mole_{H2}.mol_{Ru}^{-1}.h^{-1}$and 5,600 $mole_{H2}.mol_{Pt}^{-1}.h^{-1}$, respectively (Figure 4.14b). The superior activity obtained with Ru/C aligns with its effectiveness in the hydrolysis of DMAB, as previously noted. A review of the literature revealed that initial TOFs for PtNP-catalysed hydrolysis of AB range from 1,962 h^{-1} to 28,800 h^{-1}, while those for RuNP-based catalysts range between 2,400 h^{-1} and 43,000 h^{-1}. Encouragingly, **4.3** and **4.4** clearly compete with the most active of these catalysts.

Table 4.4: Summary of the initial turnover frequencies for hydrolysis of 0.27 M solutions of DMAB, AB and $NaBH_4$ catalysed by **4.3**, **4.4**, Pt/C and Ru/C at 313 K. *Reaction conditions*: 2.0 mL of a 0.27 M solution of substrate, temp = 303 K, 0.25 mol% **4.3**, **4.4**, Pt/C, Ru/C

Initial TOF ($mole_{H2}.molcat^{-1}.h^{-1}$)				
Substrate	**4.3**	**Pt/C**	**4.4**	**Ru/C**
DMAB	3,050	2,200	8,300	2,800
AB	8,500	5,700	21,200	7,250
$NaBH_4$	5,900	5,050	6,250	5,400

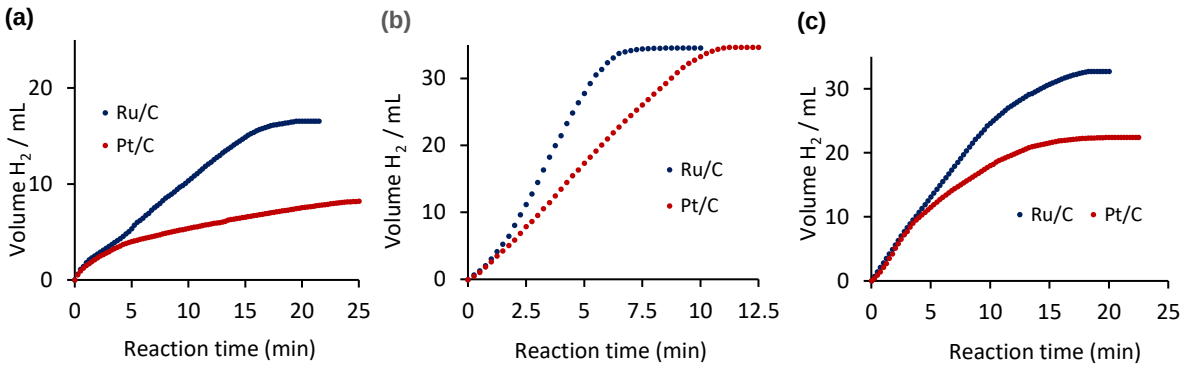

Figure 4.14: Comparison of the hydrolytic release of hydrogen from dimethylamine borane, ammonia borane and $NaBH_4$ as a function of time using 5wt% Pt/C and 5wt% Ru/C as catalysts. (a) Hydrolytic release of hydrogen from a 0.27 M solution of DMAB, (b) hydrolytic release of hydrogen from a 0.27 M solution of AB, and (c) hydrolytic release of hydrogen from a 0.27 M solution of $NaBH_4$.

Although caution should be applied when comparing the rates of hydrolysis of DMAB and AB discussed here with those documented in the literature, this investigation revealed a similar pattern in the rates, showing that the hydrolysis of AB is generally much faster than DMAB, for both ruthenium and platinum nanoparticles.[54–57] Nevertheless, while there are no direct comparisons available between the effectiveness of platinum and ruthenium nanoparticles stabilised or confined on the same support, it seems that catalysts based on ruthenium nanoparticles are more active than those based on platinum nanoparticles.

Lastly, since $NaBH_4$ is considered a promising hydrogen storage material, an investigation of the effectiveness of **4.3** and **4.4** as catalysts for the hydrolytic release of hydrogen from aqueous 0.27 M sodium borohydride was carried out. In contrast to DMAB and AB, we found that the initial total turnover frequencies (TOFs) for the hydrolysis of $NaBH_4$ catalysed by **4.3** and **4.4** as shown in Figure 4.13c, were 5,900 $mole_{H2}.mol_{Pt}^{-1}.h^{-1}$ and 6,200 $mole_{H2}.mol_{Ru}^{-1}.h^{-1}$, respectively, were comparable to each other. The difference in catalyst efficacy only became apparent in the final conversions, which were 68% for **4.3** and 92% for **4.4**. When comparing the hydrolysis of $NaBH_4$ catalysed by 0.25 mol% Pt/C and Ru/C, we observed similar performance to the reactions catalysed by **4.3** and **4.4**. In this case, the conversions reached 45% and 67%, respectively, and the initial total TOFs were 5,050 $mole_{H2}.mol_{Pt}^{-1}.h^{-1}$and 5,400 $mole_{H2}.mol_{Ru}^{-1}.h^{-1}$, respectively (Figure 4.14c). Furthermore, these initial rates were only slightly lower than those obtained with the same catalyst loading of **4.3** and **4.4**; however, both nanoparticles were notably more active as catalysts for the hydrolytic dehydrogenation of DMAB and AB compared to their Ru/C and Pt/C counterparts.

When comparing the effectiveness of **4.3** and **4.4** as catalysts for the hydrolysis of DMAB with reports in the literature for ruthenium nanoparticle-based systems, it may be difficult to assess their credibility or value due to the varying protocols and conditions. Upon reviewing the most recent literature, it seems that **4.4** stands out as one of the most efficient ruthenium nanoparticle-based catalysts for the aqueous phase dehydrogenation of DMAB. For instance, the initial TOF of 8,300 h^{-1} represents a significant improvement compared to 896 h^{-1}, 403 h^{-1}, and 362 h^{-1} achieved with RuNPs stabilised by a PVP-graphene hybrid support, PVP, and GO, respectively.[58] Similarly, it exceeds the rates of 812 h^{-1} obtained with ceria-supported RuNPs,[8] 51 h^{-1} and 56 h^{-1} for $Ru(acac)_3$ derived nanoclusters generated in the presence of Al_2O_3 and

PVP, respectively,[10] 282 h^{-1} with a graphite-supported ruthenium nanocatalyst,[59] 59 h^{-1} for RuNPs stabilised by confinement in the metal-organic framework ZIF-8,[25] and 46 h^{-1} for the solventless dehydrogenation of DMAB with RuNPs loaded on cellulose.[9] Additionally, these rates are higher than those reported for various bimetallic and trimetallic nanoparticles stabilised by reduced graphene oxide,[60] PVP,[20,61,62] multi-walled carbon nanotubes,[28] graphene oxide,[55,63] polymer hydrogels,[64] and silica.[65] However, it is only marginally higher than the 7,500 h^{-1} obtained with PtNPs immobilised onto $Ni(OH)_2$ colloid[7] and significantly lower than the 14,926 h^{-1} achieved with platinum-ruthenium nanoparticles decorated on Vulcan carbon. This currently stands as the most efficient supported nanoparticle catalyst for the hydrolytic evolution of hydrogen from DMAB.[23]

To the best of our knowledge, the initial turnover frequency (TOF) of 8,300 h^{-1} obtained with **4.4** is the highest to be reported for the aqueous phase hydrolytic dehydrogenation of DMAB catalysed by a monometallic RuNP-based catalyst. This could be attributed to the small size of the nanoparticles and the hydrophilic environment created by the PEGylated support. These factors may affect the dispersion of the catalyst in the aqueous phase and facilitate the formation of a surface-coordinated hydrogen bonded array of the type [NMe_2HBH_2-H--H-OH], which is responsible for the activation of one of the H-OH bonds in water. Even though there are not many literature reports of the hydrolysis of DMAB using PtNP-based catalysts, the overall TOF of 3,050 h^{-1} achieved with **4.3** is significantly higher than 49.2 h^{-1} with PtNPs stabilised with a polyaniline-reduced graphene oxide composite,[55] and 59 h^{-1} with platinum supported on Vulcan carbon,[23] but lower than the 4,151 h^{-1} obtained with Pt/C alloyed with nickel and 7,500 h^{-1} for PtNPs immobilised on $Ni(OH)_2$ colloid.[7]

4.2.3 A Comparative Kinetic Studies.

4.2.3.1 Determination of Activation Energies.

The different performances of catalysts **4.3** and **4.4** in promoting the hydrolysis of DMAB and AB compared to their performance in promoting the hydrolysis of $NaBH_4$ led us to conduct comparative kinetic studies on each reaction. This study aimed to investigate the reaction rates as a function of temperature to determine the activation energies and explore the impact of the catalyst as well as the concentrations of DMAB, AB, and $NaBH_4$ on the kinetics of hydrolysis.

The catalytic hydrolysis reactions were typically conducted in water at the appropriate temperature in a thermostated 50 mL round bottom flask. The flask was charged with a stir bar, an appropriate quantity of catalyst (0.25 mol% **4.3** and **4.4**) and either DMAB, AB or $NaBH_4$ and fitted with a gas outlet which was connected to the top of an inverted water-filled burette. The reaction was initiated by adding water (2 mL), immediately sealing the system by replacing the gas outlet, opening the tap of the water-filled burette and recording the time zero volume. Gas evolution began immediately, and the progress of the reaction was monitored by measuring the amount of gas liberated by recording the volume of water displaced from the burette at regular time intervals (15 sec). Kinetic studies were also conducted as described above using **4.3** and **4.4** across a range of temperatures (21 °C, 25 °C, 30 °C, 35 °C, 40 °C and 45 °C) 294 K to 318 K. The apparent activation energies (E_a) for the hydrolysis of a 0.27 M solution of DMAB using 0.25 mol% of catalysts **4.3** and **4.4** were determined to be 74.6 kJ mol^{-1} and 55.7 kJ mol^{-1}, respectively, from the Arrhenius plot of ln(k) against 1/T shown in (Figure 4.15 c-d). The initial rates were calculated from the linear portion of the graphs in (Figure 4.15 a-b). These distinct activation energies align with the relative catalytic effectiveness of **4.3** and **4.4**, as indicated by the initial turnover frequencies (TOFs) of 3050 $mole_{H2}.mol_{Pt}^{-1}.h^{-1}$ and 8,300 $mole_{H2}.mol_{Ru}^{-1}.h^{-1}$, respectively (as described above).

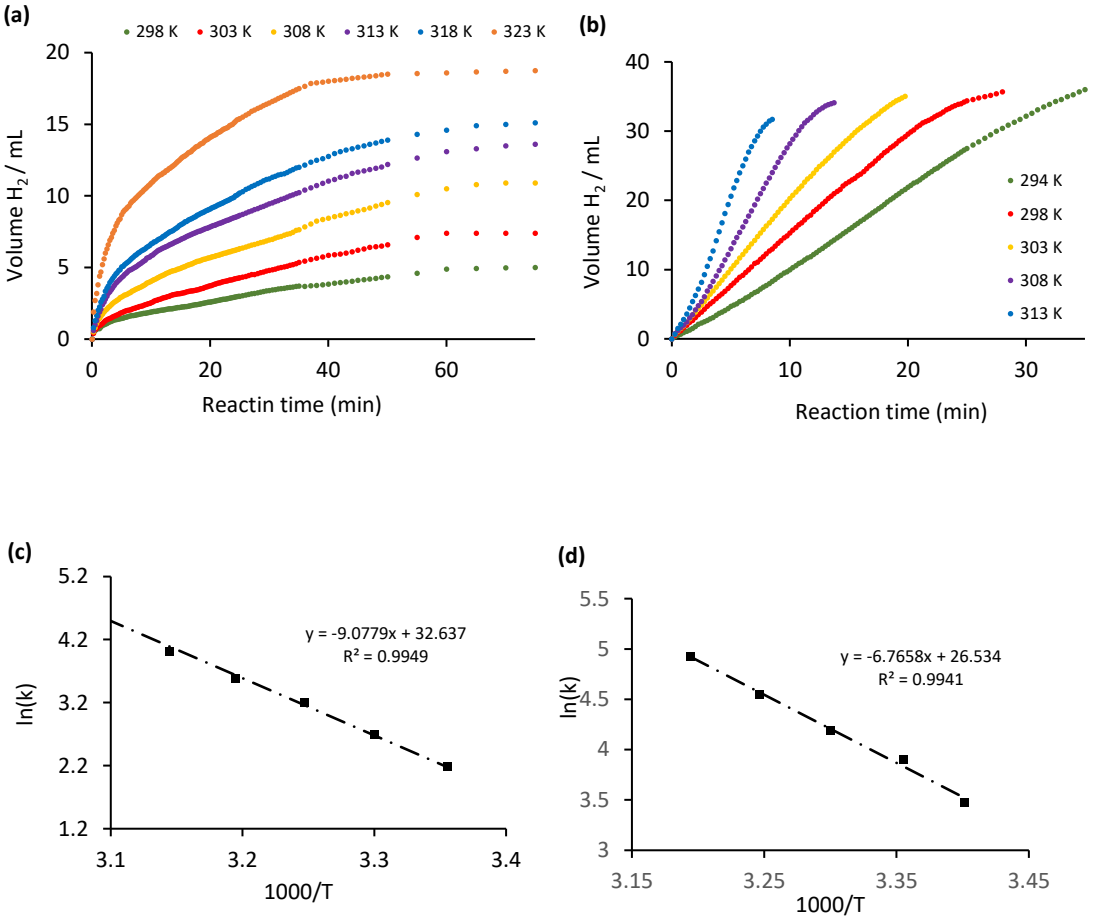

Figure 4.15: Plots of volume of hydrogen generated against reaction time for the hydrolysis of 2 mL of a 0.27 M solution of DMAB across a range of temperatures catalysed by 0.25 mol% of (a) **4.3** and (b) **4.4,** (c) and (d) the corresponding Arrhenius plots for the hydrolysis of DMAB catalysed by **4.3** and **4.4**; respectively, the initial rates (k) were determined from the slopes of the fitted lines. Initial rate (k) = $molH_2.min^{-1}$.

The apparent activation energies for the hydrolysis of a 0.27 M solution of ammonia borane under the same conditions and over a similar temperature range were found to be 35.7 kJ mol^{-1} and 27.9 kJ mol^{-1} for **4.3** and **4.4**, respectively. These values are notably lower than those determined for the hydrolysis of DMAB due to the higher hydrolysis rates of AB under comparable conditions. For comparison, the apparent activation energies for the hydrolysis of a 0.27 M solution of sodium borohydride were measured as 44.1 kJ mol^{-1} and 46.5 kJ mol^{-1} for **4.3** and **4.4**, respectively, and the similarity of these activation energies reflects the comparable initial turnover frequencies of 6,200 $mole_{H2}.mol_{Ru}^{-1}.h^{-1}$ and 5,900 $mole_{H2}.mol_{Pt}^{-1}.h^{-1}$, respectively, obtained with these catalysts at 40 °C. The Arrhenius plots and the plots of

the volume of hydrogen versus time-related to the hydrolysis of AB and $NaBH_4$ are shown in Figure 4.16 and 4.17.

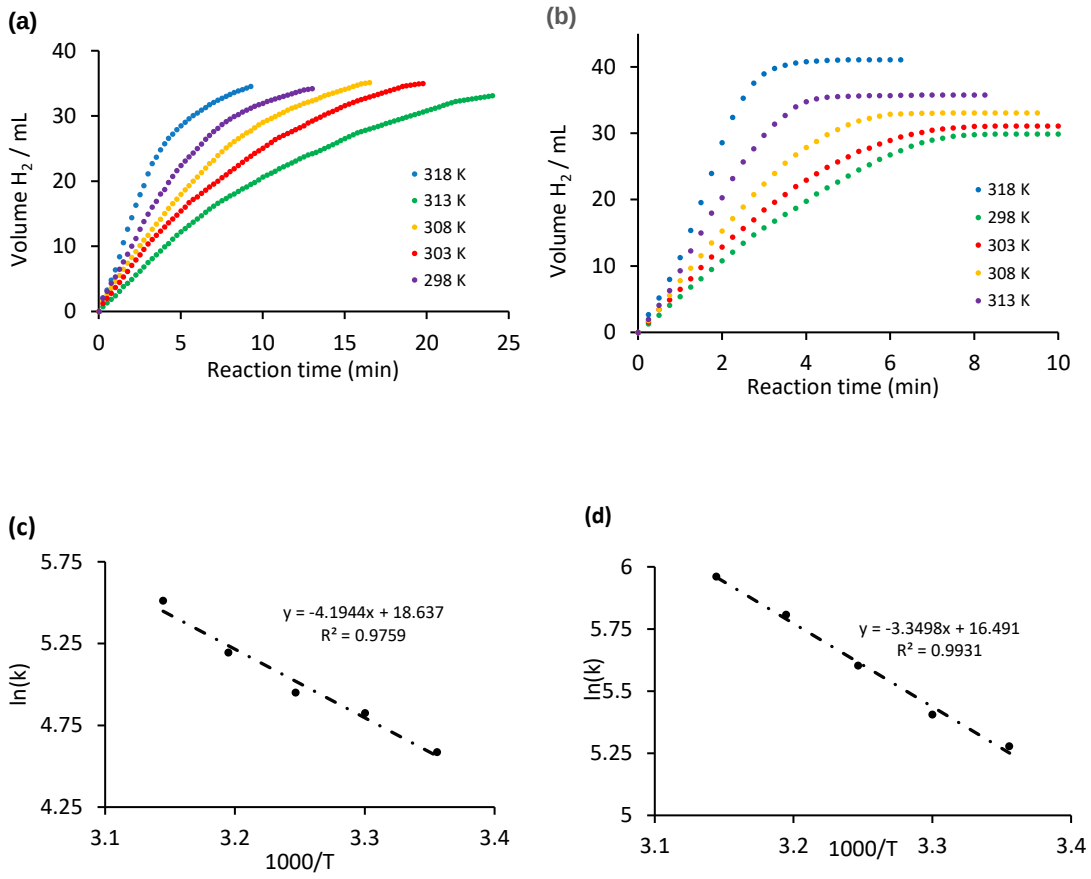

Figure 4.16: Plots of the volume of hydrogen generated against reaction time for the hydrolysis of 2 mL of a 0.27 M solution of (AB) across a range of temperatures 298- 318 K catalysed by 0.25 mol% (a) **4.3** and (b) **4.4**, (c) and (d) the corresponding Arrhenius plots for the hydrolysis of AB catalysed by **4.3** and **4.4**, respectively.

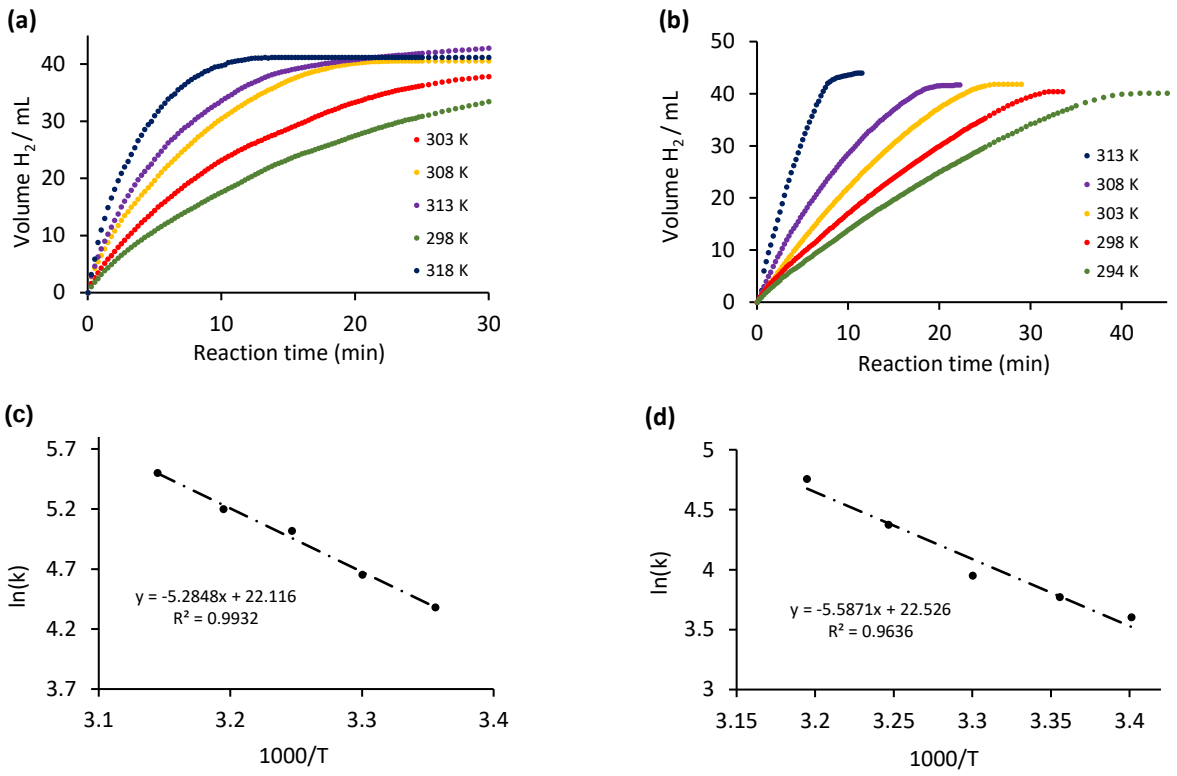

Figure 4.17: Plots of the volume of hydrogen generated against reaction time for the hydrolysis of 2 mL of a 0.27 M solution of $NaBH_4$ across a range of temperatures catalysed by 0.25 mol% (a) **4.3** and (b) **4.4**, (c) and (d) the corresponding Arrhenius plots for the hydrolysis of $NaBH_4$ catalysed by **4.3** and **4.4**, respectively.

4.2.3.2 Determination of the Reaction Order for the Catalytic Hydrolysis of DMAB, AB and $NaBH_4$.

The release of hydrogen through the hydrolysis of DMAB was further studied by examining its activity at various concentrations of **4.3** and **4.4** at a temperature of 30 °C in a solution containing 0.27 M DMAB.

Plotting the logarithm of the hydrogen generation rate against the catalyst concentration resulted in linear plot, with **4.3** having a slope of 1.04 and **4.4** having a slope of 0.96. This confirms that the hydrolysis of DMAB follows first-order kinetics for both catalysts (Figure 4.18 c-d).

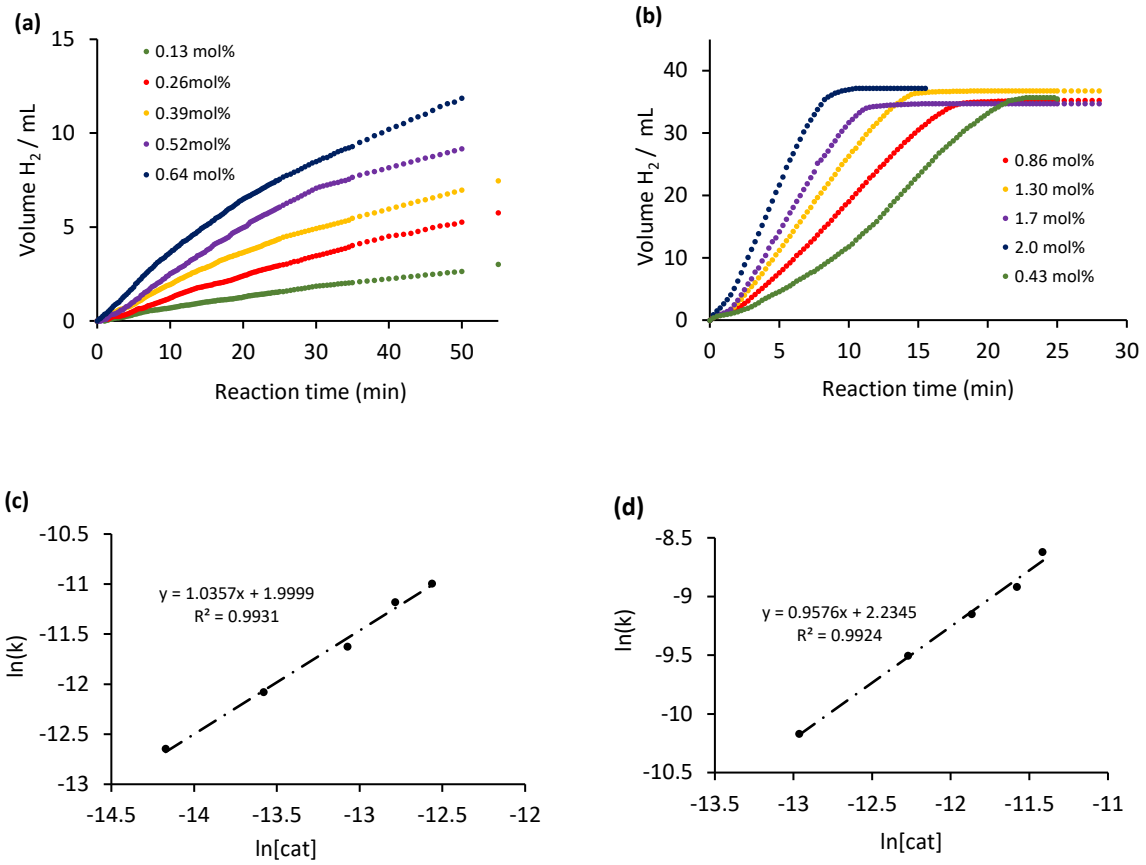

Figure 4.18: (a) and (b) Plots of volume of hydrogen generated as a function of time for the hydrolysis of 2 mL of a 0.27 M solution of DMAB at 303 K catalysed by various concentrations of **4.3** and **4.4**, respectively; (c) and (d) plots of initial hydrogen generation rate versus concentration of catalyst in logarithmic scale for **4.3** and **4.4**, respectively. The initial rates (*k*) were determined from the slopes of the fitted lines.

In the same way, corresponding experiments for the hydrolysis of AB using different concentrations of **4.3** and **4.4** gave slopes of 0.98 and 0.91, for the logarithmic plot of the rate of hydrogen production versus the concentration of the catalyst, confirming that the hydrolysis of AB is first order with respect to both catalysts (Figure 4.19).

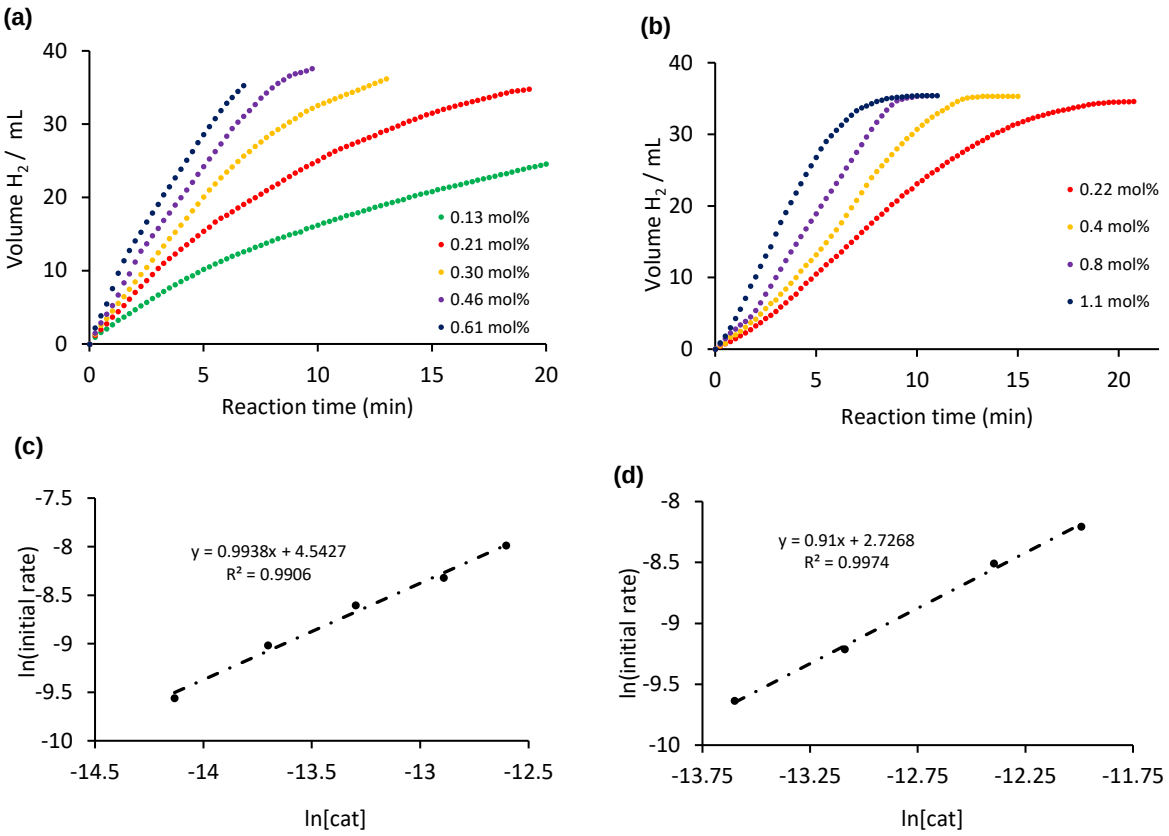

Figure 4.19: (a) and (b) Plots of volume of hydrogen generated as a function of time for the hydrolysis of 2 mL of a 0.27 M solution of ammonia borane (AB) at 303 K catalysed by various concentrations of **4.3** and **4.4**, respectively; (c) and (d) plots of initial hydrogen generation rate versus concentration of catalyst in logarithmic scale for **4.3** and **4.4**, respectively.

Recently published literature indicated this data is consistent with other studies on the use of noble metal nanoparticles to catalyse the hydrolysis of DMAB and AB. Previous reports include slopes of 1.08 for ceria-supported RuNPs,[8] 1.03 for RuNPs loaded on cellulose,[9] 0.86 for RuNP stabilised by a graphene oxide-PVP hybrid support,[58] 1.01 for RuCu alloy NPs immobilised on reduced graphene oxide,[60] 0.98 for RuPd@GO, and 1.04 for RuNiPd nanoclusters immobilized on horse chestnut seed.[66] In addition, when studying the hydrolysis of a 0.27 M solution of sodium borohydride with respect to the concentration **of 4.3** and **4.4**, similar linear plots were obtained for the logarithm plot of the initial hydrogen generation rate against catalyst loading, with slopes of 1.07 and 0.99, respectively. These slopes once again indicate first-order kinetics (Figure 4.20).

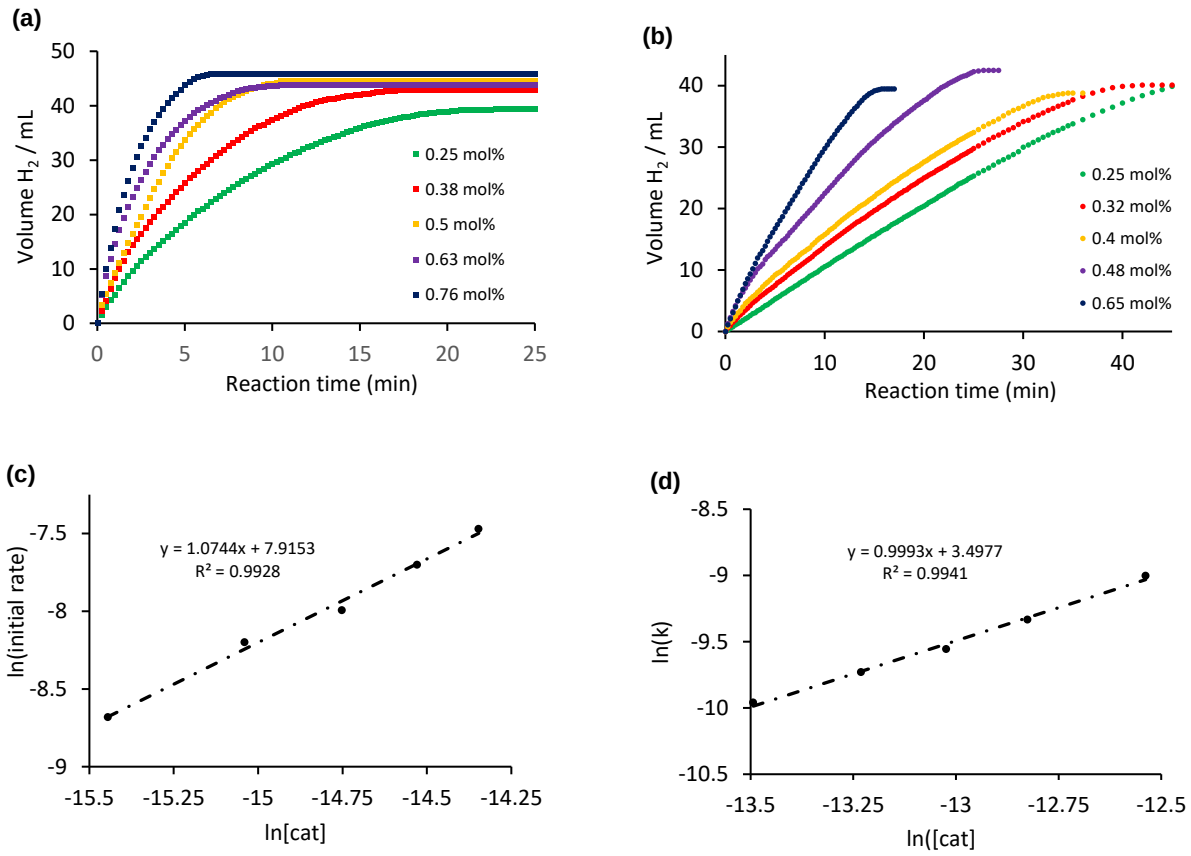

Figure 4.20: (a) and (b) Plots of volume of hydrogen generated as a function of time for the catalytic hydrolysis of 2 mL of a 0.27 M solution of $NaBH_4$ at 303 K across a range of concentrations of **4.3** and **4.4**, respectively; (c) and (d) plots of initial hydrogen generation rate versus concentration of catalyst in logarithmic scale for **4.3** and **4.4**, respectively.

4.2.3.3 Kinetic study as a function of DMAB, AB and $NaBH_4$ concentration.

An investigation into how the initial substrate concentration affects the rate of DMAB hydrolysis was conducted using 17 µmol of **4.3** and **4.4** and varying the initial concentration of DMAB ($[DMAB]_0$ = 0.085 mM to 0.51 mM) to obtain kinetic data across catalyst/substrate ratios from 1:1 to 1:5 (Figure 4.21). These low catalyst-to-substrate mole ratios were employed to prevent the saturation of surface-active sites, which would result in zero-order kinetics. The graph of hydrogen volume produced over time for each substrate concentration (Figure 4.21 a-b) was used to determine the initial rates. The corresponding logarithmic plots of the initial hydrogen generation rate against DMAB concentration showed slopes of 0.99 and 1.12 for **4.3** and **4.4**, respectively, confirming that the hydrolysis follows first-order

kinetics with respect to the substrate and that the activation of DMAB is integral to the rate-limiting step (Figure 4.21 c-d).

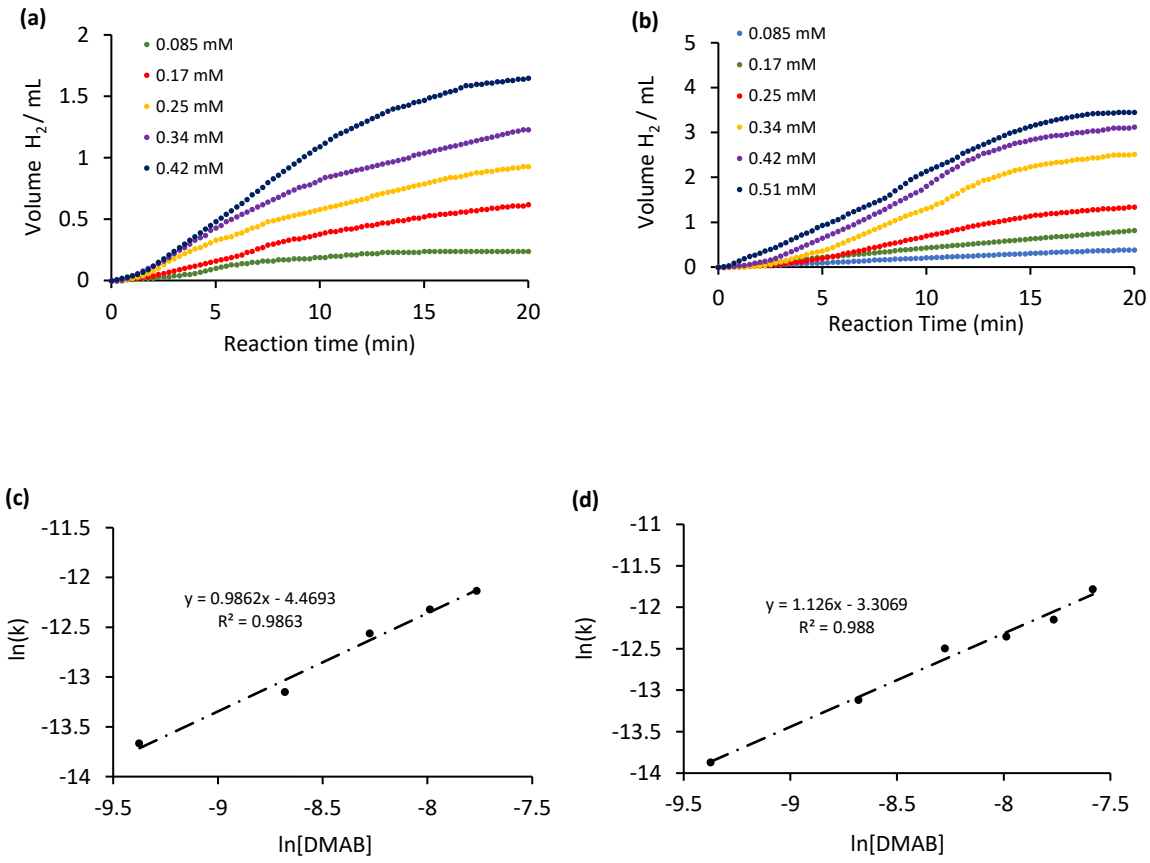

Figure 4.21: (a-b) Plots of volume of hydrogen liberated against time for the hydrolytic dehydrogenation of DMAB at 303 K catalysed by **4.3** and **4.4** (17 µmol) in water (200 mL), initial concentrations of DMAB ($[DMAB]_0$ = 0.085, 0.17, 0.25, 0.34, 0.42, 0.51 mM); (c-d) the corresponding plots of the initial hydrogen generation rate against initial concentration of DMAB in logarithmic scale. The initial rates (k) were determined from the slopes of the fitted lines.

The hydrolysis of DMAB or ethylenediamine bisborane has been reported to exhibit first-order kinetics when using RuNPs supported on graphene oxid,[58] cellulose,[9] 2-hydroxyethyl starch-p-(2-acrylamide-2-methyl-1-propanesulfonic acid) hydrogel network,[11] monodisperse graphite,[59] a graphene oxide PVP hybrid,[58] and oleylamine.[67] This phenomenon has also been reported with PtRu nanocatalysts supported on Vulcan carbon,[23] graphene oxide stabilised PdCoNPs,[22] monodispersed palladium-ruthenium alloy nanoparticles assembled on PVP,[20] silica-based gold-nickel nanohybrid,[65] and a MOF adorned with monodisperse palladium-cobalt nanohybrids.[26] Similar kinetics have been observed with RuCu nanomaterials on

reduced graphene oxide.[60] The study examining the kinetics of hydrolysis of AB as a function of the substrate concentration produced linear plots for the logarithm of the initial hydrogen generation rate versus AB concentration with slopes of 1.08 and 1.03 for **4.3** and **4.4**, respectively, indicating that the rate-limiting step involves activation of the AB (Figure 4.22). While some reports have suggested first-order kinetics for AB hydrolysis,[68] most studies indicate that the hydrolysis of AB is independent of substrate concentration, suggesting that AB activation is not integral to the rate determining step. In such cases, the rate-limiting step is proposed to involve the activation of an O–H bond of water, potentially facilitated by a hydrogen bonding interaction between a hydrogen atom of water and either a hydridic B-H bond of a surface coordinated AB[69,70] or a hydridic NP-H.[71]

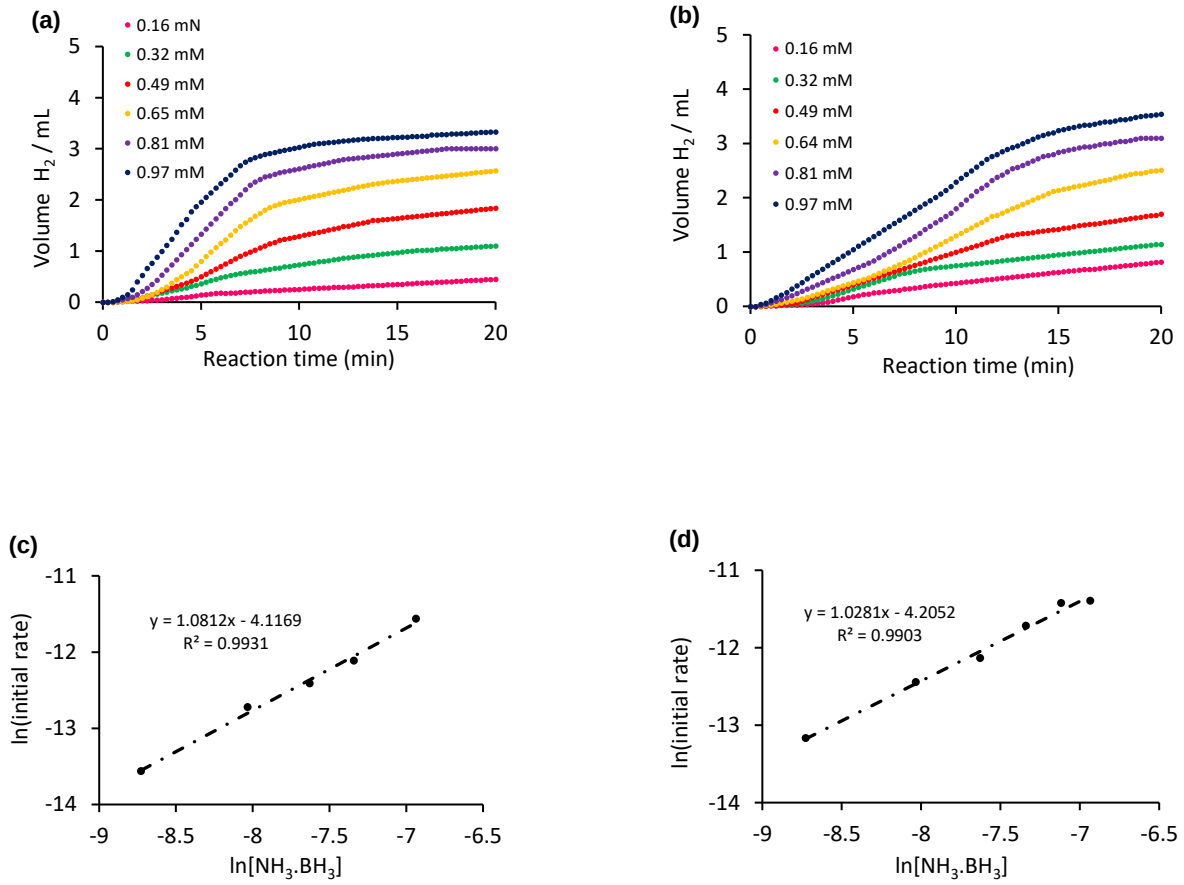

Figure 4.22: (a-b) Plots of volume of hydrogen liberated against time for the hydrolytic dehydrogenation of ammonia borane (AB) at 303 K catalysed by **4.3** and **4.4** (32 *m*mol) in water (200 mL), initial concentrations of AB ($[DMAB]_0$ = 0.16, 0.32, 0.49, 0.65, 0.81, 0.97 mM); (c-d) the corresponding plots of the initial hydrogen rate against initial concentration of AB in logarithmic scale.

Under identical conditions, the corresponding kinetic investigation involving the hydrolytic dehydrogenation of $NaBH_4$ utilising 26 μmol of **4.3** and **4.4** and adjusting the initial concentration of $NaBH_4$ to correspond to catalyst:substrate ratios from 1:1 to 1:6, resulted in slopes of 1.01 and 0.97 for **4.3** and **4.4**, respectively, for the logarithmic plot of the initial hydrogen production rate versus $NaBH_4$ concentration. This implies that the hydrolysis is first-order with respect to $NaBH_4$ (Figure 4.23).

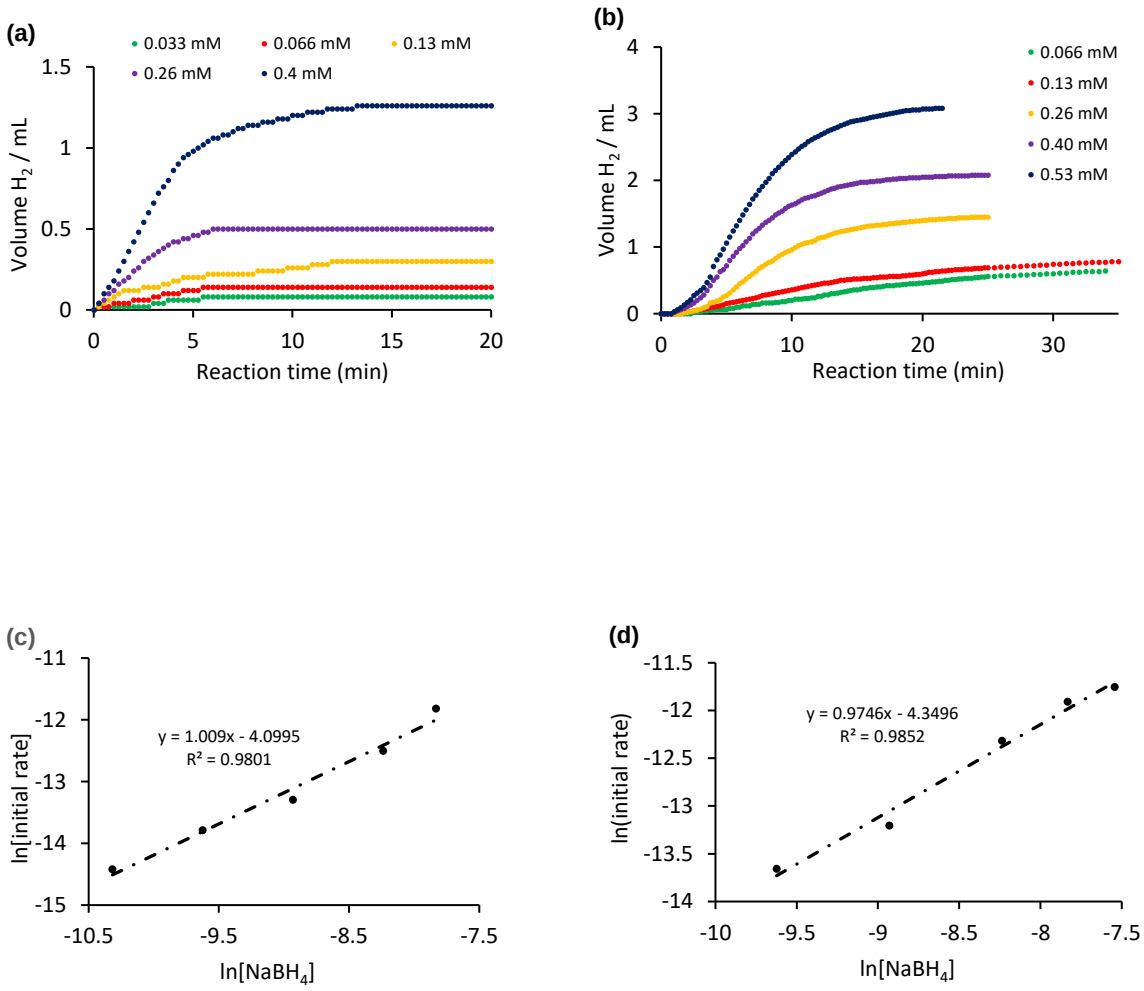

Figure 4.23: (a-b) Plots of volume of hydrogen liberated against time for the hydrolytic dehydrogenation of $NaBH_4$ at 303 K catalysed by **4.3** and **4.4** (26 *m*mol) in water (200 mL), initial concentrations of $NaBH_4$ ($[NaBH_4]_0$ = 0.033, 0.066, 0.13, 0.26, 0.40, 0.53 mM); (c-d) the corresponding plots of the initial hydrogen rate against initial concentration of $NaBH_4$ in logarithmic scale.

4.2.4 Kinetic Studies

Studies on the kinetic isotope effect have proven to be valuable in providing insights into the crucial rate-limiting step (RLS) for the nanoparticle catalysed hydrolytic release of hydrogen from ammonia borane and sodium borohydride. Several mechanistic scenarios have been suggested for the hydrolysis of ammonia boranes, including:

1) Rate limiting formation of an activated surface coordinated ammonia borane followed by the attack of water to break the B-N bond and the hydrolysis of the BH_3.[72]

2) Formation of BH_3OHNH_4 by attack of water held proximal to a surface coordinated AB.[73]

3) Activation of surface-bound ammonia borane by water with dissociation of the B-N bond, followed by the release of H_2 through attack of water on a transient hydridic NP-H similar to the metal-catalysed hydrolysis of $NaBH_4$.[74]

4) Activation of one of the O–H bonds of water in a hydrogen-bonded arrangement that includes a hydridic B-H bond of a surface-bound ammonia borane and a water proton.[69,70]

The functions of ammonia borane and $NaBH_4$ are to act as sources of hydride and to provide a hydrogen atom to the resulting hydrogen. At the same time, the water supplies the other as a proton. To investigate the role of water in the hydrolysis of DMAB catalysed by **4.3** and **4.4**, reactions were carried out in H_2O and D_2O, and the amount of liberated hydrogen was monitored over time to compare the initial rates and determine the KIE.

Reactions were conducted under the same conditions described above using 0.25 mol% **4.3** and **4.4** to catalyse the hydrolysis of a 0.27 M solution of DMAB at 303 K. A comparison of the initial rates of hydrolysis of DMAB in H_2O and D_2O catalysed by **4.3** and **4.4** showed that reactions were faster in H_2O than in D_2O with primary kinetic isotope effects (k_H/k_D) of 2.5 and 3.8, respectively, (Figure 4.24 a-b); similar values of k_H/k_D were also obtained for the catalytic hydrolysis of a 0.27 M solution of AB in H_2O and D_2O using 0.25 mol% **4.3** (k_H/k_D = 2.6) and **4.4** (k_H/k_D = 4.0) and the associated data is presented in Figure 4.25. In contrast, the hydrolysis of 0.27 M $NaBH_4$ in H_2O and D_2O is presented in Figure 4.26.

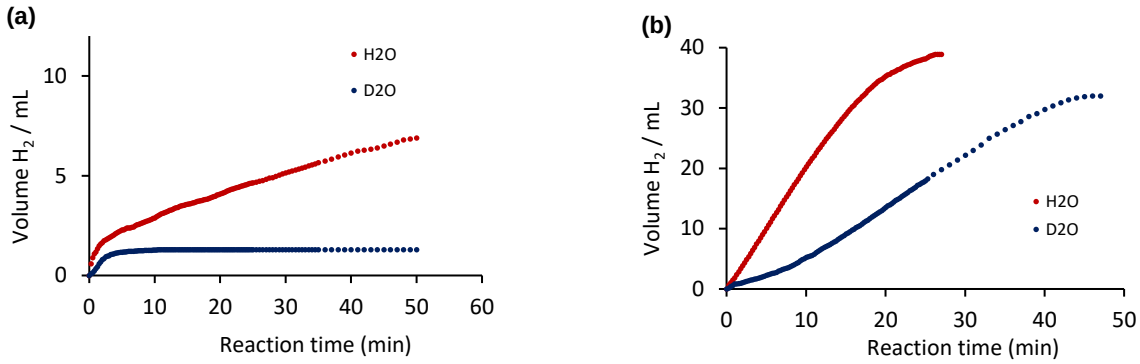

Figure 4.24: Hydrogen evolution from 2 mL of a 0.27 M solution of DMAB in H_2O (red) and D_2O (blue) at 303 K catalysed by 0.25 mol% (a) **4.3** and (b) **4.4**.

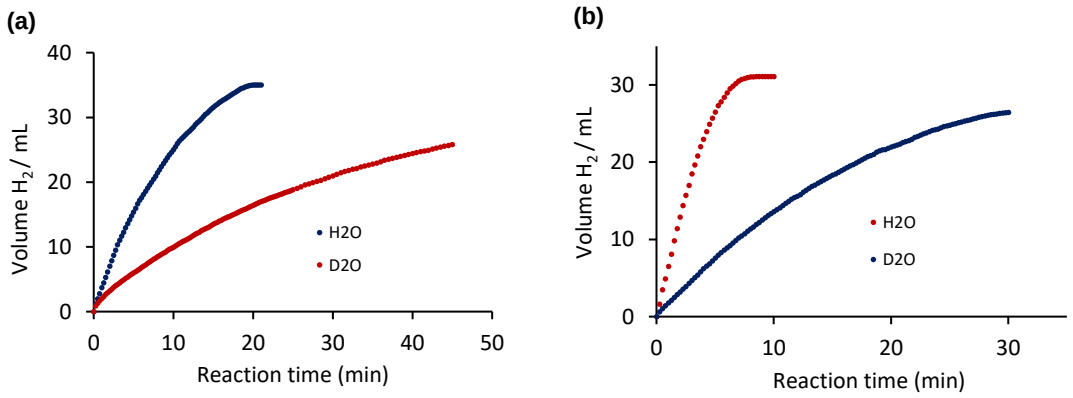

Figure 4.25: Hydrogen evolution from 2 mL of a 0.27 M solution of ammonia borane (AB) in H_2O (red) and D_2O (blue) at 303 K catalysed by 0.25 mol% (a) **4.3** and (b) **4.4**.

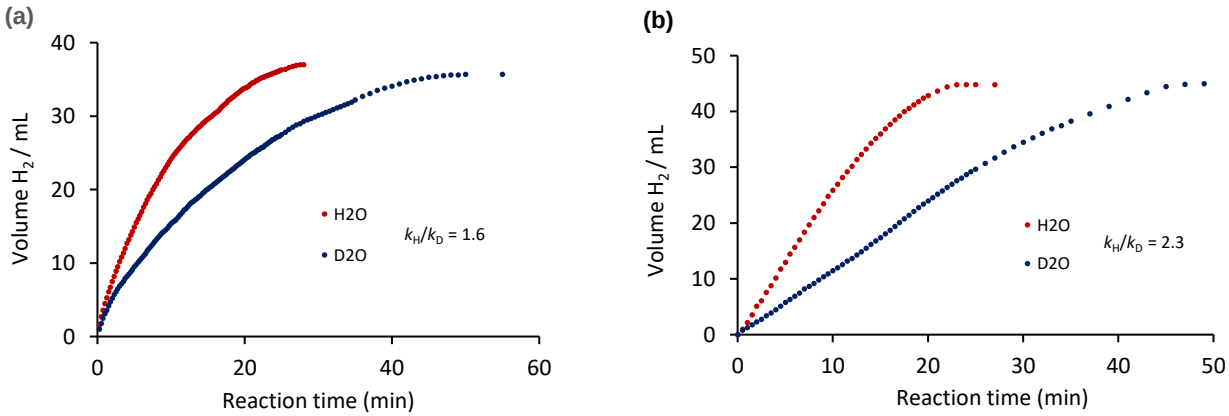

Figure 4.26: Hydrogen evolution from 2 mL of a 0.27 M solution of $NaBH_4$ in H_2O (red) and D_2O (blue) at 303 K catalysed by 0.25 mol% (a) **4.3** and (b) **4.4**.

The KIE values mentioned are similar to the value of 4.95 reported for the Ni_2Pt@ZIF-8-catalysed hydrolysis of ammonia borane,[51] as well as atomically dispersed platinum on the surface of Ni particles (k_H/k_D = 4.0),[75] CoNPs supported on a covalent triazene framework (k_H/k_D = 2.8),[76] ultrasmall Pt nanoclusters on heterostructured NiO/Ni (k_H/k_D = 2.8),[77] and CoPt nanocatalysts encapsulated in click dendrimer (k_H/k_D = 2.46).[78]

Suggesting a mechanism in which one of the O–H (or O-D) bonds of water is activated in the rate-determining step, possibly by hydrogen bonding to one of the hydridic hydrogen atoms of DMAB. Although these KIE values are in line with previously reported mechanisms in which a surface-coordinated hydrogen bonded ensemble such as Me_2NH-BH_2-H——H—OH, which involves a hydridic B-H hydrogen and a water proton, activates an O–H bond towards oxidative addition to produce a water-derived M-H and a surface-coordinated DMAB, as illustrated in Figure 4.27, they do not differentiate between oxidative addition of an O–H bond combined with concerted hydride transfer from DMAB (Figure 4.27 path a) and double oxidative addition of O–H and B-H bonds (Figure 4.27 path c).

The former pathway would release the hydrogen through the reductive elimination of a water-derived M-H and a DMAB-derived M-H and liberate NMe_2HBH_2-OH as an intermediate through electrophilic abstraction of a surface-coordinated M-OH by the $[NMe_2HBH_2]^+$ cation (Figure 4.27 path b). In contrast, the second pathway would release hydrogen and Me_2HBH_2-OH through reductive elimination (Figure 4.27, path d). The other two B-H bonds in the boron intermediate with a single hydroxyl group would then undergo a similar activation process, leading to the eventual formation of $[NMe_2H]_2[BO_2]$.

The pathways mentioned above are set in motion by the slow step of breaking the O–H bond of water in a cooperative surface-coordinated hydrogen-bonded arrangement. It is important to note that there is a chance that an O–H bond could be activated by the hydrogen bonding between a surface-adsorbed water and a transient metal hydride derived from DMAB. Jagidar has described this in the context of the copper and Cu@Cu_2O core-shell nanoparticle catalysed hydrolysis of sodium borohydride,[74] as well as by Guella for the palladium-catalysed hydrolysis of $NaBH_4$.[79] Alternatively, the hydrogen may be liberated via rate-limiting activation of an O–H bond in water followed by a concerted σ-bond metathesis-type process between the

resulting water-derived M-H and the σ-bonded B-H of a surface-coordinated DMAB (Figure 4.27 path e–f).

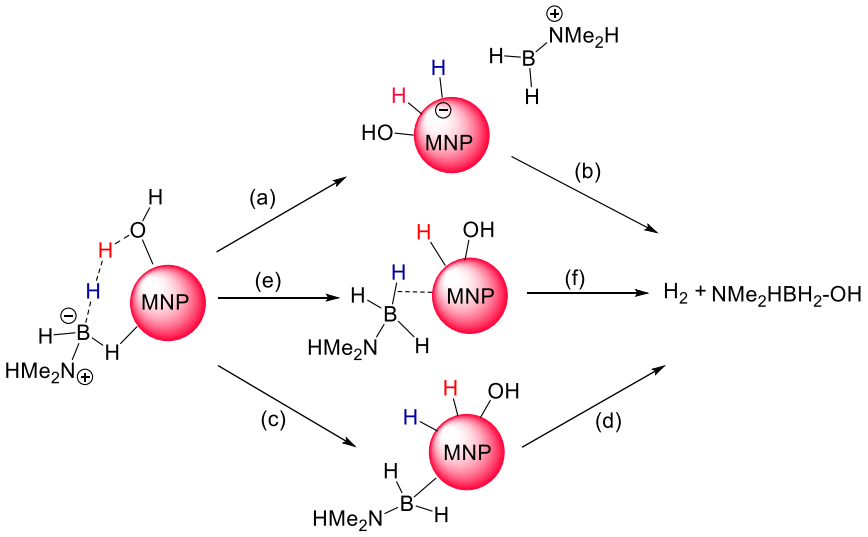

Figure 4.27: Proposed pathways for the metal nanoparticle catalysed hydrolytic evolution of hydrogen from the hydrogen-bonded ensemble Me_2NH-BH_2-H------H----OH.

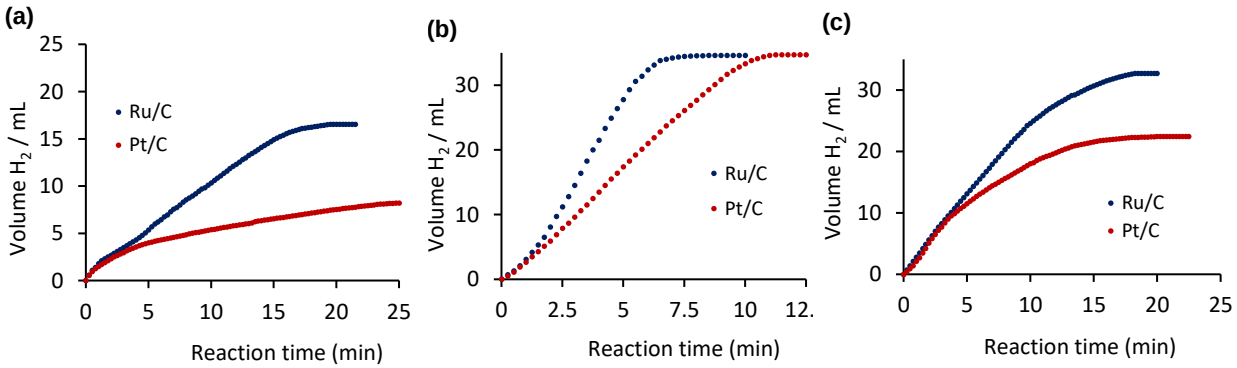

Figure 4.28: (a) Hydrolytic release of hydrogen from a 0.27 M solution of DMAB as a function of time at 313 K catalysed by 0.25 mol% Pt/C (5 wt%) and Ru/C (5 wt%), (b) hydrolytic release of hydrogen from a 0.27 M solution of AB as a function of time at 303 K catalysed by 0.25 mol% Pt/C (5 wt%) and Ru/C (5 wt%), (c) hydrolytic release of hydrogen from a 0.27 M solution of $NaBH_4$ as a function of time at 303 K catalysed by 0.25 mol% Pt/C (5 wt%) and Ru/C (5 wt%).

4.2.5 Catalyst Recycle and Hot Filtration Studies

Recycle studies were conducted at 303 K as described above using 2 mol% **4.4** to catalyse the hydrolysis of 20 mL of a 0.027 M solution of dimethylamine borane to assess the activity profile as a function of reuse and thereby determine its longevity and potential for integration into a flow-based system. After gas evolution had ceased, the flask was recharged with a fresh portion of dimethylamine borane and the gas evolution was monitored by recording the volume of water displaced from the burette at regular time intervals; this procedure was repeated 5 times. After the 5th run, a sample of **4.4** was isolated and analysed by TEM-EDX to explore the extent of boron fouling.

The data resulting in Figure 4.29a displays the time profile for hydrogen evolution as a function of the run number. The initial turnover frequencies (TOFs) depicted in Figure 4.29b were calculated based on the first 3 minutes of the hydrolysis to be able to reliably compare the initial rates across consecutive runs. Although high conversions were achieved in five successive uses (84–88%), the initial TOF rose from 505 h^{-1} in the first run to 781 h^{-1} in the second run and then remained relatively stable in subsequent runs. The catalyst retained 97% of its initial activity over the next 4 runs.

The elevated activity observed during the first run may be attributed to either reduction of surface ruthenium oxide species increasing the number of active sites or a structural modification. Reliable conversions and consistent activity patterns during repeated use have also been documented for the catalytic hydrolytic evolution of hydrogen from DMAB using supported nanoparticles, including ultrafine RuNPs anchored on porous g-C_3N_4,[80] cellulose,[60] PVP,[10] and Amberlyst-15,[68,80] as well as nickel-polymer nanogel hybrid particles.[64] Monodisperse RuCu alloy nanoparticles stabilised by reduced graphene oxide also showed a stable activity profile while ceria-supported RuNPs,[8] PVP-supported Ru and RuNi nanoparticles,[61,81] and monodisperse PdNPs, along with bimetallic PdCo and PdRu nanoparticles anchored on graphene oxide,[20] all displayed a substantial decrease in activity after four or five reuses.

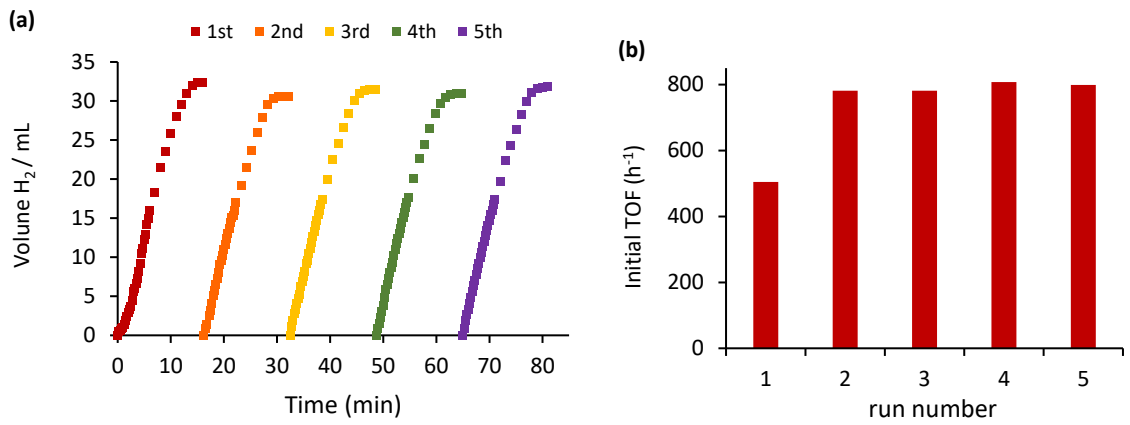

Figure 4.29: (a) The plot of the volume of hydrogen liberated against time for the hydrolysis of a 0.027 M solution of DMAB catalysed by 2 mol% **4.4** at 303 K to map catalyst performance during a reusability study across 5 runs; (b) initial TOF in $mole_{H2}.mol_{Ru}^{-1}.h^{-1}$ for each run. Volumes are an average of three runs. *Conditions:* 0.54 mmol DMAB (0.032 g), 2 mol% **4.4** (0.0149 g, 0.0103 mmol), water (20 mL), 303 K.

A hot filtration study was carried out at 303 K to explore the heterogeneous nature of the catalyst according to the previously described procedure, employing 0.25 mol% of **4.4** to catalyse the hydrolysis of 0.27 M dimethylamine borane. The progress of the reaction was monitored by periodically measuring the gas produced. Once the reaction had approximately reached 50% conversion (4 min), the reaction mixture was rapidly filtered through a 0.45 µm syringe filter, and the gas produced was observed for an additional 30 minutes. In a parallel experiment, 0.25 mol% of **4.4** was used to catalyse the complete hydrolysis of 0.27 M solution of DMAB. Following the completion of the reaction, the mixture was filtered through a 0.45 µm syringe filter, a fresh portion of DMAB was added, and the gas evolution was monitored.

Observations from (Figure 4.30a) confirm that there was no apparent gas release after filtration, suggesting that the effective ruthenium components had been removed during the filtration process.

Furthermore, examination of the liquid phase collected after the hot filtration indicated that the amount of ruthenium present was undetectable by the ICP-OES (<0.1 mg L^{-1}), suggesting

that leaching of the ruthenium to form inactive or less active species is unlikely. However, these tests cannot distinguish between heterogeneous catalysis at defect sites on the NP surface and homogeneous catalysis through rapid leaching and re-deposition.

Lastly, TEM analysis of the catalyst recovered after the fifth cycle of the reuse experiment indicated that the ruthenium nanoparticles remained nearly monodisperse in size with an average diameter of 1.65 ± 0.3 nm, which is similar to the 1.60 ± 0.3 nm size of a freshly prepared sample of **4.4**, confirming that agglomeration does not occur and that leaching and re-deposition are unlikely, as this would likely cause a perceptible change in the size and/or distribution of the NPs (Figure 4.30 b-d).

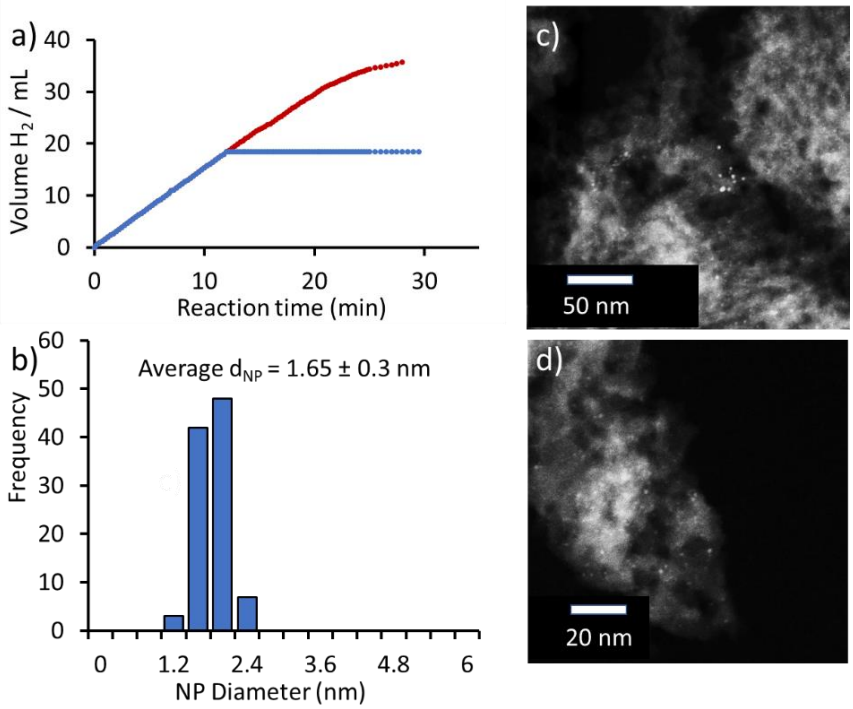

Figure 4.30: (a) Hot filtration test for the hydrolysis of a 0.27 M solution of DMAB using 0.25 mol% **4.4** showing that the activity has been fully quenched after filtering at t = 12 min. Red line – reaction in the presence of catalyst; blue line – reaction catalysed by **4.4** and filtered at t = 12 min. (b) Sizing histogram of RuNPs for **4.4** after 5 hydrolysis cycles. (c-d) TEM images of the material.

4.3 Conclusion

This study aimed to investigate the efficacy of amino-modified PIIL stabilised platinum and ruthenium nanoparticles as catalysts for the hydrolytic evolution of hydrogen from DMAB, AB and $NaBH_4$ in a systematically comparative manner. Although the RuNP@NH_2-PEGPIILS catalyst is significantly more active than its platinum counterpart for the hydrolysis of DMAB and AB, both catalysts gave comparable initial TOFs and conversions for the hydrolysis of $NaBH_4$.

In the hydrolysis of DMAB and AB using RuNP@NH_2-PEGPIILS as the catalyst, the apparent activation energies of 55.7 kJ mol^{-1} and 27.9 kJ mol^{-1} are significantly lower than those 74.6 kJ mol^{-1} and 35.7 kJ mol^{-1}, respectively, for its platinum counterpart which is consistent with the significantly higher initial TOFs for both substrates when using RuNPs. Kinetic studies revealed that the hydrolysis of DMAB, AB and $NaBH_4$ are all first order in both the catalyst and substrate.

A further interesting point is that activation energies for the hydrolysis of AB are significantly lower than the activation energies for the hydrolysis of DMAB, which is consistent with the significantly faster rates of hydrogen evolution from the former. When compared with DMAB and AB, both catalysts gave comparable initial rates for the hydrolysis of $NaBH_4$, which could be explained by the similarity of their apparent activation energies.

Future studies should extend this project to explore the influence of various factors such as the type of amine its loading, the ionic environment, porosity, and hydrophilicity on catalyst efficacy. The modular construction of the PIIL support allows for easy modification, and our group are currently working on catalyst modifications in *operando* surface investigations, kinetic studies, and the synthesis of multimetallic nanoparticles to gain a more detailed understanding of this system and to identify more active catalysts for scale-up. We are confident that these efforts will lead to the development of more efficient and effective catalysts for large-scale chemical reactions.

4.4 References

1. P. Nejat, F. Jomehzadeh, M. M. Taheri, M. Gohari and M. Z. Abd. Majid, *Renew. Sustain. Energy Rev.*, 2015, **43**, 843–862.
2. L. Schlapbach and A. Züttel, *Nature*, 2001, **414**, 353–358.
3. Z. Abdin, A. Zafaranloo, A. Rafiee, W. Mérida, W. Lipiński and K. R. Khalilpour, *Renew. Sustain. Energy Rev.*, 2020, **120**, 109620.
4. E. Rivard, M. Trudeau and K. Zaghib, *Materials*, 2019, **12**, 1973.
5. Q. Sun, N. Wang, Q. Xu and J. Yu, *Adv. Mater.*, 2020, **32**, 2001818.
6. C. Yüksel Alpaydın, S. K. Gülbay and C. Ozgur Colpan, *Int. J. Hydrog. Energy*, 2020, **45**, 3414–3434.
7. Q. Zhang, F. Xu, W. Huang, Y. Wang and X. Liu, *Fuel*, 2022, **324**, 124695.
8. S. Karaboga and S. Özkar, *Int. J. Hydrog. Energy*, 2019, **44**, 26296–26307.
9. D. Ozhava and S. Duman, *ChemCatChem*, 2023, **15**, e202201563.
10. B. Bukan and S. Duman, *Int. J. Hydrog. Energy*, 2018, **43**, 8278–8289.
11. H. Ozay, P. Ilgin, M. K. Sezgintürk and O. Ozay, *Int. J. Hydrog. Energy*, 2020, **45**, 9892–9902.
12. A. Friedrich, M. Drees and S. Schneider, *Chem. – Eur. J.*, 2009, **15**, 10339–10342.
13. M. E. Sloan, A. Staubitz, T. J. Clark, C. A. Russell, G. C. Lloyd-Jones and I. Manners, *J. Am. Chem. Soc.*, 2010, **132**, 3831–3841.
14. D. Astruc, F. Lu and J. R. Aranzaes, *Angew. Chem. Int. Ed.*, 2005, **44**, 7852–7872.
15. F. Chen, X. Jiang, L. Zhang, R. Lang and B. Qiao, *Chin. J. Catal.*, 2018, **39**, 893–898.
16. D. Astruc, F. Lu and J. R. Aranzaes, *Angew. Chem. Int. Ed.*, 2005, **44**, 7852–7872.
17. X.-F. Yang, A. Wang, B. Qiao, J. Li, J. Liu and T. Zhang, *Acc. Chem. Res.*, 2013, **46**, 1740–1748.
18. G. Schmid, *Nanoparticles: From Theory to Application*, John Wiley & Sons, 2011.
19. C. Gao, F. Lyu and Y. Yin, *Chem. Rev.*, 2021, **121**, 834–881.
20. B. Sen, A. Aygün, M. Ferdi Fellah, M. Harbi Calimli and F. Sen, *J. Colloid Interface Sci.*, 2019, **546**, 83–91.
21. L. Fisher, *RSC Adv.*, 2021, **11**, 32905–32905.

22. B. Şen, A. Aygün, A. Şavk, M. H. Çalımlı, S. K. Gülbay and F. Şen, *Int. J. Hydrog. Energy*, 2020, **45**, 3569–3576.

23. Y. Karatas, H. Acidereli, M. Gulcan and F. Sen, *Sci. Rep.*, 2020, **10**, 7149.

24. S. Tanyildizi, İ. Morkan and S. Özkar, *ChemistrySelect*, 2017, **2**, 5751–5759.

25. M. Yurderi, A. Bulut, M. Zahmakiran, M. Gülcan and S. Özkar, *Appl. Catal. B Environ.*, 2014, **160–161**, 534–541.

26. B. Şen, A. Aygün, A. Şavk, C. Yenikaya, S. Cevik and F. Şen, *Int. J. Hydrog. Energy*, 2019, **44**, 2988–2996.

27. S. Caliskan, M. Zahmakiran, F. Durap and S. Özkar, *Dalton Trans.*, 2012, **41**, 4976–4984.

28. B. Sen, S. Kuzu, E. Demir, S. Akocak and F. Sen, *Int. J. Hydrog. Energy*, 2017, **42**, 23292–23298.

29. G. Lu, S. Li, Z. Guo, O. K. Farha, B. G. Hauser, X. Qi, Y. Wang, X. Wang, S. Han, X. Liu, J. S. DuChene, H. Zhang, Q. Zhang, X. Chen, J. Ma, S. C. J. Loo, W. D. Wei, Y. Yang, J. T. Hupp and F. Huo, *Nat. Chem.*, 2012, **4**, 310–316.

30. X. Wang, Y.-F. Jiang, Y.-N. Liu and A.-W. Xu, *New J. Chem.*, 2018, **42**, 19901–19907.

31. L. Lu, S. Zou and B. Fang, *ACS Catal.*, 2021, **11**, 6020–6058.

32. C. Janiak, *Z. Für Naturforschung B*, 2013, **68**, 1059–1089.

33. S. Lau, D. Gasperini and R. L. Webster, *Angew. Chem. Int. Ed.*, 2021, **60**, 14272–14294.

34. D. Kundu, G. Pugazhenthi and T. Banerjee, *Energy Fuels*, 2020, **34**, 13167–13178.

35. F. Giacalone and M. Gruttadauria, *ChemCatChem*, 2016, **8**, 664–684.

36. A. Wolny and A. Chrobok, *Molecules*, 2022, **27**, 5900.

37. S. Karimi, M. Gholinejad, R. Khezri, J. M. Sansano, C. Nájera and M. Yus, *RSC Adv.*, 2023, **13**, 8101–8113.

38. Y. Gong, H. Zhong, W. Liu, B. Zhang, S. Hu and R. Wang, *ACS Appl. Mater. Interfaces*, 2018, **10**, 776–786.

39. V. B. Saptal, T. Sasaki and B. M. Bhanage, *ChemCatChem*, 2018, **10**, 2593–2600.

40. R. Paterson, L. E. Fahy, E. Arca, C. Dixon, C. Y. Wills, H. Yan, A. Griffiths, S. M. Collins, K. Wu, R. A. Bourne, T. W. Chamberlain, J. G. Knight and S. Doherty, *Chem. Commun.*, 2023, **59**, 13470–13473.

41. R. Paterson, A. A. Alharbi, C. Wills, C. Dixon, L. Šiller, T. W. Chamberlain, A. Griffiths, S. M. Collins, K. Wu, M. D. Simmons, R. A. Bourne, K. R. J. Lovelock, J. Seymour, J. G. Knight and S. Doherty, *Mol. Catal.*, 2022, **528**, 112476.

42. S. Doherty, J. G. Knight, H. Y. Alharbi, R. Paterson, C. Wills, C. Dixon, L. Šiller, T. W. Chamberlain, A. Griffiths, S. M. Collins, K. Wu, M. D. Simmons, R. A. Bourne, K. R. J. Lovelock and J. Seymour, *ChemCatChem*, 2022, **14**, e202101752.

43. A. A. Alharbi, C. Wills, T. W. Chamberlain, R. A. Bourne, A. Griffiths, S. M. Collins, K. Wu, P. Mueller, J. G. Knight and S. Doherty, *ChemCatChem*, 2023, **15**, e202300418.

44. G. Greczynski and L. Hultman, *Prog. Mater. Sci.*, 2020, **107**, 100591.

45. K. N. Han, C. A. Li, M.-P. N. Bui, X.-H. Pham, B. S. Kim, Y. H. Choa and G. H. Seong, *Sens. Actuators B Chem.*, 2012, **174**, 406–413.

46. R. Vakili, E. K. Gibson, S. Chansai, S. Xu, N. Al-Janabi, P. P. Wells, C. Hardacre, A. Walton and X. Fan, *ChemCatChem*, 2018, **10**, 4238–4242.

47. F. Xiao, X. Luo, X. Fu and Y. Zheng, *J. Phys. Chem. B*, 2013, **117**, 4893–4900.

48. E. Alwin, M. Zieliński, A. Suchora, I. Gulaczyk, Z. Piskuła and M. Pietrowski, *J. Mater. Sci.*, 2022, **57**, 15705–15721.

49. K. Klauke, I. Gruber, T.-O. Knedel, L. Schmolke, J. Barthel, H. Breitzke, G. Buntkowsky and C. Janiak, *Organometallics*, 2018, **37**, 298–308.

50. V. Alderucci, L. Pino, P. L. Antonucci, W. Roh, J. Cho, H. Kim, D. L. Cocke and V. Antonucci, *Mater. Chem. Phys.*, 1995, **41**, 9–14.

51. F. Fu, C. Wang, Q. Wang, A. M. Martinez-Villacorta, A. Escobar, H. Chong, X. Wang, S. Moya, L. Salmon, E. Fouquet, J. Ruiz and D. Astruc, *J. Am. Chem. Soc.*, 2018, **140**, 10034–10042.

52. J. R. Deka, D. Saikia, K.-S. Hsia, H.-M. Kao, Y.-C. Yang and C.-S. Chen, *Catalysts*, 2020, **10**, 267.

53. B. Cai, Y. Zhang, J. Feng, C. Huang, T. Ma and H. Pan, *Renew. Energy*, 2021, **177**, 652–662.

54. A. Aijaz, A. Karkamkar, Y. J. Choi, N. Tsumori, E. Rönnebro, T. Autrey, H. Shioyama and Q. Xu, *J. Am. Chem. Soc.*, 2012, **134**, 13926–13929.

55. B. Sen, S. Kuzu, E. Demir, S. Akocak and F. Sen, *Int. J. Hydrog. Energy*, 2017, **42**, 23284–23291.

56. M. A. Khalily, H. Eren, S. Akbayrak, H. H. Susapto, N. Biyikli, S. Özkar and M. O. Guler, *Angew. Chem. Int. Ed.*, 2016, **55**, 12257–12261.

57. K. Yang, L. Zhou, G. Yu, X. Xiong, M. Ye, Y. Li, D. Lu, Y. Pan, M. Chen, L. Zhang, D. Gao, Z. Wang, H. Liu and Q. Xia, *Int. J. Hydrog. Energy*, 2016, **41**, 6300–6309.

58. B. Şen, A. Aygün, A. Şavk, S. Duman, M. H. Calimli, E. Bulut and F. Şen, *J. Mol. Liq.*, , DOI:10.1016/j.molliq.2019.02.003.

59. B. Şen, B. Demirkan, A. Savk, R. Kartop, M. S. Nas, M. H. Alma, S. Sürdem and F. Şen, *J. Mol. Liq.*, 2018, **268**, 807–812.

60. B. Sen, E. Kuyuldar, A. Şavk, H. Calimli, S. Duman and F. Sen, *Int. J. Hydrog. Energy*, 2019, **44**, 10744–10751.

61. B. Sen, E. Kuyuldar, B. Demirkan, T. Onal Okyay, A. Şavk and F. Sen, *J. Colloid Interface Sci.*, 2018, **526**, 480–486.

62. R. N. E. Tiri, A. Aygün, S. K. Gülbay, F. Sen, C. K. Cheng, H. Jafarzadeh, A. Abouei Mehrizi and Y. Vasseghian, *Chem. Eng. Res. Des.*, 2022, **182**, 305–311.

63. B. Sen, B. Demirkan, A. Şavk, S. Karahan Gülbay and F. Sen, *Int. J. Hydrog. Energy*, 2018, **43**, 17984–17992.

64. H.-K. Cai, Z.-Y. Jiang, S. Xu, Y. Xu, P. Lu and J. Dong, *Polymers*, 2022, **14**, 4647.

65. O. Alptekin, B. Sen, A. Savk, U. Ercetin, S. D. Mustafov, M. F. Fellah and F. Sen, *Sci. Rep.*, 2020, **10**, 7215.

66. K. Ulutas, M. Alshawesh and S. Duman, *Int. J. Hydrog. Energy*, 2022, **47**, 38198–38218.

67. S. Duman and S. Özkar, *Int. J. Hydrog. Energy*, 2013, **38**, 10000–10011.

68. D. Ö. Özgür, T. Şimşek, G. Özkan, M. S. Akkuş and G. Özkan, *Int. J. Hydrog. Energy*, 2018, **43**, 10765–10772.

69. N. Kang, Q. Wang, R. Djeda, W. Wang, F. Fu, M. M. Moro, M. de los A. Ramirez, S. Moya, E. Coy, L. Salmon, J.-L. Pozzo and D. Astruc, *ACS Appl. Mater. Interfaces*, 2020, **12**, 53816–53826.

70. Q. Wang, F. Fu, A. Escobar, S. Moya, J. Ruiz and D. Astruc, *ChemCatChem*, 2018, **10**, 2673–2680.

71. H. Ma and C. Na, *ACS Catal.*, 2015, **5**, 1726–1735.

72. Q. Xu and M. Chandra, *J. Power Sources*, 2006, **163**, 364–370.

73. C.-Y. Peng, L. Kang, S. Cao, Y. Chen, Z.-S. Lin and W.-F. Fu, *Angew. Chem.*, 2015, **127**, 15951–15955.

74. S. Babu Kalidindi, U. Sanyal and B. R. Jagirdar, *Phys. Chem. Chem. Phys.*, 2008, **10**, 5870–5874.

75. Z. Li, T. He, D. Matsumura, S. Miao, A. Wu, L. Liu, G. Wu and P. Chen, *ACS Catal.*, 2017, **7**, 6762–6769.

76. Z. Li, T. He, L. Liu, W. Chen, M. Zhang, G. Wu and P. Chen, *Chem. Sci.*, 2017, **8**, 781–788.

77. X. Ren, H. Lv, S. Yang, Y. Wang, J. Li, R. Wei, D. Xu and B. Liu, *J. Phys. Chem. Lett.*, 2019, **10**, 7374–7382.

78. Q. Wang, F. Fu, S. Yang, M. Martinez Moro, M. de los A. Ramirez, S. Moya, L. Salmon, J. Ruiz and D. Astruc, *ACS Catal.*, 2019, **9**, 1110–1119.

79. G. Guella, C. Zanchetta, B. Patton and A. Miotello, *J. Phys. Chem. B*, 2006, **110**, 17024–17033.

80. Y.-T. Li, S.-H. Zhang, G.-P. Zheng, P. Liu, Z.-K. Peng and X.-C. Zheng, *Appl. Catal. Gen.*, 2020, **595**, 117511.

81. Y. Karataş, A. Aygun, M. Gülcan and F. Şen, *J. Taiwan Inst. Chem. Eng.*, 2019, **99**, 60–65.

Chapter 5: Ruthenium and Platinum Nanoparticles Immobilised on Ionic Functionalised Mesoporous Silica as Catalysts for Selective Hydrogen Evolution from $NaBH_4$

This work was conducted to gain experience in synthesising ordered mesoporous silica materials for catalysis and to finalize collaborative research with a group member for publication.

5.1 Introduction

Over the last two decades, significant progress has been made in the development of ordered mesoporous materials. These materials are synthesised by using surfactant templates, around which silica frameworks are formed. Once the surfactants are removed, the resulting structure consists of well-defined pores surrounded by silica walls. This method has enabled the creation of periodic mesoporous solids with precisely controlled pore sizes and structural order to be prepared. These solids, which can exhibit cubic, lamellar, or hexagonal arrangements, represent a significant advancement in material science.[1,2]

In recent years, there has been a growing focus on mesoporous nanoscience, nanotechnology, and nanomaterials in the field of chemistry, especially in relation to catalysis.[3] This increased attention is due to the impressive ability of mesoporous materials to stabilise nanoparticles, thereby impacting catalytic performance. Research has shown that the interplay between mesoporous materials and nanoparticle surfaces helps to enhance the selectivity and efficiency of active sites, thus improving their effectiveness in catalytic processes.[3] The supports provide site isolation and intrinsic steric stabilisation, as well as synergistic metal-support interactions. These interactions between the metal nanoparticles and the surrounding material can enhance or modify the catalyst activity, selectivity, and stability.[4–6]

The chemical industry highly values supported systems that contain metal or metal oxide.[7,8] For instance, supported ruthenium catalysts are essential in various industrial processes, such as the selective hydrogenation of benzene to cyclohexane and ammonia synthesis.[9,10] Furthermore, ruthenium is employed for the catalytic decomposition of nitrous oxide and catalytic oxidation of alcohols and amines to produce aldehydes and nitriles, respectively.[11,12]

The growing number of reports of improved catalyst performance for nanoparticles stabilised by an amino-modified support has led us to expand our research to investigate how the effectiveness of catalysts is influenced by the confinement of RuNPs in various amine-decorated large pore-ordered mesoporous silica immobilised ionic liquid supports and to

compare their efficacy against their polymer immobilised counterparts to assess the relative merits of the two types of support.[3,13] As such this project set out to explore the influence on catalyst performance of varying the amine loading and the type of amine. This chapter will provide details about the preparation of a range of amine and/or imidazolium modified Ordered Mesoporous Silica Immobilised Ionic Liquids (OMSIILs) as supports for confining and stabilising RuNPs, along with a comparative assessment of their performance as catalysts for the evolution of hydrogen from sodium borohydride. Initial investigations into this type of catalyst found that RuNPs stabilised by amino-modified Ordered Mesoporous Silica Immobilised Ionic Liquids (RuNP@NH_2-OMSIIL) demonstrated superior performance as compared to their unmodified counterparts (RuNP@OMSIIL). In addition, a preliminary investigation with the amino-modified catalyst RuNP@NH_2-OMSIIL revealed that it was more efficient than its platinum counterpart (PtNP@NH_2-OMSIIL).

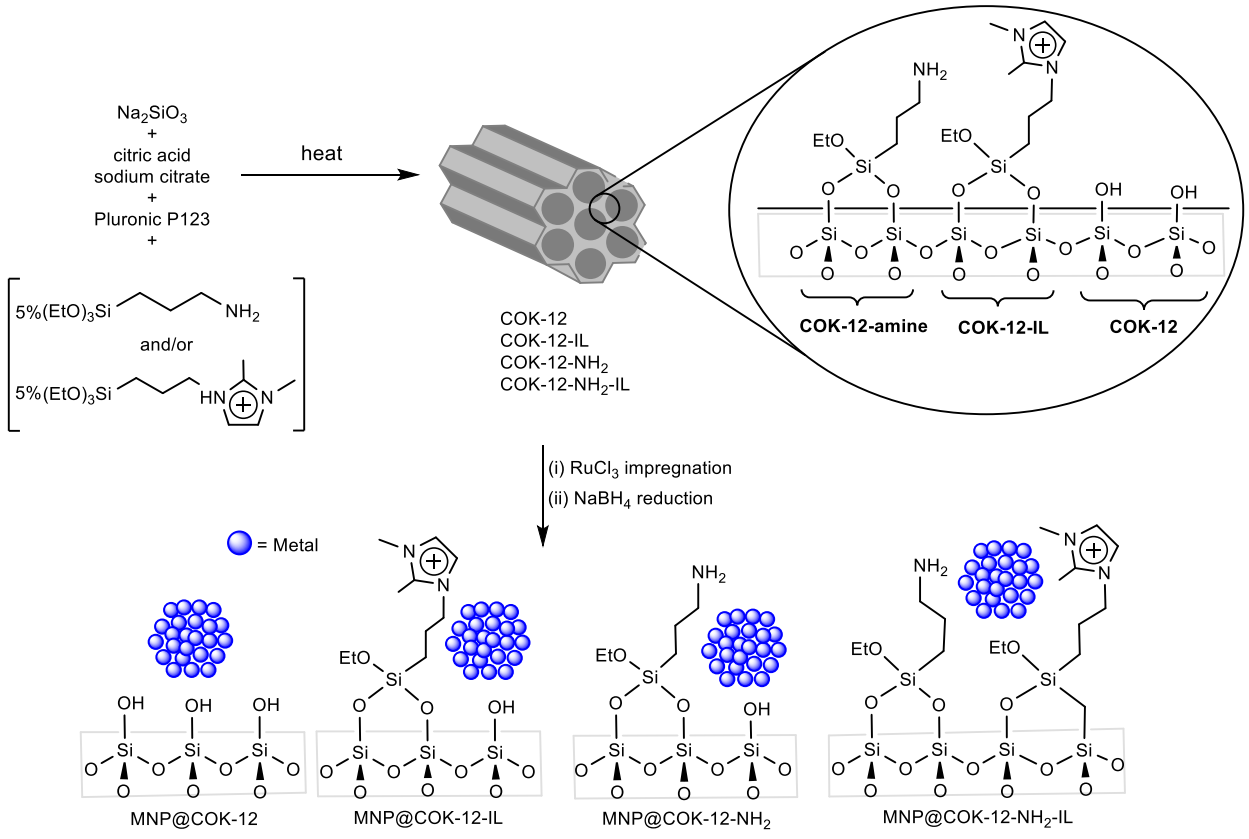

Scheme 5.1: Synthesis and composition of ordered mesoporous silica COK-12, ionic liquid (IL) and/or amine-modified COK-12 and the corresponding metal NP.

5.2 Result and Discussion

5.2.1 Synthesis of metal nanoparticles Immobilised on Ionic Functionalised Mesoporous Silica.

This phase of the project involved the synthesis of mesoporous materials based on the known COK-12 motif by incorporating additional ionic liquid like imidazolium groups and neutral amines. To demonstrate the influence of each component, a series of functionalised COK-12 materials **5.8**-**5.12**, including unfunctionalised COK-12, were targeted, as shown in Figure 5.1.

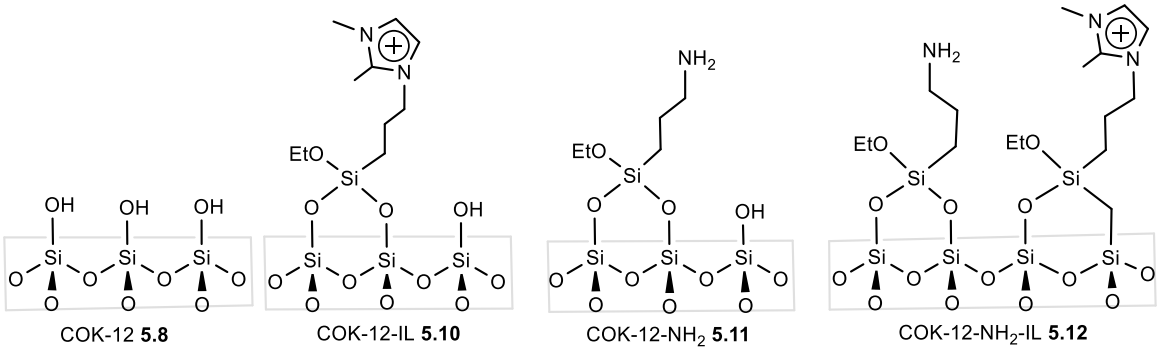

Figure 5.1: Synthesis and composition of ordered mesoporous silica COK-12 **5.8**, ionic liquid (IL) **5.10**, amine modified COK-12 **5.11** and COK-12-NH_2-IL **5.12.**

5.2.2 Synthesis of 1,2-dimethyl-3-(3-triethoxysily)propyl-imidazole-3-ium chloride 5.3.

The González-Abrego group has previously documented the synthesis of imidazolium silica precursor **5.3** (Scheme 5.2).[14] Following this method, 1,2-dimethylimidazole **5.1** was heated with (3-chloropropyl)triethoxysilane **5.2** at 90 °C for 48 hours, resulting in the formation of 1,2-dimethyl-3-(3-(triethoxysilyl)propyl)-1H-imidazol-3-ium chloride **3.6** in a yield of 95%. Any unreacted starting materials were removed through trituration with diethyl ether and the product was stored under nitrogen to prevent undesired hydrolysis and was utilised promptly after preparation. The success of the reaction was confirmed by comparing the ^{1}H NMR spectrum of the product with that of the reactants, as depicted in Figure 5.2.

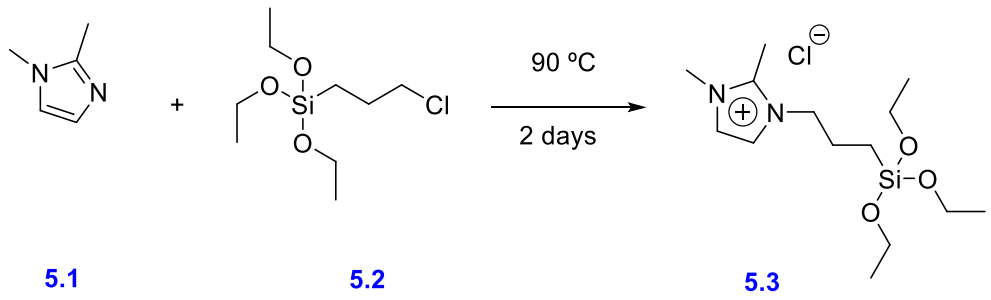

5.1 5.2 5.3

Scheme 5.2: Synthesis of 1,2-dimethyl-3-(3-(triethoxysilyl)propyl)-1H-imidazol-3-ium chloride **5.3.**

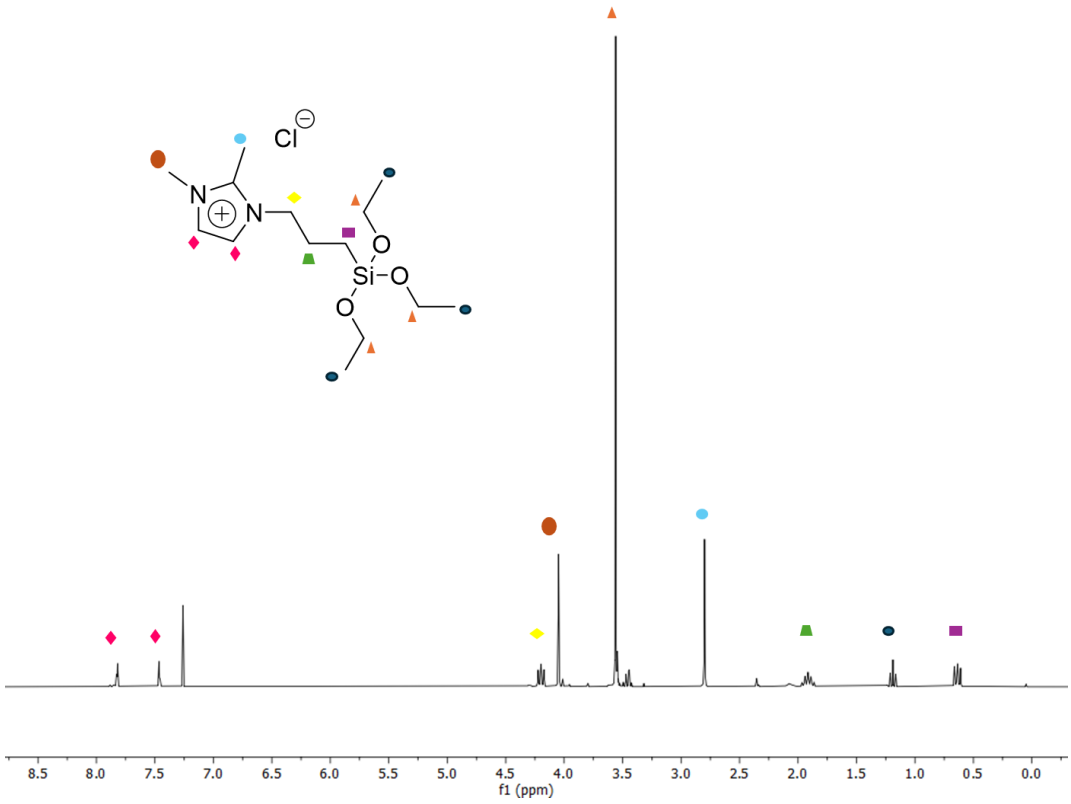

Figure 5.2: Solution ^{1}H NMR spectrum of 1,2-dimethyl-3-(3-triethoxysily)propyl-imidazole-3-ium chloride **5.3** recorded in $CDCl_3$

5.2.3 Synthesis of unfunctionalised COK-12 ordered mesoporous silica 5.8.

Following the approach by Jammer *et al.*,[15] the ordered mesoporous silica COK-12 **5.8** was synthesised using poly(ethylene glycol)-block-poly(propylene glycol)-block-poly(ethylene glycol), (P123) triblock copolymer as a template to prepare P123@COK-12 (**5.7**) in an aqueous buffer solution of citric acid/sodium citrate with sodium silicate **5.8** as the silica source at room temperature for 24 hours, as shown in Scheme 5.3.

After that, the organic template was removed by exhaustive Soxhlet extraction with ethanol for 15 days, to afford the ordered mesoporous silica COK-12 **5.8** with a yield of 96%. The buffer solution was used to maintain a stable pH when an alkaline solution (sodium silicate) was added to the triblock copolymer solution.

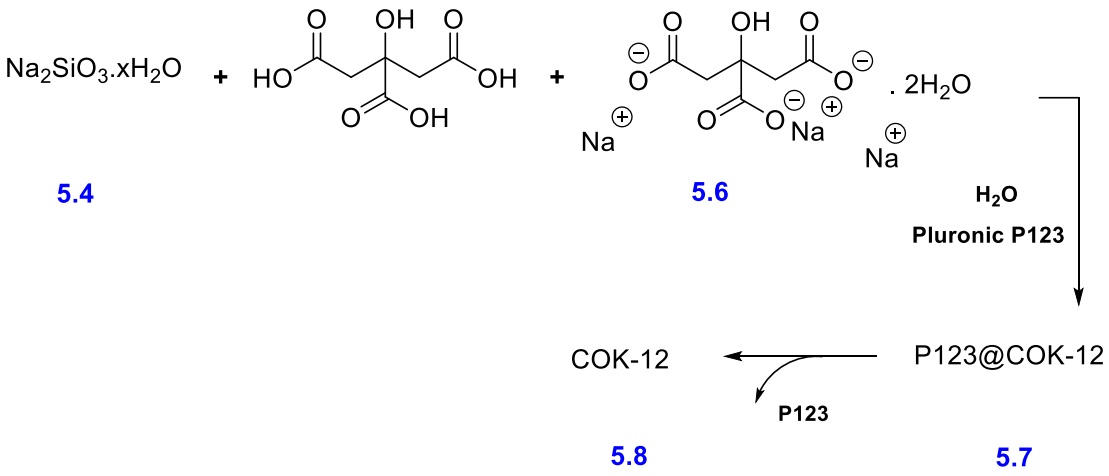

Scheme 5.3: Synthesis of unfunctionalised COK-12 (**5.8**).

5.2.4 Synthesis of functionalised COK-12 mesoporous materials.

Scheme 5.4 shows the preparation of the three functionalised materials: COK-12-IL (**5.10**), COK-12-NH_2 (**5.11**), and COK-12-IL-NH_2 (**5.12**). The procedure for their preparation was identical to that used for the unfunctionalised COK-12 but involved the incorporation of functionalised R-triethoxysilane, where R stands for imidazolium or NH_2.

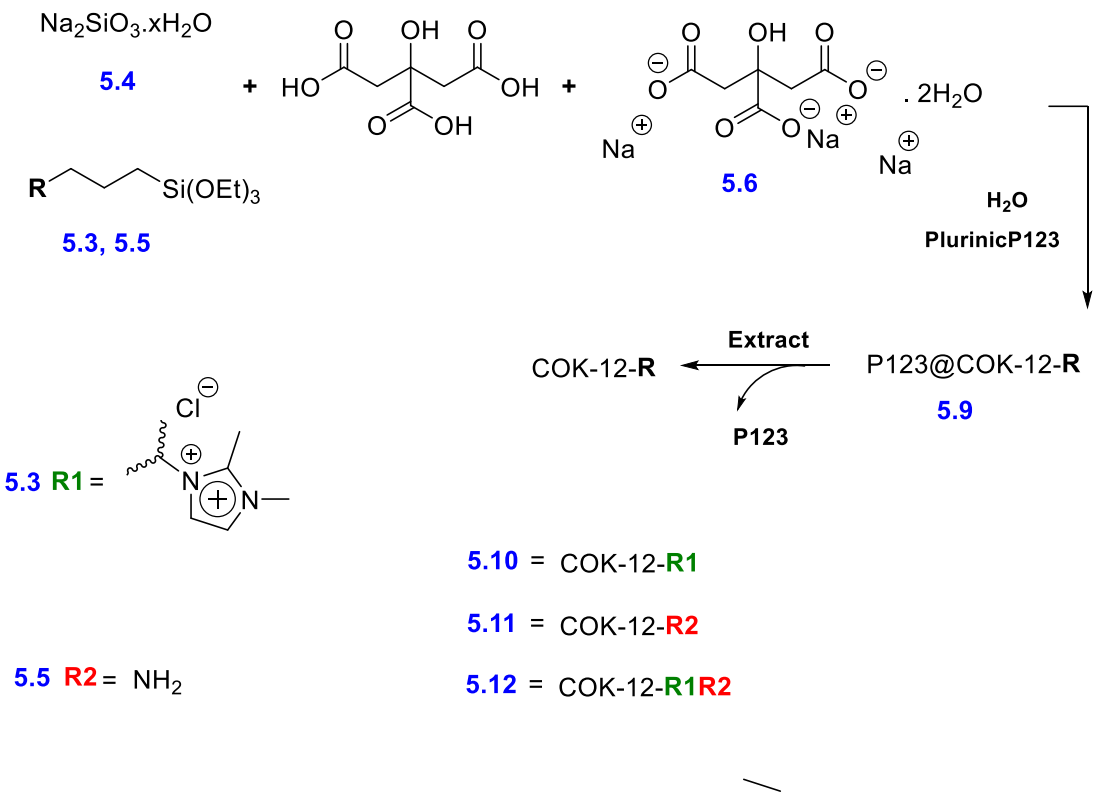

Scheme 5.4: Synthesis of COK-12-IL (**5.10**), COK-12-NH_2 (**5.11**) and COK-12-NH_2-IL (**5.12**)

Imidazolium-functionalised COK-12-IL (**5.10**) was prepared using a 95:5 ratio of sodium silicate **5.4** and 1,2-dimethyl-3-(3-(triethoxysilyl)propyl)-1H-imidazol-3-ium chloride (**5.3**) (Table 5.2). The mesoporous silica was obtained in a yield of 89% after the template was removed using ethanol. Following the same protocol, the amine-functionalised COK-12-NH_2 (**5.11**) was synthesised in 83% yield from a 95:5 ratio of sodium silicate **5.4** and 3-(triethoxysilyl) propylamine **5.5**. In addition, the bifunctional organic mesoporous silica COK-12-imid-NH_2 (**5.12**) was generated by hydrolysis of a 90:5:5 ratio of sodium silicate (**5.4**) 1,2-dimethyl-3-(3-(triethoxysilyl)propyl)-1H-imidazol-3-ium chloride (**5.3**) and 3-(triethoxysilyl)propylamine (**5.5**), achieving a 95% yield.

Table 5.2: Ratio used for the synthesis of functionalised-COK-12 materials.

R	**R** ratio (%)	Sodium silicate ratio (%)	Product
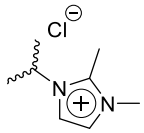	**5**	**95**	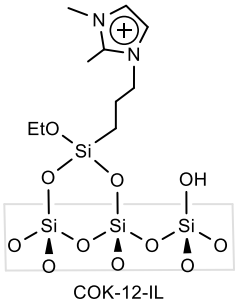 COK-12-IL
NH_2	**5**	**95**	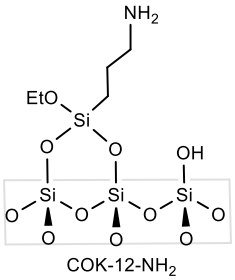 COK-12-NH_2
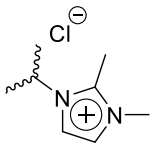 NH_2	**5** **5**	**90**	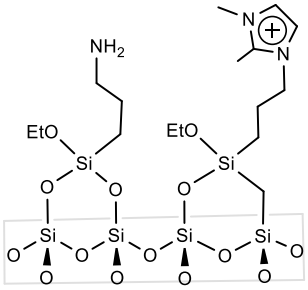 COK-12-NH_2-IL

5.2.5 The Removal of Surfactant.

Specifically tailored for this function, mesoporous silica is widely recognised for its efficient absorption and retention of residual solvents. The final step of the synthesis of the ordered mesoporous silicas involved the removal of the template to allow access to the pores for further processes.[16]

The surfactant used in this project was the neutral block copolymer poly(ethylene glycol)-block-poly(propylene glycol)-block-poly(ethylene glycol), which is known as (Pluronic P123). The surfactant triblock copolymer consists of the hydrophilic poly(ethylene oxide) (PEO) and hydrophobic poly(propylene oxide) (PPO) blocks, as shown in Figure 5.2.[17,18] This particular surfactant is widely used for the synthesis of reverse micelles, mesoporous silica-based materials, and a host of nanomaterials. Furthermore, micelles and reverse micelles can serve as "nanoreactors" for various chemical reactions.[19]

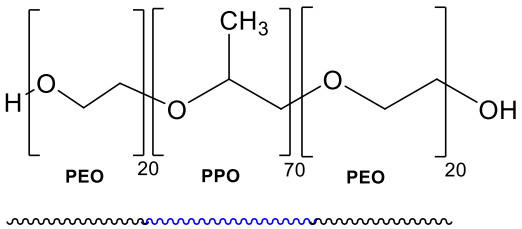

Figure 5.2: Pluronic P-123 structure.

The surfactant was removed using a technique known as Soxhlet extraction. Normally, alcohol, aqueous acid, or a combination of the two is used as the solvent in this method. However, in certain situations, the use of acids may pose challenges when basic functional groups like amines are present. That is why only ethanol was used in this extraction (Figure 5.3).[20] In a relevant study, Ko and Bae,[21] have explained that the process of removing the template is more effective in ethanol compared to water because the template is more soluble in alcohol.[22] When using Soxhlet extraction to purify ordered mesoporous silicas, organic molecules should not be damaged or eliminated since the extraction is conducted at about 80^{o}C.

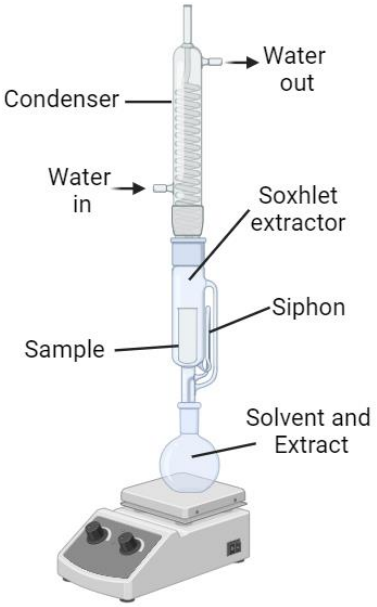

Figure 5.3: Schematic of a Soxhlet extraction used to remove surfactant from mesoporous materials.

The process of eliminating the organic surfactant was carefully tracked by continuously measuring the mass of the resulting organic extraction products (Figure 5.4) at regular time intervals. Table 5.2 illustrates the outcomes from the continuous ethanol extraction of COK-12 (**5.8**), COK-12-IL (**5.10**), COK-12-NH_2 (**5.11**), and COK-12-NH_2-IL (**5.12**). After 15 days of extraction, no additional surfactant was removed from **5.8** and **5.10.** Similarly, after 16 days, no more surfactant was obtained from **5.11** and **5.12**. The desired mesoporous silicas were isolated as fine off-white powders.

Table 5.2: The result of the extraction of COK-12 mesoporous materials.

	Weight before extraction (g)	**Total extraction time (days)**	**Product weight after extraction (g)**
COK-12 **5.8**	**17**	**15**	**10**
COK-12-IL **5.10**	**8.8**	**16**	**4**
COK-12-NH_2 **5.11**	**13**	**15**	**6**
COK-12-NH_2-IL **5.12**	**9**	**16**	**5**

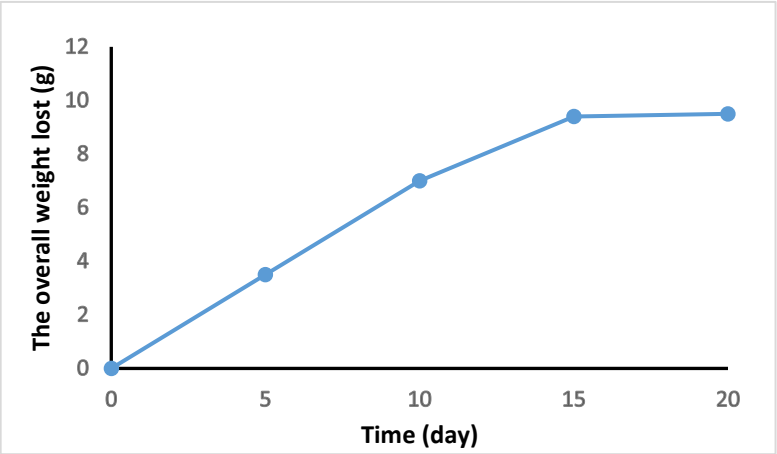

Figure 5.4: Mass of template extracted as a function of time for the purification of COK-12- NH_2

It can be seen from (Table 5.2) and (Figure 5.4) that the mass of COK-12-NH_2 (**5.11**) after extraction (6 g) is higher than expected from the loss of 9.5 g of surfactant from an initial mass of 13 g of material, as the mass isolated should be 3.5. This is likely due to the incorporation of some extracting solvent (EtOH) into the final material.

A comparison of the ^{13}C NMR spectra of an original P123 sample with the corresponding spectra for **5.11** after extraction validated the successful elimination of the surfactant. This was evidenced by the lack of any peaks between 70–80 ppm characteristic of the poly(ethylene oxide)-poly(propylene oxide) co-polymer.

5.2.6 Synthesis of supported ruthenium materials RuNPs@OMSIIL

COK-12 and the modified COK-12 stabilised ruthenium nanoparticles were synthesised by wet impregnation of each silica with an aqueous solution of $RuCl_3 \cdot 3H_2O$ followed by reductions of the resulting Ru (III) loaded material with $NaBH_4$ to afford the corresponding COK-12 stabilised RuNPs RuNP@COK-12 (**5.13**), RuNP@COK-12-IL (**5.14**), RuNP@COK-12-NH_2 (**5.15**), and RuNP@COK-12-NH_2-IL (**5.16**), in the form of black powders. The reduction was rapid and very apparent, as evidenced by the instantaneous colour change from grey to black as expected.

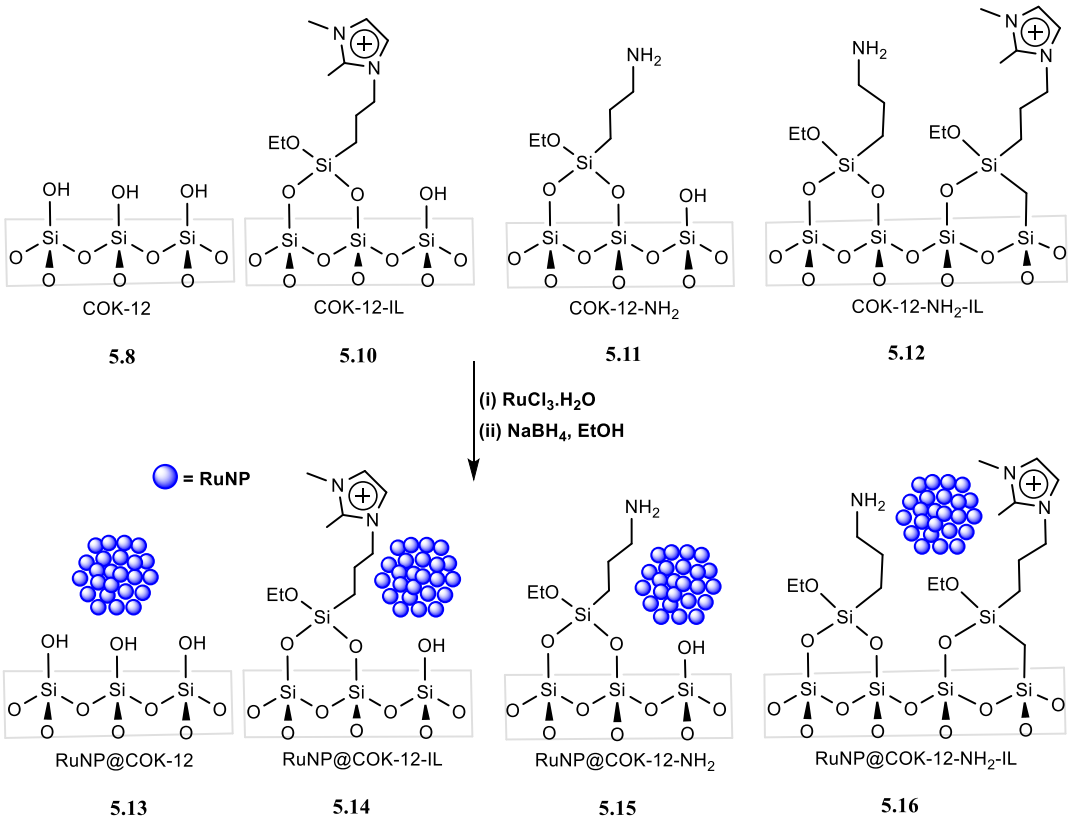

Scheme 5.5: Synthesis of RuNP@Cok-12 (**5.13**), RuNP@COK-12-IL (**5.14**), RuNP@COK-12-NH_2 (**5.15**) and RuNP@COK-12-NH_2-IL (**5.16**)

5.2.7 Synthesis of supported platinum materials PtNP@OMSIIL

The synthesis of PtNP@COK-12-NH_2 (**5.17**) was achieved following the procedure shown in Scheme 5.6. The mesoporous silica material COK-12-NH_2 (**5.11**) was first impregnated with $K_2[PtCl_4]$ in water by exchange of the chloride anions for the tetrachloroplatinate anion to afford $[PtCl_4]$@COK-12-NH_2 which was subsequently reduced with $NaBH_4$ to afford PtNP@COK-12-NH_2 (**5.17**) as a grey powder.

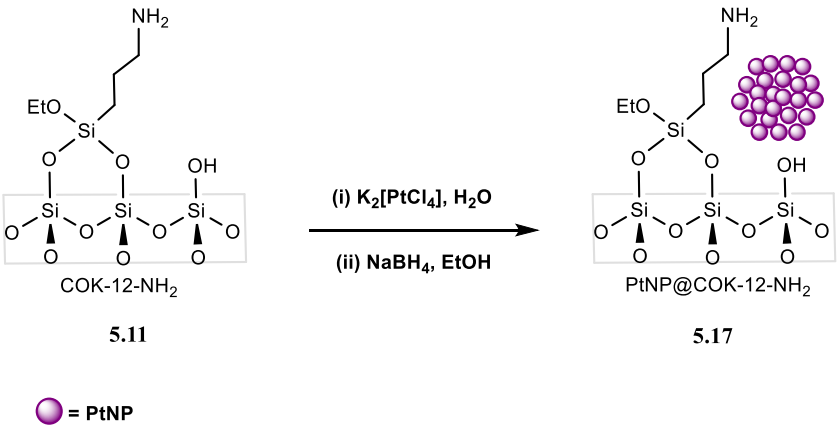

Scheme 5.6: Synthesis of PtNP@COK-12-NH_2 (**5.17**)

5.3 Characterisation of the mesoporous materials.

I. Scanning Electron Microscopy (SEM)

The SEM (Scanning electron microscopy) images (Figure 5.6) show the surface morphologies of the four COK-12 silicas **5.8**, **5.10**, **5.11** and **5.12**, which revealed that 5.8 and 5.11 have granular surface structures with porous features, while **5.10** and **5.12** have smooth surfaces. The SEM images of the RuNP@COK-12 materials **5.13**, **5.14**, **5.15** and **5.16** in Figure 5.7 show that **5.13** and **5.14** are comprised of small clusters of particles < 1 µm in size (Figure 5.7a,b), whereas **5.15** and **5.16** consist of larger particles 10-20 µm in size and similar to that of the corresponding OMSIIL prior to metal loading (Figure 5.7, d).

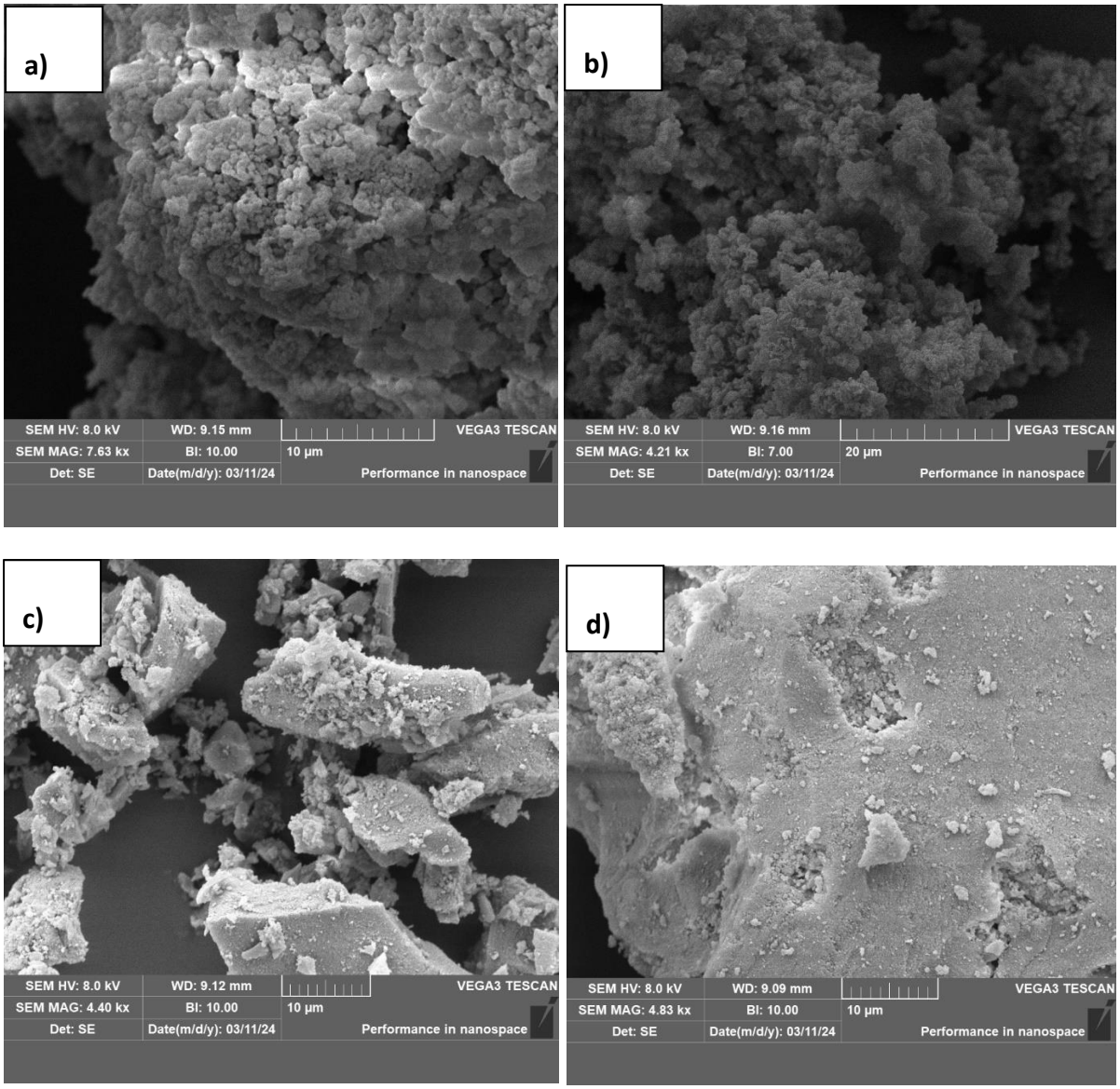

Figure 5.6: SEM images of a freshly prepared sample of a) COK-12 (**5.8**) and b) COK-12-NH_2 (**5.11**), c) COK-12-IL (**5.10**) and d) COK-12-NH_2-IL (**5.12**)

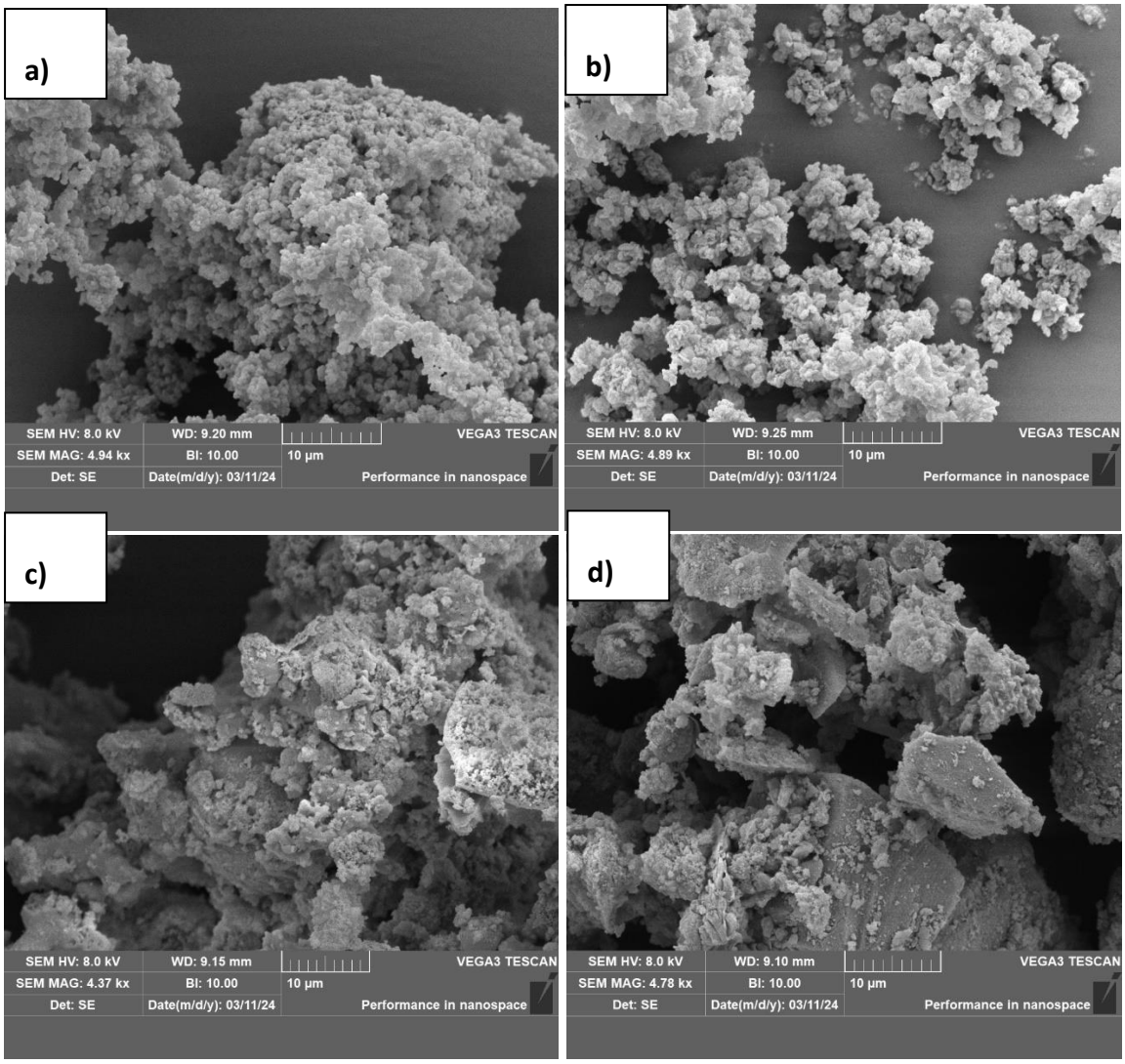

Figure 5.7: SEM images of a freshly prepared sample of a) RuNP@COK-12 (**5.13**) and, b) RuNP@COK-12-NH_2 (**5.14**), c) RuNP@COK-12-IL (**5.15**) and d) RuNP@COK-12-NH_2-IL (**5.16**)

II. Solid-State NMR

The composition of organically functionalised COK-12 mesoporous silica materials was studied by solid-state nuclear magnetic resonance (NMR) spectroscopy, in which the carbon and silicon spectra were recorded using a cross-polarisation method. The ^{13}C CP-MAS spectrum of **5.11**, recorded using the TOSS pulse sequence, contains resonances characteristic of the surface-attached propylamine functionality (Figure 5.8). The 13C spectra of the supports containing supports also have a surface anchored NH_2 also contain a set of signals associated with the methylene groups of the propylamine chain.

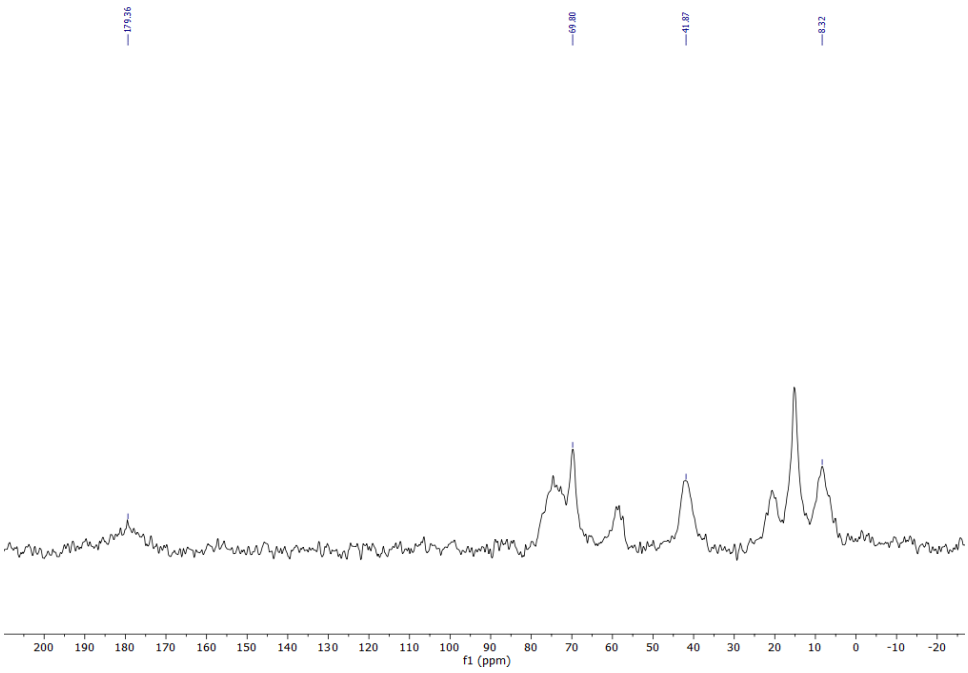

Figure 5.8: Solid state $^{13}C\{^{1}H\}$ NMR spectrum of amine-modified mesoporous COK-12 support **5.11**

The solid state ^{29}Si spectrum of **5.11** (Figure 5.9) contains two groups of signals typical for silica; a set of three **Q** series signals at (δ 92, 102 and 111 ppm) for the tetrasubstituted silicon species $Si(SiO_2)_2(OH)_2]$, $[Si(OSi)_3(OH)]$ and $[Si\text{-}(OSi)_4]$ in the inorganic silica framework, respectively, and a broad ill-defined T-series signal at (δ 66 ppm) associated with the aminopropyl-modified silica $R\text{-}Si(OSi)_3$.[23,24] The disparate intensities of these T ad Q series resonances confirm that these catalysts are comprised mainly of inorganic silicate together with a minor amount of organo-modified silicate resulting from immobilisation of the silylated ionic liquid and/or amine on the walls of the mesoporous silica.

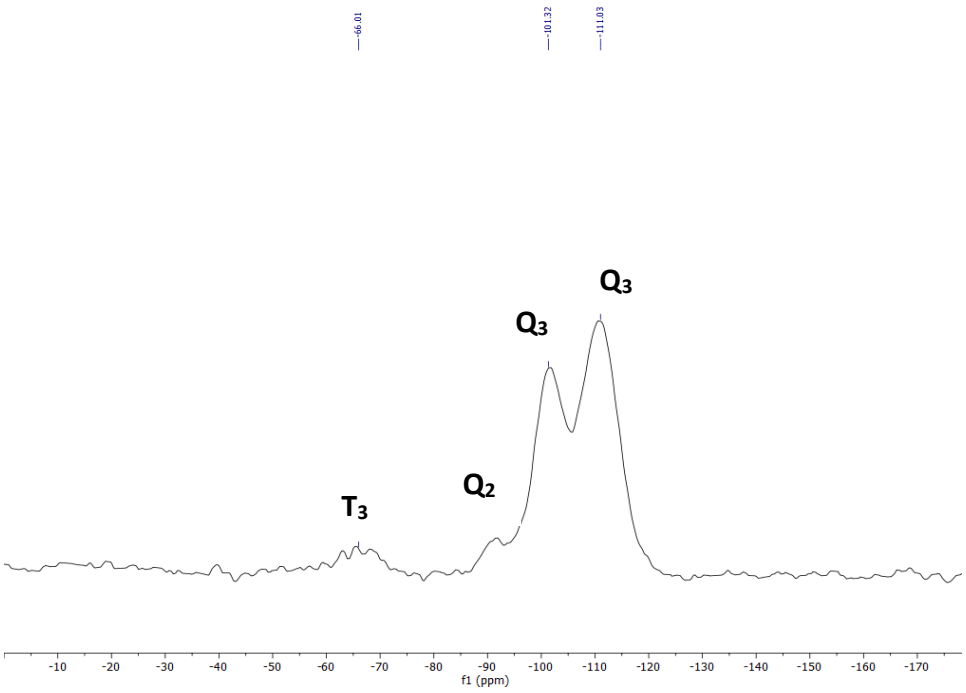

Figure 5.9: Solid state ^{29}Si NMR spectrum of amine-modified mesoporous COK-12 support **5.11**

5.4 Supported Ruthenium and Platinum Nanoparticle-Catalysed Hydrolysis of Sodium Borohydride.

As illustrated previously in chapters two and four, our group has recently reported a comparison of the efficacy of platinum metal nanoparticles (PtNPs) and ruthenium nanoparticles (RuNPs), stabilised by a heteroatom donor-modified polymer immobilised ionic liquids (PIIL), as catalysts for the hydrolytic evolution of hydrogen from sodium borohydride[25,26] and DMAB.[27] This study demonstrated that RuNPs were significantly more active than their platinum counterparts.

Building on this discovery study, the effectiveness of amino-decorated OMSIIL-stabilised Ru and Pt nanoparticles as catalysts for the hydrolysis of sodium borohydride has been investigated to compare the relative efficacy of this catalyst against their polymer-stabilised counterparts. These comparative findings revealed that RuNP@NH2-OMSIIL (**5.11**) exhibited higher catalytic activity and was markedly more efficient as a catalyst for the hydrolysis of $NaBH_4$ than its platinum counterpart **5.17.**

When comparing the effectiveness of **5.11** and **5.17** with previous studies on other supported ruthenium nanoparticles, it is important to approach the comparison with caution due to the different experimental conditions and data collection protocols. Reactions were initially conducted at 30 °C using 0.2 mol% of **5.11** and **5.17** to catalyse the hydrolysis of a 0.28 M solution of sodium borohydride (Figure 5.10). Progress of the reactions was tracked by measuring the quantity of hydrogen released over time by displacement of water from an inverted burette; subsequently, the data was adjusted by adjusting for the baseline quantity of hydrogen released under the same circumstances at the same time but in the absence of a catalyst. Under these conditions, RuNP@NH_2-OMSIIL (**5.11**) gave an initial TOF of 157 $mole_{H2}.molcat^{-1}.min^{-1}$, whereas its Pt counterpart PtNP@NH_2-OMSIIL (**5.17**) was less active with a slightly lower TOF of 139 $mole_{H2}.molcat^{-1}.min^{-1}$. This is only a preliminary study due to time constraints and further studies are clearly required to complete this comparison, identify optimum conditions and assess the relative merits of COK-12 based supports versus PIIL.

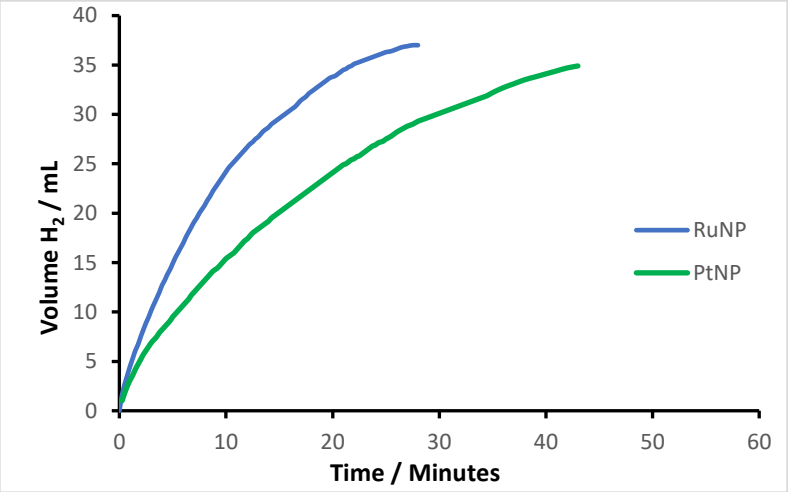

Figure 5.10: Comparison of the hydrolytic release of hydrogen from sodium borohydride as a function of time using RuNP@NH_2-OMSIIL and PtNP@NH_2-OMSIIL as catalysts.

5.5 Conclusion

The purpose of this study was to examine the effectiveness of RuNPs and PtNPs stabilised by mesoporous COK-12 modified with a primary amine and/or an imidazolium based ionic liquid as catalysts for the hydrolytic evolution of hydrogen from sodium borohydride and undertake a systematic comparison against their polymer immobilised ionc liquid stabilised counterparts. It was found that RuNPs stabilised by mesoporous COK-12 and modified with a primary amine and an imidazolium-based ionic liquid (RuNP@NH_2-OMSIIL) are more active than their platinum counterparts for the hydrolysis of $NaBH_4$ as the former gave an initial TOF of 157 $mole_{H2}.molcat^{-1}.min^{-1}$, compared with 139 $mole_{H2}.molcat^{-1}.min^{-1}$ for the latter.

To this end, there have been notable advancements in the effectiveness of nanoparticle-based catalysts with amine-modified supports. These improvements have been attributed to various factors, including the efficient dispersion of the NPs, modification of the surface electronic structure of the NP, regulation of the NP size, and a collaborative function in the fundamental stages of the catalytic process, and as such OMSIIL-stabilised NPs may well find wider applications in catalysis.[28–31]

Moving forward, it will be informative to investigate how different factors affect catalyst performance, such as the type and loading of amine, the ionic microenvironment, porosity, and hydrophilicity. The Doherty group is currently exploring the effect of surface modifications on catalyst performance, undertaking kinetic and mechanistic studies, and applying the synthetic protocol to develop bi and multimetallic systems to diversify the range of catalytic transformations. Ultimately, future studies will aim to achieve a deeper, more detailed understanding of this system and identify more effective catalysts for use in scale-up.

5.6 Reference

1. C. T. Kresge, M. E. Leonowicz, W. J. Roth, J. C. Vartuli and J. S. Beck, *Nature*, 1992, **359**, 710–712.

2. J. S. Beck, J. C. Vartuli, W. J. Roth, M. E. Leonowicz, C. T. Kresge, K. D. Schmitt, C. T. W. Chu, D. H. Olson, E. W. Sheppard, S. B. McCullen, J. B. Higgins and J. L. Schlenker, *J. Am. Chem. Soc.*, 1992, **114**, 10834–10843.

3. M. Rawolle, M. A. Niedermeier, G. Kaune, J. Perlich, P. Lellig, M. Memesa, Y.-J. Cheng, J. S. Gutmann and P. Müller-Buschbaum, *Chem. Soc. Rev.*, 2012, **41**, 5131–5142.

4. T. W. van Deelen, C. Hernández Mejía and K. P. de Jong, *Nat. Catal.*, 2019, **2**, 955–970.

5. C. Gao, F. Lyu and Y. Yin, *Chem. Rev.*, 2021, **121**, 834–881.

6. Z. Cao, J. Bu, Z. Zhong, C. Sun, Q. Zhang, J. Wang, S. Chen and X. Xie, *Appl. Catal. Gen.*, 2019, **578**, 105–115.

7. D. Zhao, J. Feng, Q. Huo, N. Melosh, G. H. Fredrickson, B. F. Chmelka and G. D. Stucky, *Science*, 1998, **279**, 548–552.

8. D. Zhao, Q. Huo, J. Feng, B. F. Chmelka and G. D. Stucky, *J. Am. Chem. Soc.*, 1998, **120**, 6024–6036.

9. V. Mazzieri, F. Coloma-Pascual, A. Arcoya, P. C. L'Argentière and N. S. Fígoli, *Appl. Surf. Sci.*, 2003, **210**, 222–230.

10. J. Zhang, H. Xu, Q. Ge and W. Li, *Catal. Commun.*, 2006, **7**, 148–152.

11. K. Yamaguchi and N. Mizuno, *Angew. Chem. Int. Ed.*, 2003, **42**, 1480–1483.

12. X. Yu, M. Wang and H. Li, *Appl. Catal. Gen.*, 2000, **202**, 17–22.

13. N. Wei, X. Zou, H. Huang, X. Wang, W. Ding and X. Lu, *Eur. J. Org. Chem.*, 2018, **2018**, 209–214.

14. D. O. González-Abrego, F. J. Zuno-Cruz, M. Carpio-Granillo, N. Andrade-López, J. Cruz-Borbolla, C. Martínez-Macias, D. Mendoza-Espinosa, M. J. Rosales-Hoz, M. A. Leyva, J. R. Torres-Lubián, J. A. López-Jiménez, V. Jancik and G. Sánchez-Cabrera, *Polyhedron*, 2017, **137**, 97–111.

15. J. Jammaer, A. Aerts, J. D'Haen, J. Won Seo and J. A. Martens, *J. Mater. Chem.*, 2009, **19**, 8290–8293.

16. A. Taguchi and F. Schüth, *Microporous Mesoporous Mater.*, 2005, **77**, 1–45.

17. D. Zhao, J. Feng, Q. Huo, N. Melosh, G. H. Fredrickson, B. F. Chmelka and G. D. Stucky, *Science*, 1998, **279**, 548–552.

18. K. M. Ryan, N. R. B. Coleman, D. M. Lyons, John. P. Hanrahan, T. R. Spalding, M. A. Morris, David. C. Steytler, R. K. Heenan and J. D. Holmes, *Langmuir*, 2002, **18**, 4996–5001.

19. R. D. Falcone, N. M. Correa and J. J. Silber, *Langmuir*, 2009, **25**, 10426–10429.

20. B. L. Cushing, V. L. Kolesnichenko and C. J. O'Connor, *Chem. Rev.*, 2004, **104**, 3893–3946.

21. Y. K. Bae and O. H. Han, *Microporous Mesoporous Mater.*, 2007, **106**, 304–307.

22. M. Kruk, M. Jaroniec, C. H. Ko and R. Ryoo, *Chem. Mater.*, 2000, **12**, 1961–1968.

23. C. Calabrese, L. F. Liotta, F. Giacalone, M. Gruttadauria and C. Aprile, *ChemCatChem*, 2019, **11**, 560–567.

24. Q. Sun, N. Wang, Q. Bing, R. Si, J. Liu, R. Bai, P. Zhang, M. Jia and J. Yu, *Chem*, 2017, **3**, 477–493.

25. S. Doherty, J. G. Knight, H. Y. Alharbi, R. Paterson, C. Wills, C. Dixon, L. Šiller, T. W. Chamberlain, A. Griffiths, S. M. Collins, K. Wu, M. D. Simmons, R. A. Bourne, K. R. J. Lovelock and J. Seymour, *ChemCatChem*, 2022, **14**, e202101752.

26. R. Paterson, A. A. Alharbi, C. Wills, C. Dixon, L. Šiller, T. W. Chamberlain, A. Griffiths, S. M. Collins, K. Wu, M. D. Simmons, R. A. Bourne, K. R. J. Lovelock, J. Seymour, J. G. Knight and S. Doherty, *Mol. Catal.*, 2022, **528**, 112476.

27. A. A. Alharbi, C. Wills, C. Dixon, E. Arca, T. W. Chamberlain, A. Griffiths, S. M. Collins, K. Wu, H. Yan, R. A. Bourne, J. G. Knight and S. Doherty, *Catal. Lett.*, DOI:10.1007/s10562-024-04725-8.

28. S. Masuda, K. Mori, Y. Futamura and H. Yamashita, *ACS Catal.*, 2018, **8**, 2277–2285.

29. K. Koh, M. Jeon, C. Won Yoon and T. Asefa, *J. Mater. Chem. A*, 2017, **5**, 16150–16161.

30. S. Masuda, K. Mori, Y. Kuwahara and H. Yamashita, *J. Mater. Chem. A*, 2019, **7**, 16356–16363.

31. X. Lv, G. Lu, Z.-Q. Wang, Z.-N. Xu and G.-C. Guo, *ACS Catal.*, 2017, **7**, 4519–4526.

Chapter 6: Experimental

6.1 General Comments

All reagents were purchased from commercial suppliers and used without further purification. All reactions involving air-sensitive compounds were carried out using standard Schlenk line techniques under an atmosphere of N_2 in oven-dried glassware. All reaction solvents were distilled before use: toluene, dichloromethane, and chloroform were dried over calcium hydride; diethyl ether and tetrahydrofuran were dried over sodium wire in the presence of benzophenone; methanol and ethanol from magnesium; acetonitrile from calcium hydride ; and dimethyl formamide was dried over molecular sieves.[23]

^{1}H,^{13}C and ^{15}N spectra were recorded on JEOL ECS400 MHz, JEOL ECS-500 MHz, Bruker Avance III 300 MHz, or Bruker Ascend 700 MHz spectrometer. Solid-state ^{13}C NMR spectra were recorded at 125.78 MHz, while ^{15}N MAS NMR spectra were recorded at 50.68 MHz. FT-IR spectroscopy was performed using Perkin Elmer spectrum two with the UATR accessory spectrometer scanning from 6000-550 cm^{-1}.

The SEM (Scanning electron microscopy) images were acquired on a Tescan Vega 3LMU scanning electron microscope with digital image collection. X-ray photoelectron spectroscopy (XPS) analysis was conducted using a Thermo Scientific K-alpha X-ray Photoelectron Spectrometer™ (Thermo Scientific, East Grinstead, UK) at NEXUS, Newcastle University. Also, several XPS analysis was conducted using a Kratos Axis Ultra DLD (Kratos, Harwell, UK) with a monochromatic Al Kα (λ =1486.7 eV) X-ray source operated at 225 W.

XPS analysis was conducted using a Kratos Axis Ultra DLD (Kratos, Harwell, UK) with a monochromatic Al Kα (λ =1486.7 eV) X-ray source operated at 225 W. The analysis chamber base-pressure was better than $1x10^{-8}$ mbar. Samples were mounted using double-sided copper tape for the polymer and $PtCl_4$ precatalyst, and copper tape for PtNP and RuNP samples. Surface charge compensation was performed using a low energy electron flood gun. Initial survey spectra were recorded at a pass energy of 80 eV, using a step size of 0.5 eV, with a scan range between 0 – 1400 eV. High resolution spectra were then collected for individual elements at a pass energy of 20 eV, using a step size of 0.1 eV. The data presented has not been rescaled with respect to any internal or external reference, instead interpretation relied on the comparison of binding energy separations.[1] Data analysis was performed using Igor Pro

software with a custom-written program from Schmid *et al*.[2] Curves were fitted using a Gaussian/Lorentzian peak shape with a ratio of 70:30 and backgrounds were subtracted using a Shirley algorithm. Pt 4f core levels were fit using a spin-orbit doublet separation of 3.33 eV and an area ratio of 4:3 between $4f_{7/2}$ and $4f_{5/2}$ components while the Ru 3p core levels were fit using a spin orbit doublet separation of 22 eV and an area ratio of 2:1 between the $3p_{3/2}$ and $3p_{1/2}$ peaks. Metallic Pt 4f peaks were fit using an asymmetric Gaussian-Lorentzian line shape, similar to asymmetric pseudo-Voigt profiles previously reported. Cl 2p signals were fit as doublets with $2p_{3/2}$ and $2p_{1/2}$ components constrained to a peak area ratio of 2:1 and a doublet separation of 1.6 eV and the Br 3d signals were also fit as doublets with $3d_{5/2}$ and $3d_{3/2}$ components constrained to a peak ratio of 3:2 with a doublet separation of 1.05 eV.

The ruthenium and platinum loadings were quantified using inductively coupled plasma optical emission spectroscopy (ICP-OES) on an Agilent 5800 ICP-OES instrument. For TEM (transmission electron microscopy), samples were dispersed in ethanol using an ultrasonic bath and deposited on lacey carbon film-coated copper grids. TEM images were acquired on an FEI Tecnai TF20 field emission gun microscope operating at 200 kV. NP size distribution histograms were obtained from measurements of at least 100 different NPs assuming a spherical shape and with random distribution. EDX spectra were taken using a field emission SEM FEI Nova 450, EDAX TEAM software and a voltage of 18 kV.[23] Samples were dispersed using ethanol onto a silicon wafer and attached to a stub. Images were prepared without coating using a CBS detector (back-scattered electron detector). The typical voltage used was 3 kV.

6.2 Experimental for Chapter 2: Synthesis of Polymer Immobilised Ionic Liquid Stabilised Ruthenium Nanoparticles and Application in the Hydrogen Evolution from Sodium Borohydride

6.2.1 Synthesis of 1,2-dimethyl-3-(4-vinylbenzyl)-1H-imidazole-3-ium chloride (2.1)

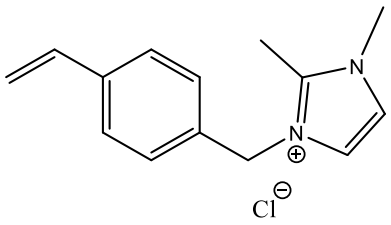

An oven-dried Schlenk flask was charged with 1,2-dimethyl imidazole (7.95 g, 82.8 mmol) and 4-vinylbenzyl chloride (16.32 g, 35.6 mmol) and dissolved in dry chloroform (70 mL). The mixture was then left to stir overnight at 50 °C under nitrogen. The next day, the solvent was removed under reduced pressure, and the resultant dissolved in a minimum amount of DCM (40 mL). The organic phase was added dropwise to a solution of diethylether (400 mL) with stirring. The precipitation of white solid was observed, and the solid was isolated by filtration and dried under vacuum to obtain a white crystalline solid (18.7 g, 90.82 %). ^{1}H NMR (300 MHz, $CDCl_3$, δ): 5.56 (s, 2H), 5.25 (d, *J* = 9 Hz, 1H), 3.95 (s, 3H), 2.76 (s, 3H); ^{13}C NMR (75 MHz, $CDCl_3$, δ): 144.02, 138,19, 135.71, 132.45, 128.47, 126.94, 122.91, 121,94, 115.93, 51.93, 35.76, 10.79.

6.2.2 Synthesis of 2-methyl-1-(4-vinylbenzyl)-1H-imidazole (2.2).

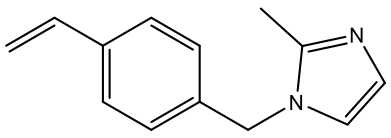

An oven dried flask was charged with sodium hydride (1.73 g, 72.16 mmol) and dry DMF (30 mL). The solution was then cooled to 0 °C before slowly adding 2-methyl imidazole (5.0 g, 60.8 mmol). Once the exotherm had subsided, 4-chloromethyl styrene (9.28 g, 60.8 mmol) was added dropwise. The reaction solution was then heated to 75 °C and stirred for 30 min. The

reaction mixture was poured onto water (50 mL), and the product was extracted with ethyl acetate (3 × 50 mL). The combined organic extracts were combined and washed with water (150 mL) and brine (50 mL) and extracted with 6N HCl (2 × 25 mL). The aqueous layer was washed with diethylether (1 × 50 mL) and then treated with NaOH pellets to pH = 12.0. The product was then extracted with diethyl ether (3 × 50 mL), dried over $MgSO_4$ and the solvent removed under reduced pressure to afford a pale-yellow oil (3.83 g, 63.6 %). ^{1}H NMR (300 MHz, $CDCl_3$, δ): 7.36 (d, *J* = 8.2 Hz, 2H), 7.01 (d, *J* = 8.3 Hz, 2H), 6.59 (d, *J* = 1.3 Hz, 1H), 6.84 (d, *J* = 1.3 Hz, 1H), 6.70 (dd, *J* = 17.6, 10.9 Hz, 1H), 5.73 (d, *J* = 17.6 Hz, 1H), 5.25 (d, *J* = 10.9 Hz, 1H), 5.03 (s, 2H), 2.33 (s, 3H); ^{13}C NMR (75 MHz, $CDCl_3$, δ): 144.98, 137.44, 136.17, 135.91, 127.38, 126.98, 126.83, 119.99, 114.86, 49.59, 13.18; FT-IR (neat, cm^{-1}): ŭ = 3350, 3005, 2932, 2360, 1630, 1510, 1495, 1420, 1407, 1282, 1133, 988, 914, 825, 735, 675. This is consistent with data reported in the literature.[23,24]

6.2.3 Synthesis of 2-methyl-1,3-bis(4vinylbenzyl)-1H-imidazol-3-ium chloride (2.3).

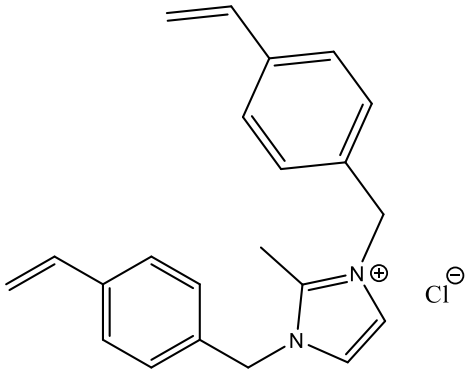

An oven dried Schelnk flask was charged with 2-methyl-1-(4vinylbenzyl)-imidazole **2.2** (3.0 g, 15.2 mmol) and dry chloroform (30 mL). 4-Chloromethyl styrene (2.77 g, 18.2 mmol) was then added dropwise and the resulting mixture was heated to 50 °C and allowed to stir overnight. The next day, the solvent was removed to afford a concentrated yellow solution which was added dropwise to diethyl ether (250 mL) with vigorous stirring, to afford a white precipitate. The suspension was allowed to stir for a further 30 min before the product was isolated by filtration. The product was washed with diethyl ether (2 × 10 mL) and dried under a high vacuum to afford a white powder solid (4.2 g, 78.8 %). ^{1}H NMR (300 MHz, $CDCl_3$, δ): 7.57 (s, 2H), 7.36 (d, *J* = 8.2 Hz, 4H), 7.28 (d, *J* = 7.5 Hz, 4H), 6.63(dd, *J* = 17.6, 10.9 Hz, 2H), 5.73 (d, *J* = 18.2 Hz, 2H), 5.52 (s, 4H), 5.28 (d, *J* = 10.9 Hz, 2H), 2.76 (s, 3H); ^{13}C NMR (75 MHz, CDCl3) δ ^{13}C

NMR (75 MHz, $CDCl_3$, δ): 144.89, 138.98, 136.28, 132.61, 129.02, 127.65, 122.45, 115.87, 52.69, 11.86.; mp = 115– 117 °C; FT-IR (neat, cm^{-1}): ŭ = 3379, 3110, 3070, 2970, 1635, 1580, 1525, 1513, 1409, 1170, 985, 910, 829, 785, 715. This is consistent with data reported in the literature.[3,23,24]

6.2.4 Synthesis of *N*-[(4-vinylphenyl) methyl] phthalimide (2.4)

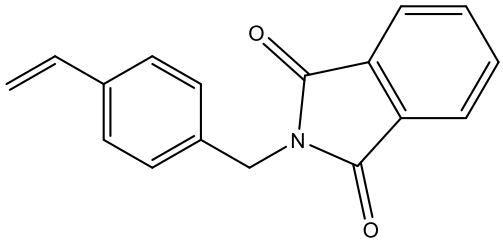

An oven-dried Schlenk flask was charged with potassium phthalimide (5.07 g, 27.4 mmol) in dry DMF (30 mL). 4-Vinylbenzyl chloride (4.06 g, 26.6 mmol) was added dropwise to the reaction flask. The resulting pale orange solution was then heated to 55 °C and allowed to stir overnight. The pale-yellow reaction solution was then taken in DCM (250 mL) and washed with water (6 × 100 mL). The solution was diluted in chloroform (50 mL), washed with 0.2 M NaOH (15 mL) and water (2 × 15 mL) and dried over $MgSO_4$. The solvent was removed under reduced pressure to afford a crude white solid, which was recrystallised from methanol to afford a white crystalline solid, which was isolated by filtration (2.64 g, 37.6 %). ^{1}H NMR (300 MHz, $CDCl_3$, δ): 7.83 (dd, *J* = 5.5, 3.0 Hz, 2H), 7.70 (dd, *J* = 5.5, 3.0 Hz, 2H), 7.41 – 7.33 (m, 4H), 6.66 (dd, *J* = 17.6, 10.9 Hz, 1H), 5.71 (d, *J* = 18.5 Hz, 1H), 5.21 (d, *J* = 10.9 Hz, 1H), 4.83 (s, 2H); ^{13}C NMR (75 MHz, $CDCl_3$, δ): 168.44, 137.63, 136.74, 136.29, 134.42, 132.54, 129.28, 126.91, 123.77, 114.57, 41.76. This is consistent with data reported in the literature.[24]

6.2.5 Synthesis of (4-vinylphenyl) amine (2.5).

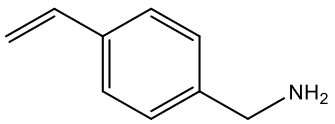

An oven dried Schlenk flask was allowed to cool to room temperature and charged with phthalimide **2.4** (19.0 g, 37.7 mmol) and 95 % ethanol (100 mL) under nitrogen. A solution of hydrazine hydrate (2.66 g, 53.17 mmol) in 95 % ethanol (15 mL) was added dropwise to the reaction flask. After 5 min of stirring a white solid residue began to precipitate. An additional portion of hydrazine hydrate was added and the resulting mixture was stirred and heated to 80 °C overnight. Afte this time, the solvent was removed under reduced pressure and the solid residue taken into chloroform (50 mL) and treated with 20 % aqueous sodium hydroxide (50 mL). The aqueous phase was separated, extracted with chloroform (3 × 50 mL) and the extracts combined and dried over magnesium sulfate and the chloroform was removed under reduced pressure to afford the product as a pale-yellow oil monomer (3.86 g, 76 %). ^{1}H NMR (300 MHz, $CDCl_3$, δ): 7.33 – 7.29 (m, 2H), 7.20 – 7.16 (m, 2H), 6.63 (dd, *J* = 17.6, 10.9 Hz, 1H), 5.65 (d, *J* = 17.6, 1.0 Hz, 1H), 5.14 (d, *J* = 10.9, 1.0 Hz, 1H), 3.77 (d, *J* = 5.7 Hz, 2H), 1.57 (br s, NH_2); ^{13}C NMR (75 MHz, $CDCl_3$, δ): 143.10, 136.74, 136.37, 127.44, 126.57, 113.63, 46.36. This is consistent with data reported in the literature.[23,24]

6.2.6 Synthesis of PEG-chloride (25-chloro-2,5,8,11,14,17,20,23-octaoxapentacosane) (2.6).

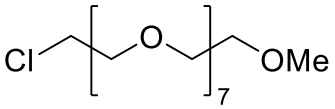

Polyethylene glycol monomethyl ether (7.00 g, 20.0 mmol) was placed under nitrogen in an oven-dried Schlenk flask. pyridine (6.3 g, 80.0 mmol) in dry toluene (80 mL) was then added, and the mixture was stirred and heated slowly to 80 °C. Then, the thionyl chloride (9.5 g, 80.0 mmol) was added dropwise over 20 minutes, and the mixture was stirred for two days at 115 °C. After that, the reaction mixture was cooled to room temperature, and then (10 mL) of water was added to quench the excess of thionyl chloride. The mixture was extracted with toluene (3 x 30 mL), the organic fractions were combined and dried over $MgSO_4$, filtered, and the solvent was removed under reduced pressure to afford PEG-chloride as a pale-yellow oil (8.1 g, 85%). ^{1}H NMR (300 MHz, $CDCl_3$, δ): 3.69 (t, *J* = 5.5 Hz, 2H), 3.63 – 3.55 (m, 28H), 3.50 – 3.46 (m, 2H), 3.31 (s, 3H); ^{13}C NMR (75 MHz, $CDCl_3$, δ): 71.79, 71.88, 70.60, 70.53, 70.45, 58.96, 42.69. This is consistent with data reported in the literature.[4,23]

6.2.7 Synthesis of 2-methyl-1-(2,5,8,11,14,17,20,23-octaoxapentacosan-25-yl)-1H-imidazole (2.7).

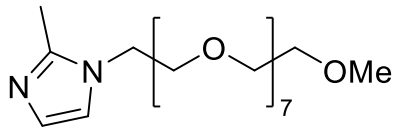

Sodium hydride in oil (0.86 g, 36 mmol) was added to an oven-dried Schlenk flask and washed with dry hexane (2 × 15 mL). The solvent was then removed by cannula filtration, and the reaction flask was charged with dry THF (70 mL) to afford a grey suspension which was cooled to 0 °C. 2-Methyl-imidazole (1.98 g, 24 mmol) was then slowly added to the solution, immediately resulting in effervescence. Once the exotherm had subsided, methyl octaethylene glycol chloride **2.6** (11 g, 29 mmol) was added dropwise to the reaction flask. The dark brown solution was then heated to 75 °C and stirred overnight under N_2. After this time, the reaction mixture was allowed to cool to room temperature and water (2 mL) was added to the solution. After stirring ror 10 min the solvent was removed under high vacuum with an external solvent trap. The resulting dark brown residue was extracted with diethylether (4 × 75 mL), the organic fractions collected and dried with $MgSO_4$ and the solventremoved under reduced pressure to afford an orange viscous oil (6.63 g, 73.7 %). ^{1}H NMR (400 MHz, $CDCl_3$, δ): 6.78 (d, *J* = 1.3 Hz, 1H), 6.75 (d, *J* = 1.3 Hz, 1H), 3.90 (t, *J* = 5.5 Hz, 2H), 3.66 – 3.37 (m, 30H), 3.25 (s, 3H), 2.27 (s, 3H); ^{13}C NMR (101 MHz, $CDCl_3$, δ): 144.59, 126.84, 119.39, 71.76, 70.59, 70.41, 70.32, 58.82, 45.87, 12.97. This is consistent with data reported in the literature.[4,23,24]

6.2.8 Synthesis of 4-vinylbenzyl bromide (2.8).

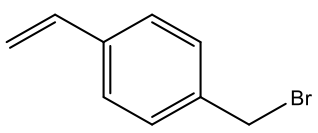

An oven dried Schlenk flask was charged with sodium bromide (15.4 g, 150 mmol), dry acetonitrile (50 mL) and 4-vinylbenzyl chloride (5.72 g, 37.5 mmol). The reaction mixture was stirred and heated overnight at 85 °C. After this time, the mixture was allowed to cool to room temperature, filtered and filtrate dissolved in DCM (60 mL). The solvent was removed under reduced pressure to afford 4 vinylbenzyl bromide as a yellow oil (7.2 g, 97%). ^{1}H NMR (400 MHz, $CDCl_3$) δ 7.43 – 7.33 (m, 4H), 6.71 (dd, *J* = 17.6, 10.9 Hz, 1H), 5.77 (d, *J* = 17.5 Hz, 1H), 5.28 (d, *J* = 10.9 Hz, 1H), 4.50 (s, 2H). ^{13}C NMR (101 MHz, $CDCl_3$) δ 137.80, 137.29, 136.24, 129.35, 126.67, 114.71, 33.52. This is consistent with data reported in the literature.[11,23]

6.2.9 Synthesis of 2-methyl-1-(2,5,8,11,14,17,20,23-octaoxapentacosan-25-yl)-3-(4-vinylbenzyl)-1H-imidazol-3-ium bromide (2.9).

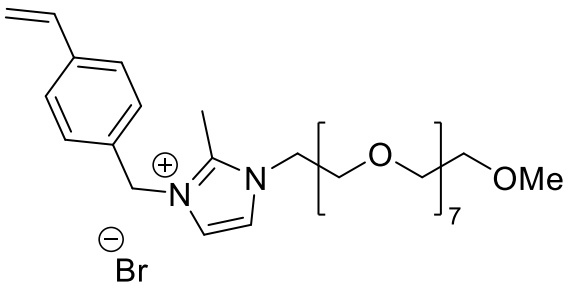

An oven-dried Schlenk under nitrogen was charged with 4-vinyl benzyl bromide **2.8** (3.13 g, 15.9 mmol), 2-methyl-1-PEG-imidazole **2.7** (6.0 g, 14.4 mmol) and dry DCM (100 mL) and the mixture stirred overnight at 35 °C. Afte this time, the solvent was removed under reduced pressure, and the resultant residue was triturated with diethyl ether (5 x 50 mL), forming a viscous pally-yellow oil. The ether was removed under vacuum, and the remaining crude oil was dissolved in DCM (30 mL). The solvent was then removed under reduced pressure to afford **2.9** as a yellow-orange oil (8.3 g, 89%). ^{1}H NMR (400 MHz, $CDCl_3$, δ): 7.85 (s, 1H), 7.48 (s, 1H), 7.37 (d, *J* = 8.0 Hz, 2H), 7.24 (d, *J* = 7.9 Hz, 2H), 6.63 (dd, *J* = 17.6, 10.9 Hz, 1H), 5.72 (d, *J* = 17.6 Hz, 1H), 5.48 (s, 2H), 5.25 (d, *J* = 10.9 Hz, 1H), 4.48 (t, *J* = 4.8 Hz, 2H), 3.86 (t, *J* = 4.7 Hz, 2H), 3.65 – 3.40 (m, 28H), 3.36 – 3.25 (m, 3H), 2.76 (s, 3H);^{13}C NMR (75 MHz, $CDCl_3$, δ): 144.54, 137.63, 135.70, 132.96, 128.15, 126.69, 121.87, 121.57, 114.75, 71.55, 71.45, 70.16, 70.11,

70.04, 68.96, 58.63, 53.66, 51.43, 48.81, 10.63. This data is consistent with data reported in the literature.[11,23]

6.2.10 Synthesis of PIILP (6.1).

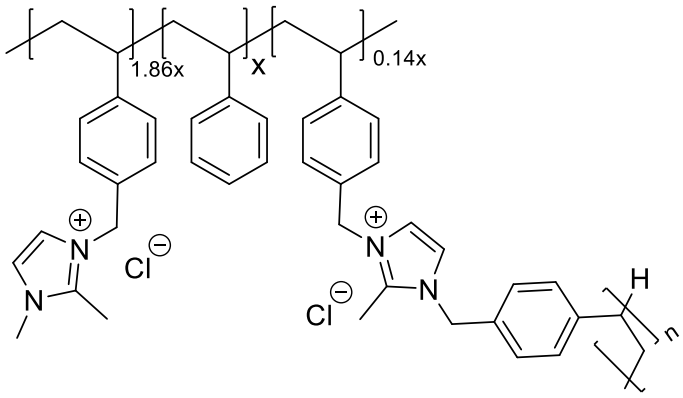

An oven-dried Schlenk flask was charged with styrene (1.5 g, 4.90 mmol), 1,2-dimethyl-3-(4-vinylbenzyl)-1H-imidazole-3-ium chloride **2.1** (6.66 g, 9.10 mmol), 2-methyl-1,3-bis(4vinylbenzyl)-1H-imidazol-3-ium chloride **2.3** (0.70 g, 0.69 mmol) and dry ethanol (80 mL). AIBN (0.331 g, 0.69 mmol) was then added to the reaction flask, which was then immediately immersed in liquid nitrogen and placed under vacuum. The reaction solution was degassed via freeze-thawing the reaction solution six times before being heated to 80 °C and allowed to stir for 4 days. After this time a further portion of AIBN (0.331 g, 0.69 mmol) was then added to the reaction solution and the freeze-thaw cycles repeated. The solution was then allowed to stir for a further day at 80 °C. The crude product was then dissolved in methanol (40 mL), concentrated under reduced pressure and then added to diethyl ether (250 mL) with vigorous stirring. After *ca*. 30 min, the solvent was decanted, the sticky yellow solid residue dried under high vacuum and the resulting solid ground to afford a pale-yellow powder (7.4 g, 86 %).[24]

6.2.11 Synthesis of NH_2-PIILP (2.10).

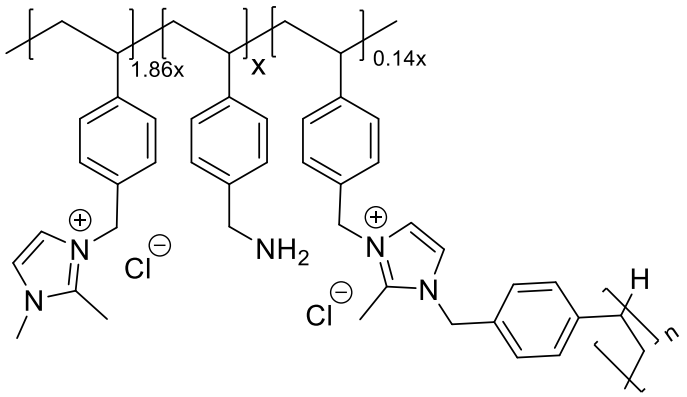

An oven-dried Schlenk flask was charged with 4-vinylbenzyl amine **2.5** (3 g, 22.53 mmol), 1,2-dimethyl-3-(4-vinylbenzyl)-1H-imidazole-3-ium chloride **2.1** (10.42 g, 41.91 mmol) and 2-methyl-1,3-bis(4vinylbenzyl)-1H-imidazol-3-ium chloride **2.3** (1.11 g, 3.15 mmol) and dry ethanol (120 mL). AIBN (0.53 g, 3.15 mmol) was then added to the reaction flask, which was immediately immersed in liquid nitrogen and placed under vacuum The reaction solution was degassed via six freeze-thawing cycles and then heated to 80 °C and allowed to stir for 4 days. After this time a further portion of AIBN (0.53 g, 3.15 mmol) was added to the reaction solution, the freeze-thaw procedure repeated and the solution allowed to stir for a further day at 80 °C. The crude product was then dissolved in methanol (40 mL) concentrated under reduced pressure and the resulting slurry added slowly to diethyl ether (250 mL) with vigorous stirring. The solvent was decantedd the sticky yellow residue dried under a high vacuum and the resulting solid residue ground to afford a pale-yellow powder (15.38 g, 95 %).[24]

6.2.12 Synthesis of NH_2-PEGPIILP (2.11).

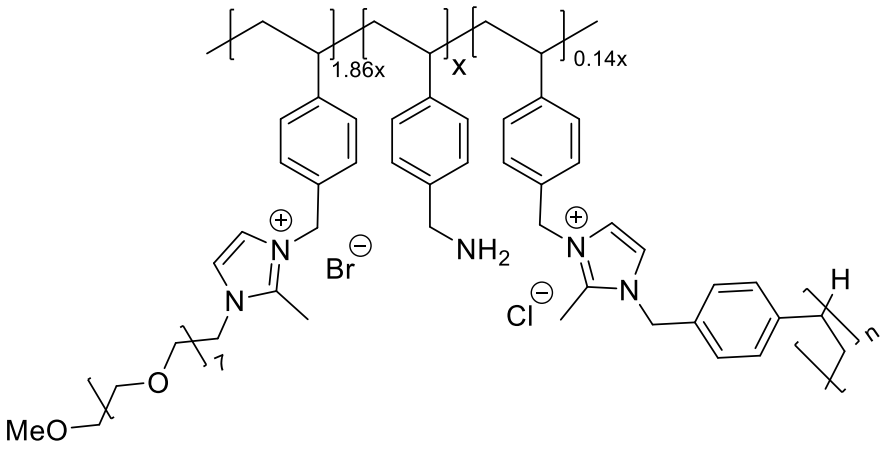

An oven-dried Schlenk flask was charged with 4-vinylbenzyl amine **2.5** (0.65 g, 4.90 mmol), 2-methyl-1-(2,5,8,11,14,17,20,23-octaoxapentacosan-25-yl)-3-(4-vinylbenzyl)-1H-3λ4-imidazolium chloride **2.9** (6.0 g, 9.10 mmol),2-methyl-1,3-bis(4vinylbenzyl)-1h-imidazol-3-ium chloride **2.3** (0.24 g, 0.69 mmol) and dry ethanol (40 mL). AIBN (0.11 g, 0.69 mmol) was then added to the reaction flask, which was immediately immersed in liquid nitrogen and placed under vacuum. The mixture was degassed via six freeze-thawing cycles and then heated to 80 °C and allowed to stir for 4 days. After this time, a further portion of AIBN (0.11 g, 0.69 mmol) was added and the freeze-thaw procedure repeated. The solution was then allowed to stir for a further day at 80 °C. The crude product was then dissolved in methanol (40 mL) concentrated under reduced pressure and the resultingpale-yellow reaction slurry added to diethyl ether (250 mL) with vigorous stirring. The solvent was decanted off and the sticky yellow solid residue was dried under a high vacuum. The resulting solid residue was ground to afford a pale-yellow powder (4.9 g, 71.2 %).[4,24]

6.2.13 Synthesis of RuNP@PIILS (6.2).

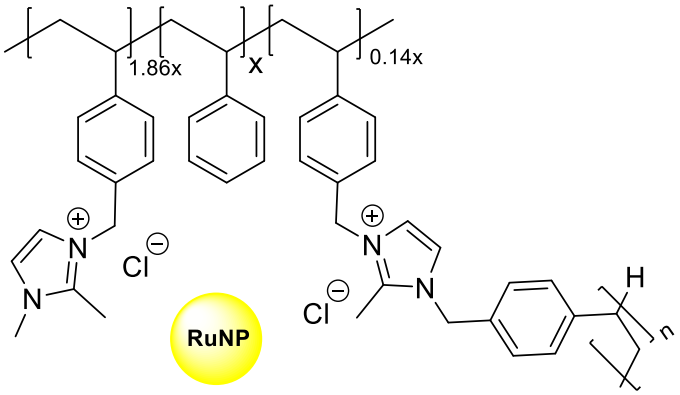

A round bottom flask was charged PIILP **6.1** (5.0 g, 6.21 mmol) and ethanol (80 mL). To this, was added a solution of $RuCl_3 \cdot 3H_2O$ (1.28 g, 6.21 mmol) in ethanol (20 mL) in a single portion and the resulting mixture stirred vigorously overnight at room temperature. After this time, an aqueous solution of $NaBH_4$ (1.87 g, 49.68 mmol in 2 mL of water) was added dropwise to the stirring suspension. The suspension was stirred overnight at room temperature before concentrating to near dryness under vacuo. The crude black solid was triturated with cold

acetone (3 x 10 mL), washed with water (80 mL) and ethanol (2 x 40 mL) the resulting black solid was recovered from the washings via centrifugation followed by filtration through a frit. The final product was washed with ether to afford a fine black powderwhich r was dried under vacuo to afford **6.2** in 87% yield (7.3 g). ICP-OES data: 6.57 wt% ruthenium and a ruthenium loading of 0.65 mmol·g^{-1}.

6.2.14 Synthesis of RuNP@NH$_2$-PIILS (2.14).

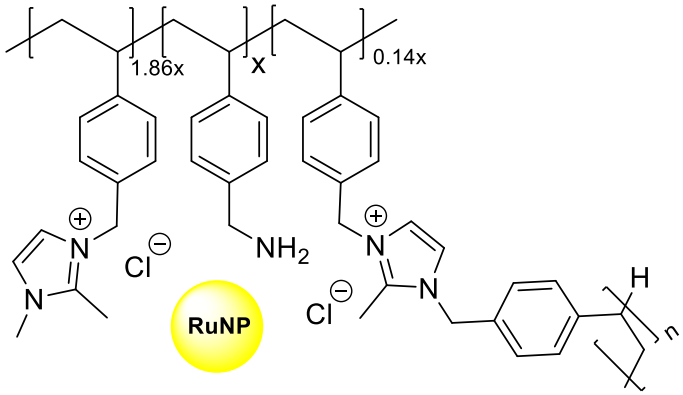

A round bottom flask was charged NH$_2$-PIILP **2.10** (5.0 g, 7.75 mmol) and ethanol (150 mL). To this, a solution of $RuCl_3 \cdot 3H_2O$ (1.60 g, 7.75 mmol) in ethanol (20 mL) was added in a single portion, and the mixture was stirred vigorously overnight at room temperature. After this time, an aqueous solution of $NaBH_4$ (2.34 g, 62 mmol in 2 mL of water) was added dropwise to the stirring suspension. After stirring overnight at room temperature the mixure was concentrated to near dryness under vacuum and the resulting crude black solid triturated with cold acetone (3 x 10 mL) and then washed with water (80 mL) and ethanol (2 x 40 mL). The resulting black solid was recovered from the washings via centrifugation followed by filtration through a frit. The final product was washed with ether until a fine black powder was obtained. The powder was then dried under vacuum to afford **2.14** as a fine black powder in 67% yield (3.88 g). ICP-OES data: 3.43 wt% ruthenium and a ruthenium loading of 0.34 mmol·g^{-1}.

6.2.15 Synthesis of RuNP@NH_2-PEGPIILS (2.15).

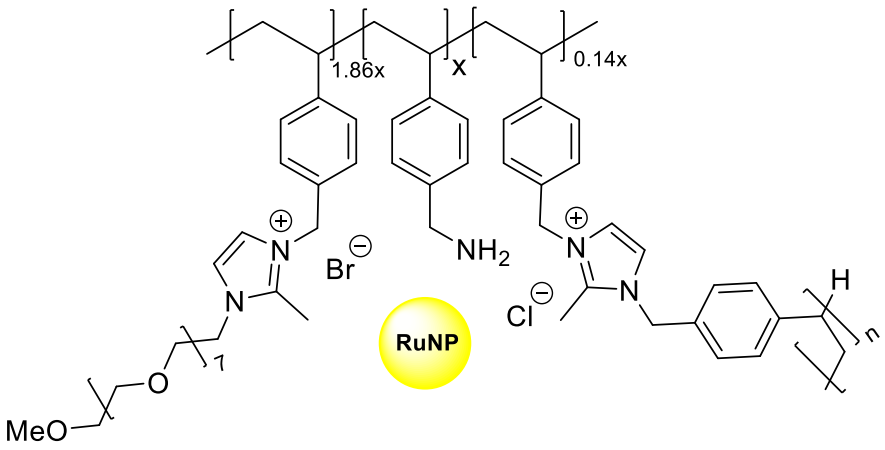

A round bottom flask was charged with NH_2-PIILP **2.11** (4.0 g, 5.11 mmol) and ethanol (150 mL). To this, a solution of $RuCl_3 \cdot 3H_2O$ (1.06 g, 5.11 mmol) in ethanol (20 mL) was added in a single portion and the mixture was stirred vigorously overnight at room temperature. After this time, an aqueous solution of $NaBH_4$ (1.54 g, 40.9 mmol in 2 mL of water) was added dropwise to the stirring suspension. The suspension was stirred overnight at room temperature before concentrating to near dryness under vacuum to afford ablack solid which was triturated with cold acetone (3 x 10 mL) and then washed with water (80 mL) and ethanol (2 x 40 mL). The resulting black solid was recovered from the washings via centrifugation and isolated by filtration through a frit. The final product was washed with ether until a fine black powder was obtained which was then dried under vacuum to afford **2.15** as a fine black powder in 79% yield (3.45 g). ICP-OES data: ICP-OES data: 7.54 wt% ruthenium and a ruthenium loading of 0.75 mmol g^{-1}.

6.2.16 Ruthenium Nanoparticle-Catalysed Hydrolysis of Sodium Borohydride.

Comparative catalytic hydrolysis reactions were conducted in water at the appropriate temperature in a 50 mL round bottom flask. The flask was charged with a stir bar, an appropriate quantity of catalyst (0.2 mol%) and $NaBH_4$ (0.021 g, 0.57 mmol) and fitted with a gas outlet connected to the top of an inverted water-filled burette. The flask was stabilised at

303 K, and the reaction was initiated by adding water (2 mL), immediately sealing the system by replacing the gas outlet, opening the tap of the water-filled burette and recording the time zero volume. Gas evolution began immediately, and the progress of the reaction was monitored by measuring the amount of gas generated by recording the volume of water displaced from the burette at regular time intervals (15 sec).[23] The optimum turnover frequency for each catalyst was determined by conducting experiments with catalyst loadings ranging from 0.08 – 0.32 mol% at 303 K and measuring the hydrogen generated, as described above. Kinetic studies were also conducted as described above using the following catalyst loadings: 0.16 mol% **2.14** and 0.32 mol% **2.15** across a range of temperatures (294 K, 298 K, 303 K, 308 K, 313 K) and the corresponding activation energies (E_a) were determined from an Arrhenius plot of the initial rate against 1/T.

6.2.17 Determination of the Reaction Order for the RuNP-Catalysed Hydrolysis of Sodium Borohydride.

The rate law was investigated by conducting the catalytic hydrolysis reactions at 298 K with a constant concentration of $NaBH_4$ (0.28 M, 0.021 g in water (2 mL)) across a range of catalyst concentrations from 0.12 mol% to 0.27 mol% for **2.14** and 0.24 mol% to 0.64 mol% for **2.15**. The influence of sodium borohydride concentration on the rate of hydrolysis was determined by conducting reactions at 298 K in water (200 mL) using 0.026 mmol of catalyst **2.14** (0.0764 g) and **2.15** (0.0376 g) and varying the quantity of sodium borohydride between 6.6 μmole and 18.5 μmole (i.e. $[NaBH_4]_0$ = 0.035, 0.07, 0.13, 0.26, 0.39, 0.53, 0.65, 0.78, 0.9 mM), which corresponds to catalyst:$NaBH_4$ ratios between 4:1 and 1:6. The influence of sodium borohydride concentration on the rate of hydrolysis at high concentrations of sodium borohydride, *i.e*. under the conditions of catalysis, was also determined using **2.14** (0.0026 g, 0.884 μmol) to catalyse the hydrolysis of $NaBH_4$ solutions (2 mL) across a range of sodium borohydride concentrations from 0.55 mmol to 2.2 mmol (i.e. $[NaBH_4]_0$ = 0.28, 0.56, 0.83, 1.11 M).

6.2.18 Study of the Catalytic Efficiency as a Function of the Concentration of NaOH.

The influence of the concentration of NaOH on catalyst efficacy was investigated by conducting catalytic hydrolysis reactions at 303 K with 2 mL of alkaline 0.28 M $NaBH_4$ (0.021 g) across a range of sodium hydroxide concentrations (i.e. [NaOH] = 0.035, 0.07, 0.14, 0.28, 5.0, 10, 50, 100 mM) catalysed by 0.26 mol% **2.14** (0.0025 g) and monitoring the gas evolution as a function of time.

6.2.19 Catalyst Recycle Studies for the Hydrolysis of Sodium Borohydride.

Recycle studies were conducted at 303 K as described above using 2mol% of **2.14** (0.0335 g, 0.0114 mmol) to catalyse the hydrolysis of sodium borohydride (0.021 g, 0.57 mmol in water (20 mL).[24] After gas evolution had ceased, the flask was recharged with a fresh portion of sodium borohydride (0.021 g, 0.57 mmol) and the gas evolution monitored by recording the volume of water displaced from the burette at regular time intervals; this procedure was repeated five times. After the 5th run, samples of the catalysts were isolated and analysed by TEM.

6.2.20 Catalyst Recycle Studies in the Presence of Buffer.

A borate-buffered solution was prepared by dissolving $Na_2B_4O_7{\cdot}10H_2O$ (9.53 g, 25 mmol) and NaCl (4.39 g, 75 mmol) in distilled water (900 mL) in a volumetric flask. When the borate was completely dissolved, the pH of the solution was adjusted to 7.2 by gradually adding boric acid (20.99 g, 0.34 mol); the solution was then made up to one litre. Recycle studies were conducted by adding $NaBH_4$ (0.021 g, 0.57 mmol) to a flask containing 1 mol% **2.14** (0.0165 g, 0.0056 mmol) and 20 mL of the aqueous borate buffer solution. The flask was maintained at 303 K, and the progress of the reaction monitored as described above. When the hydrolysis was complete, an additional portion of fresh sodium borohydride (0.021 g, 0.57 mmol) was added, and the procedure was repeated for comparison with the recycling study described above in the absence of buffer.[25]

6.2.21 Filtration Tests.

Hot filtration studies were conducted at 303 K following the protocol described above using 0.16 mol% **2.14** (0.0026 g) to catalyse the hydrolysis of sodium borohydride (0.021 g, 0.57 mmol in water (2 mL). The reaction was monitored by periodically measuring the amount of gas generated, and when the reaction had reached about 50% conversion (7.75 min for 2.14), the reaction mixture was quickly filtered through a 0.45 μm syringe filter, and the gas generated was monitored for a further 30 min. In an alternative procedure, a catalytic hydrolysis of $NaBH_4$ (0.021 g, 0.57 mmol) using 0.16 mol% **2.14** was allowed to reach completion, after which the reaction mixture was filtered through a 0.22 μm diameter syringe filter, a further portion of $NaBH_4$ added (0.021 g, 0.57 mmol) and the amount of gas evolved measured.[25]

6.2.22 Catalyst Poisoning Study.

A 50 mL round bottom flask was charged with a stir bar, 2 mol% catalysts **2.14** (0.0335 g), water (20 mL) and sodium metaborate (0.0765 g, 0.57 mmol) and the mixture stirred at 303 K for the allocated time (t = 0 min, 20 min, 40 min, 60 min) to explore the effect of poisoning time on catalyst efficacy.[23] The reaction was initiated by adding $NaBH_4$ (0.021 g, 0.57 mmol) and the progress of the reaction was monitored by periodically measuring the amount of gas generated according to the procedure described above.[25]

6.3 Experimental for Chapter 3: Application of NH_2-PEGPIILS Catalyst to the Partial and Complete Reduction of Quinolines

6.3.1 General Procedure for the Reduction of Quinolines

An oven-dried Schlenk flask was cooled to room temperature under a vacuum back-filled with nitrogen and charged with 0.25 mol% of RuNP@NH_2-PEGPIILS **3.1** (0.0145 g, 2.5 mmol), dimethylamine borane (0.1472 g, 2.5 mmol) and anhydrous toluene (3 mL). After stirring the resulting suspension for 5 minutes, quinoline (0.118 mL, 1.0 mmol) was added, and the mixture was stirred at the specified temperature for the allocated time. The reaction mixture was quenched by adding deionised water (5 mL), the product extracted with ethyl acetate (3 x 5 mL), the organic fractions collected, and the solvent removed under reduced pressure to obtain the product. The residue was analysed by ^{1}H NMR spectroscopy using 1,4-dioxane as an internal standard to quantify the composition of the starting material and products and to determine the selectivity.[25]

6.3.2 Procedure for the Hot Filtration Study

Following the abovementioned general procedure, quinoline (0.118 mL, 1.0 mmol) was reduced to tetrahydroquinoline in toluene at 65 °C using 0.1 mol% **3.1** (0.0058 g, 1.0 mmol). After 60 minutes, the reaction mixture was filtered through a 0.45-micron syringe filter into a clean Schlenk flask under an inert atmosphere. The filtered reaction mixture was then stirred at 65 ^{o}C for a further 180 minutes, and the progress of the reaction was monitored as a function of time by removing aliquots every 30 min for analysis by NMR spectroscopy.[25]

6.3.3 Procedure for the Catalyst Reuse Study

Quinoline (0.118 mL, 1.0 mmol) was reduced to tetrahydroquinoline at 65 °C in toluene using 0.25 mol% **3.1** (0.0145 g, 2.5 mmol) following the general procedure described above and the progress of the reaction was monitored by ^{1}H NMR spectroscopy. When the quinoline had been completely consumed, the reaction flask was recharged with a further portion of quinoline and five equivalents of dimethylamine borane (0.294 g, 5.0 mmol) and the procedure was repeated. Following the 4th run, the catalyst was isolated, washed with water (2 x 10 mL) and ethyl acetate and analysed by TEM.[26]

6.3.4 General Procedure for the Poisoning Studies as a Function of Pre-stirring Time

An oven-dried Schlenk flask was cooled to room temperature under vacuum, backfilled with nitrogen and charged with 0.25 mol% **3.1** (0.0145 g, 2.5 mmol), dimethylamine borane (0.1472 g, 2.5 mmol), anhydrous toluene (3 mL) and 1,2,3,4-tetrahydroquinoline (1.0 mmol) and the resulting mixture was stirred for the allocated time (0, 20, or 60 min) to explore the effect of pre-stirring time on catalyst efficacy. The reaction was initiated by adding quinoline (0.118 mL, 1.0 mmol) and the mixture was left to stir for four hours at room temperature. The reaction mixture was quenched by adding deionised water (5 mL), the product extracted with ethyl acetate (3 x 5 mL), the organic fractions collected, and the solvent removed under reduced pressure. The resulting residue was analysed by ^{1}H NMR spectroscopy to quantify the composition of the starting material and products and to determine the selectivity.[26]

6.3.5 Characterisation Data for 1,2-Dihydroquinolines and 1,2,3,4-Tetrahydroquinolines.

I. 1,2,3,4-Tetrahydroquinoline

1,2,3,4-Tetrahydroquinoline was obtained with 99% selectivity at 96% conversion after 4 h by reduction of quinoline following the general procedure described above. ^{1}H NMR (300 MHz, $CDCl_3$, δ): 7.15 (ddd, *J* = 7.4, 3.9, 2.6 Hz, 2H), 6.80 (td, *J* = 7.4, 1.1 Hz, 1H), 6.62 (d, *J* = 8.4 Hz, 1H), 3.92 (br s, 1H), 3.34 (t, *J* = 6.5 Hz, 2H), 2.94 (t, *J* = 6.5 Hz, 2H), 2.13 – 2.07 (m, 2H). ^{13}C NMR (300 MHz, $CDCl_3$, *δ*): 144.96, 129.66, 126.88, 121.53, 117.16, 114.37, 42.05, 27.22, 22.55. The spectroscopic data is consistent with that reported in the literature.[5]

II. 6-Bromo-1,2,3,4-tetrahydroquinoline

6-Bromo-1,2,3,4-tetrahydroquinoline was obtained with 51% selectivity at 93% conversion after 10 h by reduction of 6-bromoquinoline following the general procedure described above. ^{1}H NMR (300 MHz, $CDCl_3$, *δ*): 7.07 – 7.00 (m, 2H), 6.33 (d, *J* = 8.4 Hz, 1H), 3.83 (br s, 1H), 3.27 (t, *J* = 6.5 Hz, 2H), 2.72 (t, *J* = 6.5 Hz, 2H), 1.94 – 1.86 (m, 2H). ^{13}C NMR (300 MHz, $CDCl_3$, *δ*): 144.2, 132.51, 130.06, 123.86, 114.5, 109.04, 42.44, 27.06, 22.32. The spectroscopic data is consistent with that reported in the literature.[6–8]

III. 5-Bromo-1,2,3,4-tetrahydroquinoline

5-Bromo-1,2,3,4-tetrahydroquinoline was obtained with 40% selectivity at 91% conversion after 10 h by reduction of 5-bromoquinoline following the general procedure described above. ^{1}H NMR (300 MHz, $CDCl_3$, *δ*): 6.88 – 7.78 (m, 2H), 6.40 (d, *J* = 8.4 Hz, 1H), 3.83 (br s, 1H), 3.26 (t, *J* = 6.5 Hz, 2H), 2.76 (t, *J* = 6.5 Hz, 2H), 1.99 – 1.91 (m, 2H). ^{13}C NMR (300 MHz, $CDCl_3$, *δ*): 146.66, 127.73, 126.54, 121.03, 120.88, 113.33, 40.92, 27.82, 22.39. The spectroscopic data is consistent with that reported in the literature.[9–11]

IV. 6-Methoxy-1,2,3,4-tetrahydroquinoline

6-Methoxy-1,2,3,4-tetrahydroquinoline was obtained with 100% selectivity at 76% conversion after 16 h by reduction of 6-methoxyquinoline following the general procedure described above. ^{1}H NMR (300 MHz, $CDCl_3$, *δ*): 6.62 – 6.55 (m, 2H), 6.45 (d, *J* = 8.6 Hz, 1H), 3.73 (s, 3H), 3.28 – 3.23 (t, *J* = 6.5 Hz, 2H), 2.76 (t, *J* = 6.5 Hz, 2H), 1.97 – 1.90 (m, 2H). ^{13}C NMR (300 MHz, $CDCl_3$, *δ*): 151.95, 139.00, 123.00, 115.68, 115.03, 113.03, 55.95, 42.47, 27.30, 22.58. The spectroscopic data is consistent with that reported in the literature.[7,12,13]

V. 6-Methyl-1,2,3,4-tetrahydroquinoline

6-Methyl-1,2,3,4-tetrahydroquinoline was obtained with 98% selectivity at 100% conversion after 16 h by reduction of 6-methylquinoline following the general procedure described above. ^{1}H NMR (300 MHz, $CDCl_3$, δ): 6.77 (s, 2H), 6.41 (d, *J* = 8.6 Hz, 1H), 3.86 (bs, 1H), 3.27 (t, *J* = 6.4 Hz, 2H), 2.73 (t, *J* = 6.4 Hz, 2H), 2.20 (s, 3H), 1.96 – 1.89 (m, 2H). ^{13}C NMR (300 MHz, $CDCl_3$, *δ*): 142.76, 130.49, 127.65, 126.72, 122.05, 114.90, 42.59, 27.31, 22.83, 20.80. The spectroscopic data is consistent with that reported in the literature.[8,9,11,13,14]

VI. 5-Amino-1,2,3,4-tetrahydroquinoline

5-Amino-1,2,3,4-tetrahydroquinoline was obtained with 80% selectivity at 98% conversion after 16 h by reduction of 5-aminoquinoline following the general procedure described above. ^{1}H NMR (300 MHz, $CDCl_3$, *δ*): 6.39 (d, *J* = 9.8 Hz, 1H), 5.92 (d, *J* = 7.9 Hz, 1H), 5.30 (s, 2H), 3.61 (s, 3H), 3.24 (m, 2H), 2.48 (t, *J* = 6.6 Hz, 2H), 2.04–1.95 (m, 2H). ^{13}C NMR (300 MHz, $CDCl_3$, *δ*): 134.28, 122.07, 117.55, 116.50, 115.31, 107.96, 43.01, 27.48, 23.19. The spectroscopic data is consistent with that reported in the literature.[15,16]

VII. 6-Amino-1,2,3,4-tetrahydroquinoline

6-Amino-1,2,3,4-tetrahydroquinoline was obtained with 98% selectivity at 80% conversion after 16 h by reduction of 6-aminoquinoline following the general procedure described above. ^{1}H NMR (300 MHz, $CDCl_3$, δ): 6.83 (d, J = 9.8 Hz, 1H) 6.18 (dt, J = 9.8,2.0 Hz, 1H), 5.66 (dt, J = 9.8, 4.1 Hz, 1H), 5.30 (s, 2H), 3.95 (t, J = 6.4 Hz, 2H), 3.16 (m, 2H), 2.63 (t, J = 6.4 Hz, 2H), 1.91 (m, 2H). ^{13}C NMR (300 MHz, $CDCl_3$, δ): 133.78, 121.56, 117.05, 115.99, 114.80, 107.45, 42.50, 26.97, 22.68. The spectroscopic data is consistent with that reported in the literature.[12,17]

VIII. *N*-Ethyl-1,2,3,4-tetrahydroquinoline

N-Ethyl-1,2,3,4-tetrahydroquinoline was obtained with 100% selectivity at 99% conversion after 16 h by reduction of *N*-ethylquinolinium bromide following the general procedure described above. ^{1}H NMR (300 MHz, $CDCl_3$, δ): 7.01 (t, J = 7.5 Hz, 1H), 6.85 (d, J = 7.3 Hz, 1H), 6.55 (d, J = 7.5 Hz, 2H), 6.45 (t, J = 7.3 Hz, 1H), 3.25 (q, J = 7.1 Hz, 2H), 3.44 (q, J = 5.6 Hz, 2H), 2.65 (t, J = 6.4 Hz, 2H), 1.75 (m, 2H), 1.10 (t, J = 7.1 Hz, 3H). ^{13}C NMR (300 MHz, $CDCl_3$, δ): 143.98, 128.12, 126.02, 121.41, 114.31, 109.49, 47.36, 44.28, 27.16, 21.27. The spectroscopic data is consistent with that reported in the literature.[18]

IX. 3-Bromo-1,2-dihydroquinoline

5-Bromo-1,2-dihydroquinoline was obtained with 97% selectivity at 100% conversion after 4 h by reduction of 3-bromoquinoline following the general procedure described above. ^{1}H NMR (300 MHz, $CDCl_3$, δ): 6.90 (td, J = 7.4, 1.1 Hz, 1H), 6.72 (dd, J = 7.5, 1.6 Hz, 1H), 6.58 (s, 1H), 6.33 (dt, J = 7.9, 1.0 Hz, 1H), 4.32 (d, J = 1.6 Hz, 2H), 3.69 (br, 1H). ^{13}C NMR (300 MHz, $CDCl_3$, δ): 137.30, 129.03, 127.67, 126.43, 118.18, 115.31, 112.70, 60.41, 50.62. The spectroscopic data is consistent with that reported in the literature.[19]

X. 3-Methyl-1,2-dihydroquinoline

3-Methyl-1,2-dihydroquinoline was obtained with 100% selectivity at 94% conversion after 8 h by reduction of 5-aminoquinoline following the general procedure described above. ^{1}H NMR (300 MHz, $CDCl_3$, δ): 6.90 (td, J = 7.6, 1.6 Hz, 1H), 6.78 (dd, J = 7.4, 1.6 Hz, 1H), 6.57 (td, J = 7.4, 1.2 Hz, 1H), 6.38 (dt, J = 7.9, 1.0 Hz, 1H), 6.08 (s, 1H), 4.05 (t, J = 1.3 Hz, 2H), 1.76 (t, J = 1.3 Hz, 3H).^{13}C NMR (300 MHz, $CDCl_3$, δ): 143.88, 129.84, 126.84, 123.03, 121.8, 119.25, 115.85,

111.8, 48.63, 18.95. The spectroscopic data is consistent with that reported in the literature.[14,19]

XI. 3-Acetyl-1,2-dihydroquinoline

3-Acetyl-1,2-dihydroquinoline was obtained with 100% selectivity at 100% conversion after 8 h by reduction of 3-acetylquinoline following the general procedure described above. ^{1}H NMR (300 MHz, $CDCl_3$, *δ*): 6.95 (td, *J* = 7.6, 1.5 Hz, 1H), 6.87 (dd, *J* = 7.4, 1.6 Hz, 1H), 6.60 (td, *J* = 7.4, 1.1 Hz, 1H), 6.43 (dt, *J* = 8.1, 1.0 Hz, 1H), 6.29 (s, 1H), 4.4 (q, *J* = 6.5 Hz, 1H), 4.12 (s, 2H), 1.34 (d, *J* = 6.5 Hz, 3H). ^{13}C NMR (300 MHz, $CDCl_3$, *δ*): 144.86, 136.1, 127.35, 126.2, 121.67, 120.14, 119.29, 109.2, 68.7, 41.1, 19.1. The spectroscopic data is consistent with that reported in the literature.[19]

XII. 1,2-Dihydroquinoline-3-carboxaldehyde

1,2-Dihydroquinoline-3-carboxaldehyde was obtained with 100% selectivity at 95% conversion after 5 h by reduction of 3-quinolinecarboxaldehyde following the general procedure described above. ^{1}H NMR (300 MHz, $CDCl_3$, *δ*): 6.94 (dt, *J* = 7.9, 1.4 Hz, 1H), 6.86 (dd, *J* = 7.4, 1.2 Hz, 1H), 6.60 (td, *J* = 7.4, 0.9 Hz, 1H), 6.41 (d, *J* = 7.9 Hz, 1H), 6.30 (s, 1H), 4.14 (d, *J* = 3.8 Hz, 2H), 3.76 (s, 1H). ^{13}C NMR (300 MHz, $CDCl_3$, δ): 143.4, 132.7, 127.6, 125.4, 120.9, 119.7, 116.97, 111.8, 64.1, 41.9. The spectroscopic data is consistent with that reported in the literature.[19]

XIII. 9,10-Dihydroacridine

9,10-Dihydroacridine was obtained with 100% selectivity at 100% conversion after 1 h by reduction of acridine following the general procedure described above. ^{1}H NMR (300 MHz, $CDCl_3$, *δ*): 7.09 (dd, *J* = 14.9, 7.9 Hz, 4H), 6.85 (td, *J* = 7.9, 1.1 Hz, 2H), 6.67 (d, *J* = 7.9 Hz, 2H), 5.95 (s, 1H), 4.06 (s, 2H). ^{13}C NMR (300 MHz, $CDCl_3$, *δ*): 140.65, 129.13, 127.53, 121.17, 120.75, 113.96, 31.92. The spectroscopic data is consistent with that reported in the literature.[5,8,19,20]

XIV. 5,6-Dihydrophenanthridine

5,6-Dihydrophenanthridine was obtained with 100% selectivity at 100% conversion after 1 h by reduction of phenanthridine following the general procedure described above. ^{1}H NMR (300 MHz, $CDCl_3$, *δ*): 7.69 (ddd, *J* = 7.7, 3.5, 1.3 Hz, 2H), 7.31 (td, *J* = 7.6, 1.3 Hz, 1H), 7.22 (td, *J*

= 7.4, 1.3 Hz, 1H), 7.11 (m, 2H), 6.84 (td, *J* = 7.5, 1.3 Hz, 1H), 6.67 (td, *J* = 7.9, 1.3 Hz, 1H), 4.40 (s, 2H), 3.98 (s, 1H). ^{13}C NMR (300 MHz, $CDCl_3$, *δ*): 144.8, 132.7, 131.1, 128.8, 128.2, 127.1, 126.6 125.3, 123.6, 122.4, 119.29, 115.13, 46.40. The spectroscopic data is consistent with that reported in the literature.[19–21]

6.4 Experimental for Chapter 4: Efficient Hydrogen Evolution from Amine Borane Catalysed by Ru and Pt Nanoparticles Stabilised by an Amine Decorated Polymer Immobilised Ionic Liquid.

6.4.1 Synthesis of $PtCl_4$@NH_2-PEGPIILS (4.2)

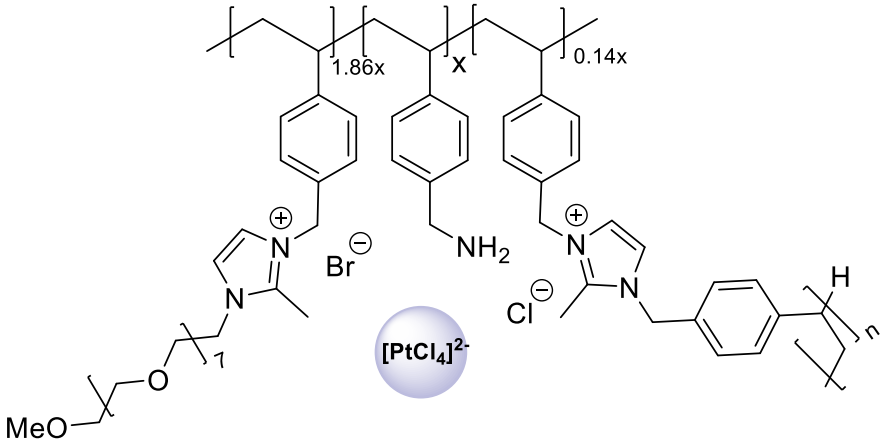

A round bottom flask was charged with NH_2-PEGPIIL **4.1** (5.0 g, 3.79 mmol) and water (70 mL) and stirred vigorously while adding a solution of $K_2[PtCl_4]$ (1.57 g, 3.79 mmol) in water (5 mL). The resulting red/orange mixture was stirred for 12 h after which time, the solvent was removed under reduced pressure, and the resulting sticky residue dissolved in the minimum volume of dichloromethane. The product was precipitated by addition to a beaker containing rapidly stirred diethyl ether (500 mL). The resulting cream-yellow precipitate was allowed to settle, and most of the solvent was decanted before isolating the product by filtration. The solid was washed with diethyl ether and dried exhaustively under a high vacuum to afford the tetrachloroplatinate-loaded precursor **4.2** in 96% yield (6.02 g, 3.64 mmol). ICP-OES data: 8.5 wt% platinum corresponding to a platinum loading of 0.43 mmol g^{-1}.

6.4.2 Synthesis of PtNP@NH_2-PEGPIILS (4.3)

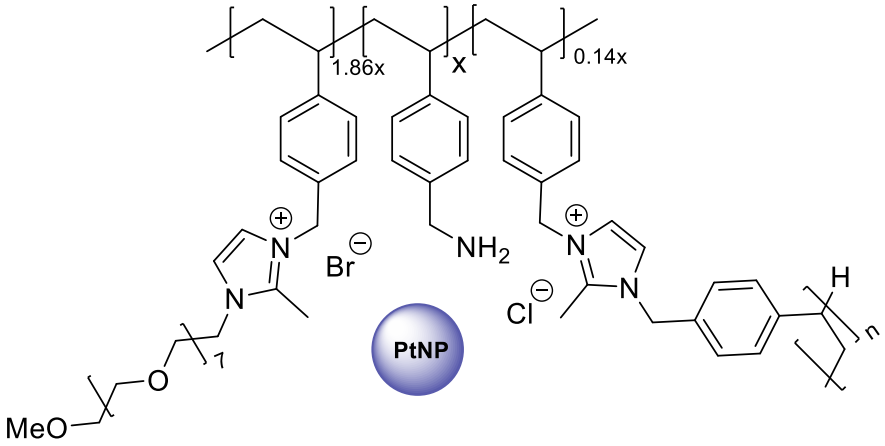

A round bottom flask was charged with [$PtCl_4$]@NH_2-PEGPIILS (**4.2**) (3.0 g, 1.18 mmol) and ethanol (60 mL), and the resulting suspension was stirred vigorously and treated dropwise with a solution of $NaBH_4$ (0.55 g, 14.49 mmol) in water (3 mL). The mixture instantly turned from cream yellow to black. After stirring at room temperature, the solvent was removed under vacuum and the resulting residue was triturated with acetone (3 x 20 mL), transferred to a sintered glass frit and washed with water (2 x 20 mL) ethanol (3 x 20 mL) and diethyl ether (3 x 20 mL) and dried under high vacuum to afford **4.3** as a black solid in 95% yield (2.85 g, 1.122 mmol). ICP-OES data: 5.3 wt% platinum corresponding to a platinum loading of 0.28 mmol g^{-1}.[23]

6.4.3 Catalytic Hydrolysis of Dimethylamine Borane, Ammonia Borane and Sodium Borohydride.

Catalytic hydrolysis reactions were typically conducted in water at the appropriate temperature in a thermostated 50 mL round bottom flask. The flask was charged with a stir bar, an appropriate quantity of catalyst (0.25 mol%, 0.005 g of PtNP@NH_2-PEGPIILS (**4.3**); 0.25 mol% 0.002 g of RuNP@NH_2-PEGPIILS (**4.4**)) and either DMAB (0.032 g, 0.57 mmol), AB (0.0176 g, 0.57 mmol) or $NaBH_4$ (0.021 g, 0.57 mmol) and fitted with a gas outlet which was connected to the top of an inverted water-filled burette. The reaction was initiated by adding water (2 mL), immediately sealing the system by replacing the gas outlet, opening the tap of the water-filled burette and recording the time zero volume. Gas evolution began immediately, and the

progress of the reaction was monitored by measuring the amount of gas liberated by recording the volume of water displaced from the burette at regular time intervals (15 sec). Kinetic studies were also conducted as described above using 0.25 mol% **4.3** and **4.4** across a range of temperatures (21 °C, 25 °C, 30 °C, 35 °C, 40 °C and 45 °C) to determine the activation energy (E_a).

6.4.4 Determination of the Reaction Order for the Catalytic Hydrolysis of Dimethylamine Borane, Ammonia Borane and Sodium Borohydride

The rate law was investigated by conducting a series of catalytic hydrolysis reactions at 298 K with a solution of DMAB (0.27 M, 0.032 g in 2 mL water), ammonia borane (0.27 M, 0.017 g in 2 mL water) or $NaBH_4$ (0.27 M, 0.021 g in 2 mL water) across a range of catalyst concentrations to determine the reaction order in catalyst. The influence of dimethylamine borane concentration on the rate of hydrolysis was also determined by conducting reactions at 298 K in water (200 mL) with catalysts **4.3** and **4.4** (17 μmol) and varying the quantity of dimethylamine borane from 17 *m*mole to 102 *m*mole ($[DMAB]_0$ = 0.085 mM – 0.51 mM), corresponding to catalyst:DMAB ratios between 1:1 and 1:6. Similarly, the influence of AB and $NaBH_4$ concentration on the rate of hydrolysis was also determined by following the same protocol using **4.3** and **4.4** and varying the quantity of substrate.

6.4.5 Catalyst Recycle Studies

Recycle studies were conducted at 303 K using 2 mol% **4.4** (0.017 g, 11.4 μmol) to catalyse the hydrolysis of dimethylamine borane (0.033 g, 0.52 mmol, 20 mL water). After gas evolution had ceased, the flask was recharged with a fresh portion of dimethylamine borane (0.033 g, 0.57 mmol) and the gas evolution was monitored by recording the volume of water displaced from the burette at regular time intervals; this procedure was repeated 5 times.[24] After the 5th run, a sample of catalyst **4.4** was isolated and analysed by TEM-EDX to explore the extent of boron fouling.

6.4.6 Hot Filtration Studies

A Hot Filtration (HF) study was conducted at 303 K following the protocol described above using 0.26 mol% **4.4** to catalyse the hydrolysis of dimethylamine borane (0.032 g, 0.57 mmol in 2 mL water). The reaction was monitored by periodically measuring the amount of gas generated and when the reaction had reached *ca*. 50% conversion (4 min) the reaction mixture was quickly filtered through a 0.45 μm syringe filter, and the gas generated was monitored for a further 30 min. In an alternative procedure, a catalytic hydrolysis of DMAB (0.032 g, 0.57 mmol) using 0.32 mol% **4.4** was allowed to reach completion, after which the reaction mixture was filtered through a 0.22 μm diameter syringe filter, a further portion of DMAB added (0.032 g, 0.57 mmol) and the amount of gas evolved measured.

6.5 Experimental for Chapter 5: Ruthenium and Platinum Nanoparticles Immobilised on Ionic Functionalised Mesoporous Silica as Catalysts for Selective Hydrogen Evolution from NaBH4

6.5.1 Synthesis of 1,2-dimethyl-3-(3-(triethoxysilyl)propyl)-1H-imidazol-3-ium chloride (5.3)

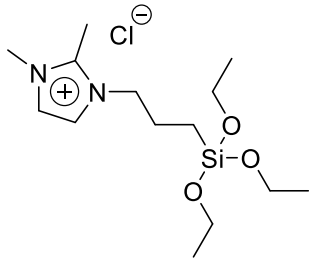

1,2-Dimethylimidazole **5.1** (2.29 g, 0.02 mol, one equiv.) and 3-chloropropyltriethoxysilane **5.2** (5.7 g, 0.02 mol, one equiv.) were combined in a dry Schlenk flask under a nitrogen atmosphere. The flask was then evacuated, purged with nitrogen five times, and heated at 90 ^{o}C for three days. Upon cooling to room temperature, the resulting solid was repeatedly mixed

with dry diethyl ether, and the solvent was removed by a syringe each time. The remaining solid was then dried under vacuum at room temperature for 2 days to afford the title compound **5.3** (7.4 g, 93 %) as a white solid. ^{1}H NMR (300 MHz, $CDCl_3$, δ): 7.89 (d, J = 2.2 Hz, 1H), 7.48 (d, J = 2.1 Hz, 1H), 4.19 (t, J = 7.4 Hz, 2H), 4.02 (s, 3H), 3.75 (q, J = 7.0 Hz, 6H), 2.77 (s, 3H), 1.94-1.78 (m, 2H), 1.15 (t, J = 7.0 Hz, 9H), 0.58-0.53 (m, 2H). ^{13}C NMR (75 MHz, $CDCl_3$, δ): 123.4, 121.0, 58.7, 50.4, 36.0, 23.8, 18.3, 10.4, 7.1. These data are consistent with those published in the literature.[22]

6.5.2 Synthesis of unfunctionalised COK-12 mesoporous material (5.8).

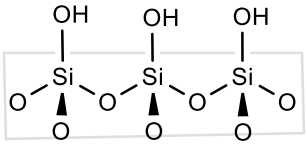

According to a previously published method,[22] the triblock copolymer Pluronic P123 (14.35 g) was dissolved in 385 mL of water and stirred at room temperature overnight until completely dissolved. The next day, citric acid monohydrate (13.21 g, 62.87 mmol) and trisodium citrate (9.10 g, 30.97 mmol) were added to the solution and stirred for 24 hours. Then, a solution of sodium silicate (37.30 g of a solution containing 26.5% SiO_2 w/w, 165 mmol) diluted in 107 mL of water was added dropwise to the surfactant solution to prevent aggregate formation. The solution was stirred for 5 minutes at 175-180 rpm using a magnetic stirrer, then left at room temperature without agitation for 24 hours. The resulting material was filtered, washed with 3 x 150 mL of water, and dried in an oven at 55 ^{o}C overnight. This process yielded P123@COK-12 (24.8 g) as a powdery white solid, which was subsequently extracted with 150 mL of ethanol for 15 days using a Soxhlet extractor to obtain **5.8** as a white solid (9.5 g, 96%).

6.5.3 General procedure for the synthesis of ionic liquid and amine modified COK-12 supports (5.10), (5.11) .

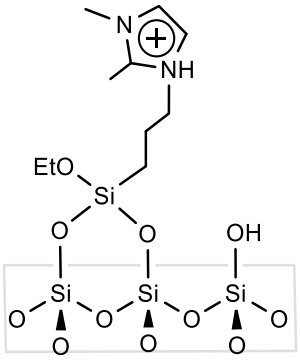

5.10

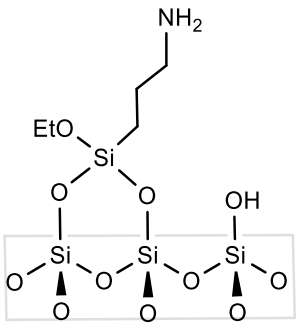

5.11

Following the procedure described above for the synthesis of COK-12 **5.8**, the triblock co-polymer Pluronic P123 (14.35 g) was dissolved in deionised water (385 mL). The mixture was stirred at room temperature until all the Pluronic had completely dissolved. Following this, 13.21 g (62.87 mmol) of citric acid monohydrate and 9.11 g (30.97 mmol) of trisodium citrate were added to the solution, and the resulting surfactant solution was stirred for 24 hours. A sodium silicate (35.4 g) of a solution containing 27 wt% SiO_2 (165 mmol) was diluted with (102 mL) of water and added dropwise to the surfactant solution, along with 5 mol% of the corresponding imidazolium silica precursor 1,2-dimethyl-3-(3-(triethoxysilyl)propyl)-1H-imidazol-3-ium chloride (1.48 g) or 5 mol% of triethoxysilylpropylamine (2.68 g) as amine silica precursors, to prevent aggregate formation. The solution was stirred at 175–180 rpm for 5 minutes and then left at room temperature without agitation for 24 hours. After this time, the solid was filtered, washed with water (4 x 150 mL), and dried in a vacuum oven overnight. The resulting white powder was continuously treated with ethanol (150 mL) for 16 days using a Soxhlet extractor to remove the organic templating agent and afford the corresponding ionic liquid, and amine-modified COK-12 supports 5.10 and 5.11, in 93%, 90% yield, respectively.

6.5.4 General procedure for the synthesis of hybrid ionic liquid-amine modified COK-12 support (5.12).

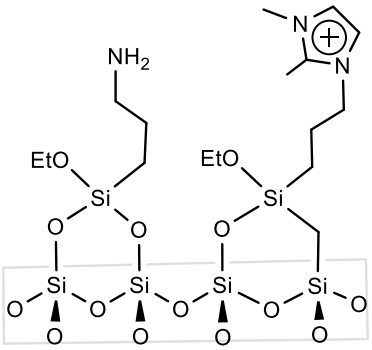

5.12

The ionic liquid-amine hybrid COK-12 support **5.12** was prepared as described above by conducting the hydrolysis with sodium silicate solution (27 wt% SiO_2) diluted with water together with a mixture of 5 mol% each of 1,2-dimethyl-3-(3-(triethoxysilyl)propyl)-1H-imidazol-3-ium chloride and triethoxysilylpropylamine to afford the product **5.12**.

6.5.5 The general procedure of Soxhlet extraction

The solid material with a surfactant template was placed in thimble of a Soxhlet extraction apparatus. A continuous extraction process was carried out using a 150 mL ethanol reservoir for a specific duration. The amount of extracted surfactant was observed by removing the solvent in the reservoir and weighing the remaining solid. Extraction was continued until no more surfactant was removed. The solid was then retrieved from the Soxhlet thimble and dried in an oven at 50 °C for 24 hours.

6.5.6 General Synthesis of COK-12 and modified COK-12 stabilised ruthenium nanoparticles (5.13), (5.14), (5.15) and (5.16).

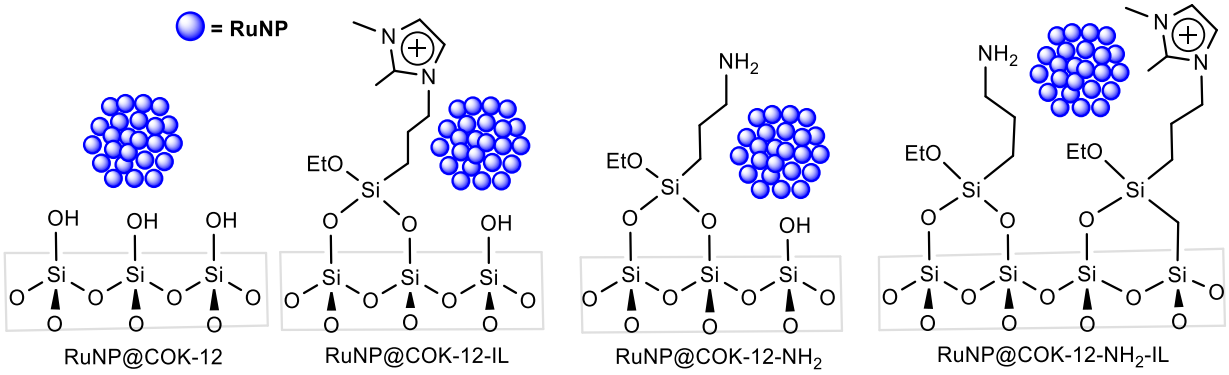

5.13 **5.14** **5.15** **5.16**

A solution of $RuCl_3 \cdot 3H_2O$ (0.064 g, 0.3 mmol) in water (2 mL) was added to a mixture of the mesoporous silica materials **5.8**, **5.10**, **5.11**, **5.12** (0.50 g) in water (5 mL). After stirring for 21 h at room temperature, the water was removed under reduced pressure to afford a grey solid, which was resuspended in ethanol (5 mL) and treated dropwise with a solution of $NaBH_4$ (0.07 g, 21 mmol) in water (2 mL). The resulting black suspension was stirred at room temperature overnight, filtered through a frit, and the final black solid was washed with water, ethanol, and diethyl ether. The product was then dried in an oven at 50 °C for 2 hours to afford a fine black powder of **5.13, 5.14, 5.15, 5.16**.

6.5.7 Synthesis of modified COK-12 stabilised Platinium nanoparticles (5.17).

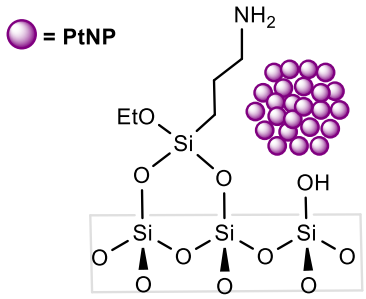

5.17

The synthesis of PtNP@COK-12-NH_2 **5.17** was achieved by adding a solution of $K_2[PtCl_4]$ (0.12 g, 0.3 mmol) in water (2 mL) to a mixture of the mesoporous silica material COK-12-NH_2(0.50 g) in 5 mL water **5.11**. After stirring for 21 h at room temperature, the water was removed under reduced pressure to afford a grey solid. The resulting $PtCl_4$@COK-12-NH_2 was resuspended in ethanol (5 mL) and treated dropwise with a solution of $NaBH_4$ (0.07 g, 21 mmol) in water (3 mL). The resulting grey suspension was stirred at room temperature overnight, filtered through a frit, and the final solid was washed with water, ethanol, and diethyl ether. The powder was then dried in an oven at 50 ^oC for two hours to afford **5.17** as a fine black powder.

6.5.8 Ruthenium and Platinium Nanoparticle-Catalysed Hydrolysis of Sodium Borohydride.

Comparative catalytic hydrolysis reactions were conducted in water at the appropriate temperature in a 50 mL round bottom flask. The flask was charged with a stir bar, an appropriate quantity of catalyst **5.15**, **5.17** (0.2 mol%) and $NaBH_4$ (0.021 g, 0.57 mmol) and fitted with a gas outlet connected to the top of an inverted water-filled burette. The flask was stabilised at 303 K, and the reaction was initiated by adding water (2 mL), immediately sealing the system by replacing the gas outlet, opening the tap of the water-filled burette and recording the time zero volume. Gas evolution began immediately, and the progress of the reaction was monitored by measuring the amount of gas generated by recording the volume of water displaced from the burette at regular time intervals (15 sec). The optimum turnover frequency for each catalyst was determined by conducting experiments with catalyst loadings ranging from 0.08 – 0.32 mol% at 303 K and measuring the hydrogen generated, as described above.[23]

6.6 Reference

1. K. N. Wood and G. Teeter, *ACS Appl. Energy Mater.*, 2018, **1**, 4493–4504.
2. M. Schmid, H.-P. Steinrück and J. M. Gottfried, *Surf. Interface Anal.*, 2014, **46**, 505–511.
3. W. Chen, Y. Zhang, L. Zhu, J. Lan, R. Xie and J. You, *J. Am. Chem. Soc.*, 2007, **129**, 13879–13886.
4. S. Doherty, J. G. Knight, T. Backhouse, E. Abood, H. Alshaikh, I. J. S. Fairlamb, R. A. Bourne, T. W. Chamberlain and R. Stones, *Green Chem.*, 2017, **19**, 1635–1641.
5. Y.-F. Zeng, Y.-N. Li, M.-X. Zhou, S. Han, Y. Guo and Z. Wang, *Adv. Synth. Catal.*, 2022, **364**, 3664–3669.
6. K. Murugesan, V. G. Chandrashekhar, C. Kreyenschulte, M. Beller and R. V. Jagadeesh, *Angew. Chem. Int. Ed.*, 2020, **59**, 17408–17412.
7. W. Ai, X. Du, Y. Yang, Z. Zheng, L. Zhai, B. Ma, S. Cui, P. Li, L. Mi and L. Qu, *J. Mater. Chem. A*, 2022, **10**, 18602–18608.
8. V. Vermaak, H. C. M. Vosloo and A. J. Swarts, *Adv. Synth. Catal.*, 2020, **362**, 5788–5793.
9. X. Jin, X. Du, G. Liu, B. Jin, K. Cao, F. Chen and Q. Huang, *J. Hazard. Mater.*, 2023, **459**, 132242.
10. E. Falk, V. C. M. Gasser and B. Morandi, *Org. Lett.*, 2021, **23**, 1422–1426.
11. Y. Wang, B. Dong, Z. Wang, X. Cong and X. Bi, *Org. Lett.*, 2019, **21**, 3631–3634.
12. Y.-G. Ji, K. Wei, T. Liu, L. Wu and W.-H. Zhang, *Adv. Synth. Catal.*, 2017, **359**, 933–940.
13. C. A. Lawson, A. P. Dominey, G. D. Williams and J. A. Murphy, *Chem. Commun.*, 2020, **56**, 11445–11448.
14. S. Zhang, H. Xu, J. He and Y. Zhang, *Adv. Synth. Catal.*, 2021, **363**, 5319–5329.
15. C. Gao, F. Lyu and Y. Yin, *Chem. Rev.*, 2021, **121**, 834–881.
16. D. Bhattacharyya, S. Nandi, P. Adhikari, B. K. Sarmah, M. Konwar and A. Das, *Org. Biomol. Chem.*, 2020, **18**, 1214–1220.
17. Y. Xia, X. Sun, L. Zhang, K. Luo and L. Wu, *Chem. – Eur. J.*, 2016, **22**, 17151–17155.
18. M. Pang, J.-Y. Chen, S. Zhang, R.-Z. Liao, C.-H. Tung and W. Wang, *Nat. Commun.*, 2020, **11**, 1249.
19. R. Pothikumar, V. T. Bhat and K. Namitharan, *Chem. Commun.*, 2020, **56**, 13607–13610.
20. H. Li, Y. Yang, X. Jing, C. He and C. Duan, *Chem. – Asian J.*, 2021, **16**, 1237–1244.

21. P. K. Giesbrecht, D. B. Nemez and D. E. Herbert, *Chem. Commun.*, 2018, **54**, 338–341.

22. D. O. González-Abrego, F. J. Zuno-Cruz, M. Carpio-Granillo, N. Andrade-López, J. Cruz-Borbolla, C. Martínez-Macias, D. Mendoza-Espinosa, M. J. Rosales-Hoz, M. A. Leyva, J. R. Torres-Lubián, J. A. López-Jiménez, V. Jancik and G. Sánchez-Cabrera, *Polyhedron*, 2017, **137**, 97–111.

23**.** H. Alharbi, *Catalysis of Organic Reactions Using Immobilised Transition Metal Nanoparticles*, PhD thesis, Newcastle University, 2022.

24. F. E. Stals, *Amine Decorated Polymer Immobilised Ionic Liquid Stabilised Ruthenium Nanoparticles,* MSc paper, Newcastle University, 2017.

25. R. Paterson, A. A. Alharbi, C. Wills, C. Dixon, L. Šiller, T. W. Chamberlain, A. Griffiths, S. M. Collins, K. Wu, M. D. Simmons, R. A. Bourne, K. R. J. Lovelock, J. Seymour, J. G. Knight and S. Doherty, *Mol. Catal.*, 2022, **528**, 112476.

26. A. A. Alharbi, C. Wills, T. W. Chamberlain, R. A. Bourne, A. Griffiths, S. M. Collins, K. Wu, P. Mueller, J. G. Knight and S. Doherty, *ChemCatChem*, 2023, **15**, e202300418.